University of Pennsylvania
ScholarlyCommons

Publicly Accessible Penn Dissertations

1-1-2015

Polymer Structure and Dynamics in Nano-Confinements: Polymer Nanocomposiets and Cylindrical Confinement

Wei-Shao Tung
University of Pennsylvania, newplayersayit@gmail.com

Follow this and additional works at: http://repository.upenn.edu/edissertations

 Part of the Engineering Commons, and the Physics Commons

Recommended Citation
Tung, Wei-Shao, "Polymer Structure and Dynamics in Nano-Confinements: Polymer Nanocomposiets and Cylindrical Confinement" (2015). *Publicly Accessible Penn Dissertations*. 1153.
http://repository.upenn.edu/edissertations/1153

This paper is posted at ScholarlyCommons. http://repository.upenn.edu/edissertations/1153
For more information, please contact libraryrepository@pobox.upenn.edu.

Polymer Structure and Dynamics in Nano-Confinements: Polymer Nanocomposiets and Cylindrical Confinement

Abstract
Polymers have been used for variety of products for decades, and the usage of polymer products is still growing. Innovative methods (e.g. adding other materials) have been created to improve properties of polymer products to fulfill targeted requirements for applications and many of these strategies impose confinement on polymers. As nanotechnology and manufacturing technology advance, the confinement lengths keep shrinking and approaching the size of a single chain. While the final properties of polymer products are important for the applications, understanding how polymers behave at the microscopic scale is also critical for manufacturing and designing polymer products, especially when the manufacturing methods or the final states of polymers impose nano-confinement.

To understand how polymers behave in nano-confinement, two main types of confinement are studied in this dissertation: polymer nanocomposites involving spherical and cylindrical nanoparticles and nanoconfinement directly imposed by impenetrable planar and cylindrical walls. Polymer structure can be affected when adding nanoparticles into polymer matrices, which may lead to a change in dynamics. Small angle neutron scattering is applied to study how polymer structure is affected by carbon nanotubes (CNTs). Polymer chains retain a Gaussian chain conformation, and the chain size expands (~ 30% for 10 wt% SWCNT loading) when the chain size (Rg) is larger than the radius of the filler (r) and the SWCNT mesh size is comparable to Rg. Chain expansion is not observed for MWCNT, where r ~ Rg. Moreover, when the SWCNT mesh is anisotropic the polymer conformation is anisotropic with greater expansion perpendicular to the SWCNT alignment, which is the direction with small mesh size.

The temperature dependence of polymer tracer diffusion is investigated. In MWCNT/PS nanocomposites, a diffusion minimum is observed with increasing nanotube concentration at 7 temperatures from 152Â°C to 214Â°C. The diffusion minimum is shallower at higher temperature, which indicates the mechanism that slows polymer diffusion is less pronounced at higher temperatures. At fixed concentration the temperature dependence data fit the WLF equation. The temperature dependence of polymer tracer diffusion in silica/PS nanocomposites also obeys the WLF equation. However, the monotonic decrease of the tracer diffusion when silica concentration increases is more pronounced at higher temperature, which shows an opposite trend than the MWCNT/PS system. The thermal expansion coefficients of free volume (αf), obtained by fitting the temperature dependence data to the WLF equation, slightly increases when silica concentration increases. In contrast, the αf obtained from the time-temperature superposition of the rheology data decreases with silica concentration increases and shows an abrupt change at the percolation concentration of silica NPs. This finding suggests that the mechanical response of silica NPs contributes to the linear viscoelastic response.

The impacts of nanoconfinement imposed by impenetrable planar or cylindrical walls were investigated by molecular dynamics simulations and experiments. The polymer conformation in thin film or cylindrical confinement is compressed parallel to the confining direction and slightly elongated perpendicular to the confining direction. The number of entanglement per polymer (Z) decreases as the pore diameter decreases. A theory, which assumes that the preferential orientation of the end-to-end vector can be directly transferred to the preferential orientation of primitive path steps, compares favorably to our simulations as a function of pore diameter.

This dissertation is available at ScholarlyCommons: http://repository.upenn.edu/edissertations/1153

From the simulation, we also found that the local relaxation is accelerated along the cylindrical axis and is retarded perpendicular to the cylindrical axis. Combining the change in chain conformation, entanglement density, and the local relaxation, we found an increase for the center-of-mass polymer diffusion (Drep) in cylindrical confinement via the reptation model. The center-of-mass diffusion coefficients (DMSD) are also directly calculated from the mean-squared displacement in the diffusive regime, and are compared to Drep. At modest confinements, Drep agrees with DMSD, which suggests the applicability of the reptation model. At strong confinement, Drep > DMSD implies the limitations of the reptation model. The center-of-mass diffusion coefficient (Dexp) is also measured experimentally using diffusing deuterated polystyrene into porous anodized aluminum oxide membranes pre-infiltrated by polystyrene. As the pore diameter decreases Dexp increases in qualitative agreement with the molecular dynamics simulations (Drep and DMSD).

The local relaxations of polymers in cylindrical confinement are measured experimentally using QENS. When polystyrene is confined in cylindrical nanopores, the segmental relaxations slow down non-monotonically with pore size. This trend is also observed for EISF, which measured the fraction of non-diffusing hydrogen within the probing time scale of QENS. At last, we found that when d/Ree > 2, hydrogen has the lowest MSD. When the pore size is decreasing to 2 > d/Ree > 1, MSD is slightly higher but still lower than that for bulk PS. When the pore size is further decrease to d/Ree < 1, MSD decreases again. This non-monotonic change of MSD can be explained by combining the effect of cylindrical confinement on the local segmental relaxation and non-diffusing hydrogen.

This thesis provides the first study of polymer structure in polymer nanocomposites with high-aspect ratio nanoparticles and the first systematic computer simulation study for polymer confined in cylindrical confinements. These studies contribute to the understanding of the physics of confined polymers and correlations between changes in structure and dynamics.

Degree Type
Dissertation

Degree Name
Doctor of Philosophy (PhD)

Graduate Group
Materials Science & Engineering

First Advisor
Karen I. Winey

Keywords
Polymer Diffusion, Polymer Nanocomposites, Polymer Physics, Polymer Simulation, Polymer Structure, Polymer under Confinement

Subject Categories
Engineering | Physics

This dissertation is available at ScholarlyCommons: http://repository.upenn.edu/edissertations/1153

POLYMER STRUCTURE AND DYNAMICS IN NANO-CONFINEMENTS: POLYMER NANOCOMPOSIETS AND CYLINDRICAL CONFINEMENT

Wei-Shao Tung

A DISSERTATION

in

Materials Science and Engineering

Presented to the Faculties of the University of Pennsylvania

in Partial Fulfillment of the Requirement for the Degree of Doctor of Philosophy

2015

Supervisor of Dissertation

_____

Karen I. Winey, Professor, Materials Science and Engineering

Graduate Group Chairperson

_____

Shu Yang, Professor, Materials Science and Engineering

Dissertation Committee

Russell J. Composto, Professor, Materials Science and Engineering

Nigel Clarke, Professor, Professor, Physics and Astronomy, University of Sheffield

Robert A. Riggleman, Chemical and Biomolecular Engineering

DEDICATION

This dissertation is dedicated to my parents, Tien-Yu Ho and Chia-Tien Tun. You are supportive in every aspect and every stage of my life. You encourage me when I am frustrated and depressed; you guide me when I am perplexed. Now, I want to share the joy of this achievement with you.

ACKNOWLEDGEMENT

First of all, I would like to thank my advisor, Professor Karen I. Winey, for providing me a motivating project to start my PhD and giving me clear instructions and constructive suggestions on all my projects along my PhD career. Through discussing and meeting with her, I learned the correct attitude to conduct scientific research and shaped myself to become a qualified researcher. She taught me how to systematically study and answer scientific questions, and organize meaningful projects when I pursued new directions. I am proud of myself not only because the number of papers I published or the amount of work I accomplished while being a member of her group, but also because I have tried my best to achieve her standard of a successful researcher.

I would also like to thank my dissertation committee members, Professor Russell J. Composto, Professor Nigel Clarke, and Professor Robert A. Riggleman, for providing me in-depth scientific advice and feedback on my works. Especially, I would like to thank Russell, an expert in polymer physics and elastic recoil detection (ERD), for teaching me knowledge about polymer physics and polymer diffusion experiments which heavily rely upon the ERD technique. I would like to thank Nigel for assisting my on

learning concepts of neutron scattering, conducting neutron experiments and analyzing neutron scattering data. At last, I would like to thank Robert for providing an insightful course of computer simulations, especially on simulations for soft matters, and all his assistance and support when I tried to continue my final project of his course, which later on, became an important portion of my thesis.

I had a really good time in the Winey research group and I learned a lot from all the group members who ever joined in the past four years. I would like to thank our former PhD students and post-docs, Dr. Davis Salas-de la Cruz, Dr. Jae-Hong Choi, Dr. Rose Mutiso, Dr. Francisco Buitrago, Dr. Michael O'Reilly, and Dr. Michelle Seitz for their guidance and assistance on my experiments, qualify exams, research proposals, and various kinds of presentations. I would also like to thank the current Winey group members, Sharon Sharick, Robert Middleton, Han-Chang Yang, Edward Trigg, and Dr. Philip Griffin for consistently discussing science with me, tolerating me of my messy desk and occupying office spaces, helping me proof-read my manuscripts and presentations, and more importantly encouraging me whenever I am depressed or feel stressful along my PhD career.

Outside of the Winey research group, I also obtained a lot of help from members

of other research groups. It is impossible to list out all of them here. However, I would like to especially thank Dr. Jihoon Choi, Dr. Hyun-Su Lee, Dr. Matthew Caprizzo, Dr. Mike Hore and Chia-Chun Lin, who are former or current members of Composto's research group, for their assistant with experiments and providing ideas for my research projects. I would also like to thank Vikki Bird and Dr. Argyrios Karatrantos in Clarke's research group for scientific discussions and assistance with neutron scattering experiments. Lastly, I would like to thank Amit Shavit for assisting me with computer simulations and all members in Professor Robert Riggleman's research group for sharing the computer cluster resources with me.

Besides science and lab work, I also gained a lot of help for my daily working life in the department. I would like to thank Pat Overend, Irene Clements, Vicky Lee, Fred Helming, Raymond Shao, and Enrique Vargas for their constant and kind help. I would like to especially thank Dr. Douglas Yates for providing a clear instruction on conducting ERD experiments and excellent maintenance on the ERD instrument. I would also like to thank Steve Szewczyk for setting up a better vacuum oven system and training me on a variety of instruments. Moreover, I would like to thank Dr. Jamie Ford for training me on electron microscopy.

Friendship is another important element to my successful PhD career, especially for a man like me who is thousands miles away from his family and hometown. I would like to thank all friends I met here in Philadelphia for accompanying me and helping me in my daily life. I would like to thank Chi-Mon Chen and Chien-Hua Lai for always helping me and giving me guidance when I am struggling with my PhD life. My best friends, Chia-Chun Lin, Sheng-Shun Sha, Frank Streller, Dr. Carlos Octavio Aspetti, Dr. Matteo Cargnello, are an irreplaceable part of my PhD life. Together we had a lot of fun and travelled to many different places together. They are the key to my happy and joyful PhD life.

At last, I would like to thank my family for their constant support and love. My parents sacrificed a lot to provide their children the best opportunity of education and living environment so that I can focus on my courses and research. Without their support, I would never have a chance to study in US and accomplish my PhD.

ABSTRACT

POLYMER STRUCTURE AND DYNAMICS IN NANO-CONFINEMENTS:

POLYMER NANOCOMPOSIETS AND CYLINDRICAL CONFINEMENT

Wei-Shao Tung

Karen I. Winey

Polymers have been used for variety of products for decades, and the usage of polymer products is still growing. Innovative methods (e.g. adding other materials) have been created to improve properties of polymer products to fulfill targeted requirements for applications and many of these strategies impose confinement on polymers. As nanotechnology and manufacturing technology advance, the confinement lengths keep shrinking and approaching the size of a single chain. While the final properties of polymer products are important for the applications, understanding how polymers behave at the microscopic scale is also critical for manufacturing and designing polymer products, especially when the manufacturing methods or the final states of polymers impose nano-confinement.

To understand how polymers behave in nano-confinement, two main types of

confinement are studied in this dissertation: polymer nanocomposites involving spherical and cylindrical nanoparticles and nanoconfinement directly imposed by impenetrable planar and cylindrical walls. Polymer structure can be affected when adding nanoparticles into polymer matrices, which may lead to a change in dynamics. Small angle neutron scattering is applied to study how polymer structure is affected by carbon nanotubes (CNTs). Polymer chains retain a Gaussian chain conformation, and the chain size expands (~ 30% for 10 wt% SWCNT loading) when the chain size (R_g) is larger than the radius of the filler (r) and the SWCNT mesh size is comparable to R_g. Chain expansion is not observed for MWCNT, where $r \sim R_g$. Moreover, when the SWCNT mesh is anisotropic the polymer conformation is anisotropic with greater expansion perpendicular to the SWCNT alignment, which is the direction with small mesh size.

The temperature dependence of polymer tracer diffusion is investigated. In MWCNT/PS nanocomposites, a diffusion minimum is observed with increasing nanotube concentration at 7 temperatures from 152°C to 214°C. The diffusion minimum is shallower at higher temperature, which indicates the mechanism that slows polymer diffusion is less pronounced at higher temperatures. At fixed concentration the temperature dependence data fit the WLF equation. The temperature dependence of

polymer tracer diffusion in silica/PS nanocomposites also obeys the WLF equation. However, the monotonic decrease of the tracer diffusion when silica concentration increases is more pronounced at higher temperature, which shows an opposite trend than the MWCNT/PS system. The thermal expansion coefficients of free volume (α_f), obtained by fitting the temperature dependence data to the WLF equation, slightly increases when silica concentration increases. In contrast, the α_f obtained from the time-temperature superposition of the rheology data decreases with silica concentration increases and shows an abrupt change at the percolation concentration of silica NPs. This finding suggests that the mechanical response of silica NPs contributes to the linear viscoelastic response.

The impacts of nanoconfinement imposed by impenetrable planar or cylindrical walls were investigated by molecular dynamics simulations and experiments. The polymer conformation in thin film or cylindrical confinement is compressed parallel to the confining direction and slightly elongated perpendicular to the confining direction. The number of entanglement per polymer (Z) decreases as the pore diameter decreases. A theory, which assumes that the preferential orientation of the end-to-end vector can be directly transferred to the preferential orientation of primitive path steps, compares

favorably to our simulations as a function of pore diameter.

From the simulation, we also found that the local relaxation is accelerated along the cylindrical axis and is retarded perpendicular to the cylindrical axis. Combining the change in chain conformation, entanglement density, and the local relaxation, we found an increase for the center-of-mass polymer diffusion (D_{rep}) in cylindrical confinement via the reptation model. The center-of-mass diffusion coefficients (D_{MSD}) are also directly calculated from the mean-squared displacement in the diffusive regime, and are compared to D_{rep}. At modest confinements, D_{rep} agrees with D_{MSD}, which suggests the applicability of the reptation model. At strong confinement, $D_{rep} > D_{MSD}$ implies the limitations of the reptation model. The center-of-mass diffusion coefficient (D_{exp}) is also measured experimentally using diffusing deuterated polystyrene into porous anodized aluminum oxide membranes pre-infiltrated by polystyrene. As the pore diameter decreases D_{exp} increases in qualitative agreement with the molecular dynamics simulations (D_{rep} and D_{MSD}).

The local relaxations of polymers in cylindrical confinement are measured experimentally using QENS. When polystyrene is confined in cylindrical nanopores, the segmental relaxations slow down non-monotonically with pore size. This trend is also

observed for EISF, which measured the fraction of non-diffusing hydrogen within the probing time scale of QENS. At last, we found that when $d/R_{ee} > 2$, hydrogen has the lowest MSD. When the pore size is decreasing to $2 > d/R_{ee} > 1$, MSD is slightly higher but still lower than that for bulk PS. When the pore size is further decrease to $d/R_{ee} < 1$, MSD decreases again. This non-monotonic change of MSD can be explained by combining the effect of cylindrical confinement on the local segmental relaxation and non-diffusing hydrogen.

This thesis provides the first study of polymer structure in polymer nanocomposites with high-aspect ratio nanoparticles and the first systematic computer simulation study for polymer confined in cylindrical confinements. These studies contribute to the understanding of the physics of confined polymers and correlations between changes in structure and dynamics.

Table of Contents

DEDICATION ii

ACKNOWLEDGEMENT iii

ABSTRACT vii

Table of Contents xii

List of Tables xx

List of Figures xxi

Chapter 1 Introduction 1

1.1. Nanoparticle/Polymer nanocomposites (PNCs) 5

1.1.1. Structure of Polymers in PNCs 7

1.1.2. Temperature Dependence of Polymer Diffusion in PNCs 9

1.2. Polymers under Cylindrical Nanoconfinements 13

1.2.1. Polymer Structure in Thin Film and Cylindrical Nanoconfinement 14

1.2.2. Polymer Dynamics in Cylindrical Nanocomfinements 15

1.3 References 17

Chapter 2 Polymer Structure in Carbon Nanotube/Polystyrene Nanocomposite 27

2.1 Introduction 27

2.2. Experimental Methods 31

2.2.1. Materials 31

2.2.2. Nanocomposites Preparation 32

2.2.3. Small Angle Neutron Scattering (SANS) 35

2.2.4. Glass Transition Temperature 37
2.2.5. Electrical Measurements 38
2.3. Contrast Matching and Scattering Model 40
2.3.1. Contrast Matching CNTs and Polymer Matrix 40
2.3.2. Scattering Model 41
2.3.3. Method for Fitting Scattering Model to SANS Data 46
2.4. Results and Discussion 48
2.4.1. Homopolymer 48
2.4.2. Contrast Matching in 1wt% SWCNT/dPS + hPS Nanocomposites 49
2.4.3. CNT/dPS + hPS Nanocomposites as a Function of CNT Concentration 52
2.4.4. Radius of Gyration in CNT/dPS + hPS Nanocomposites 58
2.4.5 Scattering from Voids 61
2.5. Summary 62
2.6. References 63
Chapter 3 Polymer Structure in Aligned SWCNT/Polystyrene Nanocomposites 68
3.1. Introduction 68
3.2. Experimental Methods 69
3.2.1. Sample Preparation 69
3.2.2. Small Angle Neutron Scattering (SANS) 70
3.2.3. Small Angle X-ray Scattering (SAXS) 71
3.3. Data Analysis 71
3.3.1. Orthogonal Integration and the Fitting Model for SANS Data 71
3.3.2. Homopolymer Chain Conformations 73

3.3.3. SANS on Aligned SWCNT/dPS + PS Nanocomposites.....74
3.3.4. SAXS on Aligned SWCNT/dPS + PS Nanocomposites.....77
3.4. Results and Discussion 80
3.4.1. Anisotropic Rod Network Scattering.....80
3.4.2. Anisotropic Chain Conformation.....82
3.4.3. Theoretical Analysis for Mesh Sizes in Anisotropic Rod Networks.....84
3.5. Summary.....87
3.6. References.....88
Chapter 4 Temperature Dependence of Polymer Diffusion in MWCNT/PS Nanocomposites.....90
4.1 Introduction.....90
4.2 Experimental Methods.....94
4.2.1 Materials 94
4.2.2 Bilayer sample preparation 95
4.2.3 Elastic Recoil Detection (ERD).....96
4.3 Results and discussion 100
4.3.1 Temperature dependence of diffusion minimum 100
4.3.2 Temperature dependence of tracer diffusion coefficients at fixed MWCNT loadings 103
4.4 Summary.....110
4.5 References.....111
Chapter 5 Temperature Dependence of Polymer Dynamics in Silica/Polystyrene Nanocomposites: Comparison between Diffusion Study and Rheology Study.....117

5.1. Introduction....117
5.2. Experimental methods....124
5.2.1. Materials and Nanocomposites Fabrication....124
5.2.2. Elastic Recoil Detection to Measure Tracer Diffusion....125
5.2.3. Rheology Test....129
5.3. Results and discussion....130
5.3.1. Temperature Dependence of the Tracer Diffusion....130
5.3.2. Linear Viscoelasticity in Silica/PS Nanocomposites....133
5.3.3. Comparison between the Diffusion Study and the Rheology Study....138
5.3.4. Discussion on Polymer Diffusion in Silica/PS Nanocomposites....140
5.4. Summary....142
5.5. References....144
Chapter 6 Entanglement Reduction and Anisotropic Chain and Primitive Path Conformations in Polymer Melts in Thin Film and Cylindrical Confinement....149
6.1. Introduction....149
6.2. Simulations of Confined Polymers....152
6.3. Simulation Results....158
6.3.1. Chain End-to-end Distance (R_{ee}) in Confinement....160
6.3.2. Orientational Probability Distribution for Primitive Path Steps....161
6.3.3. Entanglements per Chain (Z)....162
6.4. Summary....166
6.5. References....167
Chapter 7 Local Polymer Dynamics and Diffusion in Cylindrical

Nano-Confinement.....171
7.1. introduction.....171
7.2. Molecular Dynamics Simulations of Confined Polymers 174
7.3. Experimental Methods.....175
7.3.1 Materials 175
7.3.2. Bilayer Sample Preparation 177
7.3.3. Tracer Diffusion Coefficients.....178
7.4. Results and Discussions.....182
7.4.1. Mean Square Displacement (MSD) vs. LJ time 182
7.4.2. Monomer Density and MSD vs. the Distance from the Confinement Wall.....185
7.4.3. Self-Intermediate Structure Factor $F_s(Q, t)$.....189
7.4.4. Polymer Diffusion.....194
7.5. Summary.....199
7.6. references 201
Chapter 8 Local Dynamics of Polystyrene Confined in AAO Nanopores Probed by Quasi-Elastic Neutron Scattering.....207
8.1. Introduction.....207
8.2. Experimental Methods.....212
8.2.1. Sample Preparation 212
8.2.2 Quasi-Elastic Neutron Scattering.....215
8.3. Theoretical Background.....216
8.4. results and discussion.....219

8.4.1. FWHM for the Slow Relaxation Mode.....219
8.4.2. Elastic Incoherent Scattering Factor (EISF) 226
8.4.3. Mean Square Displacement vs. Temperature.....231
8.5. summary.....237
8.6. references 238
Chapter 9 Summary and Future Work 244
9.1 Conclusion 244
9.2 Future Directions 252
9.2.1. Chain Conformation in MWCNT/PS Nanocomposites with $r/R_g < 1$ ...252
9.2.2 Chain Conformation in Nanorod/Polymer Nanocomposites with Favorable Interaction.....253
9.2.3. Polymer Structure and Dynamics in Cylindrical Nanoconfinement with Attractive Interaction.....253
9.2.4. Computer Simulations of CNT/Polymer Nanocomposites.....254
9.2.5. Theoretical Calculation or Computer Simulation for Polymers next to Flat or Curved Surfaces 255
Appendix A Carbon Nanotube Purification and CNT/PS Nanocomposites Fabrication 256
A.1. Materials.....256
A.2. CNT Purification.....259
A.3. Determining the wt% of CNT in CNT suspension: 264
A.4. Preparing CNT/PS Nanocomposites by the Coagulation Method 266
A.5. Determining Residual Fe Content.....271

A.6. Determining the CNT Bundle Size 272
A.7. References 273
Appendix B I-V Measurements on CNT/PS Nanocomposites 275
Appendix C Standard Operating Procedure for SpinLine 278
C.1. Overview of Procedure 278
C.2. Detailed Procedure 278
C.3. Issues to Consider 282
C.4. Standard Operating Conditions for Different Materials 282
Appendix D Fitting Uncertainty for ERD data 283
Appendix E Standard Operating Procedure for Rheometrics RSA-II Rheometer 284
E.1. Overview of Procedure 284
E.2. Detailed Procedure 284
E.3. Issues 289
Appendix F SEM Images of Anodized Aluminum Oxide Membranes 290
Appendix G Porosity of AAO membranes by ERD 291
Appendix H Effect of Monomer Density and Chain Length on Polymer Local Dynamics 293
Appendix I Polymer Chain Conformation for Polystyrene Confined in AAO Nanopores Using SANS 295
I.1. Sample Preparation and Characterization 295
I.2. Structure of Empty Membranes 296
I.3. scattering of Filled Membranes 298
I.4. Summary 302

I.5. References 302

List of Tables

Table 2.1. Characteristics of the single-walled and multi-walled carbon nanotubes. 33

Table 2.2. Sample information for contrast matching experiments and the study of the polymer conformation in CNT/PS nanocomposites with different CNT concentrations. SANS experiments were performed at Oak Ridge National Laboratory (ORNL), Institute Laue-Langevin (ILL), and National Institute of Standards and Technology (NIST). 34

Table 4.1. Weight averaged molecular weight, polydispersity index, and radius of gyration of the matrix polymer (PS) and the tracer polymer (dPS). 95

Table 6.1. Details about each simulation system for cylindrical and thin film confinement. All the length units are in σ..... 155

Table 6.2. Reduced density and accessible volume for the simulated systems..... 156

Table 7.1. Weight averaged molecular weight (M_w), PDI, end-to-end distance, and radius of gyration of the infiltrated polymers (PS) and the tracer polymer (dPS)..... 176

Table 8.1. Calculated maximum mass of infiltration and the final increases mass for PS, and the percentage of filling for different pore diameter samples 215

Table 8.2. Associated fitting results for D and τ for bulk PS and confined PS at 440K and 455K..... 224

Table 8.3. Results for R and ϕ obtained by fitting EISF vs. Q data to Equation 8.7..... 228

Table A.1. The above table shows an example of calculations done for 3 samples of a CNT/DMF solution. By averaging the mg CNT / mL DMF column, 1.859 mg CNT per mL DMF can be obtained..... 266

List of Figures

Figure 1.1. The random coil in the center of the figure represents the size of an amorphous polymer chain. The remaining schematics depict different types of confinements: (a) thin film, (b) nanostructure, (c) nanopore, and (d) nanofiller with confinement length approaching the size of polymer chains.[13] 3

Figure 1.2. (left) Tracer diffusion coefficients (*D*) in SWCNT/PS nanocomposites and silica/PS nanocomposites. In SWCNT/PS nanocomposites, *D* decreases with increasing CNT concentration and then increases above a critical CNT concentration. (*Macromolecules*, **2009**, *42* (21), 8365–8369). Copyright (2009) American Chemical Society (right) In silica/PS nanocomposites, *D* decreases monotonically as the volume fraction of spherical phenyl-capped silica nanoparticle increases.[14, 16] Reprinted with permission from (*Macromolecules*, **2011**, *44* (9), 3494–3501). Copyright (2011) American Chemical Society. 10

Figure 1.3. (a) Reduced polymer tracer diffusion in silica/PS nanocomposites for different tracer molecular weights as a function of interparticle distance normalized by $2R_g$. Reprinted with permission from (*Macromolecules*, **2011**, *44* (9), 3494–3501). Copyright (2011) American Chemical Society. (b)The master curve for silica/PS nanocomposites is extended to $ID/2R_g \sim 15$ by using tracers with smaller molecular weights and lower silica concentrations.[14, 60] Reprinted with permission from (*ACS Macro Lett.*, **2013**, *2* (6), 485–490). Copyright (2013) American Chemical Society. 11

Figure 2.1. Modulated DSC results provide T_g as a function of CNT concentration. The width of the second order transition is ~ 6-7 $^{\circ}$C in all the samples. 38

Figure 2.2. Schematic showing the relationship between the length scales probed (left) and the corresponding q regime along with the angular dependence of the scattering. When the probing length scale is greater (green) and smaller (red) than the mesh size (blue) formed by the CNTs, the expected angular dependencies are q^{-2} and q^{-1}, respectively..... 45

Figure 2.3. SANS scattering intensity for dPS/hPS homopolymer mixture with a volume ratio of dPS/hPS = 72.5/27.5. Equation 2.13 is fit to the data using $B = 0$. The low q upturn is described by the q^{-4} term (defect term) and the shoulder at $q \sim 0.01$Å $^{-1}$ is captured by the Debye function with $R_g = 9.50 \pm 0.03$ nm. 49

Figure 2.4. SANS scattering data for the contrast matching samples with 1wt% SWCNT and a range of dPS/hPS volume ratios. Equation 2.13 (solid line) is fit to these data with R_g as a shared parameter and $R_g = 9.69 \pm 0.02$ nm. The data are shifted for clarity..... 50

Figure 2.5. The plot of fitting parameters A and B (solid symbols) used in Figure 2.4 as a function of dPS volume fraction in the matrix. The parameter B is nearly constant for $x \sim$ 0.67 - 0.73. Although B is very small, $B > 0$ implies that perfect contrast matching is unachievable. Equation 2.16 (red line) and Equation 2.17 (blue line) were simultaneously fit. Equation 2.17 has a minimum at $x = 0.725$ that is selected as the contrast matching condition for subsequent nanocomposites. 51

Figure 2.6. SANS data (points) for SWCNT/dPS+hPS and MWCNT/dPS+hPS nanocomposites with the 72.5/27.5 dPS/hPS volume ratio and different CNT concentrations. Equation 15 (red lines) is overlayed for each data set and data are shifted for clarity..... 52

Figure 2.7. Fitting examples for the lowest (0.5wt%) and the highest (10wt%) CNT loadings for MWCNT/dPS+hPS (72.5/27.5) nanocomposites. The fitting curves broken into summations of different terms in Equation 2.15 are indicated in the legend. All three contributions are needed to represent the data and, as expected, the rod network gives a larger contribution at the higher MWCNT concentration. 53

Figure 2.8. (a) The prefactor B for the rod network term (q^{-2}) determined by fitting Equation 2.15 to the SANS data in Figure 2.6 for SWCNT/dPS+hPS (red diamond) and MWCNT/dPS+hPS (green square) nanocomposites. For homopolymers (blue circle), B is zero. 55

Figure 2.9. (a) The probability distribution of mesh sizes for SWCNT at different concentrations and 10wt% MWCNT, calculated from Equation 2.18. (b) Integration of dP/ds from s = 0 to 12 nm (shaded area) for SWCNTs and MWCNTs to correspond with the size range probed by the SANS experiments. 56

Figure 2.10. R_g for SWCNT/dPS+hPS and MWCNT/dPS+hPS nanocomposites versus CNT concentration. R_g is determined by fitting Equation 2.15 to the scattering data in Figure 2.6. For comparison, the R_g value for dPS/hPS (72.5/27.5) is included (*cf*. Figure 2.3). Error bars are directly from fitting. 58

Figure 2.11. Fitting parameter C as a function of CNT concentration. C is obtained by fitting Equation 2.15 globally to the reduced SANS data for the SWCNT/PS and MWCNT/PS nanocomposites with A' set as a shared variable. 61

Figure 3.1. (a) SANS data (low q configuration) for an aligned 3wt% SWCNT/dPS+PS nanocomposite. (b) $I(q)$ data from integrating over 25 degrees parallel and perpendicular to the direction of alignment for SWCNTs. Black lines are associated fitting to Equation 3.1.

Data are shifted for clarity. 72

Figure 3.2. SANS data from the extruded and annealed dPS+PS blend. $I(q)$ profiles correspond to scattering parallel and perpendicular to extrusion direction. Lines are the best fits to Equation 1 (A' as a shared fitting parameter; Φ_{cnt} and B set to zero) with the R_g values provided. 74

Figure 3.3. Fitting results of A and two R_gs used for cross references between different SWCNT concentrations. 75

Figure 3.4. Fits to SANS data by Equation 3.1 for SWCNT/dPS+PS nanocomposites (SWCNT concentration: 0.5wt% ~ 10wt%) with isotropic SWCNT meshes and anisotropic SWCNT meshes. Different degrees of alignment for anisotropic meshes are represented using Herman's orientation function, explained later. 0.5wt% and 3wt% samples with isotropic SWCNT orientation were not measured due to the limitation of available beam time. 77

Figure 3.5. (a) SAXS data for an aligned 6wt% SWCNT/dPS+PS nanocomposite with Herman's orientation parameter of -0.06. (b) $I(\phi)$ integrated from q ~ 0.01 to 0.12 $Å^{-1}$ versus the azimuthal angle (ϕ) for the 6wt% SWCNT/dPS+PS nanocomposite with different degrees of alignment (squares f_2 = -0.06 and circles f_2 = -0.13). 79

Figure 3.6. (a) B_{per}/B_{par} obtained from SANS and SAXS are plotted as a function of the Herman's orientation function from SAXS for aligned SWCNT/dPS+PS nanocomposites of various compositions. Lines are fits with a fixed intercept of 1 corresponding to isotropic samples. (b) Schematic of isotropic and aligned SWCNT rod networks, where the green circle represents the probing length scale of SANS and SAXS..... 81

Figure 3.7. (a) Polymer radii of gyration in isotropic and aligned SWCNT/dPS+PS

nanocomposites. The aligned nanocomposites have Herman's orientation function of -0.03 to -0.08. Lines are guides to the eye. (b) Schematic illustration of polymer chains in polymer melt with bulk Rg, in isotropic nanocomposites with isotropic expansion (Rgiso), and in anisotropic nanocomposites with anisotropic expansion (Rgper > Rgpar)..... 83

Figure 3.8. Probability distribution of aperture sizes (r) for isotropic and anisotropic rod networks (5v%; rod radius = 3.7nm). For anisotropic rod networks, distribution of aperture sizes on cross sections parallel and perpendicular to the fiber extrusion direction are shown. Shaded region represents the probing length scales of SANS and SAXS. 87

Figure 4.1. The depth profile of 680k dPS partially diffused into 2 wt% MWCNT/PS nanocomposites after annealing at 160 $^{\circ}$C for 15h and 40h. Lines correspond to the convolution of a Gaussian function and Equation 4.3, where h = 18 nm and the diffusion coefficients (D) are given in the figure. 97

Figure 4.2. Glass transition temperature and the breadth of the transition for MWCNT/PS nanocomposites as a function of MWCNT loading. 100

Figure 4.3. (a) Tracer diffusion coefficients of 680k dPS in MWCNT/PS nanocomposites as a function of MWCNT loadings at various temperatures. (b) Normalized tracer diffusion coefficients (D/D_0) for 680k dPS in MWCNT/PS nanocomposites. A diffusion minimum $(D/D_0)_{min}$ is present at every temperature at ~ 2 wt% and becomes less pronounced at higher temperature. Some data points represent duplicate samples and the standard deviation is shown, except when it is smaller than the size of the symbol. 101

Figure 4.4. Temperature dependence of tracer diffusion coefficients for 0.5, 2, and 6 wt% MWCNT/PS nanocomposites, plotted as D/T versus $1/(T-T_\infty)$ with T_∞ = 322 K. The red lines are best fits of the WLF equation (Equation 4.2) to the data and the values of C_2 are

given. These curves are vertically shifted for clarity. 105

Figure 4.5. Fitting results for C_1 and C_2 for all MWCNT concentrations, except 0.7 wt%. We include results from samples with 0.1 and 1 wt % MWCNT although the temperature range studied is narrower and, consequently, the error bars are larger. At 0.7 wt%, the temperature range is too narrow (only ~ 20°C) to have reliable fitting results. As can be seen in the figure, C_1 is approximately constant across the whole concentration, and C_2 shows a slight maximum at 2wt%. 105

Figure 5.1. (a) Schematic of an unannealed bilayer sample and an annealed sample with dPS diffusing into the silica/PS nanocomposites. (b) & (c) show example depth files for 532k dPS diffusing into silica/PS nanocomposites at 180°C. (b) For 5*v*% silica loadings the dPS depth profiles with two annealing times (160 and 300 mins) are fit with the same diffusion coefficient. (c) For 20*v*% silica loadings a surface peak is observed, and the portion of dPS diffusing into matrices with three annealing times (160, 300, and 600 mins) can be fit with the same diffusion coefficient. 128

Figure 5.2. (a) Tracer diffusion coefficients of 532k dPS diffusing into phenyl-capped silica/PS nanocomposites as a function of silica loadings at different temperatures ranging from 143°C to 197°C. (b) Tracer diffusion coefficients normalized by the tracer diffusion coefficient for 532k dPS into bulk PS homopolymer. 131

Figure 5.3. (a) Tracer diffusion coefficients for 532k dPS diffusing into silica/PS nanocomposites (0-50 v% silica) fit to the WLF equation (Equation 5.4) using a reference temperature is 168°C. D_0 is the tracer diffusion coefficient at the reference temperature. (b) Fitting parameter (B/f_0) from the WLF equation for nanocomposites are normalized by B/f_0 for homopolymer diffusion and plotted as a function of the silica concentration. 133

Figure 5.4. Master curves constructed by time-temperature-superposition for 265k PS and silica/PS nanocomposites with 10 *v*% and 20 *v*% silica loading. *G*' and *G*" are shifted vertically for clarity. 134

Figure 5.5. Master curves of *G'* and *G"* data using time-temperature superposition with the reference temperature at 170°C for 2 *v*%, 5 *v*%, 30 *v*%, and 40 *v*% samples. 135

Figure 5.6. Disentanglement time (τ_{rep}), zero shear viscosity (η), and the number of monomers in one entanglement strand (N_e) extracted from the rheology data are normalized by the corresponding values for 265k PS and plotted as a function of the silica concentration. Beyond 10*v*%, there is no crossover for *G*' and *G*" so that τ_{rep} and N_e cannot be obtained. 136

Figure 5.7. (a) Zero shear viscocity for silica/PS nanoccompoistes (0-40 v% silica) fit to the WLF equation (Equation 5.4) using a reference temperature of 170°C. η_0 is the zero shear viscosity at the reference temperature. (b) Fitting parameters (B/f_0) from the WLF equations for nanocomposites are normalized by B/f_0 from the homopolymer and plotted as a function of silica concentration. 138

Figure 5.8. Tracer diffusion coefficients at 168°C are normalized to the corresponding value for homopolymer and plotted together with $1/\eta \times N_e$ normalized to $1/\eta \times N_e$ for bulk PS extracted from the master curves using 170°C as reference temperature. 140

Figure 6.1. Representative configurations of the simulated systems and the corresponding primitive path networks (as obtained via the Z1 algorithm). The top pair of images correspond to a bulk configuration; the bottom pair to a cylindrically confined system, where the orientational ordering of the primitive paths along the cylinder is clear from visual inspection. 159

Figure 6.2. (a) Root-mean-square component of the end-to-end vector for cylindrical (solid blue line; circles) and thin-film (dashed red line; diamonds) confinement. Filled symbols are the simulation results of this work, and lines are the theoretical predictions (Equation 1 in our publication).[20] Upper points indicate components parallel to the surface and lower points indicate components normal to the surface, and the dash-dotted line indicates the bulk value of $R_{ee,\ bulk}/(3^{1/2})$. The confinement parameter, δ, is either the effective film thickness or cylinder diameter divided by the bulk root-mean-square end-to-end chain distance. (b) The same plot, but where additionally thin film simulation results from Refs. [13, 14] are included as open squares.[13-14] 161

Figure 6.3. Representative comparisons between theoretical (curves) and simulation (points) results for the orientational distribution of PP segments. (a) Thin film $f(\theta)$ for δ = 1.7 (solid curve; circles) and δ = 0.40 (dashed curve; squares). (b) Cylindrical confinement $f(\theta)$ for δ = 0.84 (solid curve; circles) and δ = 0.34 (dashed curve; squares)..... 162

Figure 6.4. (a) Normalized number of entanglements per chain for cylindrical (thick solid line; large circles) and thin-film (thick dashed line; large diamonds) confinement. Large points are the simulation results of this work, and the thick curves are the theoretical predictions (Equation 17 in our publication).[20] Light blue hexagons are ZZbulk as calculated by the CReTA algorithm for a subset of the cylindrically-confined systems.[26] (b) The same plot, but with additional data from the literature. Small diamonds are experimentally estimated data for three different length polymers in thin-film confinement from Ref. [3] and small squares are thin-film simulations from Ref. [15]. The two thin lower curves show the "anisotropic packing length" argument estimate for entanglement loss in cylinders (thin solid line) and films (thin dashed line) using the theoretically

predicted changes in chain end-to-end distances. 164

Figure 7.1. Depth profile of 400k dPS diffused into 200k PS-infiltrated AAO membranes with 80nm (a) and 18nm (b) nanopores after annealing at 160 °C for 6 h. Blue lines denote the surface peak due to the residual dPS on the membranes. The red lines correspond to the best fit of the experimental dPS volume fraction profile in the nanopores using Equation 7.3. For the narrow 18nm pores, the purple line captures the slower diffusion of dPS entering nanopores. The green lines are the summation of all curves (i.e., Equation 7.4 and residual dPS) 180

Figure 7.2. (a) Log(MSD_z) as a function of log(LJ time) obtained from MD simulations for bulk polymer and polymers under cylindrical confinement of diameter 20σ. From short time scale to long time scale, ballistic dynamics, Rouse dynamics, and the diffusive regime are observed. (b) $MSD_z/2t$ for bulk and cylindrically-confined polymers as a function of LJ time. A time-independent region is observed and diffusion coefficients are obtained from the average value across this diffusive regime. 184

Figure 7.3. (a) Monomer density for confined polymers versus the distance from wall for d = 10σ, 20σ, and 40σ. (b) Short-time MSDs (LJ time = 4.8) along the z axis (open symbols) and the x axis (filled symbols) are plotted as a function of the distance from the wall for d = 10σ, 20σ, and 40σ. Note that the scale for the distance from wall (r/σ) is larger in part b. 187

Figure 7.4. Self-intermediate structure factor $F_s(Q, t)$ for cylindrically-confined polymers (N = 350, $R_{ee} \sim 22.7\sigma$) along the x axis for $Q_x = 2\sigma^{-1}$ (a), $0.5\sigma^{-1}$ (b), and $0.1\sigma^{-1}$ (c) and along the z axis for $Q_z = 2\sigma^{-1}$ (d), $0.5\sigma^{-1}$ (e), and $0.1\sigma^{-1}$ (f). Arrows show the effect of increasing cylindrical confinement (smaller d) on $F_s(Q, t)$. 191

Figure 7.5. (a) Example fitting of $F_s(Q_z, t)$ for bulk polymers and cylindrically-confined polymers ($d = 10\sigma$) by Equation 7.6. (b) Normalized relaxation times from $F_s(Q, t)$ fits are plotted as a function of the diameter of confinement for monomers moving along the *x* and *z* directions. 194

Figure 7.6. Normalized parameters R_z^2, N_e, and $1/\tau z$ from the simulations are combined to predict the normalized $D_{rep,z}$ using the reptation model (Equation 7.2)..... 196

Figure 7.7. Normalized $D_{rep,z}$ from Figure 7.6(b) and $D_{MSD,z}$ obtained by averaging the long time values in Figure 7.2(b) are plotted together as a function of d_{eff}/R_{ee}. The tracer diffusion coefficients D_{exp} for 400kg/mol dPS diffusing into AAO nanopores pre-infiltrated with 200kg/mol PS with a range of pore diameters is normalized by the homopolymer diffusion and plotted as a function of d/R_{ee}. 197

Figure 8.1. Normalized mass of PS infiltrated into AAO membranes as a function of annealing time for different diameter nanopores. Mass is normalized by the porosity of the membranes, obtained from the elastic recoil detection experiments (Appendix G), so that y axis can also be viewed as the infiltration rate. 214

Figure 8.2. (a) fitting results of FWHM for the slow relaxation mode as a function of Q^2 for linear PS and PS confined in 55nm and 18nm nanopores. (b) Fitting results of FWHM for the slow relaxation mode as a function of Q^2 for PS confined in 35nm, 55nm, and 80nm nanopores. 220

Figure 8.3. (a) $FWHM_{slow}$ vs Q^2 for bulk PS at 455K and associated fitting to Equation 8.6 (b) $FWHM_{slow}$ vs Q^2 for PS confined in 55nm and 18nm diameter nanopores at 455K. Data at $Q^2 > 0.5 Å^{-2}$ are fit to Equation 8.6 to obtain an estimated waiting time τ_0..... 222

Figure 8.4. FWHMslow vs Q^2 for PS confined in 55nm and 80nm nanopores at 455K and

all samples at 440K and associated fitting to Equation 8.6. 225

Figure 8.5. (a) Normalized D and (b) Normalized τ as a function of nanopore diameter 226

Figure 8.6. (a) EISF for bulk PS and PS confined in 55nm and 18nm nanopores (b) EISF for bulk PS and PS confined in 80nm and 18nm nanopores..... 227

Figure 8.7. EISF as a function of Q for all samples and the associated fitting to Equation 8.7..... 229

Figure 8.8. (a)Normailized ϕ and (b) normalized R as a function of the pore diameter. 230

Figure 8.9. -3ln[$I_{el}(Q, T)/ I_{el}(Q, 50K)$] versus Q^2 for bulk PS and PS confined in nanopores and associated linear fitting for the lowest five Q values..... 232

Figure 8.10. (a) Mean square displacement as a function of temperature for bulk PS and confined PS. (b) The increase of mean square displacement above T_g for bulk PS and confined PS. 233

Figure A.1. If using a ceramic porous filter (right, above) no filter paper is needed. If using a normal filter with holes (left, above), choose filter paper that will not dissolve in strong acid. Attach vacuum hose to system. Make sure vacuum is working. Glass ceramic filter is strongly recommended. 262

Figure A.2. Dried CNTs in Al dishes. 265

Figure A.3. Resulting composites may look different depending on the wt% of CNTs. After filtering, wet composite are scraped off from the filter (Left). After drying, all composites should look uniform and black (middle). After pressing they should look black and shiny (right). 270

Figure B.1. Conductivity for SWCNT/dPS+hPS and MWCNT/dPS+hPS nanocomposites

as a function of CNT loading. 276

Figure B.2. Fitting the conductivity of SWCNT/dPS+hPS and MWCNT/dPS+hPS nanocomposites as a function of the CNT concentration with Equation S1 The percolation concentration is higher for SWCNTs (0.47v%) than MWCNTs (1.45v%). 277

Figure D.1. The depth profile of 680k dPS partially diffused into 0.5wt% MWCNT/PS nanocomposites after annealing at 160 $^{\circ}$C for 40 hours. Lines correspond to the convolution of a Gaussian function and Equation 4.3, where h = 18 nm and three different diffusion coefficients as given in the figure. This figure illustrates the uncertainty in fitting the diffusion coefficients using the depth profile with the convolution of Fick's second low and a Gaussian function. The uncertainty is about 10 %. The diffusion coefficients we obtained from the fitting is 2.7E-15 cm^2/s, and ± 10 % of that diffusion coefficient still provide relatively good fits. 283

Figure G.1. Counts of hydrogens measured from ERD for a 100% thick PS film and for a PS infiltrated AAO membranes with 55nm pore diameter. 292

Figure H.1. (a) Monomer density as a function of the distance from wall for d = 40 σ before and after scaling the simulation box. (b) MSD (T = 1, LJ time = 4.8) versus r along the z axis (empty symbol) and the x axis (filled symbol) for d = 40 σ before and after the scaling. 293

Figure H.2. (a) Monomer density versus r for 50N and 350N polymers confined in 10σ and 20σ cylindrical confinements. (b) MSD (T = 1, LJ time = 4.8) versus r along the z axis (empty symbol) and the x axis (filled symbol) for N = 50 and 350 polymers confined in 10σ and 20σ cylindrical confinements. 294

Figure I.1. (a) Schematic of incident neutron beam and AAO membranes. Beam

direction is parallel to the cylindrical axis of nanopores. (b) Neutron scattering intensities for empty membranes with 35nm, 55nm, and 80nm diameter nanopores. For each diameter, two individual membranes were measured. (c) Schematic of the top view of the membranes, showing hexagonal packing of nanopores as seen along the beam direction. 297

Figure I.2. Neutron scattering intensity for an empty 35nm membrane and two membranes with two degrees of infiltration of 400k dPS..... 299

Figure I.3. (a) Scattering intensities of an empty 35nm membrane and filled membranes with different dPS/hPS volume ratios. (b) Intensity (q = 0.00707 $Å^{-1}$) as a function of dPS volume fraction and associated fitting to Equation I.1. 301

Chapter 1

Introduction

Polymers have a very broad range of properties and applications since they were discovered centuries ago. People started to use polymers occurring in nature (e.g. natural rubber), and manufactured different products with them. In the mid twentieth centuries chemists started to synthesize polymers, which quickly lead to the commercialization of polymeric materials with low cost and ubiquitous presence in modern life. Early on scientists and engineers started to mix polymers with other materials, like ceramics or metals, to produce composite materials that maintain the advantages of materials of which they are composed. Moreover, as nanofabrication techniques advance, there are some circumstances where polymers are in extremely confined states, such as thin films. Scientists started to notice that polymer physics are different when polymers are mixing with other materials or in severely confined states, which may further broaden the properties of polymers and their applications. The topic of confinement has drawn a lot of research interest in the past twenty years,[1-13] and more research is needed to advance our understanding in this field.

The goal of this dissertation is to investigate the confinement effect on polymer structure and dynamics, and the two main kinds of confinements are polymer nanocomposites and cylindrical nanoconfinement. Polymer structure and dynamics are affected when exposed to different kinds of confinements.[13] The effect is more significant when the confinement length scale is comparable to the equilibrated polymer chain size, which is usually represented by the end-to-end distance (R_{ee}) or the radius of gyration (R_g).[13] There are four common types of confinements, namely thin films, nanostructures, nanopores, and nanofillers, as shown in Figure 1.1.[13] This thesis focuses on the confinement imposed by thin films, nanopores, and particularly nanofillers.

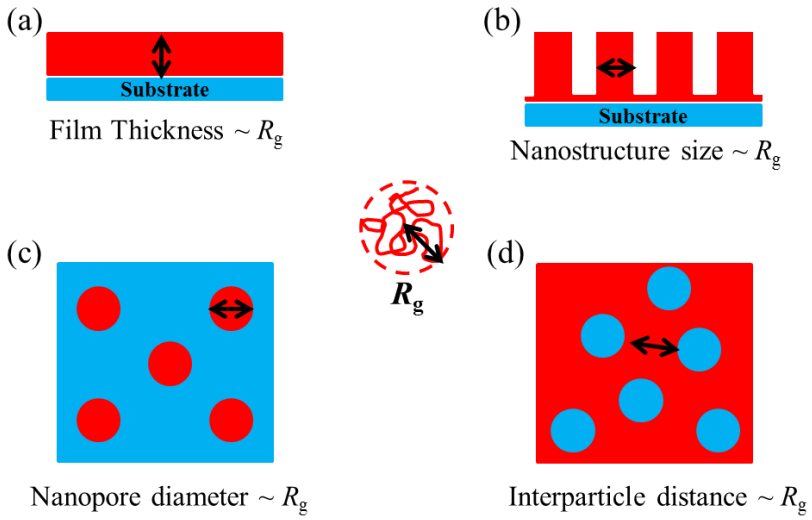

Figure 1.1. The random coil in the center of the figure represents the size of an amorphous polymer chain. The remaining schematics depict different types of confinements: (a) thin film, (b) nanostructure, (c) nanopore, and (d) nanofiller with confinement length approaching the size of polymer chains.[13]

In 2010 I joined the Materials World Network (MWN) research project, which is in collaboration with Professor Russell J. Composto in Department of Materials Science and Engineering at the University of Pennsylvania and Professor Nigel Clarke in Department of Physics and Astronomy at University of Sheffield, UK. At that time, the research team focused on investigating the effect of nanoparticles, particularly silica nanoparticles and carbon nanotubes, on polymer structure and dynamics using experimental techniques and computer simulations. Some very interesting results on polymer diffusions in nanoparticle/polymer (PNCs) nanocomposites had already been

published by two previous graduate students,[14-16] Dr. Sangah Gam and Dr. Minfang Mu. However, the mechanism of polymer diffusion in polymer nanocomposites and its correlation with the polymer structure were unclear. Therefore, I tried to expand our knowledge on polymer diffusion in PNCs by studying the temperature dependence of polymer tracer diffusion and linear viscoelastic properties in previously-studied polymer nanocomposites. I was also interested in connecting the effect of nanoparticles on polymer structure to polymer diffusion. Polymer nanocomposites with carbon nanotubes were especially interesting, because we observed a minimum in the polymer diffusion coefficient with increasing nanotube concentration in CNT/PS nanocomposites,[15-16] and also most of the research work focused on the effect of spherical nanoparticles on polymer structure.[17-21] Chapter 2 to 5 of my thesis will focus on the effect of nanoparticles on polymer structure and dynamics.

Polymer structure and dynamics under direct geometric confinement is also an interesting topic, and has been widely studied for the past 20 years.[13, 22-34] Since research on thin film confinement started earlier and has been more thoroughly conducted, I decided to work on the effect of cylindrical confinement using both experimental techniques and computer simulations. Professor Robert A. Riggleman's insightful course

about computer simulations sparked my interest and launched my simulation work. We established a collaborative project with Professor Riggleman to investigate polymer structure and dynamics under cylindrical nanoconfinements using course-grained molecular dynamics simulations. Later, we built a collaboration with Dr. Daniel M. Sussman in the Department of Physics and Astronomy at the University of Pennsylvania and Professor Kenneth S. Schweizer of the University of Illinois, Urbana to combine our simulation work and their theoretical work to successfully show the disentanglement behavior of polymer chains under severe confinements. My work on the effect of cylindrical confinement on polymer structure and dynamics will be introduced in Chapter 6 to 8.

1.1. NANOPARTICLE/POLYMER NANOCOMPOSITES (PNCS)

Polymer nanocomposites, which are composed of nanoparticles (e.g. spherical nanoparticles, nanotubes, nanowires, nanofibers, etc.) and polymer, have captured significant research interest because adding nanofillers can change the electrical conductivity[35-36], flame retardation[37-38], mechanical strength,[6, 39] optical properties,[40-41] and viscosity[42] of the nanocomposites.[3, 43-44] Nanofillers are several orders of magnitude smaller than traditional micrometer sized fillers and provide an opportunity to study how

polymer physics is affected by particles with length scales between monomer size and polymer chain size. At a fixed filler concentration, nanoparticles create much more interface between nanoparticles and polymers than macroscopic particles, which dramatically increases the volume fraction of polymer matrix influenced by the nanoparticles.[45] Thus, small amounts of nanoparticles (< 2wt%) can significantly change the bulk properties of polymer matrix.[5, 46-47] Understanding how nanoparticles affect the polymer matrix at the microscopic length scale, particularly polymer structure and dynamics, and how this controls the macroscopic behavior of polymer nanocomposites is critical for advancing the field. Moreover, it is crucial for designing and manufacturing future polymer nanocomposites with desired properties.

Carbon nanotubes and silica nanoparticles are two common nanoparticles mixed with polymer matrices to fabricate nanocomposites. Many studies have focused on these two systems, including fabrication,[48-50] rheological properties,[51-53] dynamics,[14-16, 54] and structure.[18, 20-21] Key information, like how polymer structure is affected by cylindrical nanofillers, is still missing, and more research is needed to further understand the structure and dynamics of polymer chains in these two systems.

1.1.1. Structure of Polymers in PNCs

For polymer structure in PNCs, most of the research has been focused on spherical nanoparticles and has found that the effect mainly depends on the quality of nanoparticle distribution and the size ratio between nanoparticles (particle radius, r) and polymer chains (R_g). When the particle dispersion is poor, no effect on polymer structure is observed.[18] For good particle dispersion, people observed chain expansion when $r/R_g < 1$,[17, 19] and no change on polymer chain size when $r/R_g > 1$.[21] However, a recent study investigating polymer chain conformation in silica nanoparticles/polystyrene nanocomposites showed that no change on R_g was observed for r/R_g ranges from ~ 0.3 to 1.25 with uniform nanoparticle dispersions.[55] These contradictory results imply that a thorough understanding of how spherical nanoparticles affect polymer structure has not been achieved.

For cylindrical nanoparticles, Mu *et al.* observed that tracer diffusion is slowing down when CNTs are firstly added into polystyrene matrices, but recovered when the CNT concentration is above a percolation threshold.[15-16] This diffusion minimum only happens when R_g is greater than the radius of the CNT. In the reptation model,[56-57] which has been used to describe polymer diffusion in bulk entangled systems, polymer diffusion

is determined by chain end-to-end distance (R_{ee}), monomer friction coefficients (ξ_0), and number of monomer in one entangled stand (N_e). Therefore, investigating how polymer structure is affected by CNTs can probably help us understand the diffusion minimum and broaden the knowledge of polymer structure in polymer nanocomposites.

We studied polymer structure in CNT/PS nanocomposites using small angle neutron scattering (SANS), and found that polymer chain size (R_g) increases in SWCNT/PS nanocomposites ($R_g > r_{SWCNT}$) and is un-affected in MWCNT/PS nanocomposites ($R_g \sim r_{MWCNT}$). The concentration of the rod networks (meshes) formed by percolated CNTs can also be revealed by analyzing the SANS data for CNT/PS nanocomposites. Chapter 2 presents polymer chain conformations in CNT/PS nanocomposites probed by SANS, which is the first study to investigate polymer structure in polymer nanocomposites with cylindrical shape nanoparticles.

After we observed a chain expansion in SWCNT/PS systems, we became interested in a question: do polymer chains expand perpendicular or parallel to the direction of SWCNT? To investigate this problem, the SWCNTs in the nanocomposites were aligned using a melt fiber spinning technique, and the nanocomposites with aligned SWCNTs were measured using SANS. We found that aligning SWCNTs created

anisotropic meshes with smaller mesh sizes perpendicular to nanotube alignment. Subsequently, the polymer conformations expand perpendicular to the alignment direction of SWCNTs. In Chapter 3, we look at the polymer chain conformation in aligned SWCNT/PS nanocomposites to answer the question of the direction of polymer chain expansion relative to the alignment direction of SWCNTs.

1.1.2. Temperature Dependence of Polymer Diffusion in PNCs

Elastic recoil detection (ERD) detects the concentration profiles of deuterated polymers in non-deuterated polymers and thereby probes polymer diffusion with the diffusion length more than 10 times of the polymer chain size (~ 200 to 600 nm). As mentioned in Section 1.1.1, Mu *et al.* found a diffusion minimum behavior in CNT/PS nanocomposites, as shown in Figure 1.2. For multi-walled carbon nanotubes (MWCNT)/ polystyrene (PS) nanocomposites, the normalized D/D_0 at 170°C reaches a minimum of ~ 0.3 at 2 wt% MWCNT concentration, which corresponds approximately to the MWCNT concentration for network formation in these composites.[15] Dr. Jihoon Choi further extended the study by investigating the tracer diffusion in nanorod/polymer systems and discovered that the diffusion minimum only happens when the polymer chain size is

greater than the rod radius but smaller than the rod length.[58]

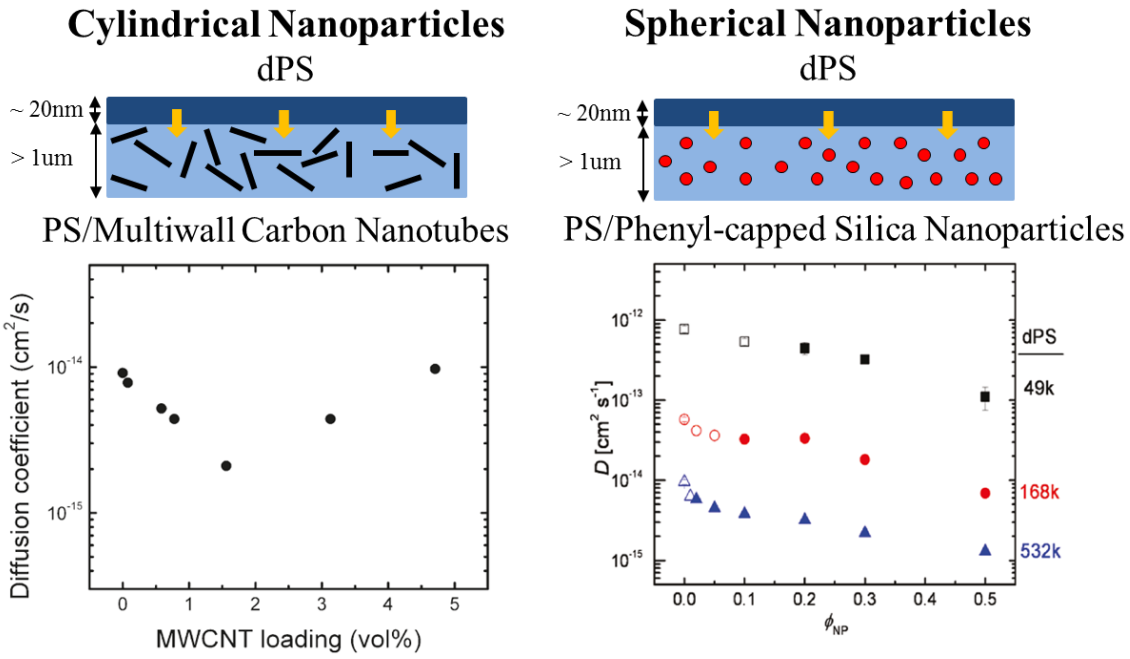

Figure 1.2. (left) Tracer diffusion coefficients (*D*) in MWCNT/PS nanocomposites and silica/PS nanocomposites. In MWCNT/PS nanocomposites, *D* decreases with increasing CNT concentration and then increases above a critical CNT concentration. Reprinted with permission from (*Macromolecules*, **2009**, *42* (21), 8365–8369). Copyright (2009) American Chemical Society (right) In silica/PS nanocomposites, *D* decreases monotonically as the volume fraction of spherical phenyl-capped silica nanoparticle increases.[14, 16] Reprinted with permission from (*Macromolecules*, **2011**, *44* (9), 3494–3501). Copyright (2011) American Chemical Society.

Gam *et al*. measured the tracer diffusion coefficients (*D*) of polymers in silica/polystyrene nanocomposites and found that *D* decreases monotonically as the volume fraction of spherical phenyl-capped silica nanoparticle increases, shown in Figure

1.2.[14] Data for a variety of tracer molecular weights and nanoparticle sizes collapse onto a master curve (Figure 1.3(a)) when the normalized tracer diffusion coefficient at a constant T is plotted as a function of $ID/2R_g$, where ID is the interparticle distance and R_g is the radius of gyration of the tracer molecule. Lin *et al*. investigated a silica/PMMA nanocomposite system and found that the master curve still applies at fixed T - T_g when polymers and nanoparticles have attractive interactions.[59] Choi *et al*. further extended the master curve to the range from $ID/2R_g$ ~ 0.1 to 15 (Figure 1.3(b)).[60]

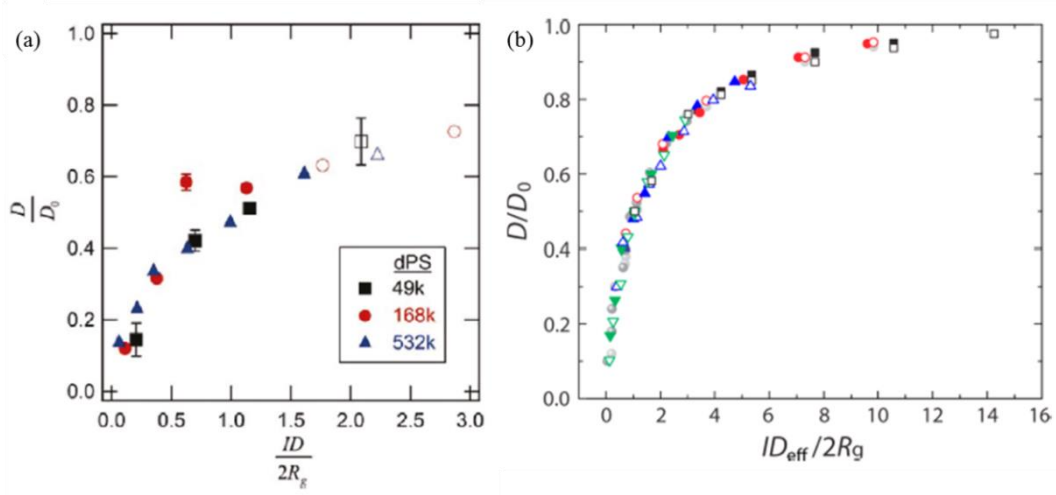

Figure 1.3. (a) Reduced polymer tracer diffusion in silica/PS nanocomposites for different tracer molecular weights as a function of interparticle distance normalized by $2R_g$. Reprinted with permission from (*Macromolecules*, **2011**, *44* (9), 3494–3501). Copyright (2011) American Chemical Society. (b)The master curve for silica/PS nanocomposites is extended to $ID/2R_g$ ~ 15 by using tracers with smaller molecular weights and lower silica concentrations.[14, 60] Reprinted with permission from (*ACS Macro Lett.*, **2013**, *2* (6), 485–490). Copyright (2013) American Chemical Society.

The fundamental mechanisms that produce a diffusion minimum in D for CNT/PS nanocomposites and a master curve for D/D_o in silica/PS nanocomposites remain under investigation. Since these experiments were conducted at fixed temperature, we decided to study the tracer diffusion in MWCNT/PS nanocomposites and silica/PS nanocomposites at a series of different temperatures. We found that the diffusion minimum and the monotonic decrease persists in nanocomposites with CNT and silica nanoparticles, respectively, but the extent of slowing down is different. The Williams–Landel–Ferry (WLF) equation is routinely used to describe the temperature dependence of polymer diffusion in bulk homopolymer system.[61-62] We examined the applicability of the WLF equation in MWCNT/PS and silica PS systems and found that it can still be applied to describe the temperature dependence of polymer diffusion in nanocomposite systems. However, we observed a change in the thermal expansion coefficients of free volume (α_f) in MWCNT/PS and silica/PS nanocomposites.

Chapter 4 introduces the temperature dependence of polymer tracer diffusion in MWCNT/PS nanocomposites, which provide more insight into the mechanism underlying the diffusion minimum reported by Mu *et al.*[15-16] In Chapter 5, the temperature dependence of polymer tracer diffusion in silica/PS nanocomposites is

combined with the rheological study of the composites to investigate the mechanisms of the diffusion slowdown induced by the addition of silica nanoparticles.

1.2. POLYMERS UNDER CYLINDRICAL NANOCONFINEMENTS

Applying direct geometric confinement (e.g., 1D-confinement: polymer thin films, 2D-confinement: polymers in cylindrical nanopores) is another way of perturbing the structure and dynamics of polymer chains. Polymer chains behave differently when under direct confinement, especially when the length scale of the confinement is smaller than the polymer chain size, radius of gyration (R_g).[27, 29-30, 32, 63-67] However, a quantitative understanding of how polymer chains are perturbed by geometric confinement is still in its infancy and more research is required. As the nanofabrication technology advances and devices shrink, the structure and dynamics of confined polymer chains have significant implications on manufacturing nanoscale devices.[68-70]

Thin film geometry is one type of confinement that has been extensively studied , e.g. chain mobility,[64, 71] mechanical strength,[31-32, 72-73] and glass transition temperature (T_g).[63, 74-76] Conflicting results for the change in T_g as a function of film thickness have been reported from different research groups.[76] Others have also observed different effect of film thickness on the plateau modulus for polymer thin films,[31-32, 73] which invokes further discussion of how the

entanglement molecular weight (M_e) is affected by this 1D confinement.[24] Controversial results for mechanical strength and T_g further prove the lack of comprehensive knowledge. In addition to thin films, this dissertation will also focus on the structure and dynamics of polymers under cylindrical nano-confinement, which has been studied less and is a new direction to study the confinement effect on polymers. Both experimental and simulation methods are used to study this problem to advance and broaden our knowledge about how polymer structure and dynamics change under cylindrical confinement.

1.2.1. Polymer Structure in Thin Film and Cylindrical Nanoconfinement

Structure and dynamics of polymers are related to each other, and understanding the change for polymer structure under confinement may provide a better understanding of the concurrent changes in polymer dynamics. The change of polymer structure arises due to the confinement effect of the impenetrable walls of thin films and cylindrical nanopores, and the main confinement parameter to investigate will be the size ratio between the thickness of the thin film and the diameter of the nanopores (d) and the radius of gyration (R_g) or the end-to-end distance (R_{ee}). Small angle neutron scattering has previously been used to study the structure with cylindrical pores, and no significant changes of polymer

chain conformation were found when d/R_{ee} is as small as 0.25.[22, 30] Moreover, the change in polymer structure may affect the entanglement density. It has been reported that severe cylindrical confinement can induce a decrease of entanglement density.[27] We applied computer simulations to study the change in polymer chain size and entanglement molecular weight for polymers under thin film and cylindrical confinement. By combining with theoretical work,[77-80] we successfully predict the increases of entanglement molecular weight from the change in the polymer end-to-end distance caused by nano-confinements. Chapter 6 introduces the simulation work for the confinement effect on polymer chain size (R_{ee}) and entanglement molecular weight (N_e). Combining with theoretical works, we are able to connect the change in N_e with the change in R_{ee}.

1.2.2. Polymer Dynamics in Cylindrical Nanocomfinements

Polymer dynamics under cylindrical confinement (2D confinement) has been investigated by different techniques.[23, 25-30, 33-34, 66-67, 81-83] Fatkullin *et al*. studied this problem using nuclear magnetic resonance (NMR). They reported that due to impenetrable confinement walls, the uncrossability of polymer chains, and the low

compressibility of polymer melts, the tube size in entangled polymer melts decreases to only a few tenths of a nanometer, even when the confinement length is considerably larger than the chain size. This is called the "corset effect".[33-34, 83] However, Krutyeva *et al*. used quasi-elastic neutron scattering (QENS) to study the change of chain dynamics in cylindrical confinement and failed to observe the corset effect.[66] Instead, they claimed no confinement effect was observed for Rouse dynamics, but the effect was observed in shorter length scale where polymer exhibits segmental relaxations. Neutron spin echo (NSE) probes the chain dynamics up to the 100ns time scale, allowing the observation of entanglement effect on polymer chains.[23, 27-29, 67, 81-82] Martin *et al*. using NSE to investigate PEO severely confined in AAO membranes (d/R_{ee} ~ 0.43 and 2.6).[27] The author observed a clear slowing down for Rouse dynamics for confined polymers compared to the bulk polymers. An expanded entanglement network (increased tube diameter for reptation model) was also reported which shows that confinement effect can affect the topological structure of polymer chains.[27] These techniques (NMR, QENS and NSE) only probe the chain dynamics on short time scales (ps ~ 100 μs), and no experimental results have been reported for time scales well above the disentanglement time of polymer chains. Measuring polymer diffusion in confined systems provides more

information about the dynamics of polymers under cylindrical confinement.

We studied this topic using both experimental techniques and computer simulations to further understand polymer dynamics in short and long time scales under cylindrical nanoconfinements. For computer simulations, broader range of time scale (ps to s) can be studied for polymer dynamics so that we can investigate Rouse dynamics, long range polymer diffusion, and reptation. Simulation results on local dynamics were combined with the results of R_{ee} and N_e in Chapter 6 to predict the center-of-mass polymer diffusion (D_{rep}) through the reptation model. In computer simulations, the center-of-mass diffusion can also be directly calculated from the log(MSD_z) versus log(LJ time) plot in the diffusion regime (D_{MSD}). Polymer diffusion can also be probed experimentally using ERD (D_{exp}). Diffusion coefficients obtained from these three ways will be compared to each other in Chapter 7. Local dynamics of PS under AAO nanopores studied by QENS are included in Chapter 8. A non-asymptotic slowing down of segmental relaxations when the diameter of AAO nanopores decreases is observed.

1.3 REFERENCES

1. Alexandre, M.; Dubois, P., *Mater. Sci. Eng. R-Rep.* **2000,** *28* (1-2), 1-63.

2. Gangopadhyay, R.; De, A., *Chem. Mat.* **2000,** *12* (3), 608-622.

3. Thostenson, E. T.; Ren, Z. F.; Chou, T. W., *Compos. Sci. Technol.* **2001,** *61* (13), 1899-1912.

4. Huang, Z. M.; Zhang, Y. Z.; Kotaki, M.; Ramakrishna, S., *Compos. Sci. Technol.* **2003,** *63* (15), 2223-2253.

5. Balazs, A. C.; Emrick, T.; Russell, T. P., *Science* **2006,** *314* (5802), 1107-1110.

6. Coleman, J. N.; Khan, U.; Gun'ko, Y. K., *Adv. Mater.* **2006,** *18* (6), 689-706.

7. Paul, D. R.; Robeson, L. M., *Polymer* **2008,** *49* (15), 3187-3204.

8. Zou, H.; Wu, S. S.; Shen, J., *Chem. Rev.* **2008,** *108* (9), 3893-3957.

9. Sumpter, B. G.; Kumar, P.; Mehta, A.; Barnes, M. D.; Shelton, W. A.; Harrison, R. J., *J. Phys. Chem. B* **2005,** *109* (16), 7671-7685.

10. Binder, K.; Horbach, J.; Vink, R.; De Virgiliis, A., *Soft Matter* **2008,** *4* (8), 1555-1568.

11. Schick, C., *Eur. Phys. J.-Spec. Top.* **2010,** *189* (1), 3-36.

12. Milchev, A., *J. Phys.-Condes. Matter* **2011,** *23* (10).

13. Peng, H.; Nieuwendaal, R.; Soles, C. L., Polymer Dynamics in Constrained Geometries. In *Polymer Science: A Comprehensive Reference*, Moeller, M.; Matyjaszewski, K., Eds. Elsevier B. V. : Amsterdam, 2012; Vol. 7, pp 345-376.

14. Gam, S.; Meth, J. S.; Zane, S. G.; Chi, C. Z.; Wood, B. A.; Seitz, M. E.; Winey, K. I.; Clarke, N.; Composto, R. J., *Macromolecules* **2011,** *44* (9), 3494-3501.

15. Mu, M. F.; Composto, R. J.; Clarke, N.; Winey, K. I., *Macromolecules* **2009,** *42* (21), 8365-8369.

16. Mu, M. F.; Clarke, N.; Composto, R. J.; Winey, K. I., *Macromolecules* **2009,** *42* (18), 7091-7097.

17. Nakatani, A. I.; Chen, W.; Schmidt, R. G.; Gordon, G. V.; Han, C. C., *Int. J. Thermophys.* **2002,** *23* (1), 199-209.

18. Sen, S.; Xie, Y. P.; Kumar, S. K.; Yang, H. C.; Bansal, A.; Ho, D. L.; Hall, L.; Hooper, J. B.; Schweizer, K. S., *Phys. Rev. Lett.* **2007,** *98* (12).

19. Tuteja, A.; Duxbury, P. M.; Mackay, M. E., *Phys. Rev. Lett.* **2008,** *100* (7).

20. Jouault, N.; Dalmas, F.; Said, S.; Di Cola, E.; Schweins, R.; Jestin, J.; Boue, F., *Macromolecules* **2010,** *43* (23), 9881-9891.

21. Nusser, K.; Neueder, S.; Schneider, G. J.; Meyer, M.; Pyckhout-Hintzen, W.; Willner, L.; Radulescu, A.; Richter, D., *Macromolecules* **2010,** *43* (23), 9837-9847.

22. Noirez, L.; Stillings, C.; Bardeau, J. F.; Steinhart, M.; Schlitt, S.; Wendorff, J. H.; Pepy, G., *Macromolecules* **2013,** *46* (12), 4932-4936.

23. Colmenero, J.; Arbe, A., *J. Polym. Sci. Pt. B-Polym. Phys.* **2013,** *51* (2), 87-113.

24. Rathfon, J. M.; Cohn, R. W.; Crosby, A. J.; Rothstein, J. P.; Tew, G. N., *Macromolecules* **2011,** *44* (13), 5436-5442.

25. Hofmann, M.; Herrmann, A.; Ok, S.; Franz, C.; Kruk, D.; Saalwachter, K.; Steinhart, M.; Rossler, E. A., *Macromolecules* **2011,** *44* (11), 4017-4021.

26. Ok, S.; Steinhart, M.; Serbescu, A.; Franz, C.; Chavez, F. V.; Saalwachter, K., *Macromolecules* **2010,** *43* (10), 4429-4434.

27. Martin, J.; Krutyeva, M.; Monkenbusch, M.; Arbe, A.; Allgaier, J.; Radulescu, A.; Falus, P.; Maiz, J.; Mijangos, C.; Colmenero, J.; Richter, D., *Phys. Rev. Lett.* **2010,** *104* (19).

28. Kusmin, A.; Gruener, S.; Henschel, A.; Holderer, O.; Allgaier, J.; Richter, D.; Huber, P., *J. Phys. Chem. Lett.* **2010,** *1* (20), 3116-3121.

29. Kusmin, A.; Gruener, S.; Henschel, A.; de Souza, N.; Allgaier, J.; Richter, D.; Huber, P., *Macromolecules* **2010,** *43* (19), 8162-8169.

30. Shin, K.; Obukhov, S.; Chen, J. T.; Huh, J.; Hwang, Y.; Mok, S.; Dobriyal, P.; Thiyagarajan, P.; Russell, T. P., *Nat. Mater.* **2007,** *6* (12), 961-965.

31. Si, L.; Massa, M. V.; Dalnoki-Veress, K.; Brown, H. R.; Jones, R. A. L., *Phys. Rev.*

Lett. **2005,** *94* (12).

32. O'Connell, P. A.; McKenna, G. B., *Science* **2005,** *307* (5716), 1760-1763.

33. Mattea, C.; Fatkullin, N.; Fischer, E.; Beginn, U.; Anoardo, E.; Kroutieva, M.; Kimmich, R., *Appl. Magn. Reson.* **2004,** *27* (3-4), 371-381.

34. Fatkullin, N.; Kimmich, R.; Fischer, E.; Mattea, C.; Beginn, U.; Kroutieva, M., *New J. Phys.* **2004,** *6*.

35. Zhang, A. B.; Luan, J. F.; Zheng, Y. P.; Sun, L.; Tang, M., *Appl. Surf. Sci.* **2012,** *258* (22), 8492-8497.

36. White, S. I.; Vora, P. M.; Kikkawa, J. M.; Winey, K. I., *Adv. Funct. Mater.* **2011,** *21* (2), 233-240.

37. Madathingal, R. R.; Wunder, S. L., *Thermochim. Acta* **2011,** *526* (1-2), 83-89.

38. Kashiwagi, T.; Du, F. M.; Douglas, J. F.; Winey, K. I.; Harris, R. H.; Shields, J. R., *Nat. Mater.* **2005,** *4* (12), 928-933.

39. Wang, Y. T.; Wang, C. S.; Yin, H. Y.; Wang, L. L.; Xie, H. F.; Cheng, R. S., *Express Polym. Lett.* **2012,** *6* (9), 719-728.

40. Srivastava, S.; Haridas, M.; Basu, J. K., *Bull. Mat. Sci.* **2008,** *31* (3), 213-217.

41. Hore, M. J. A.; Frischknecht, A. L.; Composto, R. J., *ACS Macro Lett.* **2012,** *1* (1),

115-121.

42. Oh, H.; Green, P. F., *Nat. Mater.* **2009,** *8* (2), 139-143.

43. Kiamahalleh, M. V.; Zein, S. H. S.; Najafpour, G.; Abd Sata, S.; Buniran, S., *Nano* **2012,** *7* (2), 1230002-1 - 1230002-27.

44. Pandey, G.; Thostenson, E. T., *Polym. Rev.* **2012,** *52* (3-4), 355-416.

45. Winey, K. I.; Vaia, R. A., *MRS Bull.* **2007,** *32* (4), 314-319.

46. Crosby, A. J.; Lee, J. Y., *Polym. Rev.* **2007,** *47* (2), 217-229.

47. Jeon, I. Y.; Baek, J. B., *Materials* **2010,** *3* (6), 3654-3674.

48. Du, F. M.; Fischer, J. E.; Winey, K. I., *J. Polym. Sci. Pt. B-Polym. Phys.* **2003,** *41* (24), 3333-3338.

49. Moniruzzaman, M.; Winey, K. I., *Macromolecules* **2006,** *39* (16), 5194-5205.

50. Meth, J. S.; Zane, S. G.; Chi, C. Z.; Londono, J. D.; Wood, B. A.; Cotts, P.; Keating, M.; Guise, W.; Weigand, S., *Macromolecules* **2011,** *44* (20), 8301-8313.

51. Dalmas, F.; Cavaille, J. Y.; Gauthier, C.; Chazeau, L.; Dendievel, R., *Compos. Sci. Technol.* **2007,** *67* (5), 829-839.

52. Jouault, N.; Vallat, P.; Dalmas, F.; Said, S.; Jestin, J.; Boue, F., *Macromolecules* **2009,** *42* (6), 2031-2040.

53. Nusser, K.; Schneider, G. J.; Pyckhout-Hintzen, W.; Richter, D., *Macromolecules* **2011,** *44* (19), 7820-7830.

54. Schneider, G. J.; Nusser, K.; Willner, L.; Falus, P.; Richter, D., *Macromolecules* **2011,** *44* (15), 5857-5860.

55. Crawford, M. K.; Smalley, R. J.; Cohen, G.; Hogan, B.; Wood, B.; Kumar, S. K.; Melnichenko, Y. B.; He, L.; Guise, W.; Hammouda, B., *Phys. Rev. Lett.* **2013,** *110* (19).

56. Doi, M.; Edwards, S. F., *Journal of the Chemical Society-Faraday Transactions Ii* **1978,** *74*, 1789-1801.

57. Degennes, P. G., *J. Chem. Phys.* **1971,** *55* (2), 572-&.

58. Choi, J.; Clarke, N.; Winey, K. I.; Composto, R. J., *ACS Macro Lett.* **2014,** *3* (9), 886-891.

59. Lin, C. C.; Gam, S.; Meth, J. S.; Clarke, N.; Winey, K. I.; Composto, R. J., *Macromolecules* **2013,** *46* (11), 4502-4509.

60. Choi, J.; Hore, M. J. A.; Meth, J. S.; Clarke, N.; Winey, K. I.; Composto, R. J., *ACS Macro Lett.* **2013,** *2* (6), 485-490.

61. Green, P. F.; Kramer, E. J., *Journal of Materials Research* **1986,** *1* (1), 202-204.

62. Rubinstein, M.; Colby, R. H., *Polymer Physics*. Oxford University Press: New York,

2003.

63. Ellison, C. J.; Torkelson, J. M., *Nat. Mater.* **2003,** *2* (10), 695-700.

64. Frank, B.; Gast, A. P.; Russell, T. P.; Brown, H. R.; Hawker, C. J., *Macromolecules* **1996,** *29* (20), 6531-6534.

65. Jones, R. L.; Kumar, S. K.; Ho, D. L.; Briber, R. M.; Russell, T. P., *Nature* **1999,** *400* (6740), 146-149.

66. Krutyeva, M.; Martin, J.; Arbe, A.; Colmenero, J.; Mijangos, C.; Schneider, G. J.; Unruh, T.; Su, Y. X.; Richter, D., *J. Chem. Phys.* **2009,** *131* (17).

67. Krutyeva, M.; Wischnewski, A.; Monkenbusch, M.; Willner, L.; Maiz, J.; Mijangos, C.; Arbe, A.; Colmenero, J.; Radulescu, A.; Holderer, O.; Ohl, M.; Richter, D., *Phys. Rev. Lett.* **2013,** *110* (10).

68. Suh, K. Y.; Kim, Y. S.; Lee, H. H., *Adv. Mater.* **2001,** *13* (18), 1386-1389.

69. Granick, S.; Kumar, S. K.; Amis, E. J.; Antonietti, M.; Balazs, A. C.; Chakraborty, A. K.; Grest, G. S.; Hawker, C. J.; Janmey, P.; Kramer, E. J.; Nuzzo, R.; Russell, T. P.; Safinya, C. R., *J. Polym. Sci. Pt. B-Polym. Phys.* **2003,** *41* (22), 2755-2793.

70. Dersch, R.; Steinhart, M.; Boudriot, U.; Greiner, A.; Wendorff, J. H., *Polym. Adv. Technol.* **2005,** *16* (2-3), 276-282.

71. Zheng, X.; Sauer, B. B.; Vanalsten, J. G.; Schwarz, S. A.; Rafailovich, M. H.; Sokolov, J.; Rubinstein, M., *Phys. Rev. Lett.* **1995,** *74* (3), 407-410.

72. Hu, H. W.; Granick, S., *Science* **1992,** *258* (5086), 1339-1342.

73. O'Connell, P. A.; Wang, J.; Ishola, T. A.; McKenna, G. B., *Macromolecules* **2012,** *45* (5), 2453-2459.

74. DeMaggio, G. B.; Frieze, W. E.; Gidley, D. W.; Zhu, M.; Hristov, H. A.; Yee, A. F., *Phys. Rev. Lett.* **1997,** *78* (8), 1524-1527.

75. Forrest, J. A.; Dalnoki-Veress, K., *Adv. Colloid Interface Sci.* **2001,** *94* (1-3), 167-196.

76. Alcoutlabi, M.; McKenna, G. B., *J. Phys.-Condes. Matter* **2005,** *17* (15), R461-R524.

77. Sussman, D. M.; Schweizer, K. S., *J. Chem. Phys.* **2013,** *139* (23).

78. Sussman, D. M.; Schweizer, K. S., *Phys. Rev. Lett.* **2012,** *109* (16), 168306.

79. Sussman, D. M.; Schweizer, K. S., *Phys. Rev. E* **2011,** *83* (6), 061501.

80. Sussman, D. M.; Schweizer, K. S., *Phys. Rev. Lett.* **2011,** *107* (7), 078102.

81. Lagrene, K.; Zanotti, J. M.; Daoud, M.; Farago, B.; Judeinstein, P., *Eur. Phys. J.-Spec. Top.* **2010,** *189* (1), 231-237.

82. Lagrene, K.; Zanotti, J. M.; Daoud, M.; Farago, B.; Judeinstein, P., *Phys. Rev. E* **2010,** *81* (6).

83. Kausik, R.; Mattea, C.; Fatkullin, N.; Kimmich, R., *J. Chem. Phys.* **2006,** *124* (11).

Chapter 2

Polymer Structure in Carbon Nanotube/Polystyrene Nanocomposite

This work was accomplished in collaboration with Vikki Bird at the University of Durham, Durham, U.K. and Professor Nigel Clarke at University of Sheffield, U.K. The contents of this chapter were published in a modified version. Adapted with permission from (*Macromolecules*, **2013**, *46* (13), 5345–5354). Copyright (2013) American Chemical Society.

2.1 INTRODUCTION

Polymer nanocomposites containing cylindrical, spherical or layered nanoscale fillers can have enhanced properties including mechanical, electrical, and flammability.[1-3] However, the understanding of how nanofillers impact the structural and dynamic nature of polymer chains is still in its infancy. In this chapter, we investigate polymer chain conformations in the presence of the most widely-studied cylindrical nanofiller, namely carbon nanotubes (CNTs).

Carbon nanotubes have many impressive properties including high mechanical strength, high electrical and thermal conductivities, and it has been shown that adding

CNTs into various matrices (*e.g*. polymers, ceramics, and metals) can dramatically improve the properties of the host materials[4] and different methods of making CNT/polymer nanocomposites have been reported.[5] Polymer diffusion[6-7] and polymer dynamics[8] have also been studied. The dispersion state of carbon nanotubes in polymer matrices is known to be a critical factor that determines the final properties of polymer nanocomposites.[9-14] When CNTs form aggregates or networks in solution[15] or a polymer matrix[16], the aggregates and networks have been described as fractal objects *via* small-angle scattering experiments.[17] The dispersion state of CNTs in CNT/PS nanocomposites depends on processing methods, and the coagulation or rapid precipitation method for fabricating nanotube polymer nanocomposites has been shown to yield good CNT dispersions.[18,19] At low concentrations, the CNTs exist as isolated rods and small bundles, while at high concentrations the CNTs form low-density, electrically-conductive networks in our nanocomposites. Good nanoparticle dispersion is particularly important when monitoring changes in the polymer conformation.[19]

The effect of nanofillers on polymer conformation, specifically the radius of gyration (R_g), has been previously studied for a variety of spherical nanoparticles. Nakatani et al. published the first experimental results describing a decrease for R_g in

polysilicate/poly(dimethylsiloxane) nanocomposites when R_g is about the same size as the fillers and, conversely, an increase when R_g is larger than the filler.[20] Since then, the radius of gyration has been reported for a variety of spherical-nanofiller/polymer systems. Sen *et al.*[21] showed no change in polymer conformation for a wide range of R_g to spherical nanoparticles radius (r) ratios (1-3) and filler concentrations (up to 27.5 v%), but their TEM images suggest poor nanoparticle dispersion. Recently, Jouault *et al.*[22] reported a constant R_g in silica/polystyrene (PS) nanocomposites with $r/R_g < 1$, but again the nanoparticle dispersion is less than ideal. Tuteja *et al.*[23] reported chain swelling when $r/R_g < 1$ in PS-nanoparticle/PS nanocomposites (soft particle system). In silica/poly(ethylene-propylene) nanocomposites, Nusser *et al.*[24] reported that R_g decreases when $r/R_g \sim 1$ and remains constant when $r/R_g > 1$ with increasing silica content. Their silica nanoparticles are grafted with hydrocarbon chains to improve the nanoparticle dispersion in a polymer matrix, although some aggregation is still observed at high loadings (> 35 v%). In contrast, this chapter studies polymer conformations in the presence of cylindrical nanoparticles, namely CNT/polymer nanocomposites.

Beyond experimental studies, simulations have been used to explore how polymer chain conformations are affected by varying the particle-to-polymer size ratio (r/R_g) and

the interaction energy, but the results still have discrepancies. Most of the simulations study spherical particles. For larger nanoparticles with $r/R_g > 1$, most of the simulation work found no change in R_g.[25-27] For smaller nanoparticles with $r/R_g < 1$, Termonia found chain swelling in their Monte-Carlo simulation,[25] while Vacatello found a constant R_g.[28] Hooper and Schweizer applied polymer reference site model (PRISM) to study the miscibility of nanoparticles and polymers and the local particle-polymer structure as a function of particle-to-monomer size ratio, degree of polymerization, strength (ε_{pc}) and spatial range of monomer-particle attractions and interfiller attractions.[29-30] They have shown that the miscibility windows of hard-sphere nanoparticles and polymer melts requires intermediate ε_{pc} ($\sim 0.5 - 2\ k_BT$). At low ε_{pc}, depletion attraction between nanoparticles is observed, resulting in phase separation; while at high values of ε_{pc}, adsorbed polymer chains bridging multiple nanoparticles forming a network phase. Other parameters have been investigated to shape the miscibility window. Using self-consistent PRISM, Frischknecht *et al.* showed an expansion of chain dimensions in nanoparticle/polymer systems with $r/R_g < 1$ and attractive interactions between polymers and fillers,[31] These simulation results were discussed in conjunction with experiments.[23] For the case of cylindrical nanoparticles, Karatrantos *et al.* investigated the structure and

conformations of polymer chains in SWCNT/polystyrene (PS) nanocomposites, where R_g is larger than the radii of the SWCNTs.[32] Although the local chain structure is affected, they found R_g to be constant over a range of polymer-nanotube interaction energies and SWCNT radii. These simulations are the most analogous to our system and will be compared to our experimental results.

In this chapter, we use small angle neutron scattering (SANS) to determine the R_g in CNT/PS nanocomposites. Our nanocomposites are prepared by a coagulation method, which has been previously shown to yield good dispersion of CNTs in a polymer matrix.[18] Moreover, the interaction energies between CNTs and PS are negligible.[7] The R_g of the matrix PS is larger than the radius of the SWCNTs and about the same as the radius of the MWCNTs, so as to explore both $r/R_g < 1$ and $r/R_g \approx 1$. Importantly, we experimentally determine and apply the contrast matching condition between CNTs and the PS matrix to minimize the scattering contribution from the CNTs.

2.2. EXPERIMENTAL METHODS

2.2.1. Materials

The nanocomposites used in this work are composed of single-walled carbon nanotubes (SWCNT), multi-walled carbon nanotubes (MWCNT), deuterated polystyrene

(dPS), and hydrogenated polystyrene (hPS). SWCNTs synthesized by high-pressure carbon monoxide conversion (HiPco) were purchased from Unidym; MWCNTs produced by chemical vapor deposition (CVD) were purchased from Nanolab. SWCNTs and MWCNTs were purified by oxidizing in air at 150°C for 24 hrs followed by an HCl treatment.[33] The dPS and hPS were synthesized via standard living anionic polymerization methods.[34] The weight averaged molecular weight and PDI for dPS (116 kg/mol, 1.03) and hPS (117 kg/mol, 1.05) were measured by size exclusion chromatography (SEC) using a Viscotek TDA 302 with refractive index, viscosity and light scattering detectors (with a 690 nm wavelength laser).

2.2.2. Nanocomposites Preparation

All nanocomposites were synthesized by the coagulation method.[18] CNTs were well dispersed in dimethylformamide (DMF) by sonication for 24 hrs, and a mixture of dPS and hPS with the desired volume ratio were dissolved in DMF by stirring for 24 hrs. After mixing these two solutions, the CNT/dPS+hPS mixtures were rapidly precipitated in DI water. The precipitate was dried, annealed at 150°C under vacuum for 24 hrs, and then hot pressed into thin circular disks (diameter ~ 25 mm; thickness ~ 0.17 mm). Standard

operation procedures of CNT purification and the coagulation method can be found in Appendix A. The size of SWCNTs and MWCNTs were measured by atomic force microscopy (AFM) and scanning electron microscopy (SEM), respectively, and the results are given in Table 2.1.

Table 2.1. Characteristics of the single-walled and multi-walled carbon nanotubes.

	Diameter (nm)	Length (nm)	Aspect ratio
SWCNT	7.4 ± 3.1	327 ± 142	~44
MWCNT	20 ± 6	650 ±450	~33

Note that the CNTs used for size determination and for the SANS samples were sonicated for the same amount of time, so the size distributions reported in Table 2.1 are indicative of the CNTs in the polymer nanocomposites. For contrast matching experiments, the nanocomposites were made with 1wt% SWCNT in nine polymer matrices with dPS/hPS ratios from 79/21 to 63/37. The contrast matching experiments with 1wt% SWCNTs found the contrast matching condition is dPS/hPS = 0.725/0.275 (see Section 2.4.2). Subsequently, the remaining CNT/dPS+hPS nanocomposites use this dPS/hPS ratio. For comparison a dPS+hPS homopolymer mixture dPS/hPS = 72.5/27.5 was prepared by

the same coagulation procedure to provide the radius of gyration of PS in the absence of CNTs. Table 2.2 lists the details of the samples along with the location of the SANS experiments. In these nanocomposites, the CNTs are hollow, which implies that the scattering length density will depend on the radius of a SWCNT and on both the radius and number of layers in a MWCNT, thereby complicating the effort to define a contrast matched state.

Table 2.2. Sample information for contrast matching experiments and the study of the polymer conformation in CNT/PS nanocomposites with different CNT concentrations. SANS experiments were performed at Oak Ridge National Laboratory (ORNL), Institute Laue-Langevin (ILL), and National Institute of Standards and Technology (NIST).

	CNT concentration (wt %)	**dPS/hPS (vol/vol)**	**SANS**
Contrast Matching Experiments			
SWCNT/dPS+hPS	1	79/21, 77/23, 75/25, 73/27, 71/29, 69/31, 67/33, 65/35, 63/37	ORNL
Polymer Conformation Experiments			
dPS+hPS	0	72.5/27.5	NIST
SWCNT/dPS+hPS	0.3, 0.5, 1, 1.5, 2, 4, 6, 10	72.5/27.5	ILL
MWCNT/dPS+hPS	0.5, 1, 1.5, 2, 4, 6, 8, 10	72.5/27.5	ILL

2.2.3. Small Angle Neutron Scattering (SANS)

The differential scattering cross-section normalized by a unit volume, $(d\Sigma/d\Omega)(q)$, contains information about the size, shape, and interactions between the scattering centers. It is also called the macroscopic differential scattering cross-section, and has dimensions of inverse length, usually cm^{-1}. Sometimes it is inaccurately referred to as the scattering intensity $I(q)$, which actually represents the number of neutrons scattered through a particular angle and arriving on a small area of the detector in a unit time and has the unit (# of neutrons/sec). The relationship between $I(q)$ and $(d\Sigma/d\Omega)(q)$ can be expressed as[35]

$$I(q) = I_0(\lambda)\Delta\Omega\eta(\lambda)T(\lambda)V_s\frac{\partial\Sigma}{\partial\Omega}(q) \tag{2.1}$$

The first three terms on the right side of Equation 2.1 are instrument specific, where $I_0(\lambda)$ is the incident neutron flux (unit: # of neutrons/sec·cm^2), $\Delta\Omega$ is the solid angle element determined by the physical size and position of the detector, and $\eta(\lambda)$ represents the detector efficiency. The remaining terms are sample specific: $T(\lambda)$ is the neutron transmission of the sample, and V_s is the sample volume impinged by the neutron beam, and finally $(d\Sigma/d\Omega)(q)$ is the differential scattering cross-section normalized by a unit volume. To determine $(d\Sigma/d\Omega)(q)$ of a sample, we measure the scattering intensity from

the sample of interest, an empty cell, the calibration sample, and background noise. For a fixed wavelength instrument, the $(d\Sigma/d\Omega)(q)$ of our sample can be calibrated in absolute units (cm^{-1}) according to[35]

$$\frac{d\Sigma}{d\Omega}(q)_{sa} = \frac{\left[\left(\frac{I(q)_{sa}}{count_{sa}} - \frac{I(q)_{ba}}{count_{ba}}\right) - \frac{T_{sa}}{T_{ec}} \times \left(\frac{I(q)_{ec}}{count_{ec}} - \frac{I(q)_{ba}}{count_{ba}}\right)\right]}{\left[\left(\frac{I(q)_{ca}}{count_{ca}} - \frac{I(q)_{ba}}{count_{ba}}\right) - \frac{T_{ca}}{T_{ec}} \times \left(\frac{I(q)_{ec}}{count_{ec}} - \frac{I(q)_{ba}}{count_{ba}}\right)\right]} \times \frac{L_{sa}^2 t_{ca} T_{ca}}{L_{ca}^2 t_{sa} T_{sa}} \times \frac{\partial \Sigma}{\partial \Omega}(q)_{ca} \quad (2.2)$$

Here for the subscripts, *ca*, *sa*, *ec*, *ba* refer to the calibration standard, sample, empty cell, and background, respectively. In addition, *L* is the sample-to-detector distance, *t* is the sample thickness, and *T* denotes the transmission. For simplicity, $i(q)$ will be used to represent $(d\Sigma/d\Omega)(q)$.

Samples were measured at three neutron scattering facilities, see Table 2.2 for details. The first experiments conducted found the contrast matching condition for the SWCNTs. 1wt% SWCNT with different dPS/hPS volume ratio polymer matrices were measured on the Bio-SANS instrument in the neutron science division of Oak Ridge National Laboratory in Oak Ridge, TN, USA. Three sample-detector distances *L* = 0.3 and 6 m for λ = 6 Å and L = 14.5 m for λ = 18 Å provide a *q*-range of 0.0025 $Å^{-1}$ to 0.15 $Å^{-1}$. After obtaining the contrast matching conditions for SWCNTs, SANS measurement for SWCNT/PS and MWCNT/PS nanocomposites with a fixed dPS/hPS ratio and different

CNT concentrations were performed on instrument D11 in the Institute Laue-Langevin in Grenoble, France. Three sample-detector distances with L = 1.2, 8, 20 m for λ = 9.7 Å cover the q-range of 0.0018 $Å^{-1}$ to 0.3 $Å^{-1}$. It is assumed that the contrast matching condition for MWCNTs is comparable to that for SWCNTs. Finally, a homopolymer sample with dPS/hPS = 72.5/27.5, which is the contrast matched condition for SWCNTs, was measured on the NG3 instrument at the NIST center of neutron research in Gaithersburg, MD, USA. Three sample-detector distances with L = 1.3 and 4 m for λ = 6 Å and L = 13 m for λ = 8.4 Å, provided a q-range of 0.001 $Å^{-1}$ to 0.4 $Å^{-1}$.

2.2.4. Glass Transition Temperature

The glass transition temperatures (T_g's) of the CNT/dPS+hPS nanocomposites were measured using modulated-temperature differential scanning calorimetry (TA instruments Q2000) to separate the recoverable and irrecoverable processes. A modulation amplitude of ± 1°C and a period of 60s were used with a ramping rate of 2°C/min to heat the samples to 150°C. The T_g's were determined from the second order transition in the second heating curve. The T_g's of PS and CNT/PS nanocomposites are comparable, Figure 2.1, indicating that adding CNTs does not alter the average segmental motion of PS.

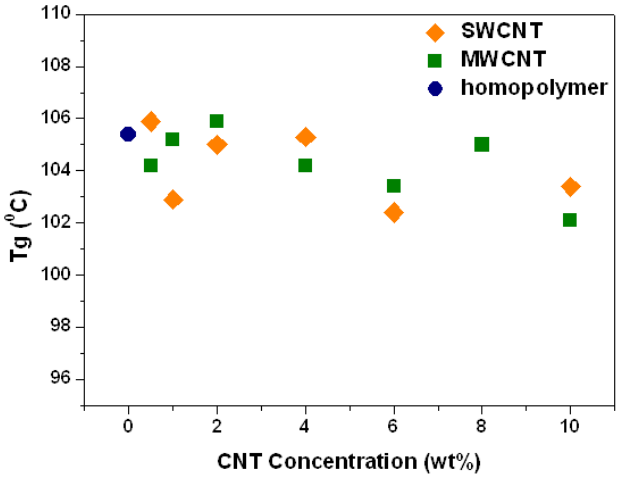

Figure 2.1. Modulated DSC results provide T_g as a function of CNT concentration. The width of the second order transition is ~ 6-7 °C in all the samples.

2.2.5. Electrical Measurements

The electrical conductivities of the CNT/dPS+hPS nanocomposites were measured to extract the critical concentrations for electrical percolation, which correspond to the point at which CNT networks form. After the SANS measurements a strip was cut from the nanocomposites and current as a function of applied voltage was measured using a Keithley 6517A electrometer with an integrated LabView program. The data were fit using the fluctuation-assisted tunneling model[36] which has been proven to describe the nonlinearities in the I-V curves for silver nanowire networks in polymer nanocomposite systems.[36,12] For a system with conducting regions separated by insulating barriers, the

model, which is based on the field enhancement of electron tunneling probability, describes the voltage-dependent transition between low-field conductance G_o ($V \rightarrow 0$) and high-field conductance G_h ($V \rightarrow \infty$).

$$\mathrm{G} = \frac{I}{V} = \frac{G_o \exp(V/V_o)}{1 + (G_o/G_h)[\exp(V/V_o) - 1]} \tag{2.3}$$

The barrier voltage V_o is related to the barrier height between the conducting regions, and gives an exponential increase in conductance as V increases. The electrical conductivity (σ) for the CNT/PS nanocomposites is $\sigma = G_h*(w_s t_s/l_s)$, where w_s, t_s, and l_s are the sample width, thickness, and length, respectively; see Figure B.1 in the Appendix B. The composition-dependent conductivities were then fit to a power law with two fitting parameters (C, α)

$$\sigma = C\left(\frac{\phi - \phi_c}{\phi_c}\right)^{\alpha} \tag{2.4}$$

to obtain the critical concentration, ϕ_c, of these nanocomposites, Figure B.2. Note that Equation 2.4 applies to concentrations above the percolation concentration and the same mass density was used for both SWCNTs and MWCNTs to convert weight fraction to volume fraction. The critical concentrations for these SWCNT/dPS+hPS and MWCNT/dPS+hPS nanocomposites are 0.47 v% and 1.45 v%, respectively. The lower percolation for the SWCNT nanocomposites is consistent with their higher aspect ratio.

2.3. CONTRAST MATCHING AND SCATTERING MODEL

2.3.1. Contrast Matching CNTs and Polymer Matrix

The characteristic length scales of the CNT networks overlap with the length scales associated with the polymer conformations. To reduce the scattering contribution from the CNT networks, we contrast matched the CNTs to the mixture of dPS and hPS. Specifically, we tune the volume ratio of dPS to hPS to match the average scattering length density of the polymer matrix to that of the SWCNTs. Note that exact contrast matching was unachievable, so our fitting model described below will still account for the CNT network. The scattering intensity for a three component system (*e.g.* SWCNT, dPS, and hPS) can be expressed as[37]

$$i(q) = [x(\rho_{dPS} - \rho_{swcnt})^2 + (1-x)(\rho_{hPS} - \rho_{swcnt})^2]P(q) + [x\rho_{dPS} + (1-x)\rho_{hPS} - \rho_{swcnt}]^2 Q(q) \quad (2.5)$$

where x is the volume fraction of dPS relative to the total volume of polymer, ρ_i is the scattering length density of dPS, hPS and SWCNT. $P(q)$ is proportional to product of the molar fraction of polymer chains Φ_{pol} and the form factor of a single Gaussian chain, which is dependent on the degree of polymerization. $Q(q)$ represents all other contributions to the total scattering intensity. The purpose of contrast matching is to

minimize $Q(q)$ and thereby accentuate the scattering from the polymer chains. The contrast matched condition is

$$x\rho_{dPS} + (1-x)\rho_{hPS} - \rho_{swcnt} = 0 \quad (2.6)$$

The scattering length density of SWCNT was calculated for λ = 10 Å using the scattering length density calculator provided by NIST[34] and a SWCNT mass density 1.5 g/cm^3: ρ_{swcnt} = ~ 5.0 × 10^{10} cm^{-2}. A single monomeric unit was taken as the smallest scattering unit (C_8D_8 for dPS and C_8H_8 for hPS) and using the scattering lengths of deuterium, hydrogen, and carbon, and the density of dPS and hPS as 1.13g/cm^3 and 1.04g/cm^3, we found ρ_{dPS} = 6.47 × 10^{10} cm^{-2} and ρ_{hPS} = 1.42 × 10^{10} cm^{-2}. Using Equation 2.6 we estimated the contrast matching condition in SWCNT/dPS+hPS nanocomposites to have a dPS/hPS ratio of 71/29. Thus, nanocomposites with dPS/hPS volume ratios from 63/37 to 79/21 were prepared.

2.3.2. Scattering Model

Our scattering model for CNT/dPS+hPS nanocomposites considers four contributions to the total scattering intensity, namely the polymer chains, the CNT network, voids in the sample and incoherent scattering. The polymer chains are described

as ideal Gaussian chains and the scattering intensity is[37]

$$i(q)_{poly} = V\Phi_{poly}\Delta\rho^2 P(q)_{poly}$$
$$= V\Phi_{poly}\Delta\rho^2 \frac{1}{N^2}\left[N\frac{1+b}{1-b} - 2b\frac{1-b^N}{(1-b)^2}\right] \quad (2.7)$$
$$b = \exp(-l_k^2 q^2/6)$$

where $P(q)_{\text{poly}}$ is the single chain form factor, N is the number of Kuhn monomers, l_{k} is the Kuhn length, V is the volume of a polymer chain, Φ_{poly} is the polymer volume fraction, and $\Delta\rho$ is the contrast between the corresponding scattering length densities of the polymer chains and the matrix. For large N, $P(q)_{\text{poly}}$ can be simplified to the Debye function[37-38]

$$Debye(q, R_g) = \frac{2}{(qR_g)^4}\left[q^2R_g^2 - 1 + exp\left(-q^2R_g^2\right)\right] \quad (2.8)$$

where R_{g} is the radius of gyration of the polymer chain. Therefore, the first term in our scattering model is $A \times$ Debye(q, R_{g}), where A is the prefactor of the Debye function related to the scattering length densities of the different species, monomer volumes, the degree of polymerization, and the volume ratio of the polymers. In miscible polymer blends where the polymer-polymer interactions might perturb the polymer conformation, the scattering intensity is given by the random phase approximation.[37] However, given that the Flory-Huggins parameter for dPS and hPS is ~ 10^{-4} at 160°C,[39] we neglect the effect of interactions and use just one Debye function to describe a Gaussian conformation in the

fitting model.

The nanocomposites contain CNT networks that can be described as mass fractal objects, a concept first introduced by Mandelbrot.[40] A fractal object has a self-similar structure and its mass can be described by

$$M(R) \sim (R/r_0)^D \tag{2.9}$$

where R is a linear dimension, r_0 is the gauge of measurement, and D is the fractal dimension. The structure factor, $S(q)$, for a fractal rod-like network has previously been derived[41]

$$S(q, D, \xi, r_0) = 1 + \frac{D exp\big(\Gamma(D-1)\big) \sin(D-1) \tan^{-1}(q\xi)}{(qr_0)^D [1 + (q\xi)^{-2}]^{(D-1)/2}} \tag{2.10}$$

where $\Gamma(x)$ is the gamma function and ξ is the characteristic length of the fractal object above which the mass distribution of the object can no longer be described as fractal. The scattering intensity, $i(q)$, is proportional to the product of the structure factor, $S(q)$, and the form factor, $P(q)$. In CNT nanocomposites, $S(q)$ describes the scattering from CNT networks (Equation 2.10), and $P(q)$ is the form factor for CNTs. Similar approaches have been used previously to describe the scattering intensity for CNTs in solutions or polymers.[16,42,43] Figure 2.2 illustrates that the characteristic length scales accessed by SANS and associated with the CNT network can be larger or smaller than the diameters

of CNT bundles. Thus, at modest scattering angles ($\xi^{-1} \leqq q \leqq r_0^{-1}$: green circle indicates that the probing length scale is larger than the average mesh size, *s*) the scattering intensity is dominated by the network structure factor and reduces to $S(q) \sim q^{-D}$. Previous work has reported that $D \sim 2$ for well dispersed rod networks.[15, 44] At higher scattering angles the second term in Equation 2.10 is negligible, so $S(q) \sim 1$ and the *i(q)* is dominated by $P(q)$, which for rods $\sim q^{-1}$. Specifically, for $P(q)$ to dominate the length scales being probed by the scattering experiment, q^{-1} must be smaller than the mesh size of the rod networks ($q^{-1} << s$: red circle). In these experiments this high *q*-range is in accessible or overlapped with the region dominated by the polymer chain scattering. Thus, the scattering model accounts for the CNT network with a term that is proportional to q^{-2}, specifically $B \times q^{-2}$.

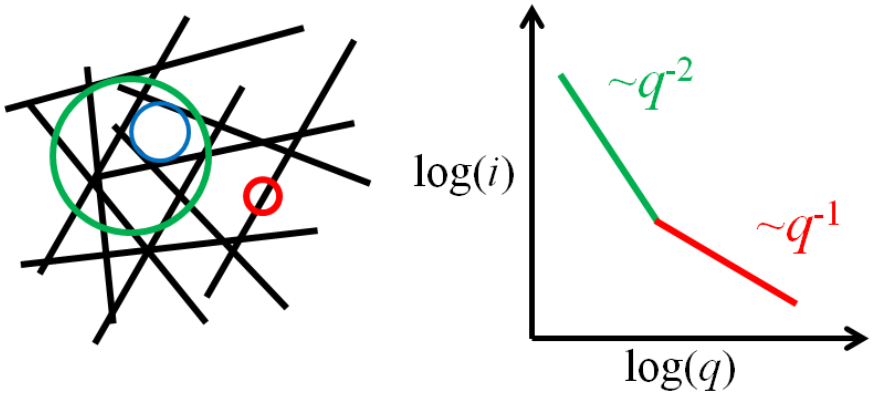

Figure 2.2. Schematic showing the relationship between the length scales probed (left) and the corresponding q regime along with the angular dependence of the scattering. When the probing length scale is greater (green) and smaller (red) than the mesh size (blue) formed by the CNTs, the expected angular dependencies are q^{-2} and q^{-1}, respectively.

At very low angle scattering angles, the scattering intensity is dominated by voids and defects in samples and this scattering intensity is given by Porod's law[45]

$$i(q) = \frac{2\pi(\Delta\rho)^2 S}{q^4} \tag{2.11}$$

where $\Delta\rho$ is the difference between the scattering length densities of the scattering objects (voids, *etc*.) and the matrix, and S is the total area of the boundaries.[38] Notice that the scattering cross-section shown in Equation 2.11 is not normalized by a unit volume, so its unit is cm^2. This contribution to the scattering model is $C \times q^{-4}$. Lastly, incoherent scattering, mainly from hydrogen, provides no structural information (q-independent) and this background intensity is incorporated *via* a constant, D. The four contributions

(polymer, CNT network, defects, incoherent scattering) combine to give the following scattering model,

$$i(q) = A \times Debye(q, R_g) + B \times q^{-2} + C \times q^{-4} + D \quad (2.12)$$

When fitting the SANS data, we found that including the constant *D* only slightly improved the coefficient of determination (COD) and had minimal impact on the other parameters. Therefore, we omitted the incoherent background contribution in the scattering model,

$$i(q) = A \times Debye(q, R_g) + B \times q^{-2} + C \times q^{-4} \quad (2.13)$$

This model incorporates three scattering objects. From high q to low q these objects are the polymer chain with R_g ~ 9nm, the mesh size of the nanotube network at tens to hundreds of nm, and defects and voids larger than ~ 1μm.

2.3.3. Method for Fitting Scattering Model to SANS Data

First, we investigate the dimensionality of the CNT network by analyzing the SANS data from the contrast matching samples with 1wt% SWCNT and nine dPS/hPS volume ratios using

$$i(q) = A \times Debye(q, R_g) + B \times q^{-n} \quad (2.14)$$

The best fits of Equation 2.14 to the data find that the exponent is the second term is $n \sim 2$.

This result confirms a rod-like network in these CNT/dPS+hPS nanocomposites. Subsequently, we fit Equation 2.13 to the SANS data sets to obtain all four fitting parameters (*A*, *B*, *C*, and R_g). We set R_g as a shared fitting parameter, which means that R_g is forced to be the same for every data set during the fitting process, because R_g should not be affected by the dPS/hPS volume ratio. The other parameters (*A*, *B*, and *C*) are related to the volume ratio of dPS in the sample, so they are free fitting parameters for the nine dPS/hPS ratios. For the dPS+hPS homopolymer sample, $B = 0$, because there are no CNT networks.

For CNT/dPS+hPS nanocomposites with a dPS/hPS volume ratio of 72.5/27.5, we adapt Equation 2.13 to account for the CNT concentration. The fitting parameter *A* is proportional to the volume fraction of polymer chains, so *A* is replaced by $A'(1 - \Phi_{cnt})$ to give

$$i(q) = A'(1 - \Phi_{cnt}) \times Debye(\mathrm{q}, R_g) + B \times q^{-2} + C \times q^{-4} \qquad (2.15)$$

where Φ_{cnt} denotes the volume fraction of CNTs. For SANS data from polymer nanocomposites with a fixed dPS/hPS ratio and different CNT concentrations (SWCNTs and MWCNTs are treated separately), we set A' as a shared fitting parameter, because A' is not affected by the CNT concentration. In addition, we set Φ_{cnt} as a fixed parameter for

each nanocomposite. The remaining fitting parameters (R_g, B, and C) are free fitting parameters for each CNT concentration.

2.4. RESULTS AND DISCUSSION

2.4.1. Homopolymer

The homopolymer sample of dPS+hPS (72.5/27.5) was measured at NCNR, and the $i(q)$ data reduction was done in IGOR Pro.[46] Figure 2.3 shows the scattering intensity as a function of q and the associated fitting with Equation 2.13 in Origin 8.6 with $B = 0$, because there is no CNT network. The shoulder in the scattering intensity is nicely captured by the Debye function and in the very high q region ($> 0.02 Å^{-1}$), the scattering curve shows a q^{-2} dependence according to the Debye function. In the low q region, the upturn in the scattering intensity is fit by the q^{-4} term in our scattering model (Equation 13). The R_g in the dPS+hPS 72.5/27.5 mixture is 9.50 ± 0.03 nm, which is close to the literature value of 8.8nm (the difference is within 8%).[39]

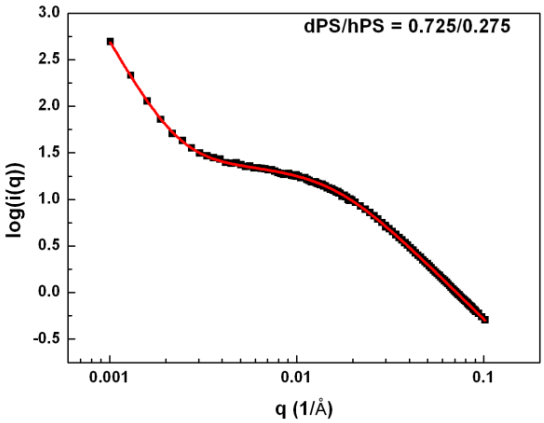

Figure 2.3. SANS scattering intensity for dPS/hPS homopolymer mixture with a volume ratio of dPS/hPS = 72.5/27.5. Equation 2.13 is fit to the data using $B = 0$. The low q upturn is described by the q^{-4} term (defect term) and the shoulder at $q \sim 0.01$Å $^{-1}$ is captured by the Debye function with $R_g = 9.50 \pm 0.03$ nm.

2.4.2. Contrast Matching in 1wt% SWCNT/dPS + hPS Nanocomposites

For the contrast matching experiments, samples with the same SWCNT concentration but different dPS/hPS volume ratios were measured at ORNL. The $i(q)$ data reduction was done using IGOR PRO and Equation 2.13 fit to the reduced $i(q)$ data using Origin 8.6. Figure 2.4 shows that the scattering intensity exhibits a shoulder and a low angle upturn. Our scattering model fits all the data well with a single value of $R_g = 9.69 \pm 0.02$ nm, which is only 2% higher than the R_g for the homopolymer.

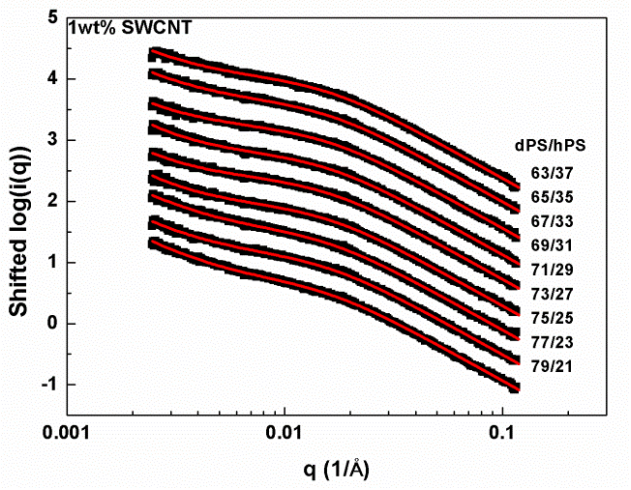

Figure 2.4. SANS scattering data for the contrast matching samples with 1wt% SWCNT and a range of dPS/hPS volume ratios. Equation 2.13 (solid line) is fit to these data with R_g as a shared parameter and R_g = 9.69 ± 0.02 nm. The data are shifted for clarity.

Figure 2.5 shows the fitting parameters *A* and *B* used in Figure 2.4 to fit Equation 2.13 as a function of dPS/hPS volume ratio (*x*). The parameter *B* is greater than zero at all dPS/hPS ratios, nearly constant from $x \sim 0.67 - 0.73$ and quite small across this range of *x*. This indicates that these dPS volume fractions are close to the ideal contrast matching condition, although perfect contrast matching was not achieved. By comparing Equation 2.5 and Equation 2.13 we find,

$$A = A_o[x(\rho_{dPS} - \rho_{swcnt})^2 + (1-x)(\rho_{hPS} - \rho_{swcnt})^2] \quad (2.16)$$

$$B = B_o[x\rho_{dPS} + (1-x)\rho_{hPS} - \rho_{swcnt}]^2 \quad (2.17)$$

where ρ_{dPS} = 6.47×10^{10} cm^{-2} and ρ_{hPS} =1.42×10^{10} cm^{-2} are known.[37] Figure 2.5 includes

Equation 2.16 and Equation 2.17 simultaneously fit using A_o = 1.03, B_o = 1.7 × 10^{-3}, and ρ_{swcnt} = 5.06 × 10^{10} cm^{-2}. As expected, *A* depends linearly on *x*. Moreover, the value of the scattering length density for SWCNT is very close (~ 1 %) to the value we obtained from the scattering density calculator.[34] The minimum in Equation 2.17 is used as the best contrasting matching condition between SWCNTs and the polymer matrix, namely *x* = 0.725. Therefore, we used a dPS/hPS volume ratio equal to 72.5/27.5 to prepare all our samples with different CNT concentrations.

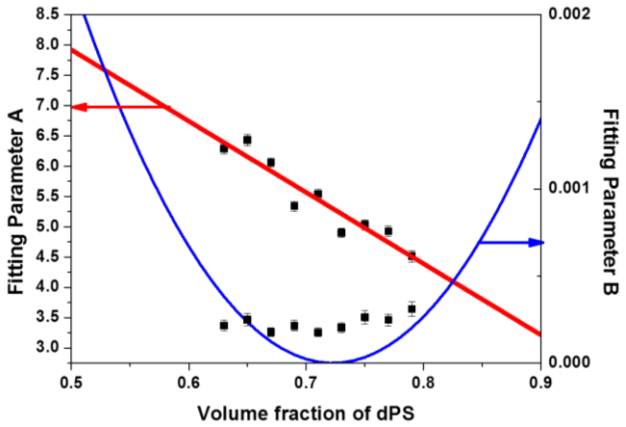

Figure 2.5. The plot of fitting parameters *A* and *B* (solid symbols) used in Figure 2.4 as a function of dPS volume fraction in the matrix. The parameter *B* is nearly constant for *x* ~ 0.67 - 0.73. Although *B* is very small, *B* > 0 implies that perfect contrast matching is unachievable. Equation 2.16 (red line) and Equation 2.17 (blue line) were simultaneously fit. Equation 2.17 has a minimum at *x* = 0.725 that is selected as the contrast matching condition for subsequent nanocomposites.

2.4.3. CNT/dPS + hPS Nanocomposites as a Function of CNT Concentration

All SWCNT/dPS+hPS and MWCNT/dPS+hPS nanocomposites with the same dPS/hPS volume ratio and different CNT concentrations were measured at ILL and the data reduction performed with LAMP which is developed by ILL. Figure 6 shows the SANS results for the SWCNT/dPS+hPS and MWCNT/dPS+hPS nanocomposites with 72.5/27.5 dPS/hPS volume ratio across a wide CNT-concentration range.

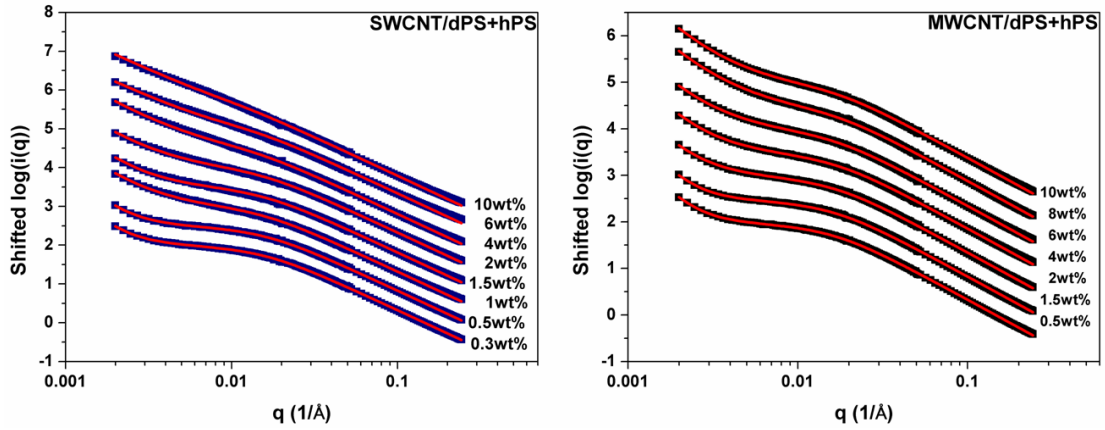

Figure 2.6. SANS data (points) for SWCNT/dPS+hPS and MWCNT/dPS+hPS nanocomposites with the 72.5/27.5 dPS/hPS volume ratio and different CNT concentrations. Equation 15 (red lines) is overlayed for each data set and data are shifted for clarity.

Figure 2.7 separates the various contributions to the scattering model for the MWCNT/dPS+hPS nanocomposites with the lowest and highest CNT loadings. The shoulder in the SANS data is modeled by the Debye function, which uses Gaussian chain statistics to describe the polymer conformation. The upturn at $q \sim 0.004$ to 0.02 $Å^{-1}$ is

captured by the rod network term (Bq^{-2}). At the lowest q range (q < 0.004 Å^{-1}), the rod network term is insufficient and the defect term is necessary, which is described by Cq^{-4}. At both low and high CNT concentration the combination of the three terms in Equation 2.15 is necessary to fit the experimental SANS data. At higher MWCNT concentrations, as expected, the contribution from the rod network is greater than in the lower concentration.

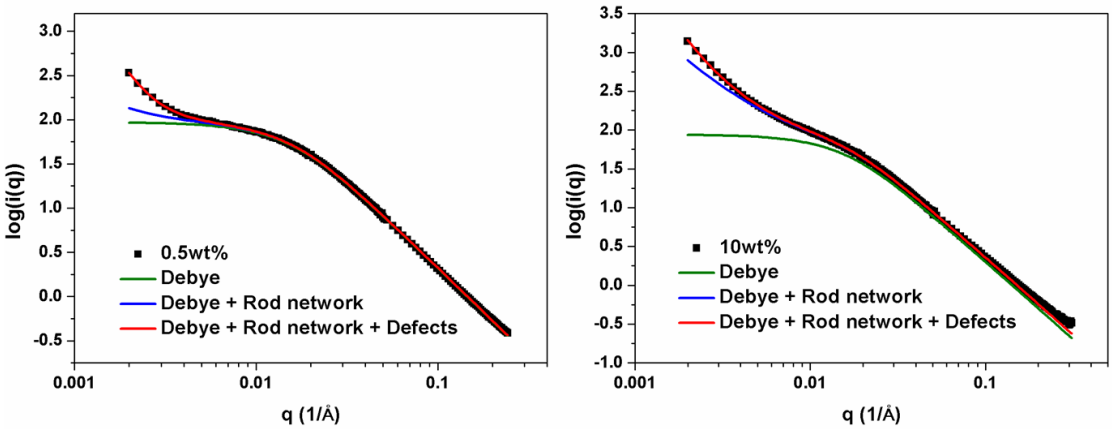

Figure 2.7. Fitting examples for the lowest (0.5 wt%) and the highest (10 wt%) CNT loadings for MWCNT/dPS+hPS (72.5/27.5) nanocomposites. The fitting curves broken into summations of different terms in Equation 2.15 are indicated in the legend. All three contributions are needed to represent the data and, as expected, the rod network gives a larger contribution at the higher MWCNT concentration.

In Figure 2.6, Equation 2.15 is globally fit using Origin 8.6 to the reduced SANS data for the SWCNT nanocomposites with A' set as a shared variable; similarly the results from MWCNT nanocomposites were fit using shared A' parameters. Equation 2.15, which uses the volume fraction of nanotubes, Φ_{cnt}, provides very good fits to all the SANS results.

The fitting parameter C is quite small in all cases (< 1.1 x 10^{-8}) and does not exhibit a monotonic trend with CNT concentration (as expected), see Section 2.4.5. The fitting parameters for B and R_g will now be discussed separately.

As expected, the parameter B, which is the prefactor for the CNT network term in Equation 2.15, increases with the CNT concentration, Figure 2.8. Interestingly, at a fixed CNT concentration B is larger for SWCNT nanocomposites than for MWCNT nanocomposites. To assess the observed difference in B in nanocomposites containing MWCNTs and SWCNTs we consider the mesh size as a function of both particle concentration and size. The probability distribution of mesh sizes for randomly and isotropically-dispersed fibers in three dimensions is given by[47]

$$\frac{dP}{ds} = (4\pi\nu Ls + 4\pi\nu s^2)exp\left[-\left(2\pi\nu Ls^2 + \frac{4\pi}{3}\nu s^3\right)\right] \quad (2.18)$$

where ν is the number density of fibers (1/nm^3), L is the half length of the fiber, and s represents the mesh size. For comparison to our experiments the half length (L) is half the average CNT length (Table 2.1) and the length, diameter and mass density were used to convert the weight percent of CNT to a number density of fibers (ν). Figure 2.9(a) shows the probability distribution of mesh sizes (Equation 2.18) for nanocomposites with 0.5, 2, 6 and 10 wt% SWCNT and 10 wt% MWCNT. The most probable mesh size decreases with

increasing SWCNT content and at a fixed CNT concentration (10 wt%) the SWCNT nanocomposite has a smaller average mesh size, because the SWCNTs have a higher aspect ratio and are smaller. The higher aspect ratio of the SWNCT is also evident in the lower critical concentration for electrical percolation found for the SWCNT nanocomposites relative to the MWCNT nanocomposites, as detailed in Section 2.2.5.

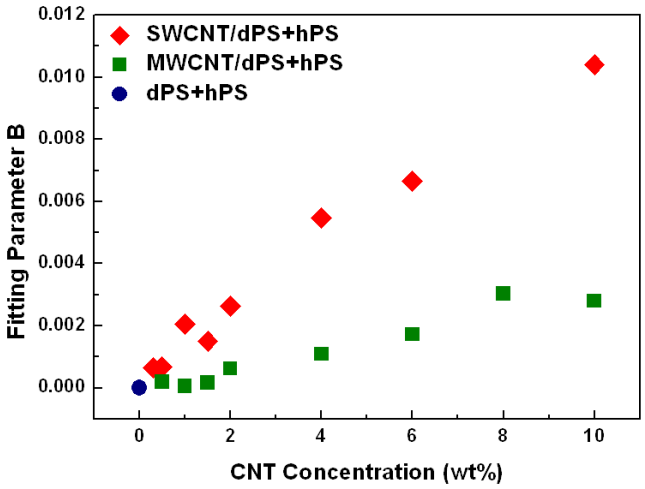

Figure 2.8. (a) The prefactor *B* for the rod network term (q^{-2}) determined by fitting Equation 2.15 to the SANS data in Figure 2.6 for SWCNT/dPS+hPS (red diamond) and MWCNT/dPS+hPS (green square) nanocomposites. For homopolymers (blue circle), *B* is zero.

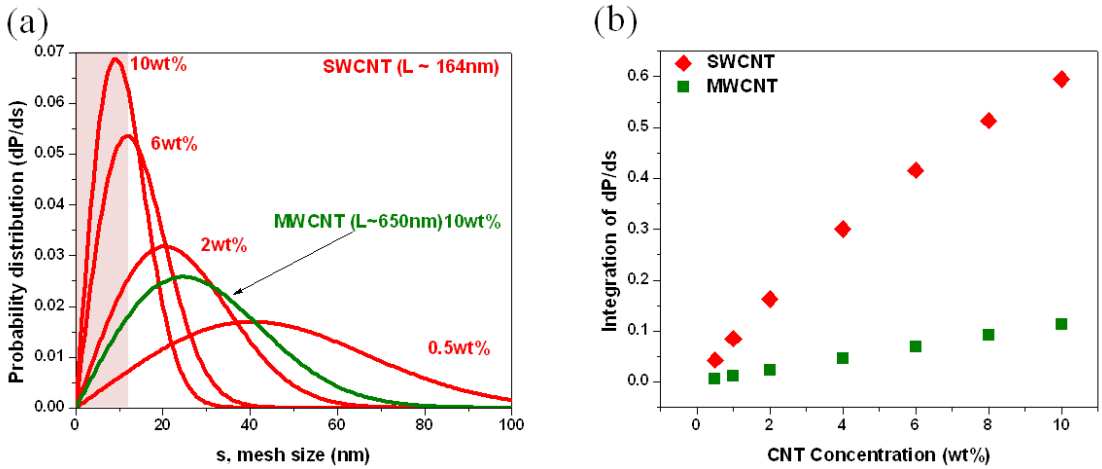

Figure 2.9. (a) The probability distribution of mesh sizes for SWCNT at different concentrations and 10wt% MWCNT, calculated from Equation 2.18. (b) Integration of dP/ds from s = 0 to 12 nm (shaded area) for SWCNTs and MWCNTs to correspond with the size range probed by the SANS experiments.

While Equation 2.18 and Figure 2.9(a) describe the full size distribution of the CNT mesh (s = 0 to ∞), the SANS experiments probe only a finite range of mesh sizes. Specifically, the contribution from the CNT network is most evident from $q \sim 0.004$ Å^{-1} to 0.02 Å^{-1}, corresponding to mesh sizes s from ~2 to 12 nm. Thus, to compare the fitting parameter B, which is proportional to the mesh concentration only within the length-scale probed by SANS, we integrate dP/ds for both SWCNTs and MWCNTs from s = 0 to s = 12 nm, Figure 2.9(b). Firstly, both the fitting parameter B and the integrated probability (s = 0-12 nm) increase with CNT concentration. Secondly, the values for SWCNT nanocomposites are higher than for MWCNT nanocomposites, which is mainly due the

higher number density of SWCNTs. The rate of increase in B is ~ 3.6 times greater for SWCNTs than for MWCNTs (Figure 2.8). Similarly, the rate of increase for the integrated probability is ~ 5.6 times greater for SWCNTs, Figure 2.9(b). Given the assumptions associated with Equation 2.18 (monodisperse, straight fibers), this agreement is quite satisfying. This analysis provides valuable confirmation that at a fixed wt% CNT the SWCNT mesh is smaller in size and gives a larger contribution to the scattering. These conclusions are also qualitatively evident in the SANS plots for SWCNT/dPS+hPS and MWCNT/dPS+hPS (Figure 2.6), where the scattering contribution of the nanotube network is more pronounced in the SWCNT nanocomposites. Moreover, the shoulder in the SANS data that is associated with polymer chain scattering remains quite evident at the highest concentration in the MWCNT nanocomposites, while the contribution from the Debye function is subtle in the SWCNT nanocomposites due to the greater contribution of the CNT network. Overall, the agreement between Figure 2.8 and Figure 2.9(b) further confirms the appropriateness of our scattering model that includes a contribution from the rod network.

2.4.4. Radius of Gyration in CNT/dPS + hPS Nanocomposites

Figure 2.10 shows the R_g values extracted from the SANS data in Figure 2.6 using Equation 2.15. When the concentration is below 2wt%, R_g is approximately constant suggesting that R_g is unaffected at low SWCNT or MWCNT concentrations. Above 2wt%, R_g in the MWCNT/dPS+hPS nanocomposites appears to slightly decrease. However, R_g increases significantly in SWCNT/dPS+hPS nanocomposites as the nanotube concentration increases. At 10wt% SWCNT (i.e., highest concentration), R_g is ~ 13 nm. Relative to the homopolymer (0 wt% CNTs), this R_g represents a dramatic increase of 36% increase.

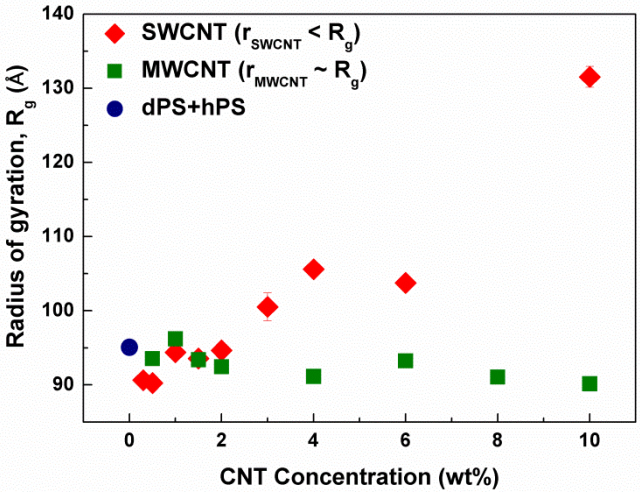

Figure 2.10. R_g for SWCNT/dPS+hPS and MWCNT/dPS+hPS nanocomposites versus CNT concentration. R_g is determined by fitting Equation 2.15 to the scattering data in Figure 2.6. For comparison, the R_g value for dPS/hPS (72.5/27.5) is included (*cf.* Figure 2.3). Error bars are directly from fitting.

In Karatrantos' molecular dynamics simulation work,[32] they studied the change in polymer structure as a function of r_{swcnt} /R_g size ratios (0.08 ~ 0.59) and CNT polymer interactions (interaction strength between polymer chains and SWCNT: 1 to 5 k_BT) and found no change in R_g. In the simulations, the highest CNT loading is only about 0.8v% and the system is represented by polymer chains surrounding an isolated SWCNT. Nevertheless, the SANS results agree with simulations, because no significant change in R_g is observed for concentrations less than 1.6v% (2wt%). Moreover, the temperature dependence of the diffusion coefficient in MWCNT/hPS nanocomposites[7] indicates only a very weak (or no) interaction between CNTs and polystyrene. This suggests that the R_g change we observe by SANS for SWCNT is not caused by the adsorption of polymer chains on SWCNT. Note that others have found that R_g increases as nanoparticle concentration increases for hard and soft *spherical* nanoparticles with $r/ R_g < 1$.[20, 23] For hard spherical nanoparticles with attractive particle-polymer interactions, Frischknecht *et al.* used self-consistent PRISM simulations to show that R_g increases as the nanoparticle concentration increases.[31] Conversely, when $r/R_g \sim 1$, R_g decreases slightly with increasing concentration in both our MWCNT nanocomposites and spherical nanoparticles at high loading.[24]

Previously we reported a diffusion minimum for polymer tracer diffusion in both SWCNT/PS and MWCNT/PS nanocomposites.[7,6,8] This behavior occurs when the polymer R_g is greater than the radius of the carbon nanotubes ($r/ R_g < 1$), and the minimum occurs near the rheological percolation threshold (~0.5wt% for SWCNT and ~ 2wt% for MWCNT). From the reptation model, it has been shown that the diffusion coefficient is proportional to R^2/τ,[48] where R is the polymer chain size and τ is the relaxation time for a polymer chain to disentangle from its original tube. If we assume that τ is unaffected by the addition of CNTs into polystyrene, we expected a similar trend in R_g when we increase the CNT concentration in both SWCNT/PS and MWCNT/PS nanocomposites. The static properties of polymer chains we report in this work are difficult to reconcile with the trend of the tracer diffusion we obtained when increasing CNT concentration, which implies that other mechanisms are responsible for the observed minimum in the melt diffusion coefficient. More experiments, possibly quasi-elastic neutron scattering (QENS), nuclear magnetic resonance (NMR), and neutron spin echo that probe the dynamics of polymer segments at short time scales might provide more insight into the molecular mechanism or mechanisms that lead to a minimum in the polymer diffusion coefficient with increase CNT content.

2.4.5 Scattering from Voids

Figure 2.11 shows the fitting parameter *C*, which is the prefactor to the q^{-4} term and corresponds to the strength of the scattering from voids inside our samples. Figure 2.11 shows that *C* is quite small in all cases ($< 1.1 \times 10^{-8}$) and does not exhibit a monotonic trend with CNT concentration (as expected). At high SWCNT concentrations (> 3 wt%) the parameter *C* has a larger uncertainty, because the scattering at $q < 0.004$ Å $^{-1}$ is dominated by the rod network term (Bq^{-2}) and fitting the q^{-4} term is less reliable. Consequently, the SANS data for SWCNT/PS nanocomposites with high SWCNT concentrations appear to have a simple q^{-2} dependence, but the fits shown in Figure 2.6 include the q^{-4} term.

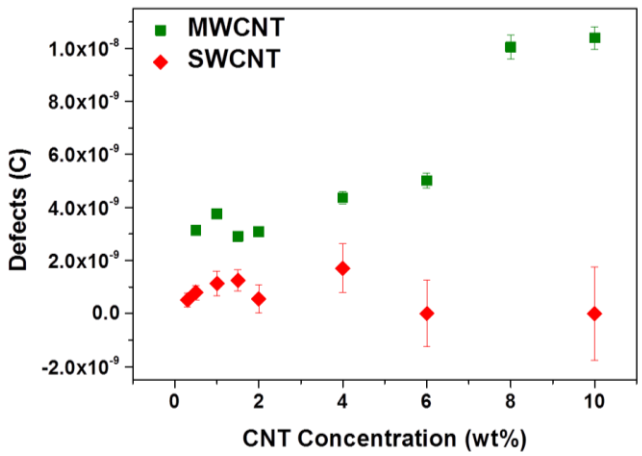

Figure 2.11. Fitting parameter *C* as a function of CNT concentration. *C* is obtained by fitting Equation 2.15 globally to the reduced SANS data for the SWCNT/PS and MWCNT/PS nanocomposites with *A′* set as a shared variable.

2.5. SUMMARY

We have set the foundation for studying polymer conformations in the presence of CNTs, and more generally in cylindrical nanoparticles. We used SANS to probe the polymer chain conformation in CNT/polymer nanocomposites as a function of nanotube concentration. Our scattering model incorporates four scattering features, namely polymer chains, rod networks, defects, and incoherent scattering, although the contribution for incoherent scattering was negligible. Contrast matching experiments identified the dPS/hPS volume ratio that minimizes the scattering contribution from CNTs, although the rod network still makes a contribution. A Debye function fit the shoulder in the SANS data, indicating that polymer chains obey Gaussian chain statistics. Our observation agrees with recent simulations[32] indicating that R_g does not change appreciably at low CNT concentration (< 2wt%). For MWCNT/polymer nanocomposites ($r/R_g \sim 1$), R_g decreases slightly as CNT concentration increases. In SWCNT/polymer nanocomposites ($r/R_g \sim 0.4$) above 2 wt%, R_g increases strongly by up to 36% as the SWCNT concentration increases.

The scattering contribution from the rod network term (B) increases as CNT concentration increases, as expected. Moreover, nanocomposites with SWCNTs have higher values for B than nanocomposites with MWCNTs at the same CNT concentration,

because SWCNTs have a higher probability of smaller mesh size at the same mass concentration, which is due to the much higher number density for SWCNTs compared to MWCNTs. This is consistent with predictions of mesh size for networks of randomly and isotropically dispersed rods.

2.6. REFERENCES

1. Alexandre, M.; Dubois, P., *Mater. Sci. Eng. R-Rep.* **2000,** *28* (1-2), 1-63.

2. Balazs, A. C.; Emrick, T.; Russell, T. P., *Science* **2006,** *314* (5802), 1107-1110.

3. Coleman, J. N.; Khan, U.; Gun'ko, Y. K., *Adv. Mater.* **2006,** *18* (6), 689-706.

4. Thostenson, E. T.; Ren, Z. F.; Chou, T. W., *Compos. Sci. Technol.* **2001,** *61* (13), 1899-1912.

5. Moniruzzaman, M.; Winey, K. I., *Macromolecules* **2006,** *39* (16), 5194-5205.

6. Mu, M. F.; Clarke, N.; Composto, R. J.; Winey, K. I., *Macromolecules* **2009,** *42* (18), 7091-7097.

7. Tung, W. S.; Clarke, N.; Composto, R. J.; Winey, K. I., *Macromolecules* **2013,** *46* (6), 2317-2322.

8. Grady, B. P., *J. Polym. Sci. Pt. B-Polym. Phys.* **2012,** *50* (9), 591-623.

9. Chatterjee, T.; Yurekli, K.; Hadjiev, V. G.; Krishnamoorti, R., *Adv. Funct. Mater.* **2005,**

15 (11), 1832-1838.

10. Song, Y. S.; Youn, J. R., *Carbon* **2005,** *43* (7), 1378-1385.

11. Xie, X. L.; Mai, Y. W.; Zhou, X. P., *Mater. Sci. Eng. R-Rep.* **2005,** *49* (4), 89-112.

12. White, S. I.; Mutiso, R. M.; Vora, P. M.; Jahnke, D.; Hsu, S.; Kikkawa, J. M.; Li, J.; Fischer, J. E.; Winey, K. I., *Adv. Funct. Mater.* **2010,** *20* (16), 2709-2716.

13. White, S. I.; Vora, P. M.; Kikkawa, J. M.; Winey, K. I., *Adv. Funct. Mater.* **2011,** *21* (2), 233-240.

14. Kashiwagi, T.; Du, F. M.; Douglas, J. F.; Winey, K. I.; Harris, R. H.; Shields, J. R., *Nat. Mater.* **2005,** *4* (12), 928-933.

15. Zhou, W.; Islam, M. F.; Wang, H.; Ho, D. L.; Yodh, A. G.; Winey, K. I.; Fischer, J. E., *Chem. Phys. Lett.* **2004,** *384* (1-3), 185-189.

16. Zhao, C. G.; Hu, G. J.; Justice, R.; Schaefer, D. W.; Zhang, S. M.; Yang, M. S.; Han, C. C., *Polymer* **2005,** *46* (14), 5125-5132.

17. Chatterjee, T.; Jackson, A.; Krishnamoorti, R., *J. Am. Chem. Soc.* **2008,** *130* (22), 6934-+.

18. Du, F. M.; Fischer, J. E.; Winey, K. I., *J. Polym. Sci. Pt. B-Polym. Phys.* **2003,** *41* (24), 3333-3338.

19. Mackay, M. E.; Tuteja, A.; Duxbury, P. M.; Hawker, C. J.; Van Horn, B.; Guan, Z. B.; Chen, G. H.; Krishnan, R. S., *Science* **2006,** *311* (5768), 1740-1743.

20. Nakatani, A. I.; Chen, W.; Schmidt, R. G.; Gordon, G. V.; Han, C. C., *Int. J. Thermophys.* **2002,** *23* (1), 199-209.

21. Sen, S.; Xie, Y. P.; Kumar, S. K.; Yang, H. C.; Bansal, A.; Ho, D. L.; Hall, L.; Hooper, J. B.; Schweizer, K. S., *Phys. Rev. Lett.* **2007,** *98* (12).

22. Jouault, N.; Dalmas, F.; Said, S.; Di Cola, E.; Schweins, R.; Jestin, J.; Boue, F., *Macromolecules* **2010,** *43* (23), 9881-9891.

23. Tuteja, A.; Duxbury, P. M.; Mackay, M. E., *Phys. Rev. Lett.* **2008,** *100* (7).

24. Nusser, K.; Neueder, S.; Schneider, G. J.; Meyer, M.; Pyckhout-Hintzen, W.; Willner, L.; Radulescu, A.; Richter, D., *Macromolecules* **2010,** *43* (23), 9837-9847.

25. Termonia, Y., *Polymer* **2009,** *50* (4), 1062-1066.

26. Ozmusul, M. S.; Picu, C. R.; Sternstein, S. S.; Kumar, S. K., *Macromolecules* **2005,** *38* (10), 4495-4500.

27. Picu, R. C.; Ozmusul, M. S., *J. Chem. Phys.* **2003,** *118* (24), 11239-11248.

28. Vacatello, M., *Macromolecules* **2002,** *35* (21), 8191-8193.

29. Hooper, J. B.; Schweizer, K. S., *Macromolecules* **2006,** *39* (15), 5133-5142.

30. Hooper, J. B.; Schweizer, K. S., *Macromolecules* **2007,** *40* (19), 6998-7008.

31. Frischknecht, A. L.; McGarrity, E. S.; Mackay, M. E., *J. Chem. Phys.* **2010,** *132* (20).

32. Karatrantos, A.; Composto, R. J.; Winey, K. I.; Clarke, N., *Macromolecules* **2011,** *44* (24), 9830-9838.

33. Zhou, W.; Ooi, Y. H.; Russo, R.; Papanek, P.; Luzzi, D. E.; Fischer, J. E.; Bronikowski, M. J.; Willis, P. A.; Smalley, R. E., *Chem. Phys. Lett.* **2001,** *350* (1-2), 6-14.

34. Szwarc, M., *Nature* **1956,** *178* (4543), 1168-1169.

35. King, S. M., Small-angle neutron scattering. In *Modern Techniques for Polymer Characterisation*, R. A. Pethrick, J. V. D., Ed. Wiley: Chichester, 1999; pp 171-232.

36. Kaiser, A. B.; Park, Y. W., *Synth. Met.* **2005,** *152* (1-3), 181-184.

37. Higgins, J. S.; Benoit, H. C., *Polymers and Neutron Scattering*. Oxford University Press: New york, 1994.

38. Ryong-Joon, R., *Methods of X-ray and Neutron Scattering in Polymer Science*. Oxford University Press: New York, 2000.

39. Bates, F. S.; Wignall, G. D., *Phys. Rev. Lett.* **1986,** *57* (12), 1429-1432.

40. Mandelbrot, B. B., *The Fractal Geometry of Nature*. W. H. Freeman and Company: San Fransisco, 1983.

41. Teixeira, J., *J. Appl. Crystallogr.* **1988,** *21*, 781-785.

42. Golosova, A. A.; Adelsberger, J.; Sepe, A.; Niedermeier, M. A.; Lindner, P.; Funari, S. S.; Jordan, R.; Papadakis, C. M., *J. Phys. Chem. C* **2012,** *116* (29), 15765-15774.

43. Justice, R. S.; Wang, D. H.; Tan, L. S.; Schaefer, D. W., *J. Appl. Crystallogr.* **2007,** *40*, S88-S92.

44. Schaefer, D. W.; Zhao, J.; Brown, J. M.; Anderson, D. P.; Tomlin, D. W., *Chem. Phys. Lett.* **2003,** *375* (3-4), 369-375.

45. Debye, P.; Anderson, H. R.; Brumberger, H., *J. Appl. Phys.* **1957,** *28* (6), 679-683.

46. Kline, S. R., *J. Appl. Crystallogr.* **2006,** *39*, 895-900.

47. Ogston, A. G., *Transactions of the Faraday Society* **1958,** *54* (11), 1754-1757.

48. Rubinstein, M.; Colby, R. H., *Polymer Physics*. Oxford University Press: New York, 2003.

Chapter 3

Polymer Structure in Aligned SWCNT/Polystyrene Nanocomposites

The contents of this chapter have been in preparation to submit to *ACS Macro letters*, in a modified version.

3.1. INTRODUCTION

In Chapter 2, we studied polymer chain in *isotropic* carbon nanotube/polystyrene nanocomposites which was the first experimental work investigating how polymer chains are affected by cylindrical nanofillers.[1] The polymer nanocomposites with single walled carbon nanotubes (SWCNTs) show an increase in R_g with increasing SWCNT concentration. Whereas, R_g is independent of filler concentration in nanocomposites with multi-walled carbon nanotubes (MWCNTs). The diameters of the SWCNT bundles are smaller than the MWCNT bundles in these composites, so that at a fixed concentration the CNT mesh size is smaller for the SWCNT nanocomposites and the polymer conformation adapt to this smaller mesh size by expanding. In this chapter, we produce anisotropic SWCNT/polystyrene nanocomposites by melt fiber spinning to explore the polymer chain conformations in anisotropic meshes.

3.2. EXPERIMENTAL METHODS

3.2.1. Sample Preparation

The SWCNT/polystyrene nanocomposites contain a mixture of polystyrene (PS, 117 kg/mol, 1.05) and deuterated polystyrene (dPS, 116 kg/mol, 1.03) to minimize the scattering from the SWCNT and were studied in Chapter 2.[1] Fabrication of SWCNT/dPS + PS nanocomposites is described in somewhere else.[1-2] Isotropic SWCNT/dPS+PS nanocomposites were measured using SANS and then melt fiber spun to align the SWCNTs.[3] The SWCNT/dPS+PS nanocomposites were placed in a piston and heated to 150°C (for SWCNT concentration <= 2wt%) or 170°C (for SWCNT concentration > 2wt%) and held for 30 minutes. The piston then extruded (1 mm/min) the nanocomposite melts through a spinneret (0.5mm) and a winder collected the nanocomposites fibers. The diameter of the fiber, which correlates with the degree of alignment for SWCNTs, is controlled by the winding speed (1 - 4m/min). For SWCNT concentrations < 2wt%, two winder rates (2 and 4m/min) were used to control the degree of alignment. Above 2wt%, nanocomposites become too solid for continuous fiber spinning, and fibers frequently broke during the process. Moreover, the fiber diameter is not uniform at the lower winder rate (2m/min). Standard operating procedures for fiber spinning can be found in Appendix

C. All the SWCNT/dPS+PS nanocomposite fibers were first annealed in a vacuum oven at 150°C for 3 days to remove all the residual stresses in the PS/dPS matrix induced by fiber spinning. The fibers were then cut, arranged in a mold to maintain the extrusion direction, and hot pressed into thin circular disks (diameter ~ 3 cm; thickness ~ 160 μm) for both SANS and SAXS experiments. For comparison, a homopolymer blend of dPS and PS (same volume ratio as the matrix for the nanocomposites) was also melt fiber spun, annealed, hot pressed, and measured by SANS.

3.2.2. Small Angle Neutron Scattering (SANS)

Samples were measured on NG3 and NG7 instruments at the NIST center of neutron research[4] in Gaithersburg, MD, USA. For NG3, three sample-detector distances with L = 1.3 and 4m for λ = 6 Å and L = 13m for λ = 8.4 Å, provided a q-range of 0.001$Å^{-1}$ to 0.4 $Å^{-1}$. For NG7, three sample-detector distances with L = 1, 4, and 13.5m for λ = 6 Å, provided a q-range of 0.001$Å^{-1}$ to 0.5 $Å^{-1}$. Detailed calibration method and data reduction process can be found in our previous publication.[1] All data reduction is done in IGOR Pro.[5]

3.2.3. Small Angle X-ray Scattering (SAXS)

The SAXS measurements were conducted using the multi-angle X-ray scattering facility at the Laboratory for Research on the Structure of Matter. Cu X-rays (wavelength ~ 1.54 Å) combining with the sample-to-detector distances of 150 cm for small angle scattering gives us a q range of 0.007 – 0.14 $Å^{-1}$. Samples were measured at room temperature and the scattering data was reduced and analyzed using Datasqueeze software.[6]

3.3. DATA ANALYSIS

3.3.1. Orthogonal Integration and the Fitting Model for SANS Data

The 2D SANS data are anisotropic and the average intensities versus q were obtained by integrating 25 degrees (+/- 12.5°) over two orthogonal directions, namely parallel and perpendicular to the extrusion direction, Figure 3.1(a). This data reduction from 2D to $I(q)$ data was applied for low and medium q ranges and subsequently combined, Figure 3.1(b). The orthogonal integrations were also performed in the absence of anisotropy (*i.e.* dPS+PS) for comparison.

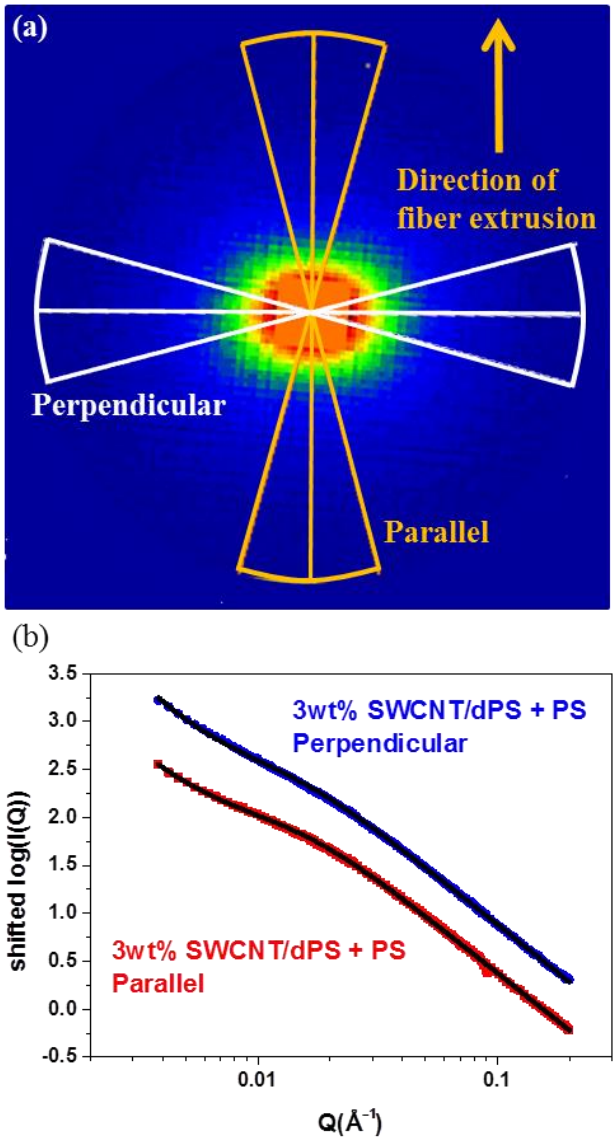

Figure 3.1. (a) SANS data (low q configuration) for an aligned 3wt% SWCNT/dPS+PS nanocomposite. (b) $I(q)$ data from integrating over 25 degrees parallel and perpendicular to the direction of alignment for SWCNTs. Black lines are associated fitting to Equation 3.1. Data are shifted for clarity.

The $I(q)$ data were fit to a model developed in Chapter 2.[1] The scattering model

includes polymer chain scattering, rod network scattering, and scattering from defects:

$$i(q) = A(1 - \Phi_{cnt}) \times Debye(\mathrm{q}, R_g) + B \times q^{-2} + C \times q^{-4} \quad (3.1)$$

where

$$Debye(q, R_g) = \frac{2}{(qR_g)^4}\left[q^2R_g^2 - 1 + exp\left(-q^2R_g^2\right)\right] \quad (3.2)$$

R_g is the radius of gyration of polymer chains, and Φ_{cnt} denotes the volume fraction of SWCNTs. The Bq^{-2} term represents the rod network scattering derived from the scattering of a fractal object, which has a self-similar structure ($S(q) \sim q^{-D}$).[7] Here D represents the fractal dimension, and it has been shown that for rod networks, $D \sim 2$.[8-9] At very low q, the scattering intensity is dominated by voids and defects as described by Porod's law[10] with a q^{-4} dependence.

3.3.2. Homopolymer Chain Conformations

Melt fiber spinning elongates polymer conformations along the fiber axis and these distorted conformations will persist indefinitely when the molten sample is cooled and held below the glass transition temperature. Thus, we first evaluate whether our annealing condition is sufficient to eliminate any chain distortions imposed by the extensional flow of fiber spinning. A dPS+PS blend was also melt fiber spun, annealed, and measured using SANS. Two data sets corresponding to parallel and perpendicular to the fiber axis from the

measurement of dPS+PS blend were fit globally to Equation 1. *A* was set as a shared fitting parameter, and Φ_{cnt} and *B* were set to zero because there is no rod network in the homopolymer blend. The same R_g perpendicular and parallel to the fiber extrusion direction was obtained (Figure 3.2), demonstrating that the annealing condition (150°C for 3 days) is sufficient to remove anisotropic chain conformations produced by the melt extrusion.

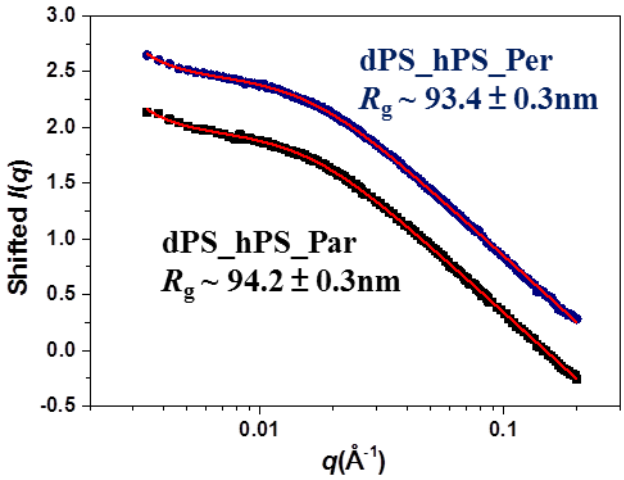

Figure 3.2. SANS data from the extruded and annealed dPS+PS blend. $I(q)$ profiles correspond to scattering parallel and perpendicular to extrusion direction. Lines are the best fits to Equation 1 (A' as a shared fitting parameter; Φ_{cnt} and *B* set to zero) with the R_g values provided.

3.3.3. SANS on Aligned SWCNT/dPS + PS Nanocomposites

For SWCNT/dPS+PS nanocomposites, scattering intensity (q = 0.004 to 0.2Å^{-1})

from the same SWCNT concentration samples (isotropic and aligned) were fit globally with the two data sets from the dPS+PS mixture to increase the reliability of fitting. *A* was set as a shared fitting parameter, Φ_{cnt} was set as a fixed parameter, and R_g, *B*, and *C* were set as free parameters. For each SWCNT concentration (0 – 10 wt%), *A* and two R_gs for the homopolymer blend were obtained from the fitting and found to be in reasonable agreement (Figure 3.3). SANS data with fits to Equation 1 are provided in Figure 3.4 and each aligned SWCNT/dPS+PS sample provides values for B_{par}, B_{per}, R_g^{par} and R_g^{per}.

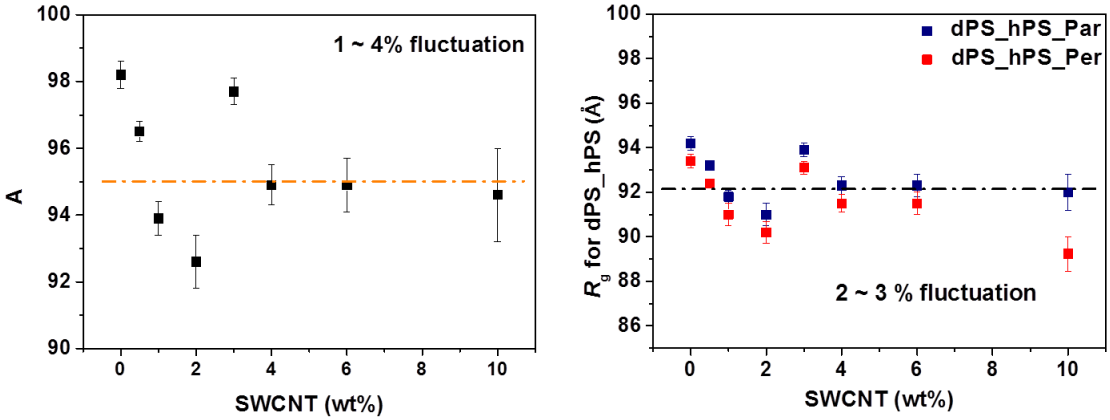

Figure 3.3. Fitting results of *A* and two R_gs used for cross references between different SWCNT concentrations.

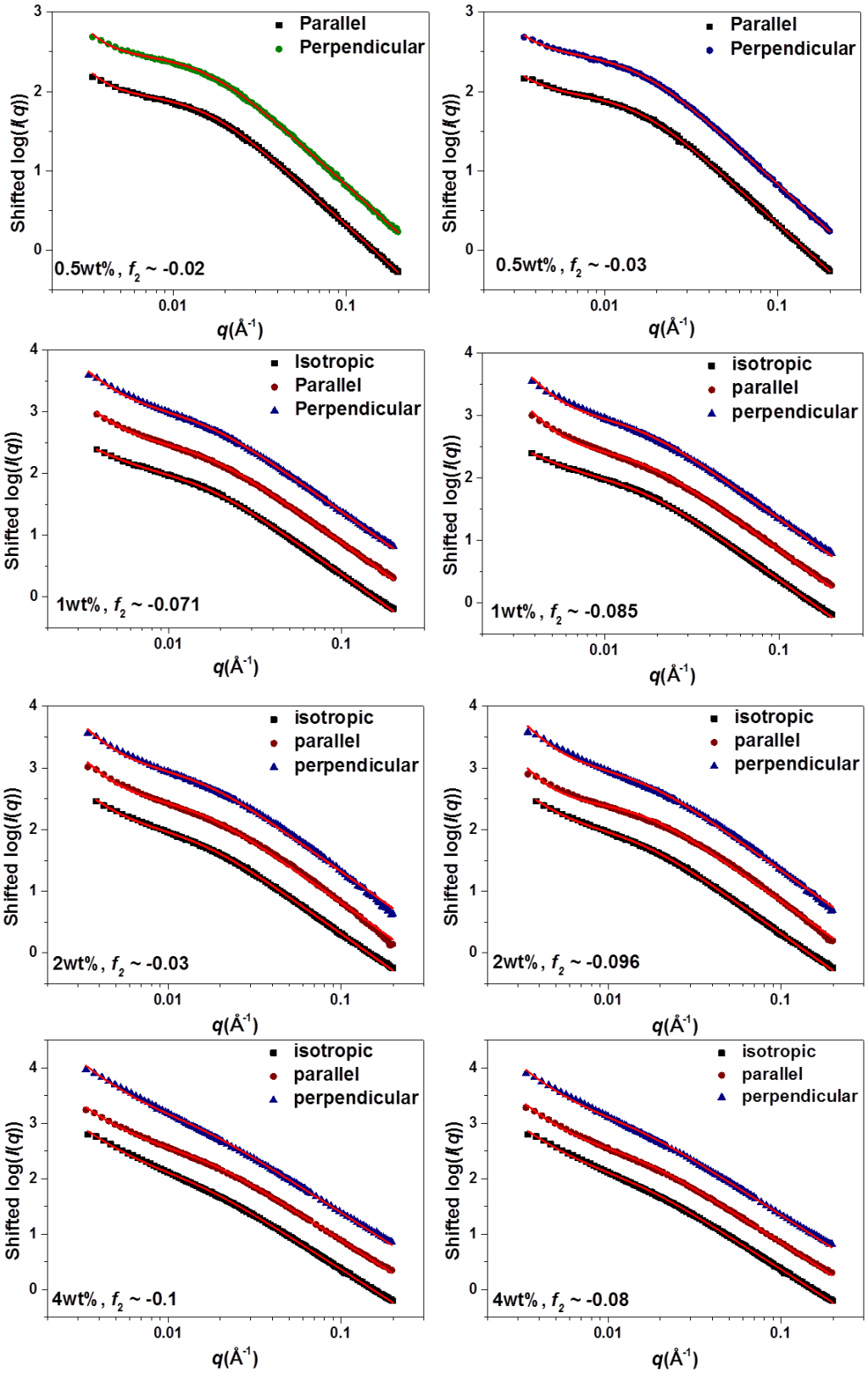
Parallel
Perpendicular
Shifted log(I(q))
q(Å-1)
0.5wt%, f2 ~ -0.02
Parallel
Perpendicular
Shifted log(I(q))
q(Å-1)
0.5wt%, f2 ~ -0.03
Isotropic
Parallel
Perpendicular
Shifted log(I(q))
q(Å-1)
1wt%, f2 ~ -0.071
isotropic
parallel
perpendicular
Shifted log(I(q))
q(Å-1)
1wt%, f2 ~ -0.085
isotropic
parallel
perpendicular
Shifted log(I(q))
q(Å-1)
2wt%, f2 ~ -0.03
isotropic
parallel
perpendicular
Shifted log(I(q))
q(Å-1)
2wt%, f2 ~ -0.096
isotropic
parallel
perpendicular
Shifted log(I(q))
q(Å-1)
4wt%, f2 ~ -0.1
isotropic
parallel
perpendicular
Shifted log(I(q))
q(Å-1)
4wt%, f2 ~ -0.08

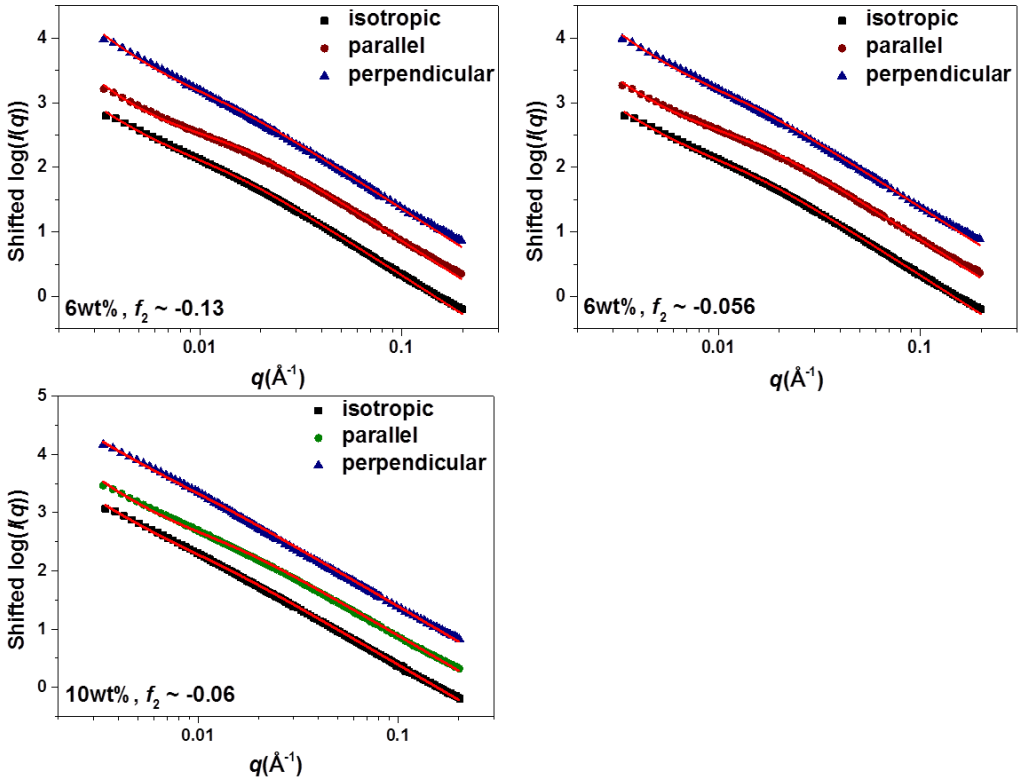

Figure 3.4. Fits to SANS data by Equation 3.1 for SWCNT/dPS+PS nanocomposites (SWCNT concentration: 0.5wt% ~ 10wt%) with isotropic SWCNT meshes and anisotropic SWCNT meshes. Different degrees of alignment for anisotropic meshes are represented using Herman's orientation function, explained later. 0.5wt% and 3wt% samples with isotropic SWCNT orientation were not measured due to the limitation of available beam time.

3.3.4. SAXS on Aligned SWCNT/dPS + PS Nanocomposites

The anisotropic SWCNT meshes in aligned SWCNT/dPS+PS samples were characterized using the Herman's orientation function (f_2). Anisotropic 2D SAXS data was integrated from q = 0.01 to 0.12 Å $^{-1}$ and plotted as function of ϕ from 0° to 90°, where ϕ is

the azimuthal angle between the fiber extrusion direction and the direction of the integrated intensity, Figure 3.5. When f_2 has the value of 1, 0, or -0.5, the SWCNTs are perfectly aligned perpendicular to the extrusion direction, the SWCNTs are isotropic, or the SWCNTs are perfectly aligned parallel to the extrusion direction, respectively. The SWCNT/dPS+PS nanocomposites studied here have f_2 values range from -0.02 to -0.14 indicating that, although the annealing condition is sufficient for the polymer matrix to relax, the SWCNTs are aligned in the direction of extrusion.

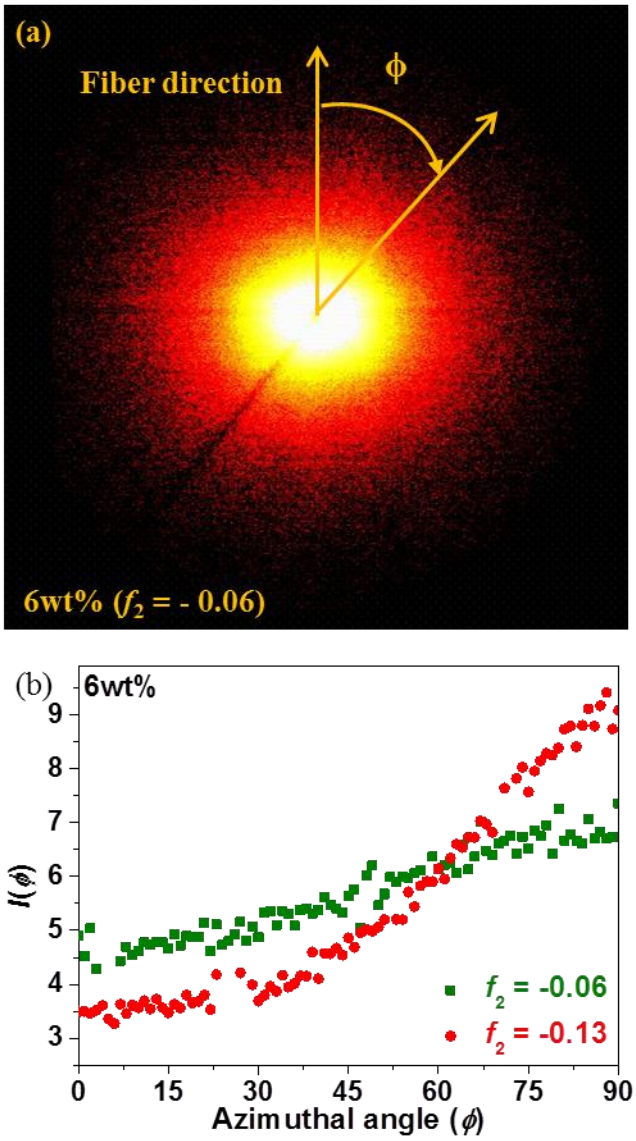

Figure 3.5. (a) SAXS data for an aligned 6wt% SWCNT/dPS+PS nanocomposite with Herman's orientation parameter of -0.06. (b) $I(\phi)$ integrated from q ~ 0.01 to 0.12 Å^{-1} versus the azimuthal angle (ϕ) for the 6wt% SWCNT/dPS+PS nanocomposite with different degrees of alignment (squares f_2 = -0.06 and circles f_2 = -0.13).

As shown in Figure 3.1 for SANS, $I(q)$ from the SAXS data was obtained by integrating 25 degrees (+/- 12.5°) over the directions parallel and perpendicular to the

extrusion direction. Polystyrene has very low X-ray scattering in this q range, so the scattering is dominated by the SWCNT meshes and maybe some defects. Thus, for SAXS with q ~ 0.02 to 0.1Å $^{-1}$ Equation 3.1 simplifies to

$$i(q) = B \times q^{-n} \tag{3.3}$$

and n is ~ 2 to 2.5.

3.4. RESULTS AND DISCUSSION

3.4.1. Anisotropic Rod Network Scattering

Figure 3.6(a) compares B_{per}/B_{par} obtained from SANS and SAXS for each sample with $-f_2$ from SAXS. In both scattering models, Equation 3.1 and Equation 3.3, B represents the scattering strength of the rod networks, which is affected by the concentration of mesh sizes smaller than the probing length scale of the scattering experiments.[1] Theoretical work on anisotropic mesh sizes of rods distributed in 3D show that, at a fixed volume fraction of rods, the distribution of mesh sizes parallel to the rod alignment direction is larger than the mesh sizes perpendicular to the rod alignment.[11] (See Section 3.4.3.) Figure 3.6(b) illustrates this finding and demonstrates that the anisotropic SWCNT meshes have higher concentrations of meshes with the mesh size within the probing length scale of the scattering experiments (green circle) perpendicular to the

alignment direction of SWCNTs. Thus, $B_{per}/B_{par} > 1$ corresponds to SWCNT/dPS+PS nanocomposites with SWCNTs preferentially along the fiber direction. Moreover, both measures of B_{per}/B_{par} correlate well with $-f_2$, further indicating that larger values of B_{per}/B_{par} corresponds to greater SWCNT alignment. Finally, the extent of SWCNT alignment is comparable as measure by SANS and SAXS.

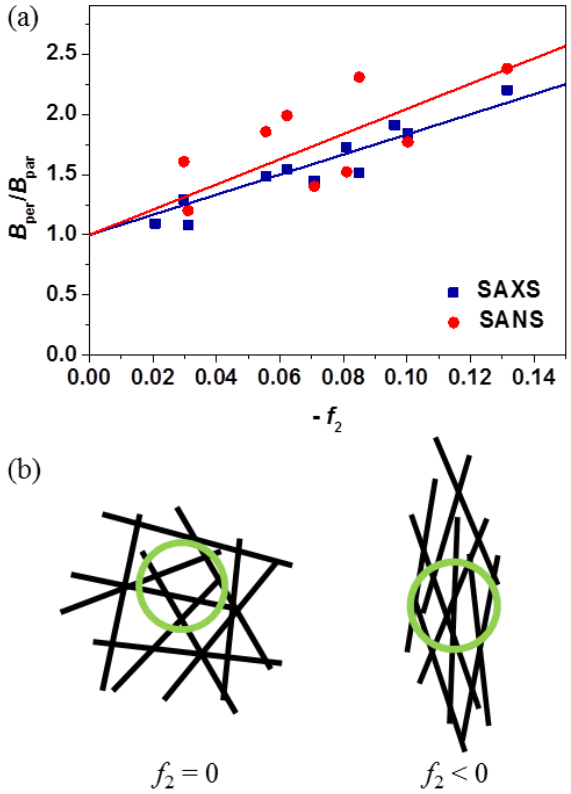

Figure 2.6. (a) B_{per}/B_{par} obtained from SANS and SAXS are plotted as a function of the Herman's orientation function from SAXS for aligned SWCNT/dPS+PS nanocomposites of various compositions. Lines are fits with a fixed intercept of 1 corresponding to isotropic samples. (b) Schematic of isotropic and aligned SWCNT rod networks, where the green circle represents the probing length scale of SANS and SAXS.

3.4.2. Anisotropic Chain Conformation

Fitting Equation 3.1 to SANS data also provides the radii of gyration parallel and perpendicular to the SWCNT alignment. Figure 3.7(a) shows R_g^{par} and R_g^{per} for anisotropic SWCNT/dPS+PS nanocomposites as a function of SWCNT concentration; for comparison R_g for the isotropic nanocomposites is included. The anisotropic nanocomposites included in Figure 3.7(a) have $-f_2$ = -0.03 to -0.08. Compares to R_g in isotropic samples, R_g^{per} is slightly higher, while R_g^{par} is substantially lower and even close to the bulk R_g. This indicates that the polymer chain expands perpendicular to the direction of SWCNTs as shown schematically in Figure 3.7(b).

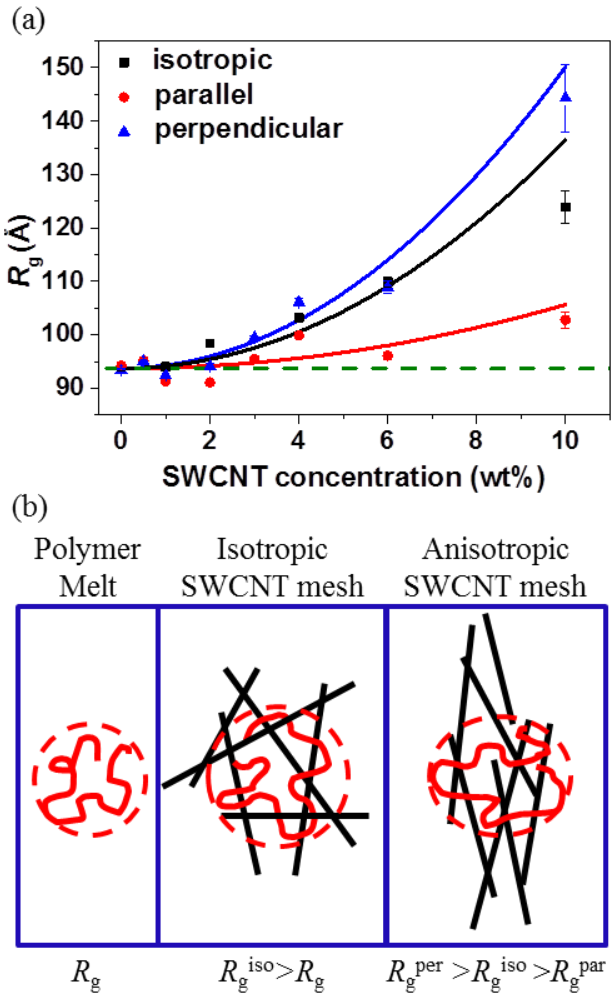

Figure 2.7. (a) Polymer radii of gyration in isotropic and aligned SWCNT/dPS+PS nanocomposites. The aligned nanocomposites have Herman's orientation function of -0.03 to -0.08. Lines are guides to the eye. (b) Schematic illustration of polymer chains in polymer melt with bulk R_g, in isotropic nanocomposites with isotropic expansion (R_g^{iso}), and in anisotropic nanocomposites with anisotropic expansion ($R_g^{per} > R_g^{par}$).

In isotropic SWCNT/dPS+PS nanocomposites, the mesh size varies with SWCNT concentration and ranges from a few nanometers to tens or hundreds nanometers.[1] When

the mesh size is smaller than the bulk polymer conformation (R_g ~ 9.50 ± 0.03 nm)[1], polymer conformations expand to circumvent the SWCNTs. When the SWCNTs are isotropic, the chain expansion is isotropic because the SWCNT mesh size is isotropic. When the SWCNTs are aligned, the mesh sizes perpendicular to the direction of alignment are smaller, so polymer chains expand perpendicular to the SWNCT alignment. The effect becomes more pronounced at higher SWCNT concentrations. In contrast, parallel to the SWCNT alignment, the mesh size increases with alignment and R_g^{par} is smaller than R_g^{per} and R_g^{iso}.

3.4.3. Theoretical Analysis for Mesh Sizes in Anisotropic Rod Networks

Theoretical work has been developed to analyze the mesh sizes in anisotropic rod networks with a fiber orientation probability density function Ω(θ, ϕ), where ϕ and θ are base angle and polar angle in a spherical coordinate system, respectively.[11] Ω(θ, ϕ) needs to fulfill the normalization condition so that $\int_0^{\pi} d\theta \int_0^{\pi} d\phi\, \Omega(\theta, \phi) \sin\theta = 1$. A plane is the 3D space is definened by its normal vector (Θ, Φ) with χ being the angle between the directions of (θ, ϕ) and (Θ, Φ). If a plane (Θ, Φ) is randomly cut through a rod network, aperture circles with various radius *r*, the miximum circle contains only empty space in

between fibers, can be found on the cross section.[12-13] The probability distribution function of the radii of the aperture circle $f(r)$ is defined as[11]

$$f(r) = 2\pi v(r+\rho)exp(\pi v\rho^2)exp(-\pi v(r+\rho)^2) \tag{3.4}$$

where $v(\Theta, \Phi)$ is the average number of fiber cut ends on the cross section, $\rho(\Theta, \Phi)$ is the average radius of the fiber cut ends. $v(\Theta, \Phi)$ is defined as

$$v(\Theta,\Phi) = \frac{V_R}{\pi r_R^2}\Omega(\theta,\Phi)\gamma(\Theta,\Phi) \tag{3.5}$$

where V_R is the colume fraction of rods, r_R is the radius of rods, and $\gamma(\Theta, \Phi)$ is the statistical mean value of $|\cos\chi|$, defined as

$$\gamma(\Theta,\Phi) = \int_0^{\pi} d\theta \int_0^{\pi} d\phi \, |\cos\chi| \, \Omega(\theta,\phi) \, \sin\theta \tag{3.6}$$

The average radius of the fiber cut ends $\rho(\Theta, \Phi)$ on the cross section can be expressed as

$$\rho(\Theta,\Phi) = r_R\sqrt{\frac{1}{\gamma(\Theta,\Phi)}} \tag{3.7}$$

Assuming an isotropic orientation of rods with $\Omega(\theta, \phi) = 1/2\pi$, $V_R = 0.05$, and $r_R = 3.7$nm (radius of our SWCNT), $f(r)$ can be calculated for a random cross section (Θ, Φ) as shown in Figure 3.8. Due to the isotropic orientation of rods, one cross section (Θ, Φ) will give the same distribution of aperture sizes. For analyzing anisotropic rod networks, assuming the fiber extrusion direction is along the direction of $\theta = \pi/2$ and $\phi = \pi/2$, so that $\Omega(\theta, \phi)$ only depends on ϕ; specifically $\Omega(\theta, \phi) = 0.5\sin\phi$ gives a preferential orientation of rods along

the fiber extrusion direction. Two cross sections with (Θ, Φ) = (π /2, π /2) and (π /2, 0) are pendicular and parallel to the fiber extrusion direction, respectively, can be cut through the anisotropiic meshes. $f(r)$ for there two cross sections are also shown in Figure 3.8. As can be seen, $f(r)$ on the cross section perpendicular to the fiber extrusion direction moves toward the smaller aperture sizes, and $f(r)$ on the cross section parallel to the fiber extrusion direction moves toward the larger aperture sizes. The shaded region at apertures less than 20 nm represents the probing length scale of SANS and SAXS. For anisotropic meshes, the direction perpendicular to the alignment direction of SWCNTs has higher mesh concentrations within the probing length scale of the scattering experiments and, thus, higher scattering intensity. Whereas, along the direction parallel to the alignment direction of SWCNTs, the scattering intensity from the meshes is lower because fewer SWCNTs are within the probing length scale of the scattering experiments. This theoretical description of anisotropic meshes is consistent with our finding that $B_{per}>B_{par}$ and B_{per}/B_{par} increases with $-f_2$.

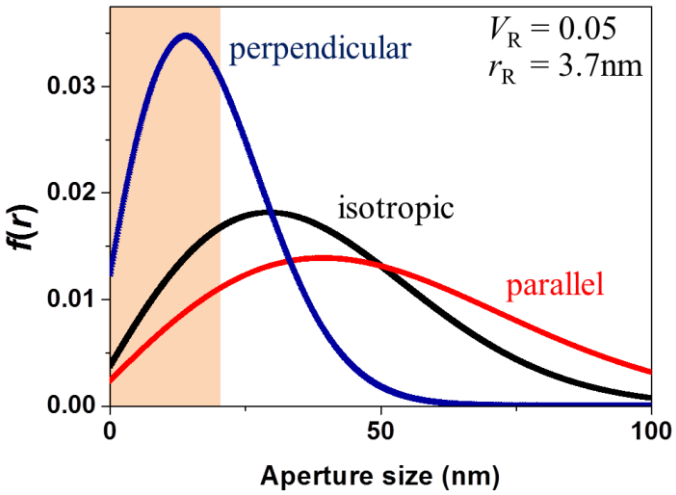

Figure 3.8. Probability distribution of aperture sizes (r) for isotropic and anisotropic rod networks (5v%; rod radius = 3.7nm). For anisotropic rod networks, distribution of aperture sizes on cross sections parallel and perpendicular to the fiber extrusion direction are shown. Shaded region represents the probing length scales of SANS and SAXS.

3.5. SUMMARY

In conclusion, SWCNT/dPS+PS nanocomposites with 0-10wt% SWCNT were extruded, annealed and characterized by SANS and SAXS. The ratio between the scattering strength of SWCNT networks perpendicular and parallel to the alignment direction of SWCNTs (B_{per}/B_{par}) is well correlated to the Herman's orientation function, which suggests that B_{per}/B_{par} can be also used to characterize the degree of alignment for SWCNTs. The orientation parameter was then used to select a set of nanocomposites with comparable SWCNT alignment to investigate the polymer conformation as a function of SWCNT concentration. At sufficiently high SWCNT concentration, polymer chains

experience smaller mesh sizes perpendicular to the alignment direction and adopt an expanded chain conformation to circumvent the SWCNTs. Simultaneously, polymer chains experience larger mesh sizes parallel to the alignment direction and adopt less expanded chain conformations to produce anisotropic polymer conformations with $R_g^{per} > R_g^{par}$. Interestingly, this finding demonstrates that these SWCNTs and PS are not strongly attractive, which would be expected to produce the converse effect of $R_g^{per} < R_g^{par}$. As more cylindrical nanoparticles become available, other size ratios between the fillers and polymer chains should be explored, as well as investigating systems with favorable nanoparticle-polymer interactions.

3.6. REFERENCES

1. Tung, W. S.; Bird, V.; Composto, R. J.; Clarke, N.; Winey, K. I., *Macromolecules* 2013, *46* (13), 5345-5354.

2. Du, F. M.; Fischer, J. E.; Winey, K. I., *J. Polym. Sci. Pt. B-Polym. Phys.* 2003, *41* (24), 3333-3338.

3. Du, F. M.; Fischer, J. E.; Winey, K. I., *Phys. Rev. B* 2005, *72* (12).

4. Glinka, C. J.; Barker, J. G.; Hammouda, B.; Krueger, S.; Moyer, J. J.; Orts, W. J., *J. Appl. Crystallogr.* 1998, *31*, 430-445.

5. Kline, S. R., *J. Appl. Crystallogr.* 2006, *39*, 895-900.

6. Heiney, P., *Commission on Powder Diffraction Newsletter* 2005, *32*, 9-11.

7. Teixeira, J., *J. Appl. Crystallogr.* 1988, *21*, 781-785.

8. Schaefer, D. W.; Zhao, J.; Brown, J. M.; Anderson, D. P.; Tomlin, D. W., *Chem. Phys. Lett.* 2003, *375* (3-4), 369-375.

9. Zhou, W.; Islam, M. F.; Wang, H.; Ho, D. L.; Yodh, A. G.; Winey, K. I.; Fischer, J. E., *Chem. Phys. Lett.* 2004, *384* (1-3), 185-189.

10. Debye, P.; Anderson, H. R.; Brumberger, H., *J. Appl. Phys.* 1957, *28* (6), 679-683.

11. Pan, N., *J. Compos Mater.* 1994, *28* (16), 1500-1531.

12. Komori, T.; Makishima, K., *Text. Res. J.* 1979, *49* (9), 550-555.

13. Ogston, A. G., *Transactions of the Faraday Society* 1958, *54* (11), 1754-1757.

Chapter 4

Temperature Dependence of Polymer Diffusion in MWCNT/PS Nanocomposites

The contents of this chapter were published in a modified version. Adapted with permission from (*Macromolecules*, **2013**, *46* (13), 5345–5354). Copyright (2013) American Chemical Society.

4.1 INTRODUCTION

Polymer nanocomposites, which are composed of nanoparticles (ex: silica nanoparticles, silver nanowires, and carbon nanotubes, etc.) and polymer, have captured significant research interest, because electrical conductivity[1-2], flame retardation[3-4], mechanical strength[5-6], and viscosity[7] can substantially change with added nanofiller.[8-10] Understanding how nanoparticles affect the polymer matrix, particularly polymer dynamics, and how this controls the behavior of polymer nanocomposites are critical for advancing the field. Nanoparticles are several orders of magnitude smaller than traditional fillers and provide an opportunity to study how polymer physics is affected by particles with length scales between monomer size and polymer chain size. At a fixed

filler concentration, nanoparticles create much more interface between nanoparticles and polymers than microscopic particles, which dramatically increases the volume fraction of polymer matrix influenced by the nanoparticles.[11] Thus, small amounts of nanoparticles can significantly change the bulk properties of polymer matrix.[12-14]

Polymer dynamics in polymer nanocomposites are impacted by the presence of impenetrable regions (that is the nanoparticles themselves), as well as by nanoparticle-polymer interactions. Polymer dynamics can be studied on various length and time scales. Nuclear magnetic resonance (NMR)[15] and quasi-elastic neutron scattering (QENS)[16-17] probe local motions. Viscosity[18] and tracer diffusion measurements[19] integrate the motions of larger polymer segments and entire polymer chains. Investigating polymer diffusion in nanocomposites is instrumental in understanding the polymer dynamics on microscopic scales and provides a foundation for understanding dynamics more broadly in polymer nanocomposites.

Tracer diffusion coefficients (D) of polymers in silica/polystyrene nanocomposites decrease monotonically as the volume fraction of spherical phenyl-capped silica nanoparticle increases.[20-21] Data for a variety of tracer molecular weights and nanoparticle sizes collapse onto a master curve when the normalized tracer

diffusion coefficient is plotted as a function of $P_d/2R_g$, where P_d is the interparticle distance and R_g is the radius of gyration of the tracer molecule. In contrast, earlier studies of polymer diffusion in carbon nanotube (CNT) polymer nanocomposites found that D decreases with increasing CNT concentration and then increases above a critical CNT concentration when R_g of the tracer polymer is larger than the radius of CNT.[22-23] For multi-walled carbon nanotubes (MWCNT)/ polystyrene (PS) nanocomposites, the normalized D/D_0 at 170°C reaches a minimum of ~ 0.3 at 2 wt% MWCNT concentration, which corresponds approximately to the MWCNT concentration for network formation in these composites. The underlying mechanism that produces a dramatic decrease in D at low CNT concentrations and allows D to recover at higher concentration remains under investigation.

Recent simulation studies have focused on how polymer structure and dynamics are affected by the addition of a single-walled carbon nanotube (SWCNT).[24-25] Although the local structure adjacent to the SWCNT is altered, R_g of the polymer was found to be unaffected by SWCNT/polymer interactions or SWCNT sizes.[24] Although polymer diffusion was unaffected when there are no interactions between SWCNT and polymers, attractive interaction slowed polymer diffusion. Interestingly, polymer diffusion parallel

to the SWCNT was found to be faster than diffusion perpendicular to the SWCNT.[25] To facilitate these simulations, the model used one SWCNT embedded in a polymer melt and given the system size this corresponds to a low SWCNT concentration (0.4 v%) and, consequently, does not address the impact of a percolated nanotube network on polymer diffusion. An alternative simulation model was used to access higher concentrations of low aspect ratio nanorods (aspect ratio ~ 5 and $R_g > R_{CNT}$) and the number of monomers between entanglement (N_e) monotonically decreases as a function of nanorod concentration.[26] The various simulations of polymer dynamics in the presence of cylindrical nanoparticles have yet to elucidate the underlying mechanism that produces the observed minimum in *D*.

Polymer diffusion in melts is described by Rouse dynamics[27] or the reptation model,[28] when the polymer chains are unentangled or entangled, respectively. In both cases the temperature dependence of polymer diffusion arises from the viscosity of Rouse monomeric units, which is associated with the free volume and captured by the Williams–Landel–Ferry (WLF) equation:

$$\log\eta(T) = C_1 + C_2 \frac{1}{T - T_\infty} \tag{4.1}$$

where C_1 and C_2 are empirical constants and T_∞ is the Vogel temperature where the free

volume is zero.[29] The WLF equation is derived by combining the Doolittle equation ($\eta \sim \exp(B/f)$) and the temperature dependence of free volume ($f = \alpha_f(T - T_\infty)$), where η is viscosity, B is an empirical constant, f is the fractional free volume, and α_f is the thermal expansion coefficient of free volume. Since D/T has the same temperature dependence as $1/\eta$, the WLF equation for D/T is

$$\log\frac{D}{T} = C_1' - C_2\frac{1}{T - T_\infty} \tag{4.2}$$

This expression accurately describes the temperature dependence of the diffusion coefficient in entangled homopolymers.[30-31] This chapter explores the temperature dependence of the tracer diffusion coefficient in MWCNT/PS nanocomposites and evaluates the applicability of the WLF equation in these polymer nanocomposites.

4.2 EXPERIMENTAL METHODS

4.2.1 Materials

Multi-walled carbon nanotubes (MWCNT) synthesized by chemical vapor deposition were purchased from Nanolab, Inc. and purified by thermal oxidation and a HCl treatment[32] before making nanocomposites. The residual iron catalyst as measured by thermal gravimetric analysis is < 2 wt%. The size and aspect ratio of MWCNT were measured by scanning electron microscopy. The mean diameter is 34 ± 6.9 nm, the mean

length is 871 ± 313 nm, and the mean aspect ratio is 26.[23]

Polystyrene (PS) and deuterated polystyrene (dPS) were purchased from Pressure Chemical and Polymer Source, respectively, and characterized by size exclusion chromatography (SEC). The weight average molecular weights (M_w) and polydispersity indices (PDI) are shown in Table 4.1. The radius of gyration (R_g) was calculated by $R_g = l_k\sqrt{N}/\sqrt{6}$, where N is the number of Kuhn monomers (M_{Kuhn} = 720 g/mol) and l_k is the Kuhn length of polystyrene, 1.8 nm.[29]

Table 4.1. Weight averaged molecular weight, polydispersity index, and radius of gyration of the matrix polymer (PS) and the tracer polymer (dPS).

Name	M_w (kg/mol)	PDI	R_g (nm)
480k PS	478.7	1.03	18.9
680k dPS	678.4	1.10	22.6

4.2.2 Bilayer sample preparation

MWCNT/PS nanocomposites were prepared by the coagulation method.[33] MWCNTs were well-dispersed in DMF by sonication for 24 hours, and PS was dissolved separately in DMF by stirring for 24 hours. After mixing these two solutions, the

MWCNT/PS nanocomposites were rapidly precipitated in DI water, which is a non-solvent for both MWCNT and PS. The precipitate was collected, dried in a fume food, annealed at 150 °C in vacuum for 24 hours and hot-pressed at 150 °C into circular disks (diameter ~ 10 mm; thickness > 100 μm).[51] All the nanocomposites used in this work were prepared and studied previously.[23] Thin dPS films (~20 nm) were made by spin coating onto silicon wafers and the thickness was measured by ellipsometry. The dPS films were floated on DI water and transferred to the nanocomposite disks. The bilayer samples were annealed in a vacuum oven with precise temperature control (within 1 °C) to activate diffusion. Seven annealing temperatures from 152 °C to 214 °C were studied. Annealing times (t) ranged from 22min to 120h to obtain diffusion lengths (x) of ~ 400 nm.

4.2.3 Elastic Recoil Detection (ERD)

ERD was used to determine the tracer diffusion coefficients of 680k dPS in MWCNT/PS nanocomposites. He^{2+} ions are accelerated to 3MeV and impinged on bilayer samples. Deuterium (^2D) and hydrogen (^1H) at different depths are expelled out from the samples by these He^{2+} ions. By detecting the energies of expelled deuterium, the concentration depth profiles of dPS in the polymer nanocomposites were determined. The

raw data from ERD measures counts (number of deuterium) versus the energy of the deuterium and the analysis includes converting deuterium counts to dPS concentrations and converting energy to sample depth. A detailed description of this technique is given in the review paper by Composto et al.[34] Example depth profiles (dPS volume fraction versus sample depth) are shown in Figure 4.1.

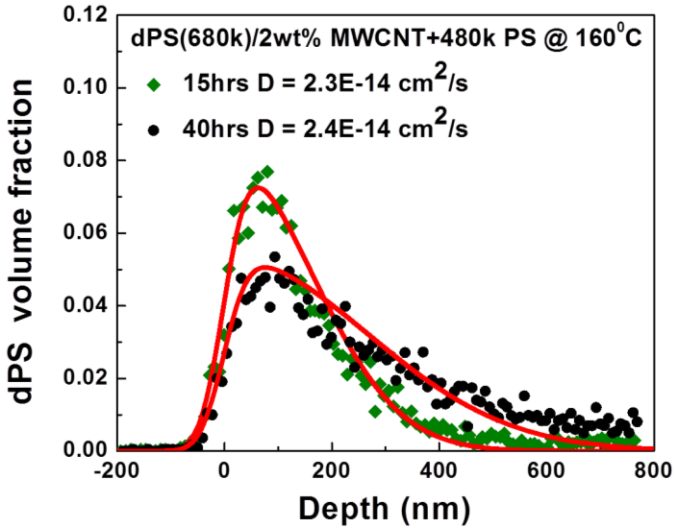

Figure 4.1. The depth profile of 680k dPS partially diffused into 2 wt% MWCNT/PS nanocomposites after annealing at 160 °C for 15h and 40h. Lines correspond to the convolution of a Gaussian function and Equation 4.3, where h = 18 nm and the diffusion coefficients (D) are given in the figure.

The depth profile is fit by convoluting the solution of Fick's second law and a Gaussian function to find the diffusion coefficient. Fick's second law for a thin film

diffusing into a semi-infinite environment, which is the MWCNT/PS nanocomposite in our case, gives the concentration profile for the tracer as

$$\Phi(\mathrm{x}) = \frac{1}{2}\left[erf\left(\frac{h-x}{\sqrt{4Dt}}\right) + erf\left(\frac{h+x}{\sqrt{4Dt}}\right)\right] \quad (4.3)$$

where $\Phi(x)$ denotes the dPS volume fraction, *h* is the original thickness of the thin film (~ 20nm), *x* is depth from the sample surface, *t* is the diffusion time, and *D* is the tracer diffusion coefficient of dPS. The parameters *h*, *x* and *t* are known, so *D* is the only fitting parameter to the experimental concentration profile. The boundary condition we used is a finite ultra-thin tracer film diffusing into a semi-infinite matrix. The total amount of tracers are constant, and the concentrations of tracers in the matrix is zero at interface at $t = 0$. A Gaussian function describes the depth resolution, 70 nm, of ERD, which was determined by measuring the front edge of a dPS thin film for an unannealed bilayer sample. An example fitting is shown in Figure 4.1, where two samples with the same matrix and tracer films were annealed at 160 °C for different times. The diffusion coefficients are independent of annealing time and are consistent with our previous work.[22-23] The uncertainty of the diffusion coefficients is ~ 10 %; see Appendix D. The time-independent diffusion coefficient also indicates that our nanocomposites do not substantially change during the diffusion experiment.

4.2.4 Modulated differential scanning calorimetry (MDSC)

Glass transition temperatures (T_g) of MWCNT/PS nanocomposites were measured by modulated-temperature differential scanning calorimetry (MDSC), using a TA instruments Q2000, to separate the recoverable and irrecoverable processes. A modulation amplitude of ±1 °C and a period of 60s were used with a ramping rate of 2 °C/min to heat the samples to 150 °C, and T_g was determined from the transition in the second heating curve. The start and end of the transition were determined by the intersections of three lines fit to the heat flow curve before, during and after the transition. Figure 4.2 shows the T_g and the breadth of the transition as a function of MWCNT loading and demonstrates no significant influence of nanotube concentration on T_g from 0 – 6wt% MWCNT.

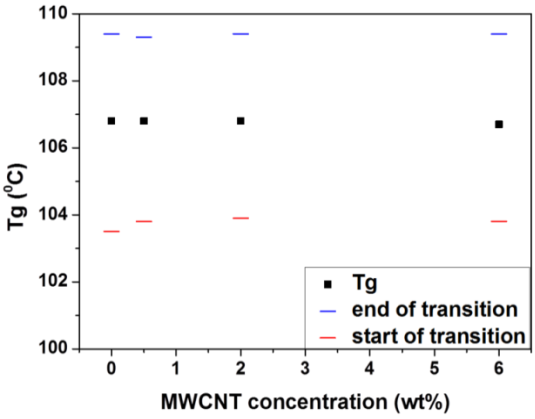

Figure 4.2. Glass transition temperature and the breadth of the transition for MWCNT/PS nanocomposites as a function of MWCNT loading.

4.3 RESULTS AND DISCUSSION

4.3.1 Temperature dependence of diffusion minimum

Bilayer samples of 680k dPS (20nm thick) on MWCNT/PS nanocomposites (>100 µm thick) were annealed at seven temperatures ranging from 152 °C to 214 °C (425 K to 487 K). Annealing times were selected to ensure that dPS diffused sufficiently into the nanocomposites (~400 nm); this distance is many times larger than R_g of the tracer (22.6 nm). The depth profiles of dPS were measured by ERD and fit by the convolution of Fick's second law and the instrument resolution to obtain the tracer diffusion coefficient of dPS, *D*. The tracer diffusion coefficients for dPS in MWCNT/PS as a function of MWCNT loading and at different temperatures are shown in Figure 4.3(a). By increasing the temperature by ~60 °C, *D* increases by 2.5-3 orders of magnitude. As previously reported,

D measured at 170 °C (444 K) exhibits a minimum at ~ 2 wt% MWCNT; although on a log scale the minimum appears subtle. Overall the effect of MWCNT concentration on polymer diffusion is less pronounced than the effect of temperature.

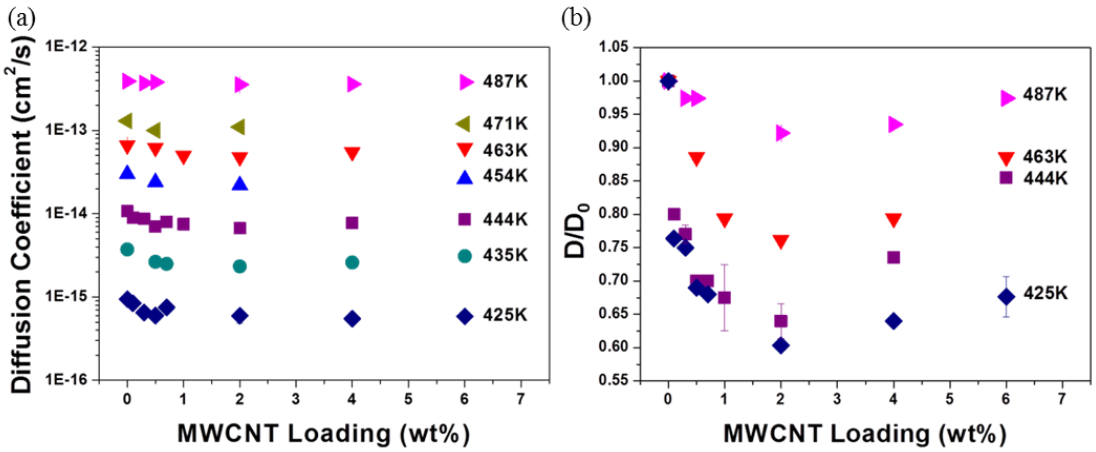

Figure 4.3. (a) Tracer diffusion coefficients of 680k dPS in MWCNT/PS nanocomposites as a function of MWCNT loadings at various temperatures. (b) Normalized tracer diffusion coefficients (D/D_0) for 680k dPS in MWCNT/PS nanocomposites. A diffusion minimum $(D/D_0)_{min}$ is present at every temperature at ~ 2 wt% and becomes less pronounced at higher temperature. Some data points represent duplicate samples and the standard deviation is shown, except when it is smaller than the size of the symbol.

In Figure 4.3(b), we plot the normalized diffusion coefficients, the tracer diffusion coefficients in nanocomposites divided by the tracer diffusion coefficients in the homopolymer at the same temperature (D/D_0), as a function of MWCNT loading at four temperatures. Here it is evident that the diffusion minimum $(D/D_0)_{min}$ occurs at ~ 2 wt%

MWCNT loading independent of the annealing temperature. The minimum becomes shallower at higher temperatures: $(D/D_0)_{min}$ at 425 K and 487 K are 0.6 and 0.92, respectively. At low temperatures the decrease in tracer diffusion coefficient at < 2 wt% MWCNT is particularly dramatic. These data suggest that the mechanism causing the decrease in diffusion coefficients is less effective at higher temperatures.

Across the temperature range of this study the minimum in D/D_0 coincides with the rheological percolation threshold reported previously for these nanocomposite.[23] Using linear viscoelastic measurements, the rheological percolation threshold is the concentration at which the nanocomposites response changes from liquid-like behavior ($G' \sim \omega^2$) to solid-like behavior ($G'' \sim \omega^0$). This phenomenon is closely tied to the formation of a nanotube network that effectively impedes the motion of the polymer matrix at modest time scales. In polycarbonate/MWCNT nanocomposites the percolation threshold extracted from rheology has been reported to depend on temperature.[35] In our diffusion studies, which correspond to longer time scales well above the disentanglement times of the polymer, the nanotube concentration corresponding to network formation is independent of temperature.

4.3.2 Temperature dependence of tracer diffusion coefficients at fixed MWCNT loadings

The tracer diffusion of homopolymers in well-entangled melts can be described by the reptation model, [36-37]

$$D = \frac{4}{15}\frac{M_e M_0 k_B T}{M^2 \xi_0(T)} \tag{4.5}$$

where T is temperature, ξ_0 is the monomeric friction coefficient, M_e is the entanglement molecular weight, M_0 is the monomeric molecular weight, and M is the tracer molecular weight. The M^{-2} dependence of D has been confirmed experimentally.[38-49] If we assume that M_e is temperature independent, Equation 4.5 shows that D/T is proportional to $\xi_0(T)^{-1}$ with the same functional dependence on temperature. Thus, the WLF equation, Equation 4.2, sufficiently describes the temperature dependence of both D/T and $\xi_0(T)$. This is well documented for the tracer diffusion coefficients in homopolymer melts.[30-31, 50]

In Figure 4.4 we plot the temperature dependence of the tracer diffusion coefficients for three polymer nanocomposites (0.5, 2, and 6 wt% MWCNT) as $log(D/T)$ versus $1/(T-T_\infty)$. The WLF equation (Equation 2) predicts a straight line with a slope of $-C_2$. For polystyrene, viscosity measurements found C_2 = 710 K and T_∞ = 322 K.[51] This T_∞ value is consistent with the generalization that the Vogel temperature is 50K lower than the

glass transition temperature (T_g). The T_g's of our polymer nanocomposites are independent of the MWCNT loading (Figure 4.1), suggesting the absence of strong attraction between the PS and MWCNTs.[52] Thus, we fix T_∞ (322 K) and use C_1' and C_2 as free parameters to fit Equation 4.2. Figure 4.4 shows the fitting results and C_2 values associated with three MWNCT loadings, where C_1' for all CNT concentrations is ~ -10.5. The fitting results of C_1 and C_2 for other MWCNT concentrations and the error analysis are provided are provided in Figure 4.5. The WLF equation accurately captures the temperature dependence of the tracer diffusion coefficient in MWCNT/PS nanocomposites across three decades of (D/T). While the variations in C_2 for the three MWCNT loadings in Figure 4.4 is small (within 10 %), the middle composition (2wt% MWCNT) has the largest C_2 value, which coincides with a minimum in D/D_0 at 2 wt% MWCNT.

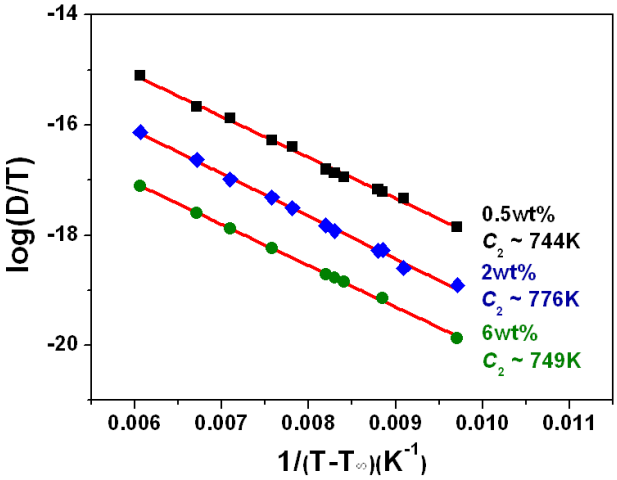

Figure 4.4. Temperature dependence of tracer diffusion coefficients for 0.5, 2, and 6 wt% MWCNT/PS nanocomposites, plotted as D/T versus $1/(T\text{-}T_\infty)$ with T_∞ = 322 K. The red lines are best fits of the WLF equation (Equation 4.2) to the data and the values of C_2 are given. These curves are vertically shifted for clarity.

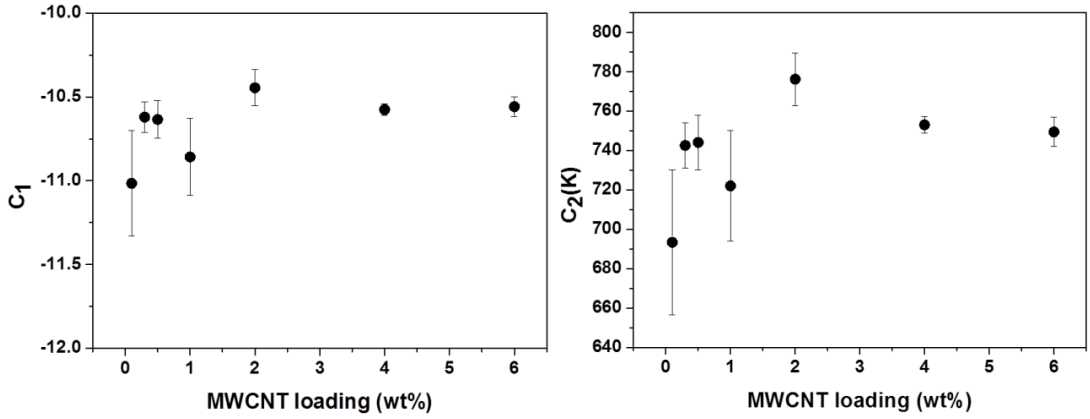

Figure 4.5. Fitting results for C_1 and C_2 for all MWCNT concentrations, except 0.7 wt%. We include results from samples with 0.1 and 1 wt % MWCNT although the temperature range studied is narrower and, consequently, the error bars are larger. At 0.7 wt%, the temperature range is too narrow (only ~ 20°C) to have reliable fitting results. As can be seen in the figure, C_1 is approximately constant across the whole concentration, and C_2 shows a slight maximum at 2wt%.

Previously, we developed a trap model[22] to describe the diffusion minimum $(D/D_0)_{min}$ that occurs in our MWCNT/PS and SWCNT/PS nanocomposites systems. It is a phenomenological model that simulates the center-of-mass diffusion of polymer chains through a three-dimensional lattice filled with cylindrical fillers. The model permits anisotropic polymer diffusion near the cylinders (D_{per} and D_{par}), but does not consider the effect of temperature. There are three parameters in the simplest variation of the trap model: p_0 describes the diffusion both inside and outside the traps, p_1 is the probability for polymer chains to diffuse into or out of the cylindrical traps, and r is the radius of the cylindrical traps. The significant slowing down of the center-of-mass diffusion at low trap concentration requires a lower jump probability for entering or escaping the cylindrical trap around the cylindrical filler ($p_1 < p_0$), and the recovery rate at higher particle concentration is due to the percolation of the traps. In our previous comparison of experimental and simulation results, an increase in r correlates to an increase in M_w of the matrix polymer chains. From Figure 4.3(b), we find that the diffusion minimum occurs at 2wt% at all temperatures, and this implies that the trap radius is independent of temperature. We also observe here that the decrease of the diffusion coefficients is smaller at higher temperature, and this correlates to a higher jump probability for polymer

chains to enter or escape the trap (higher p_1). Alternatively, ($p_0 - p_1$) appears to decrease at higher temperature, which corresponds to less anisotropy between the center-of-mass diffusion parallel and perpendicular to the cylindrical trap, MWCNT in our experiments.

Karatrantos *et al.* observed anisotropic diffusion coefficients near a SWCNT in their simulation studies,[25] although only when there is an attractive interaction between the SWCNT and polymer chain. In their simulations, they also found that self-diffusivity decreases with the addition of SWCNT. To date only one SWCNT concentration (0.4 v%) has been simulated, which is below 2wt%, where we observe $(D/D_0)_{min}$ in MWCNT/PS nanocomposites. To evaluate the polymer-MWCNT interactions in our nanocomposites, we fit the tracer diffusion coefficients to a modified WLF equation with an Arrhenius term[53]

$$\log\frac{D}{T} = C_1' - C_2\frac{1}{(T - T_\infty)} - \frac{E_a}{RT} \tag{4.6}$$

where E_a is the activation energy. The parameters C_2 and T_∞ are fixed to 710 K^{-1} and 322 K, corresponding to the PS melt.[51] This approach embodies the assumption that changes in the tracer diffusion coefficients are dictated by the polymer-MWCNT interactions. For this assumption to be valid, the activation energy should increase with polymer-MWCNT interfacial area, namely increase with MWCNT concentration. Fitting Equation 4.6 to our

data provides activation energies of 3.6 kJ/mol, 6.8 kJ/mol, and 3.9 kJ/mol, for nanocomposites with 0.5, 2, and 6 wt% MWCNT, respectively. The normalized interaction energy for the 0.5 wt% MWCNT composite is E_a/R = 433 K, which suggests that the activation energy is reasonable and comparable to temperatures used in our diffusion studies (425 K to 487 K). However, the activation energies do not increase monotonically with nanotube concentration and, thereby, invalidates the assumption of Equation 4.6 that the polymer-MWCNT interfacial interactions alone impede polymer diffusion. While polymer-MWCNT interactions might make important contributions to polymer dynamics, attractive interactions are inconsistent with the $(D/D_0)_{\min}$ found as a function of increasing MWCNT concentration for all temperatures studied. Moreover, our T_g measurements found no substantial influence upon adding MWCNTs, which further suggests the negligible effect of energetic interactions between these polymer chains and MWCNTs in this temperature range. Thus, the trap model suggests that the deeper minimum observed in D/D_0 at lower temperatures corresponds to greater anisotropy in the local diffusion coefficients parallel and perpendicular to the MWCNTs ($D_{\text{par}} > D_{\text{per}}$), and molecular dynamics simulations suggest that the origin of this anisotropy is not polymer-MWCNT interactions.

A salient finding of this paper is the good fit of the WLF equation (Equation 4.2, Figure 4.4) for the tracer diffusion coefficient in MWCNT/PS nanocomposites. This result suggests that the observed temperature dependence of the tracer diffusion arises primarily from the temperature dependence of the monomeric friction coefficient and the fractional free volume in the system. The increase of C_2 at 2 wt% MWCNT implies that near the rheological percolation threshold there is a minimum in α_f, the thermal expansion coefficient of free volume. This implies that the addition of small quantities of MWCNT (< 2 wt%) to polystyrene significantly decreases the thermal expansivity of the free volume in the nanocomposite relative to the neat homopolymer and at higher concentrations the thermal expansivity gradually returns to that of the neat homopolymer. Interestingly, tracer polymer diffusion is apparently dominated by the temperature-dependent changes in the fractional free volume of the polymer matrix. In contrast, linear viscoelastic measurements detect a combination of these changes in the fractional free volume in polystyrene (reduce *G'*) and the presence of high aspect ratio, semi-flexible rods (increase *G''*). It is well documented that the addition of carbon nanotubes, or a host of other high aspect ratio nanoscale fillers, may produce a transition from liquid-like to solid-like behavior attributed to the steadily increasing effect of the

nanoparticles and their eventual formation of a reinforcing network. Future studies of polymer dynamics in nanocomposites should seek to address the free volume in the system and its thermal expansivity as a function of nanoparticle concentration and evaluate local heterogeneities in the free volume that might account for anisotropy in polymer diffusion near high aspect ratio nanoparticles.

4.4 SUMMARY

In this chapter, we investigated the temperature-dependence of the tracer diffusion coefficient of dPS in MWCNT/PS nanocomposites. Firstly, as a function of MWCNT, D exhibits a minimum at 2wt% MWCNT, independent of temperature. Secondly, the minimum in D/D_0 becomes shallower at higher temperatures, which suggests that the mechanism causing the diffusion to slow down at low MWCNT concentrations is less effective at higher temperatures. Thirdly, at fixed nanotube concentrations, the WLF equation describes the temperature-dependence of the tracer diffusion coefficients in MWCNT/PS nanocomposites. When the WLF equation was modified to include MWCNT-polymer interactions, the results for the activation energy were not reasonable. Thus, we conclude that polymer diffusion in these polymer nanocomposites is associated with the fractional free volume in the polymer matrix and the observed minimum in D/D_0

is associated with a minimum in the thermal expansion coefficient of free volume.

4.5 REFERENCES

1. White, S. I.; Vora, P. M.; Kikkawa, J. M.; Winey, K. I., *Adv. Funct. Mater.* **2011,** *21* (2), 233-240.

2. Zhang, A. B.; Luan, J. F.; Zheng, Y. P.; Sun, L.; Tang, M., *Appl. Surf. Sci.* **2012,** *258* (22), 8492-8497.

3. Kashiwagi, T.; Du, F. M.; Douglas, J. F.; Winey, K. I.; Harris, R. H.; Shields, J. R., *Nat. Mater.* **2005,** *4* (12), 928-933.

4. Madathingal, R. R.; Wunder, S. L., *Thermochim. Acta* **2011,** *526* (1-2), 83-89.

5. Wang, Y. T.; Wang, C. S.; Yin, H. Y.; Wang, L. L.; Xie, H. F.; Cheng, R. S., *Express Polym. Lett.* **2012,** *6* (9), 719-728.

6. Coleman, J. N.; Khan, U.; Gun'ko, Y. K., *Adv. Mater.* **2006,** *18* (6), 689-706.

7. Oh, H.; Green, P. F., *Nat. Mater.* **2009,** *8* (2), 139-143.

8. Thostenson, E. T.; Ren, Z. F.; Chou, T. W., *Compos. Sci. Technol.* **2001,** *61* (13), 1899-1912.

9. Kiamahalleh, M. V.; Zein, S. H. S.; Najafpour, G.; Abd Sata, S.; Buniran, S., *Nano* **2012,** *7* (2).

10. Pandey, G.; Thostenson, E. T., *Polym. Rev.* **2012,** *52* (3-4), 355-416.

11. Winey, K. I.; Vaia, R. A., *MRS Bull.* **2007,** *32* (4), 314-319.

12. Balazs, A. C.; Emrick, T.; Russell, T. P., *Science* **2006,** *314* (5802), 1107-1110.

13. Crosby, A. J.; Lee, J. Y., *Polym. Rev.* **2007,** *47* (2), 217-229.

14. Jeon, I. Y.; Baek, J. B., *Materials* **2010,** *3* (6), 3654-3674.

15. Papon, A.; Saalwachter, K.; Schaler, K.; Guy, L.; Lequeux, F.; Montes, H., *Macromolecules* **2011,** *44* (4), 913-922.

16. Kropka, J. M.; Sakai, V. G.; Green, P. F., *Nano Lett.* **2008,** *8* (4), 1061-1065.

17. Akcora, P.; Kumar, S. K.; Sakai, V. G.; Li, Y.; Benicewicz, B. C.; Schadler, L. S., *Macromolecules* **2010,** *43* (19), 8275-8281.

18. Potschke, P.; Fornes, T. D.; Paul, D. R., *Polymer* **2002,** *43* (11), 3247-3255.

19. Manias, E.; Chen, H.; Krishnamoorti, R.; Genzer, J.; Kramer, E. J.; Giannelis, E. P., *Macromolecules* **2000,** *33* (21), 7955-7966.

20. Gam, S.; Meth, J. S.; Zane, S. G.; Chi, C. Z.; Wood, B. A.; Seitz, M. E.; Winey, K. I.; Clarke, N.; Composto, R. J., *Macromolecules* **2011,** *44* (9), 3494-3501.

21. Gam, S.; Meth, J. S.; Zane, S. G.; Chi, C. Z.; Wood, B. A.; Winey, K. I.; Clarke, N.; Composto, R. J., *Soft Matter* **2012,** *8* (24), 6512-6520.

22. Mu, M. F.; Clarke, N.; Composto, R. J.; Winey, K. I., *Macromolecules* **2009,** *42* (18), 7091-7097.

23. Mu, M. F.; Composto, R. J.; Clarke, N.; Winey, K. I., *Macromolecules* **2009,** *42* (21), 8365-8369.

24. Karatrantos, A.; Composto, R. J.; Winey, K. I.; Clarke, N., *Macromolecules* **2011,** *44* (24), 9830-9838.

25. Karatrantos, A.; Composto, R. J.; Winey, K. I.; Kroger, M.; Clarke, N., *Macromolecules* **2012,** *45* (17), 7274-7281.

26. Karatrantos, A.; Composto, R. J.; Winey, K. I.; Clarke, N., *in preparation*.

27. Rouse, P. E., *J. Chem. Phys.* **1953,** *21* (7), 1272-1280.

28. Degennes, P. G., *J. Chem. Phys.* **1971,** *55* (2), 572-579.

29. Rubinstein, M.; Colby, R. H., *Polymer Physics*. Oxford University Press: New York, 2003.

30. Green, P. F.; Kramer, E. J., *Journal of Materials Research* **1986,** *1* (1), 202-204.

31. Antonietti, M.; Coutandin, J.; Sillescu, H., *Makromolekulare Chemie-Rapid Communications* **1984,** *5* (9), 525-528.

32. Zhou, W.; Ooi, Y. H.; Russo, R.; Papanek, P.; Luzzi, D. E.; Fischer, J. E.; Bronikowski,

M. J.; Willis, P. A.; Smalley, R. E., *Chem. Phys. Lett.* **2001,** *350* (1-2), 6-14.

33. Du, F. M.; Fischer, J. E.; Winey, K. I., *J. Polym. Sci. Pt. B-Polym. Phys.* **2003,** *41* (24), 3333-3338.

34. Composto, R. J.; Walters, R. M.; Genzer, J., *Mater. Sci. Eng. R-Rep.* **2002,** *38* (3-4), 107-180.

35. Potschke, P.; Abdel-Goad, M.; Alig, I.; Dudkin, S.; Lellinger, D., *Polymer* **2004,** *45* (26), 8863-8870.

36. Doi, M.; Edwards, S. F., *Journal of the Chemical Society-Faraday Transactions Ii* **1978,** *74*, 1789-1801.

37. Graessley, W. W., *Faraday Symposia of the Chemical Society* **1983,** (18), 7-27.

38. Green, P. F.; Mills, P. J.; Kramer, E. J., *Polymer* **1986,** *27* (7), 1063-1066.

39. Antonietti, M.; Coutandin, J.; Sillescu, H., *Macromolecules* **1986,** *19* (3), 793-798.

40. Klein, J.; Briscoe, B. J., *Proc. R. Soc. London Ser. A-Math. Phys. Eng. Sci.* **1979,** *365* (1720), 53-73.

41. Fleischer, G., *Colloid Polym. Sci.* **1987,** *265* (2), 89-95.

42. Fetters, L. J.; Lohse, D. J.; Richter, D.; Witten, T. A.; Zirkel, A., *Macromolecules* **1994,** *27* (17), 4639-4647.

43. Green, P. F.; Kramer, E. J., *Macromolecules* **1986,** *19* (4), 1108-1114.

44. Pearson, D. S.; Fetters, L. J.; Graessley, W. W.; Strate, G. V.; Vonmeerwall, E., *Macromolecules* **1994,** *27* (3), 711-719.

45. Pearson, D. S.; Strate, G. V.; Vonmeerwall, E.; Schilling, F. C., *Macromolecules* **1987,** *20* (5), 1133-1141.

46. Crist, B.; Green, P. F.; Jones, R. A. L.; Kramer, E. J., *Macromolecules* **1989,** *22* (6), 2857-2858.

47. Bachus, R.; Kimmich, R., *Polymer* **1983,** *24* (8), 964-970.

48. Bartels, C. R.; Crist, B.; Graessley, W. W., *Macromolecules* **1984,** *17* (12), 2702-2708.

49. Lodge, T. P.; Rotstein, N. A.; Prager, S., *Adv. Chem. Phys.* **1990,** *79,* 1-132.

50. Fleischer, G., *Polym. Bull.* **1984,** *11* (1), 75-80.

51. Graessley, W. W.; Roovers, J., *Macromolecules* **1979,** *12* (5), 959-965.

52. Rittigstein, P.; Torkelson, J. M., *J. Polym. Sci. Pt. B-Polym. Phys.* **2006,** *44* (20), 2935-2943.

53. Ferry, J. D., *Viscoelastic Properties of Polymers*. 3rd ed.; Wiley: New York, 1980.

54. After the coagulation process, the nanocomposites are in the form of small pieces. First, we press the small bits into a circular disk using a metal window mold to eliminate

voids and consolidate the composite into a monolithic piece. Second, we press between glass pieces without a mold to make the circular disk somewhat thinner and provide a smooth surface. This two-step pressing method was previously reported and found to produce little MWCNT alignment.

Chapter 5

Temperature Dependence of Polymer Dynamics in Silica/Polystyrene Nanocomposites: Comparison between Diffusion Study and Rheology Study

The contents of this chapter are in preparation to submit to *Macromolecules*, in a modified version.

5.1. INTRODUCTION

The effect of NPs on polymer dynamics can by studied by measuring the tracer diffusion coefficients[1-5] or the linear viscoelasticity.[6-10] In this chapter, these two techniques will be used to study the temperature dependence of polymer dynamics in phenyl-capped silica/PS nanocomposites and the results of them will be compared to each other. Polymer diffusion is one of the key properties to understand the effect of nanofillers on polymer dynamics, and it has been studied in different nanoparticle/polymer systems.[1-3, 5, 11-12] In phenyl-capped silica/polystyrene (PS) nanocomposites (neutral interaction between silica NPs and PS), the author found the tracer diffusion coefficients monotonically decrease when the silica loading increases. The author proposed a

confinement parameter calculated by inter-particle distance divided by two times polymer radius of gyration (ID/2R_g) to explain the decrease in polymer diffusion and found that normalized polymer diffusion coefficients (D/D_0) at a constant T versus ID/2R_g fall on a mater curve.[3] Lin *et al*. found that the normalized polymer diffusion coefficients falls on the same master curve at a fixed $T - T_g$ in hydroxyl-capped silica/poly methyl methacrylate (PMMA) nanocomposites, where there is a favorable interaction between NPs and polymers.[12] Furthermore, polymer diffusion in nanocomposites with silica nanoparticles grafted with polymer chains shows that the penetrable depth into the polymer brushes by the tracer polymers, which is determined by the molecular weight ratio between brushes and tracers, needs to be considered when calculating ID.[11] Hu *et al*. used dynamic secondary ion mass spectrometry to measure the effect of functionalized organosilicate clay on polymer diffusion and found that the diffusion is not affected when adding clay into PS, but slows down when adding clay into PMMA.[5]

For nanoparticles with high aspect ratios, Mu *et al*. reported a diffusion minimum for tracer polymer diffusion in carbon nanotubes (CNTs)/PS nanocomposites,[1] and the diffusion minimum is only observed when R_g of the tracer polymer is larger than the radius of CNTs.[2] Choi *et al*. further extended the study to nanorods/PS nanocomposites and

showed that the diffusion minimum only appears when the polymer chain size is larger than the diameter of the cylindrical nanofillers but smaller than the length of the cylindrical nanofillers.[4] Although it has been shown that nanofillers with different geometric shapes affect polymer diffusion in different ways, detailed mechanisms of how nanofillers affect polymer diffusion are still under investigation. Temperature dependence of polymer diffusion in nanocomposites systems may help us further understand the mechanisms.

Reptation model[13-15] has been proved to describe the polymer diffusion in bulk polymer systems successfully when the polymer molecular weight (M_w) is higher than the critical molecular weight (M_c: about two times entanglement molecular weight).[16] In reptation model, polymer diffusion coefficient can be expressed as[15]

$$D_{rep} \approx \frac{R^2}{\tau_{rep}} \approx \frac{R^2}{N^3}\frac{k_B T}{\xi b^2} N_e \tag{5.1}$$

where R represents the chain end-to-end distance, N represents the number of Kuhn monomers per chain, b is the size of a Kuhn monomer, T is temperature, ξ is the monomer friction coefficient, and N_e represents the number of Kuhn monomer in one entanglement strand. It is clearly shown that the diffusion coefficient is determined by the polymer chain size (R), ξ, and N_e. According to the reptation model, the temperature dependence of polymer diffusion is affected by the temperature dependence of the polymer chain size (R),

N_e, and ξ. In homopolymers, it has been shown that the temperature dependence of polymer chain size is very small (at most 10% across 100°C).[17-18] It has also been shown that the temperature dependence of N_e is about 40% across 70°C.[19] The temperature dependence of R and N_e is relatively weak compared to the temperature dependence of the monomer friction coefficient which can change by three orders of magnitude across 70°C.[20-22] Therefore, the temperature dependence of polymer diffusion is dominated by the temperature dependence of ξ as $D(T)/T \sim 1/\xi(T)$.

Rheology tests can also be used to investigate polymer dynamics. A sinusoidal strain is applied on a silica/PS nanocomposites, and elastic modulus (G') and loss modulus (G'') can be obtained by measuring the response of the nanocomposites. G' and G'' measured at different temperatures can be superposed using time-temperature superposition by[15]

$$G^*(\omega, T) = b_T G^*(a_T \omega, T) \tag{5.2}$$

where a_T and b_T are the shift factors for frequency and monomer density, respectively. The change in b_T is usually very small (~20% across 80°C) compared to a_T (10^4 across 80°C). The reptation model also predicts the viscosity of polymers as[15]

$$\eta \approx \frac{\xi b^2}{v_0} \frac{N^3}{{N_e}^2} \tag{5.3}$$

where v_0 is the Kuhn monomer volume. Considering that the temperature dependence of v_0 (temperature dependence of the density change) and N_e are relatively weak compared to the temperature dependence of ξ, we can see that the temperature dependence of the viscosity also mainly depends on the temperature dependence of ξ as $\eta(T) \sim \xi(T)$. In homopolymer systems, the temperature dependence of both polymer diffusion and viscosity is coming from the temperature dependence of the monomer friction coefficients, which can be captured by the Williams-Landel-Ferry (WLF) equation[15] in the temperature range $T_g < T < T_g + 100K$ as

$$log\frac{D(T)}{D_0(T_0)} = log\frac{\xi T_0}{\xi_0 T} = log\frac{\eta_0}{\eta} = loga_T = \frac{B}{f_0}\frac{(T_0 - T)}{(T - T_\infty)} \quad (5.4)$$

where D_0 and η_0 are the diffusion coefficient and viscosity at the reference temperature (T_0), B is an empirical constant, f_0 is the amount of free volume at the reference temperature, and T_∞ is the Vogel temperature where the free volume is zero.[15] $f_0 = \alpha_f \times (T_0 - T_\infty)$, where α_f is the free volume expansion coefficient.

It has been shown that the WLF equation can be applied to the temperature dependence of polymer diffusion in homopolymer[23] and multi-wall carbon nanotubes (MWCNT)/PS nanocomposites at low MWCNT loadings (highest MWCNT loading is ~5v%), studied in Chapter 4.[24] However, at this high loading (up to 50v%), the

applicability of the WLF equation has not been evaluated. On the other hand, the temperature dependence of viscosity in homopolymer has also been proved to follow the WLF equation.[20] In this paper, the applicability of the WLF equation at this high nanoparticle loading will be evaluated, and temperature dependence data of the diffusion coefficients and the rheology data will be compared with each other.

Results have been published on how the chain size (R), monomer friction coefficient ξ, and N_e are affected by adding spherical nanoparticles into polymer matrices.[6-7, 25-27] It was shown that the effect of nanofillers on polymer chain size is determined by the interaction between nanofillers and polymers, dispersion of nanoparticles, and the size ratio between polymer chains and nanofillers.[25-26, 28-31] For the silica/PS nanocomposites studied in this work, silica NPs are phenyl-capped, which indicates there is no preferential interaction between NPs and polymers. The dispersion of NPs were systematically characterized by Meth *et al.* using SAXS and proved to be uniformly distributed.[32] The nanocomposites studied in this paper are provided by Dupont, and identical to the materials studied by Gam *et al.* and Meth *et al*.[3, 32] The key factor then becomes the size ratio of the polymer chains and the silica NPs. 532kg/mol deuterated polystyrene (dPS) is used as the tracer polymer in this study and the size ratio of polymer

chains (R_g ~ 20nm) and silica NPs (radius ~ 14nm) is about 1.4. The change of R_g is studied in two other works with spherical NPs/polymer nanocomposites. Nusser *et al.* reported that in short hydrocarbon chains-grafted silica/poly(ethylene-propylene) nanocomposites, R_g slightly decreases when the silica concentration increases (~10% decrease for 50*v*% silica loading) when $R_g/r \sim 1.3$.[26] Crawford *et al.* also studied the phenyl-capped silica/PS systems and found that R_g does not change for $R_g/r \sim 0.8 - 4$.[25] A recent simulation work showed that the increase of R_g is only observed when the polymer chain size is larger than nanoparticle size and nanoparticles have good dispersions.[33] The chain expansion is more pronounced for small nanoparticles (comparable to the Kuhn length). Considering that $R_g/r \sim 1.4$ and the nanoparticle is relatively large, it is reasonable to assume that the polymer chain size is barely affected by silica NPs in our systems.

Schneider *et al*. used neutron spin echo (NSE) to probe the tube diameter for polymer chains and discovered that the tube diameter (d_{tube}) increases when the silica loading increases. However, this study defined a geometric confinement due to the NPs (d_{geo}) that decreases as the nanoparticle loading increases. Overall, the apparent tube diameter d_{app} decreases as the silica loading increases above ~ 20*v*% silica loading.[7] Nusser *et al*. further proved that the tube radius measured from NSE and rheology are in

agreement.[27] In this study, we used rheology to estimate the tube diameter for our nanocomposites, which can be further used to calculate the change of N_e. With the unaffected chain size, diffusion coefficients and viscosity of polymers are both depend on the monomer friction coefficients and N_e (Equation 5.1 & 5.3). Although, polymer diffusion and linear viscoelasticity have been studied for polymer nanocomposites, no comparison has been made between these two approaches to study dynamics in PNCs. The tracer diffusion coefficients (D) measured by elastic recoil detection will be compared to the viscosity (η) and N_e extracted from the rheology data for silica/PS nanocomposites.

5.2. EXPERIMENTAL METHODS

5.2.1. Materials and Nanocomposites Fabrication

As previously described,[32] phenyl-capped silica nanoparticles (NPs) were dispersed in dimethylacetamide and mixed with polystyrene (PS) dimethylformamide solutions. The NP-PS-solvent mixtures were doctor bladed on a heated glass substrate to facilitate rapid evaporation of the solvents. The thickness of the resulting polymer nanocomposite (PNC) film is about 10 μm. The phenyl-capped silica nanoparticles have a median diameter of 28.7 ± 0.3 nm.[32] The silica NPs were grafted and the nanocomposites were fabricated at Dupont. Additional characterizations for the silica NPs and the

dispersion of silica NPs in PS matrices were previously published.[3, 32]

For tracer diffusion experiments, the weight average molecular weights of the PS matrix and the deuterated polystyrene (dPS) tracer are 650 kg/mol (PDI = 1.1) and 532 kg/mol (PDI = 1.05), respectively. For rheology experiments, the weight average molecular weight of the PS matrix is 265 kg/mol (PDI = 2.6). Nanocomposites will be defined by their volume fraction of silica nanoparticles, which were calculated using silica and polystyrene densities of 2.113 g/cm^3 and 1.1 g/cm^3, respectively, and ranged from 0 to 50 v%.

5.2.2. Elastic Recoil Detection to Measure Tracer Diffusion

Elastic recoil detection (ERD) was used to obtain the depth profile of 532kg/mol dPS diffusing into the phenyl-capped silica/PS nanocomposites. As-received PNC films were place on silicon substrates and annealed (150°C, 3days, vacuum) to adhere the film to the substrate and to relax the films. Thin dPS films (~20nm) were made by spin-coating a dilute dPS solution on a silicon substrate, and the thickness was measured by ellipsometry. The dPS film was then floated on de-ionized water and transported onto the PNC film. The bilayer samples were annealed in a customized vacuum oven with precise temperature

control (fluctuation < 1°C) to activate tracer diffusion, Figure 5.1(a). Seven temperatures from 143°C to 197°C were used and the annealing time ranges from 30 minutes to 14 days to obtain diffusion lengths of ~ 400nm.

For ERD, He^{2+} ions are accelerated to 3MeV and then impinge on annealed bilayer samples. Because hydrogen and deuterium atoms are lighter than He, they will be expelled out from the samples and then detected by a detector. Taking into account the energy lost of He^{2+} inside the nanocomposites before it impinges on deuterium, energy transfer between He^{2+} and deuterium during the collision, the energy lost of deuterium inside the nanocomposites before it left the nanocomposites, and the energy lost for deuterium passing through a ~10μm Mylar film before detected by the detector, we are able to back calculate the depth of the deuterium inside of the nanocomposites from the detected energy of deuterium. More detail of ERD can be found in a review article by Composto *et al.*[34]

Depth profiles of dPS in the PNC were fit to convolution of Fick's second law and a Gaussian function to extract the tracer diffusion coefficients. The solution to Fick's second law for a finite source diffusing into a semi-infinite matrix can be expressed as[35]

$$\Phi(x) = \frac{1}{2}\left[erf\left(\frac{h-x}{\sqrt{4Dt}}\right) + erf\left(\frac{h+x}{\sqrt{4Dt}}\right)\right] \quad (5.5)$$

where $\Phi(x)$ denotes the dPS volume fraction, h is the thickness of the dPS thin film (~20

nm), x is the depth of D from the sample surface, t is the diffusion time, and D is the diffusion coefficient of dPS. All parameters besides D are pre-determined, so D is the only fitting parameter to the depth profile. A Gaussian function used to describe the ERD resolution (~70nm) was determined by measuring the front edge of a thick dPS film. Figure 5.1(b) shows that for matrices of homopolymer and with low silica loadings, deuterium depth profiles for different diffusion times can be fitted with the same diffusion coefficients, which proves that D is independent of annealing time. For matrices with high silica loadings (> 20*v*%), because silica NPs are very crowded so that only limited amount of channels for the tracer polymer to diffuse into the matrix at the top surface, a surface peak is observed, Figure 5.1(c). An extra step function convoluted with the same Gaussian function is added into the fitting function to fit the depth profile. As shown in Figure 5.1(c), the surface peak is decreasing for longer annealing time, which means more tracer polymers are able to diffuse into the matrices. For the portion which already diffuses into the matrices, it can be fitted with the same diffusion coefficient. Both Figure 5.1(b) and 5.1(c), report time-independent diffusion coefficients that demonstrate the nanocomposites are not changing during the diffusion process. Notice that the tracer diffusion coefficients in homopolymer is used as an internal check for the oven temperature, and the slope of

$B/f_0 \sim 6$[23] and reference temperature as 174°C[16] from the literature is used to calibrate the annealing temperature.

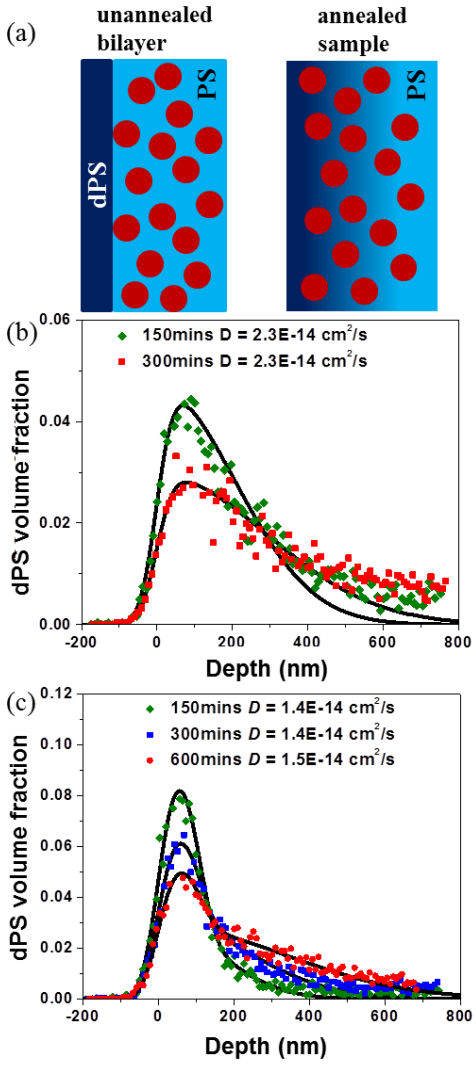

Figure 5.1. (a) Schematic of an unannealed bilayer sample and an annealed sample with dPS diffusing into the silica/PS nanocomposites. (b) & (c) show example depth files for 532k dPS diffusing into silica/PS nanocomposites at 180°C. (b) For 5*v*% silica loadings the dPS depth profiles with two annealing times (160 and 300 mins) are fit with the same diffusion coefficient. (c) For 20*v*% silica loadings a surface peak is observed, and the portion of dPS diffusing into matrices with three annealing times (160, 300, and 600 mins) can be fit with the same diffusion coefficient.

5.2.3. Rheology Test

Approximately fifty PNC films (10 μm each) were stacked and hot pressed into a window mold several times to make void-free 0.65 mm-thick samples for rheology measurements. The temperature for hot pressing increased with silica loading from 150°C to 170°C. The linear viscoelastic behavior was measured using a Rheometrics Solid Analyzer (RSAII) with a shear sandwich fixture using frequency sweeps (0.1rad/s ~ 100rad/s) at a fixed strain amplitude (0.5% strain) and five temperatures (130°C to 210°C) in a nitrogen environment. Standard operating procedures of RSAII can be found in Appendix E. All rheology data are provided later as master curves of the storage modulus (G') and loss modulus (G'') with 170°C as the reference temperature. Three parameters were extracted from the rheology data. Zero-shear viscosity was obtained by calculating $G''(\omega)/\omega$ in the low-frequency limit.[15]

$$\eta = \lim_{\omega \to 0} \frac{G''(\omega)}{\omega} \tag{5.6}$$

The reptation time (τ_{rep}) and the number of Kuhn monomers in one entanglement strand (N_e) were obtained from the intersection of G' and G''.[15, 27, 36] Reproducibility of the rheology data was checked to ensure that the nanocomposites did not have unrecoverable changes.

5.3. RESULTS AND DISCUSSION

5.3.1. Temperature Dependence of the Tracer Diffusion

Bilayer samples composed of 532kg/mol dPS (~20nm) on top of silica/PS nanocomposites (> 10 μm) were annealed at seven temperatures ranging from 143 °C to 197 °C. The depth profile of dPS were measured by ERD and fitted by the convolution of the Fick's second law and the Gaussian function (instrumental resolution) to obtain the diffusion coefficients for dPS in silica/PS NCs. The tracer diffusion coefficients as a function of silica loading (*v*%) are plotted in Figure 5.2(a). It can be seen that the diffusion coefficients increase by about 3 orders when the annealing temperature increases by ~60°C. As mentioned in Introduction, polymer chain size and N_e have relatively weak dependence on temperature in polymer bulk. Therefore, in homopolymers, the temperature dependence of tracer diffusion is mainly coming from the temperature dependence of monomer friction coefficients.

Normalized diffusion coefficients (D/D_{bulk}), the tracer diffusion coefficient in silica/PS divided by the tracer diffusion in homopolymer, as a function of silica loading at different temperatures are plotted in Figure 5.2(b). Interestingly, we found that the monotonic decrease of the tracer diffusion is more pronounced at higher temperatures. This

implies that the mechanism which causes the polymer diffusion to slow down in this crowded NPs environment is more effective at higher temperatures.

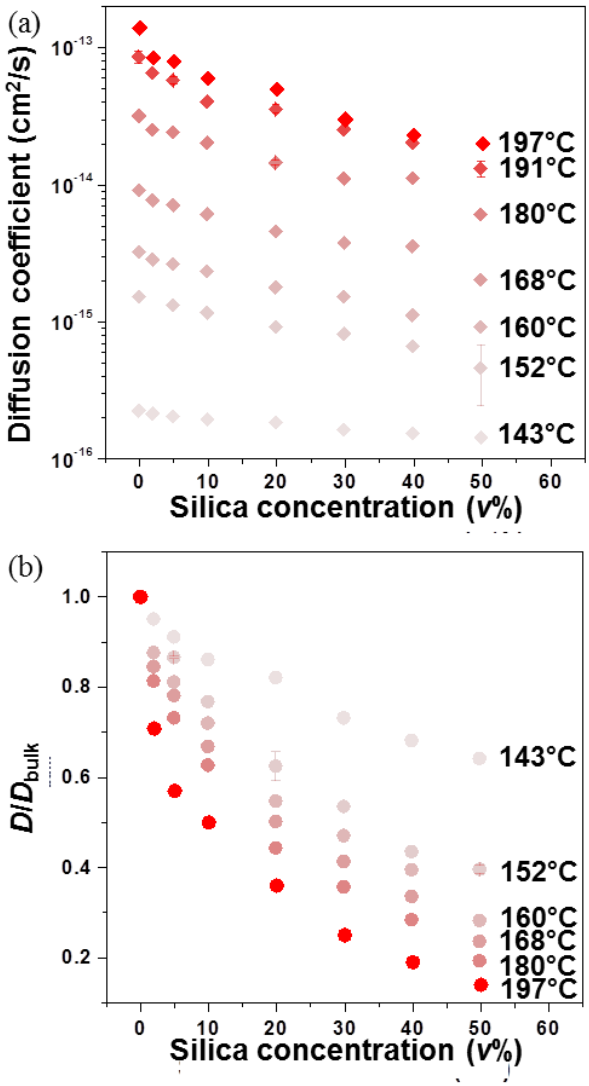

Figure 5.2. (a) Tracer diffusion coefficients of 532k dPS diffusing into phenyl-capped silica/PS nanocomposites as a function of silica loadings at different temperatures ranging from 143 °C to 197 °C. (b) Tracer diffusion coefficients normalized by the tracer diffusion coefficient for 532k dPS into bulk PS homopolymer.

The temperature dependence of the tracer diffusion coefficients are plotted as $\log(D_0/D)$ versus $(T_0\text{-}T)/(T\text{-}T_\infty)$ in Figure 5.3(a) using 168°C as the reference temperature. D_0 is the tracer diffusion coefficient at the reference temperature. The WLF fitting is performed (Equation 5.4) and predicts straight lines with different slopes for tracer diffusion in homopolymers and nanocomposties with different silica loadings. This indicates that the scaling of monomer friction coefficients as a function of temperature is affected by adding silica NPs. The successful fitting with the WLF equation implies that the fundamental assumption of the WLF equation, which assumes that the monomer friction coefficient depends on the amount of free volume around a monomer, still applies in silica/PS nanocomposites. Figure 5.3(b) shows the slope (B/f_0) for polymer nanocomposites normalized by that for homopolymers as a function of silica concentration. B/f_0 gradually decreases when the silica loading increases. Considering $f_0 = \alpha_f \times (T_0 - T_\infty)$, where α_f is the expansion coefficient of free volume, adding silica NPs increases α_f by up to ~20% at the highest loading. This phenomenon also suggests that adding nanoparticles may affect the polymer chain packing.

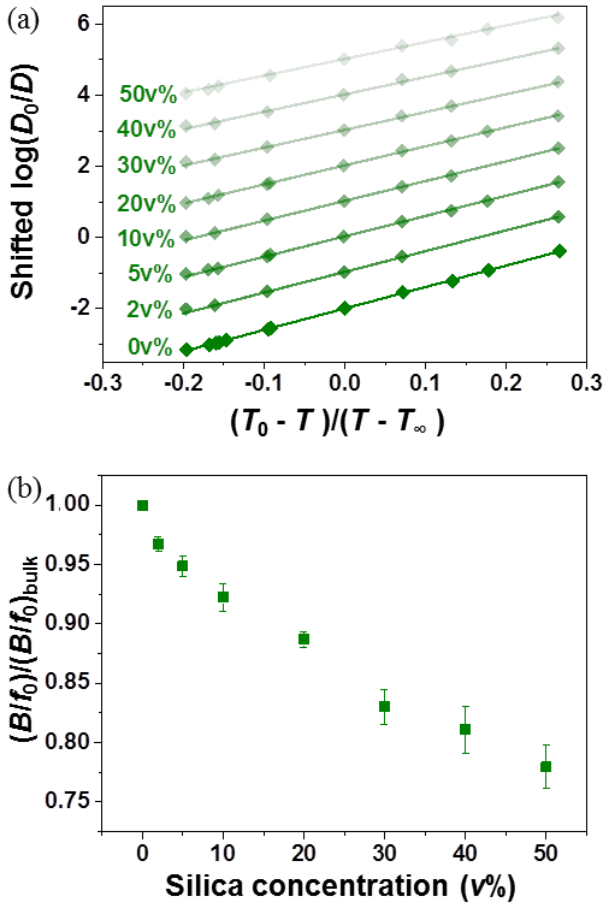

Figure 2.3. (a) Tracer diffusion coefficients for 532k dPS diffusing into silica/PS nanocomposites (0-50 v% silica) fit to the WLF equation (Equation 5.4) using a reference temperature is 168°C. D_0 is the tracer diffusion coefficient at the reference temperature. (b) Fitting parameter (B/f_0) from the WLF equation for nanocomposites are normalized by B/f_0 for homopolymer diffusion and plotted as a function of the silica concentration.

5.3.2. Linear Viscoelasticity in Silica/PS Nanocomposites

Rheology tests were conducted on silica/PS nanocomposites at temperatures from 130°C to 210°C. G' and G'' data are shifted using time-temperature superposition to

construct master curves with the reference temperature at 170 °C. Figure 5.4 shows example master curves for 265k PS and silica/PS nanocomposites with 10 *v*% and 20 *v*% loadings. Between 10 *v*% and 20 *v*%, the nanocomposites goes through a transition from liquid-like behavior to solid-like behavior because *G'* and *G"* no longer cross for 20 *v*%. The percolation volume fraction for silica NPs is around 15 *v*% according to previous studies on these nanocomposites.[32] Rheology data for other samples (2 *v*%, 5 *v*%, 30 *v*%, and 40 *v*%) are shown in Figure 5.5.

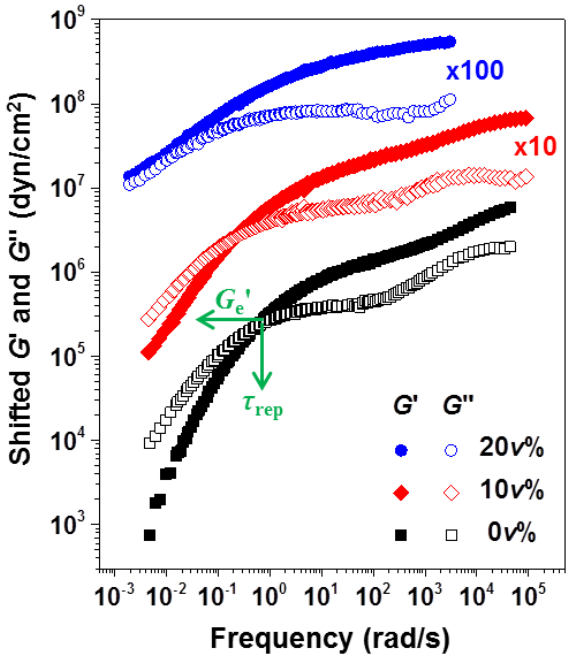

Figure 5.4. Master curves constructed by time-temperature-superposition for 265k PS and silica/PS nanocomposites with 10v% and 20v% silica loading. G' and G" are shifted vertically for clarity.

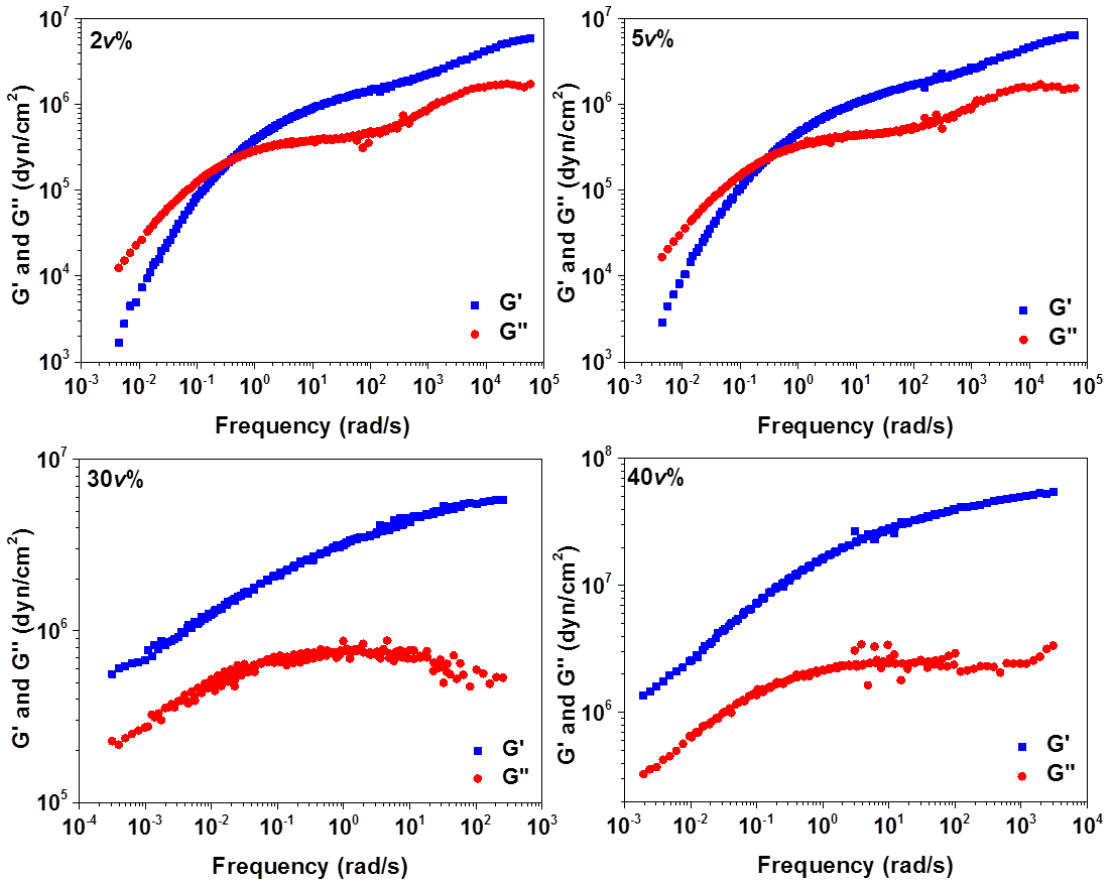

Figure 0.5. Master curves of G' and G'' data using time-temperature superposition with the reference temperature at 170°C for 2 *v*%, 5 *v*%, 30 *v*%, and 40 *v*% samples.

From the rheology data, the disentanglement time (τ_{rep}) and the plateau modulus (G_e') can be extracted from the intersection of G' and G'' as shown in Figure 5.4. The zero shear viscosity can be obtained according to Equation 5.6. Plateau modulus is inversely proportional to N_e.[15] Figure 5.6 plots the disentanglement time, plateau modulus, and zero shear viscosity for silica/PS nanocomposites normalized to the corresponding values for 265k bulk PS. Disentanglement time and viscosity increase and N_e slightly decreases as the

silica loading increases. This shows that adding silica nanoparticles affect the monomer friction coefficients and entanglement networks. Notice that beyond 10*v*%, *G'* and *G''* no longer cross and therefore we are not able to obtain τ_{rep} and G_e'. However, this solid-like phenomenon does not indicate that polymers are more entangled. Rheology tests apply an external force across the whole sample and measure the response of both polymers and nanoparticles. Nanoparticles need to restore its original distribution upon removing stress. At high silica loadings, nanoparticles start jamming and the mechanical response is dominated by these nanoparticle clusters. The measured values of rheology tests cannot be used to extract the properties of polymer matrices.

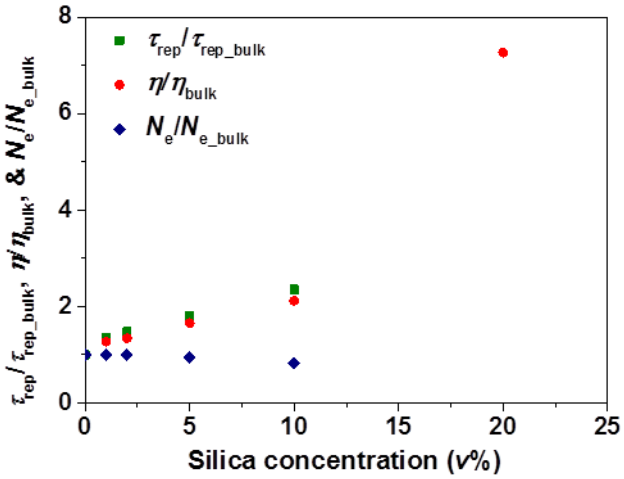

Figure 5.6. Disentanglement time (τ_{rep}), zero shear viscosity (η), and the number of monomers in one entanglement strand (N_e) extracted from the rheology data are normalized by the corresponding values for 265k PS and plotted as a function of the silica concentration. Beyond 10*v*%, there is no crossover for *G*' and *G*'' so that τ_{rep} and N_e cannot be obtained.

As mentioned previously, the master curves are constructed using time-temperature superpositions, and the corresponding shifting factors are a_T (frequency domain) and b_T (density change). According to Equation 5.4, the temperature dependence of viscosity can be calculated as $a_T \times b_T$ ($\sim a_T$ because b_T is around 1). Figure 5.7(a) plots $\log(\eta/\eta_0)$ as a function of $(T_0\text{-}T)/(T\text{-}T_\infty)$ for bulk PS and silica/PS nanocomposites and corresponding fits to the WLF equations. Figure 5.7(b) shows the slope (B/f_0) for polymer nanocomposites normalized by that for homopolymers as a function of silica concentration. B/f_0 gradually increases when the silica loading increases at low silica loadings (< 10*v*%), in contrast to B/f_0 from diffusion studies (Figure 5.3(b)). Between 10*v*% and 20*v*%, B/f_0 shows an abrupt jump and keeps increasing when silica loading increases. This is another phenomenon indicates the rheology measures nanoparticle relaxation and the temperature dependence of viscosity is affected by the nanoparticle jamming. The fact that the WLF equation still applies means that the relaxation of nanoparticles happens through the relaxation of polymers around nanoparticles which is still related to the amount of free volume in the matrices. However, α_f decreases when silica loading increases, which is in contrast to the diffusion study. One possibility is that the nanoparticle relaxation is more sensitive to the polymers around them, and this may imply a non-uniform distribution of α_f in the polymer

matrices induced by adding nanoparticles.

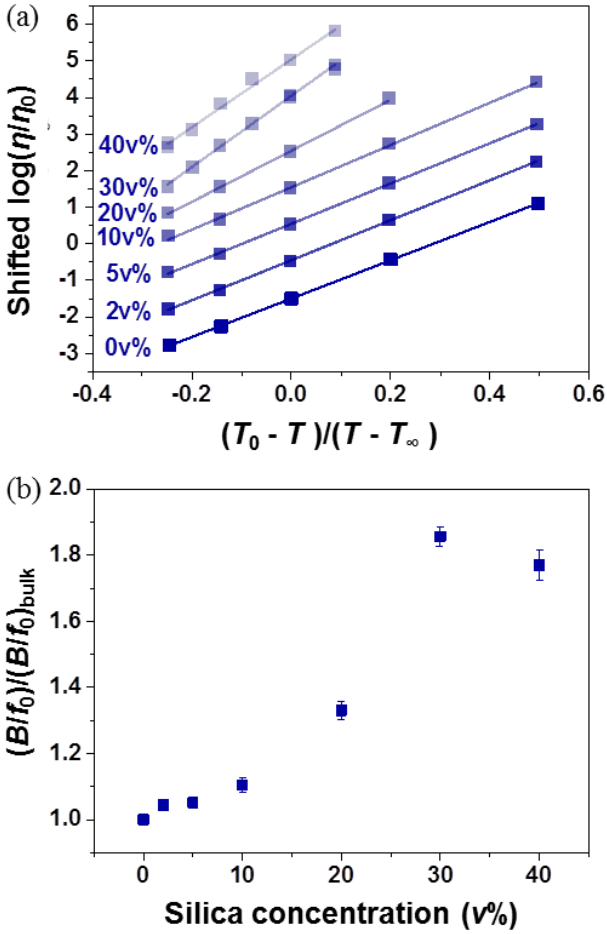

Figure 5.7. (a) Zero shear viscocity for silica/PS nanoccompoistes (0-40 v% silica) fit to the WLF equation (Equation 5.4) using a reference temperature of 170°C. η_0 is the zero shear viscosity at the reference temperature. (b) Fitting parameters (B/f_0) from the WLF equations for nanocomposites are normalized by B/f_0 from the homopolymer and plotted as a function of silica concentration.

5.3.3. Comparison between the Diffusion Study and the Rheology Study

Although the reptation model has successfully described polymer diffusion in

homopolymers,[13, 16, 37-38] The ability of reptation to capture the decrease of polymer diffusion in silica/PS nanocomposites has not been proved. According to the reptation model, the diffusion coefficient is affected by the polymer chain size (R), monomer friction coefficient (ξ), and N_e. Assuming that R is not affected by adding silica NPs (explained in Introduction), the change of diffusion coefficients is determined by the change of ξ and N_e- as $D \sim N_e/\xi$ (Equation 5.1). On the other hand, viscosity can also be described according to the reptation model where $\eta \sim \xi / N_e^2$ (Equation 5.3). This implies that D is proportional to $1/(\eta \times N_e)$. To compare the results of the diffusion study and the rheology study based on the reptation model, the tracer diffusion coefficients in silica/PS nanocomposites at 168°C are normalized to the corresponding value for homopolymer bulk and plotted together with $1/(\eta \times N_e)$, extracted from the master curves using 170°C as reference temperature, normalized to the corresponding value for PS in Figure 5.8. A discrepancy is observed where rheology study shows a more pronounced decrease in diffusion coefficients. According to the discussion Section 5.3.2, this may due to that the increase in the viscosity and N_e measured by rheology is higher because of the nanoparticle contribution.

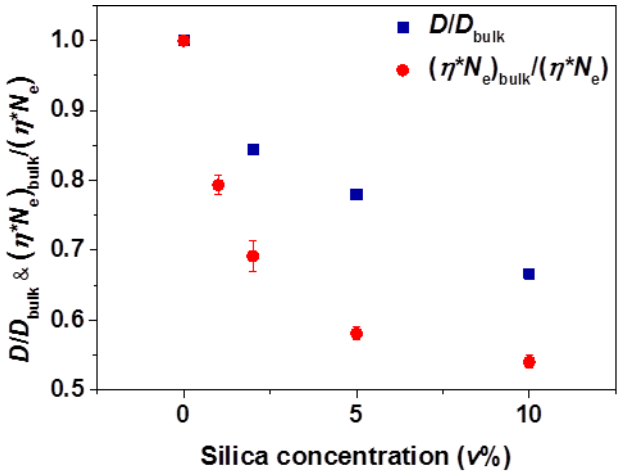

Figure 5.8. Tracer diffusion coefficients at 168°C are normalized to the corresponding value for homopolymer and plotted together with $1/(\eta \times N_e)$ normalized to $1/(\eta \times N_e)$ for bulk PS extracted from the master curves using 170°C as reference temperature.

5.3.4. Discussion on Polymer Diffusion in Silica/PS Nanocomposites

When the monotonic decrease of polymer diffusion is firstly reported in the literature.[3] The author used a confinement parameter ($ID/2R_g$) to captured the decrease, and it works quite well even in other systems with attractive interaction between spherical nanoparticles and matrix polymers[12] and nanoparticles with grafted polymer chains.[11] However, the detailed mechanisms of how these NPs affect the tracer diffusion are not clear. As shown in Section 5.3.1, the WLF equation still applies to the temperature dependence of the diffusion coefficients, which suggests that the temperature dependence of D is still determined by the temperature dependence of the monomer friction

coefficients as indicated by the reptation model. This further supports the applicability of the reptation model in silica/PS nanocomposites. However, to understand the effect of nanoparticles on the tracer diffusion, it requires an investigation for the effect of nanoparticles on the chain size (R), monomer friction coefficients (ζ), and N_e. Rheology tests is another independent measurement to obtain viscosity and N_e. However, it is shown that rheology test also captures the response of nanoparticles (restoring the original distributions or relaxation of inter-particle interaction), and a discrepancy is observed when comparing the change in the tracer diffusion coefficients to the diffusion change predicted by the change of viscosity and N_e extracted from the rheology data. Moreover, different trends for the change of the free volume expansion coefficients (α_f) as a function of the silica concentration were observed, which further suggests the fundamental differences between these two techniques.

An excluded volume model was proposed to capture the diffusion slow down at low loadings.[39] The model describes the polymer diffusion in silica/PS nanocomposites as spheres diffuse through an ensemble of cylinders formed by the packing of spherical NPs. The drag force experienced by a polymer chain diffusing through a cylindrical confinement is due to the lost of its conformational entropy,[40] and this drag force is analogy to a single

sphere suspended in a viscous liquid and moving through a cylinder. Although this model captures the diffusion slowing down at low loading quite well, it overestimates the decrease of polymer diffusion in the highly confined region when $ID_{2D}/2R_g < 5$.[39] To further resolve the mechanism of the diffusion decrease in silica/PS nanocomposites, it requires a more careful study on how nanoparticles affect R, ξ, and N_e which are the fundamental building blocks of the reptation model.

5.4. SUMMARY

In this chapter, we investigated the change of polymer dynamics in phenyl-capped silica/PS nanocomposites by the tracer diffusion and rheology. The tracer diffusion coefficients were measured at 7 temperatures ranging from 143°C to 197°C, and a monotonic decrease of the tracer diffusion coefficients as silica loading increases was observed at every temperature. When we normalized the tracer diffusion coefficients to the corresponding value for homopolymer, we observed that the monotonic decrease is more pronounced at higher temperatures, in contrast to MWCNT/PS reported in Chapter 4. The temperature dependence of the tracer diffusion coefficients were successfully fit to the WLF equation. From the change of the slope of the WLF fitting, we found that the free volume expansion coefficients, α_f, gradually increases as a function of the silica

concentration. This implies adding nanoparticles can change the polymer packing, which affects α_f.

Rheology tests, which is another independent measurement of polymer dynamics, was also used to measure the mechanical response of silica/PS nanocomposites at different temperatures ranging from 130°C to 210°C. Master curves were successfully constructed through the time-temperature superposition, and the viscosity and N_e were extracted from the master curves. From the shifting factors of the time-temperature superposition, we fit the temperature dependence of the viscosity to the WLF equation, and a successful fit was also obtained. However, a different trend of α_f was observed, where α_f slowly decreases as the silica loading increases and has an abrupt jump between 10*v*% and 20*v*% silica loading, which agrees to the percolation threshold at ~ 15 *v*%. This is also where an onset of a solid-like behavior was observed from the master curves. Therefore, we concluded that the rheology test for silica/PS nanocomposites also captures the relaxation of nanoparticles which may affect the exact value of the extracted viscosity and N_e and the temperature dependence of the viscosity. This was further proved when we tried to compare the change in the tracer diffusion coefficients to the change of viscosity and N_e at ~ 170°C using the reptation model. It was shown that the rheology test may overestimate the increase in the

viscosity and the decrease in N_e. Although some studies[39] have tried to explain this diffusion decrease in silica/PS nanocomposites, a thorough understanding of this phenomenon has not been achieved. More researches need to be done to study the effect of nanoparticles on the chain size, monomer friction coefficients, and the entanglement molecular weight to help us further understand the mechanisms of the slowing down of the polymer diffusion based on the reptation model. A simulation work to study the polymer chain packing in silica/PS nanocomposites will also be helpful to understand the temperature dependence of the polymer diffusion in silica/PS nanocomposites.

5.5. REFERENCES

1. Mu, M. F.; Clarke, N.; Composto, R. J.; Winey, K. I., *Macromolecules* **2009,** *42* (18), 7091-7097.

2. Mu, M. F.; Composto, R. J.; Clarke, N.; Winey, K. I., *Macromolecules* **2009,** *42* (21), 8365-8369.

3. Gam, S.; Meth, J. S.; Zane, S. G.; Chi, C. Z.; Wood, B. A.; Seitz, M. E.; Winey, K. I.; Clarke, N.; Composto, R. J., *Macromolecules* **2011,** *44* (9), 3494-3501.

4. Choi, J.; Clarke, N.; Winey, K. I.; Composto, R. J., *ACS Macro Lett.* **2014,** *3* (9), 886-891.

5. Hu, X. S.; Zhang, W. H.; Si, M. Y.; Gelfer, M.; Hsiao, B.; Rafailovich, M.; Sokolov, J.; Zaitsev, V.; Schwarz, S., *Macromolecules* **2003,** *36* (3), 823-829.

6. Nusser, K.; Schneider, G. J.; Pyckhout-Hintzen, W.; Richter, D., *Macromolecules* **2011,** *44* (19), 7820-7830.

7. Schneider, G. J.; Nusser, K.; Willner, L.; Falus, P.; Richter, D., *Macromolecules* **2011,** *44* (15), 5857-5860.

8. Zhao, J.; Morgan, A. B.; Harris, J. D., *Polymer* **2005,** *46* (20), 8641-8660.

9. Inoubi, R.; Dagreou, S.; Lapp, A.; Billon, L.; Peyrelasse, J., *Langmuir* **2006,** *22* (15), 6683-6689.

10. Akcora, P.; Kumar, S. K.; Sakai, V. G.; Li, Y.; Benicewicz, B. C.; Schadler, L. S., *Macromolecules* **2010,** *43* (19), 8275-8281.

11. Choi, J.; Hore, M. J. A.; Meth, J. S.; Clarke, N.; Winey, K. I.; Composto, R. J., *ACS Macro Lett.* **2013,** *2* (6), 485-490.

12. Lin, C. C.; Gam, S.; Meth, J. S.; Clarke, N.; Winey, K. I.; Composto, R. J., *Macromolecules* **2013,** *46* (11), 4502-4509.

13. Doi, M.; Edwards, S. F., *Journal of the Chemical Society-Faraday Transactions Ii* **1978,** *74*, 1789-1801.

14. Degennes, P. G., *J. Chem. Phys.* **1971,** *55* (2), 572-&.

15. Rubinstein, M.; Colby, R. H., *Polymer Physics*. Oxford University Press: New York, 2003.

16. Green, P. F.; Mills, P. J.; Kramer, E. J., *Polymer* **1986,** *27* (7), 1063-1066.

17. Wignall, G. D.; Ballard, D. G. H.; Schelten, J., *Eur. Polym. J.* **1974,** *10* (9), 861-865.

18. Boothroyd, A. T.; Rennie, A. R.; Boothroyd, C. B., *Europhys. Lett.* **1991,** *15* (7), 715-719.

19. Richter, D.; Farago, B.; Butera, R.; Fetters, L. J.; Huang, J. S.; Ewen, B., *Macromolecules* **1993,** *26* (4), 795-804.

20. Plazek, D. J., *J. Phys. Chem.* **1965,** *69* (10), 3480-3487.

21. Plazek, D. J.; Zheng, X. D.; Ngai, K. L., *Macromolecules* **1992,** *25* (19), 4920-4924.

22. Roland, C. M.; Paluch, M.; Casalini, R., *J. Polym. Sci. Pt. B-Polym. Phys.* **2004,** *42* (23), 4313-4319.

23. Green, P. F.; Kramer, E. J., *Journal of Materials Research* **1986,** *1* (1), 202-204.

24. Tung, W. S.; Clarke, N.; Composto, R. J.; Winey, K. I., *Macromolecules* **2013,** *46* (6), 2317-2322.

25. Crawford, M. K.; Smalley, R. J.; Cohen, G.; Hogan, B.; Wood, B.; Kumar, S. K.;

Melnichenko, Y. B.; He, L.; Guise, W.; Hammouda, B., *Phys. Rev. Lett.* **2013,** *110* (19).

26. Nusser, K.; Neueder, S.; Schneider, G. J.; Meyer, M.; Pyckhout-Hintzen, W.; Willner, L.; Radulescu, A.; Richter, D., *Macromolecules* **2010,** *43* (23), 9837-9847.

27. Nusser, K.; Schneider, G. J.; Richter, D., *Soft Matter* **2011,** *7* (18), 7988-7991.

28. Nakatani, A. I.; Chen, W.; Schmidt, R. G.; Gordon, G. V.; Han, C. C., *Int. J. Thermophys.* **2002,** *23* (1), 199-209.

29. Sen, S.; Xie, Y. P.; Kumar, S. K.; Yang, H. C.; Bansal, A.; Ho, D. L.; Hall, L.; Hooper, J. B.; Schweizer, K. S., *Phys. Rev. Lett.* **2007,** *98* (12).

30. Tuteja, A.; Duxbury, P. M.; Mackay, M. E., *Phys. Rev. Lett.* **2008,** *100* (7).

31. Tung, W. S.; Bird, V.; Composto, R. J.; Clarke, N.; Winey, K. I., *Macromolecules* **2013,** *46* (13), 5345-5354.

32. Meth, J. S.; Zane, S. G.; Chi, C. Z.; Londono, J. D.; Wood, B. A.; Cotts, P.; Keating, M.; Guise, W.; Weigand, S., *Macromolecules* **2011,** *44* (20), 8301-8313.

33. A., K.; Composto, R. J.; Winey, K. I.; Clarke, N., *Soft Matter* **2014,** *published online*.

34. Composto, R. J.; Walters, R. M.; Genzer, J., *Mater. Sci. Eng. R-Rep.* **2002,** *38* (3-4), 107-180.

35. Mills, P. J.; Green, P. F.; Palmstrom, C. J.; Mayer, J. W.; Kramer, E. J., *J. Polym. Sci.*

Pt. B-Polym. Phys. **1986,** *24* (1), 1-9.

36. Kannan, R. M.; Lodge, T. P., *Macromolecules* **1997,** *30* (12), 3694-3695.

37. Graessley, W. W., *Faraday Symposia of the Chemical Society* **1983,** (18), 7-27.

38. Lodge, T. P.; Rotstein, N. A.; Prager, S., *Adv. Chem. Phys.* **1990,** *79*, 1-132.

39. Meth, J. S.; Gam, S.; Choi, J.; Lin, C. C.; Composto, R. J.; Winey, K. I., *J. Phys. Chem. B* **2013,** *117* (49), 15675-15683.

40. Casassa, E. F., *Journal of Polymer Science Part B-Polymer Letters* **1967,** *5* (9PB), 773-&.

Chapter 6

Entanglement Reduction and Anisotropic Chain and Primitive Path Conformations in Polymer Melts in Thin Film and Cylindrical Confinement

This work was accomplished in collaboration with Dr. Daniel M. Sussman at the department of physics and astronomy, University of Pennsylvania. The contents of this chapter were published in a modified version. Adapted with permission from (*Macromolecules*, **2014**, *47* (18), 6462–6472). Copyright (2014) American Chemical Society.

6.1. INTRODUCTION

The structure and dynamics of polymer melts under strong confinement has attracted intense interest since large thickness-induced shifts in the glass transition temperature were reported two decades ago.[1-2] While such changes in the glassy behavior have been hotly debated, extensional measurements of thin glassy films[3] also indicate that there is an increase in the entanglement molecular weight M_e under nanoscale confinement. Separately, experiments on polymer nanocomposites, where nanoparticles provide internal

confining surfaces,[4-9] have also indicated a modification of both the melt diffusion and the rheological properties in the rubbery regime. The interpretation of all of these experiments is challenged by our lack of a microscopic picture for the changes in the entanglement network near interfaces, either under nanoscale confinement or in the vicinity of nanoparticle surfaces. As polymer nanocomposites find broader application and nanofabrication technologies mature, shrinking the sizes of devices, it will be critical to understand the modifications of the entanglement network of confined polymer systems.[10-12]

Changes in thin-film M_e and in the polymer mean-squared end-to-end distance, R_{ee}^2, have been previously investigated in both experiments[3] and simulations.[13-16] Recently, experiments have been performed under cylindrical confinement,[17] but to the best of our knowledge no corresponding simulations have been systematically performed. Crucially, the precise link between changes in polymer conformation induced by confinement and changes in the entanglement properties is not understood. This is part of a broader conversation on the nature of entanglements in polymer melts, where even questions as simple as "does the tube diameter increase or decrease" in response to chain stretch or orientation are as yet unresolved.[18] A growing consensus, however, suggests that both

confinement and continuous shear deformations lead to a dilution of the entanglement network and a larger tube diameter.[3, 13-17, 19]

In this chapter, we first report the results of molecular dynamics simulations of entangled chains under both thin film and cylindrical confinement. We find that entanglement loss is accompanied by systematic changes in not just the global chain orientational order but also the orientational distribution of the primitive path steps themselves. By probing both thin films and cylinders we expect that, in contrast to an existing comparison between thin film simulations[15] and cylindrical experiments,[17] the entanglement network is quite sensitive to the difference between 1D and 2D confinement. We then attempt to understand our results on both the equilibrium chain conformational changes and the entanglement network dilution in a unified theoretical framework. Details of the theoretical work will not be included in this chapter and can be referred to our publication.[20] Our perspective is that strong confinement modifies global polymer conformations; this modification is transmitted to the PP level, inducing a change in the orientational distribution of PP segments, which in turn affects the number of entanglements per chain. Following this perspective, we extend existing equilibrium and dynamic theories and show that we can quantitatively predict how the confined polymers'

average conformation and number of interchain entanglements change as a function of film thickness or cylinder radius.

6.2. SIMULATIONS OF CONFINED POLYMERS

Our simulations were performed using the Kremer-Grest model[21] with non-bonded interactions governed by the repulsive part of the Lennard-Jones (LJ) potential, and units normalized by the potential strength, ε, the monomer size, σ, and the time $\tau = \sigma(m/\varepsilon)^{1/2}$, where m is the monomer mass. Since we report all units in terms of the monomer or "bead" size, some care must be taken when comparing with other results in the literature, which have sometimes been presented in units of the bond length or the mean-square end-to-end distance per monomer. All simulations are run with the LAMMPS MD simulation package with the velocity Verlet algorithm.[22] To generate confined polymers at the same density as the bulk polymers we first confine our polymers with smooth, repulsive walls and equilibrate the system in an ensemble where the pressure is held constant in the unconfined directions. The pressure is set to the average pressure calculated from an unconfined NVT simulation at a monomer density (ρ) = $0.85\sigma^{-3}$. For entangled polymer chains, Monte Carlo connectivity-altering moves are used to assist chain relaxation.[23-25] The mean square displacement (MSD) is calculated to ensure each monomer has moved a distance

comparable to R_{ee}, the root-mean-square chain end-to-end distance. The pressure is computed in the unconfined directions to obtain the corresponding equilibrium box length in these directions, where we ensure that this length is larger than R_{ee} to prevent polymer chains interacting with themselves across the periodic boundaries.

To prevent polymer crystallization for both the thin film and cylindrical cases we impose geometric confinement via amorphous immobile particles of the same size and interacting with the same repulsive LJ potential as the polymer monomers. To do this a simulation box is set up with desired sizes in both unconfined and confined directions and filled with LJ monomers at a density of $1.3\sigma^{-3}$. These beads are relaxed under constant volume conditions and a subset is removed to create a cavity with the required geometric shape. We then insert the polymer chains that were equilibrated with smooth confining walls and re-equilibrate them. The length of the simulation box in the unconfined directions is then scaled to reach a polymer bead density of $0.85\sigma^{-3}$. The simulation box confined using the rescaled walls is then re-equilibrated a final time, and the accessible volume is re-evaluated to confirm that $\rho = 0.85\sigma^{-3}$ (to within $\sim 0.5\%$).

We studied $N = 50,\ 300,$ and 500 for cylindrical confinement and $N = 350$ for thin film confinement. We first quantify the degree of confinement by the accessible

volume of the system. For confined polymer chains, the closest possible separation (r_{min}) between a polymer bead and a wall bead is assumed to be the same as the closest distance between two polymer beads in a bulk condition. A random point is generated within the simulation box and is then determined as inaccessible if the point is either inside the wall region or the minimum distance between the point and any wall bead is less than r_{min}. A large number of random points (10^8) are generated and the percentage of accessible points (v_{acc}%) is obtained. Accessible volume is then simply the percentage of accessible points multiplied by the volume of the simulation box.

Note that the radius, r, and thickness, h, are the sizes of the confinement with smooth wall when we first relaxed the polymer chains, while the effective confinement dimensions ($r_{eff,}$ h_{eff}) are obtained from the accessible volume evaluation (e.g. r_{eff} = $(v_{acc}/\pi l_z)^{1/2}$. From the equilibrated configurations, MD simulations are run until the diffusion regime of the MSD is reached and then polymer configurations are recorded for post analysis. To improve the statistics of our results, configurations at seven different times separated by $3\times10^6\tau$ are used, except for the systems with $r/\sigma = 10, 15$ for $N = 500$, $r/\sigma = 15, 20$ for $N = 350$ and $h/\sigma = 40$ for $N = 350$. For those systems the diffusion time is prohibitively long, and so connectivity-altering Monte Carlo moves are used in

combination with MD simulation to obtain uncorrelated configurations. Table 6.1 lists the range of systems studied for cylindrical and thin film confinement. Table 6.2 summarizes the results of these calculations.

Table 6.1. Details about each simulation system for cylindrical and thin film confinement. All the length units are in σ.

Cylindrical Confinement					
	Radius (r)	Number of chains (M)	Size of the simulation box		Effective radius (r_{eff})
			lx (= ly)	lz (unconfined)	
N = 50	Bulk	100	18.05	18.05	N/A
	3	80	10	226.77	2.57
	5	80	15	71.61	4.58
	10	100	25	20.36	9.58
	20	640	45	20.49	19.58
N = 350	Bulk	90	33.34	33.34	N/A
	5	30	15	179.28	4.57
	7	40	19	121.35	6.57
	10	60	25	85.95	9.57
	15	60	35	36.96	14.58
N = 500	Bulk	80	36.1	36.1	N/A
	5	20	15	179.28	4.58
	7	30	19	130.23	6.57
	10	50	25	102.33	9.57
	15	60	35	52.9	14.58
Thin Film Confinement					
	Thickness (h)	Number of chains (M)	Size of the simulation		Effective thickness (h_{eff})
			lz	lx = ly (unconfined)	
N = 350	8	30	13	41.42	7.20
	10	40	15	42.31	9.15
	14	50	19	39.32	13.25
	20	70	25	38.80	19.23
	30	90	35	35.63	29.20
	40	120	45	35.49	39.24

Table 6.2. Reduced density and accessible volume for the simulated systems.

Cylindrical Confinement							
	r	Equilibrated (l_z)	v_{acc}	Density ($/\sigma^3$)	Scaled l_z	Re-evaluated v_{acc}	Density ($/\sigma^3$)
N=50	3	221.57	4597.92	0.8670	226.77	4708.42	0.8495
	5	69.61	4574.59	0.8744	71.61	4717.43	0.8479
	10	19.61	5666.82	0.8823	20.36	5869.17	0.8519
	20	19.58	23606.02	0.8896	20.49	24690.78	0.8505
N=350	5	182.70	11988.93	0.8758	188.25	12342.31	0.8507
	7	117.06	15888.21	0.8812	121.35	16474.09	0.8498
	10	82.37	23675.87	0.8870	85.95	24719.42	0.8495
	15	35.41	23666.13	0.8873	36.96	24677.13	0.8510
	20	29.38	35388.98	0.8901	30.76	37013.16	0.8510
	25	37.23	71989.52	0.8751	38.33	72775.50	0.8657
N=500	5	173.66	11396.26	0.8775	179.28	11978.11	0.8476
	7	125.30	16978.94	0.8836	130.23	17679.73	0.8484
	10	98.04	28179.48	0.8872	102.33	29418.03	0.8498
	15	50.57	33739.06	0.8892	52.90	35320.36	0.8494
Thin Film Confinement							
	h	Equilibrated l_x ($=l_y$)	v_{acc}	Density ($/\sigma^3$)	Scaled l_x ($=l_y$)	Re-evaluated v_{acc}	Density ($/\sigma^3$)
N=350	8	39.77	11390.93	0.9179	41.42	12357.54	0.8499
	10	40.87	15369.66	0.9109	42.37	16375.76	0.8549
	14	38.45	19684.72	0.8890	39.32	20479.95	0.8545
	20	37.98	27615.69	0.8872	38.80	28950.31	0.8463
	30	35.13	36020.76	0.8945	35.63	37076.87	0.8496
	40	35.12	48384.76	0.8680	35.49	49436.14	0.8496

To study the entanglement properties of our systems there are three standard techniques in the community: the two geometric methods (CReTA[26] and Z1[27-30]) and the "classical primitive path algorithm" (PPA[31]). In isotropic systems it has been argued that CReTA and Z1 give essentially identical results, and in this work we explicitly verify this for a subset of our cylindrical confinement data. In contrast, the PPA finds paths that minimize elastic energy of the chains (as opposed to the contour-length minimization of the geometric methods), and it has been argued that contour-length minimizing algorithms do a better job of reproducing the Doi-Kuzuu distribution of primitive path lengths.[28] Further complicating the use of the PPA, chain tension in the energy-minimizing algorithm can shift the position of the entanglement point, possibly changing any signature of orientational order of the primitive paths. For this reason, the original PPA method by definition does not allow one to extract the entanglement length in an anisotropic sample. Thus, combined with the fact that the PPA algorithm is not parameter free, we believe that comparing it with the geometric methods is unwarranted. Due to its computational efficiency, then, we primary focus on the Z1 algorithm, but also include some comparisons with CReTA results.

6.3. SIMULATION RESULTS

The effective cylinder radius or film thickness ($r_{eff,}$ h_{eff}) is obtained from the accessible volume, and we take the cylindrical axis and the normal to the thin films to lie along the z axis. We parameterize the degree of confinement by $\delta \equiv h_{eff}/R_{ee,bulk}$ or $\delta \equiv r_{eff}/R_{ee,bulk}$, the film thickness or cylinder diameter in units of the average bulk end-to-end distance. Our main results from the simulations concern the components of the root-mean-square end-to-end vector R_{ee}, the number of beads between entanglements, N_e, and the primitive path (PP) configuration of the system as generated by the Z1 algorithm.[27-30] This algorithm uses geometrical moves to monotonically reduce chain contour lengths to the limit of infinitely thin PP thickness, and we report the average entanglement number$\langle Z \rangle$, as the average number of kinks per chain in the resulting PP network. From the full PP configuration we calculate orientational distributions of PP steps in bulk and under confinement, which is a key point of comparison against our theoretical analysis. All simulation results shown in Figure 6.2 to 6.4 are compared to theoretical predictions (curves). For the sake of length of this chapter, derivations of theories and associated equations are not presented in this chapter and can be found in our publication.[20]

Representative simulation images of polymers in bulk and cylindrical confinement

are shown in Figure 6.1, which also shows the corresponding PP steps of those chains. We note that this algorithm has previously been used to study anisotropic entanglement networks.[19]

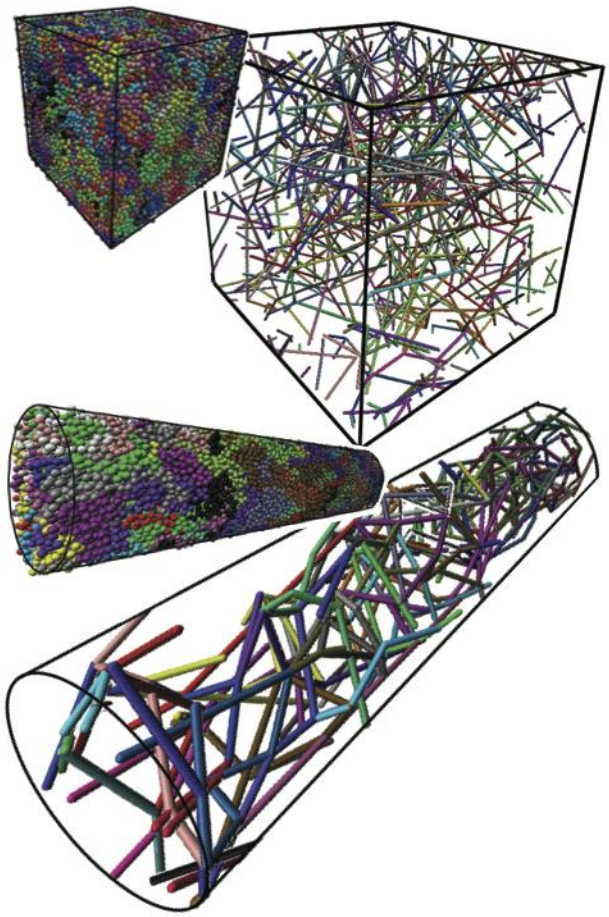

Figure 6.1. Representative configurations of the simulated systems and the corresponding primitive path networks (as obtained via the Z1 algorithm). The top pair of images correspond to a bulk configuration; the bottom pair to a cylindrically confined system, where the orientational ordering of the primitive paths along the cylinder is clear from visual inspection.

6.3.1. Chain End-to-end Distance (R_{ee}) in Confinement

Figure 6.2 (a) shows the changes in the components of R_{ee} relative to the confining surfaces as a function of δ. Generically, the chains are significantly compressed normal to a surface and modestly expand parallel to the surface, and there is a near collapse of these conformational confinement effects normal to the surface, despite the difference in the number of confining directions. We also note that our results for planar confinement agree very well with other simulation studies.[12-13] Simulation results from other works are included and shown in Figure 6.2(b).

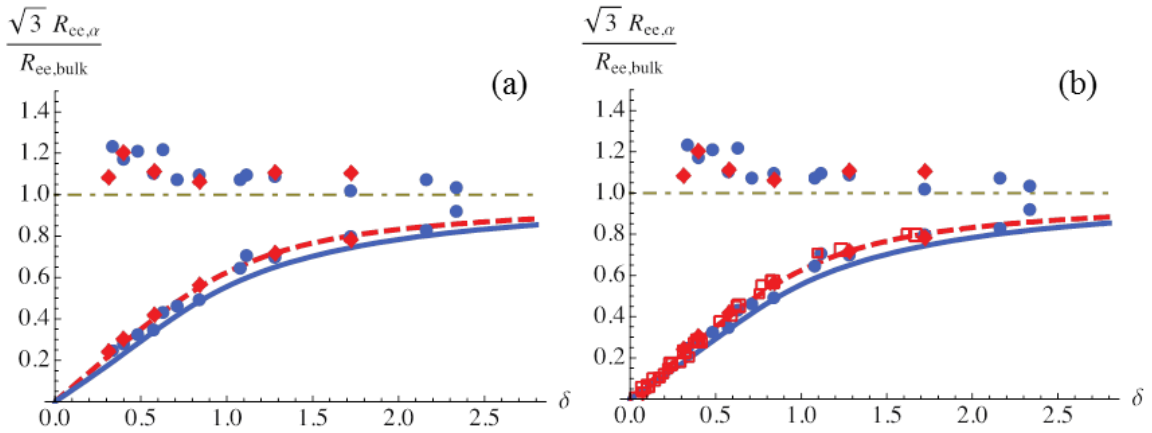

Figure 6.2. (a) Root-mean-square component of the end-to-end vector for cylindrical (solid blue line; circles) and thin-film (dashed red line; diamonds) confinement. Filled symbols are the simulation results of this work, and lines are the theoretical predictions (Equation 1 in our publication).[20] Upper points indicate components parallel to the surface and lower points indicate components normal to the surface, and the dash-dotted line indicates the bulk value of $R_{ee,\ bulk}/(3^{1/2})$. The confinement parameter, δ, is either the effective film thickness or cylinder diameter divided by the bulk root-mean-square end-to-end chain distance. (b) The same plot, but where additionally thin film simulation results from Refs. [13, 14] are included as open squares.[13-14]

6.3.2. Orientational Probability Distribution for Primitive Path Steps

Figure 6.3 illustrates the changes in the PP orientational probability distribution, $g(\vec{u})$, where $\vec{u}$ is a unit vector describing the orientation of the PP step, for representative degrees of confinement. Given the symmetry of films and cylinders, in Figure 6.3 we plot the distribution of orientations relative to the *z* axis, $g(\vec{u}) \propto f(\theta)\sin\theta$, where $\cos\theta = \vec{u}\cdot\hat{z}$, so that $f(\theta) = 1$ represents an isotropic distribution. We find that this distribution closely follows the orientational distribution of chain end-to-end vectors. Under planar

confinement, the PP steps tend to lie down in the plane of the film, and so $f(\theta)$ has a maximum near $\theta = \pi/2$. Under strong cylindrical confinement the PP steps align along the axis of cylindrical symmetry, and hence $f(\theta)$ has a maximum near $\theta = 0$.

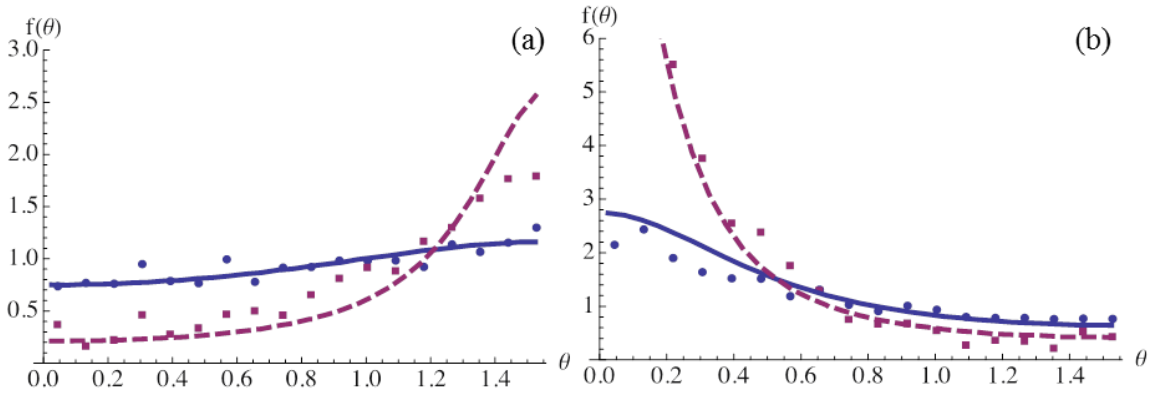

Figure 6.3. Representative comparisons between theoretical (curves) and simulation (points) results for the orientational distribution of PP segments. (a) Thin film $f(\theta)$ for δ = 1.7 (solid curve; circles) and δ = 0.40 (dashed curve; squares). (b) Cylindrical confinement $f(\theta)$ for δ = 0.84 (solid curve; circles) and δ = 0.34 (dashed curve; squares).

6.3.3. Entanglements per Chain (Z)

Figure 6.4 establishes how confinement induces a significant reduction in the number of entanglements per chain, $Z \equiv N/N_e$, and the effects of confinement on Z are significantly stronger under cylindrical confinement. Under planar confinement, the strongest reduction in the entanglement density was only approximately 20% for films

with a thickness as small as $\delta = 0.25$, while cylinders with a diameter corresponding to $\delta = 0.25$ had an approximately 50% reduction in the entanglement density. To ensure that our results were not sensitive to our choice of primitive path algorithm we have also used the CReTA algorithm[26] to compute entanglement reduction in a subset of our systems. It had previously been argued that Z1 and CReTA should yield qualitatively similar results under both isotropic and anisotropic conditions;[19, 28] here we explicitly demonstrate this for the cylindrically confined systems.

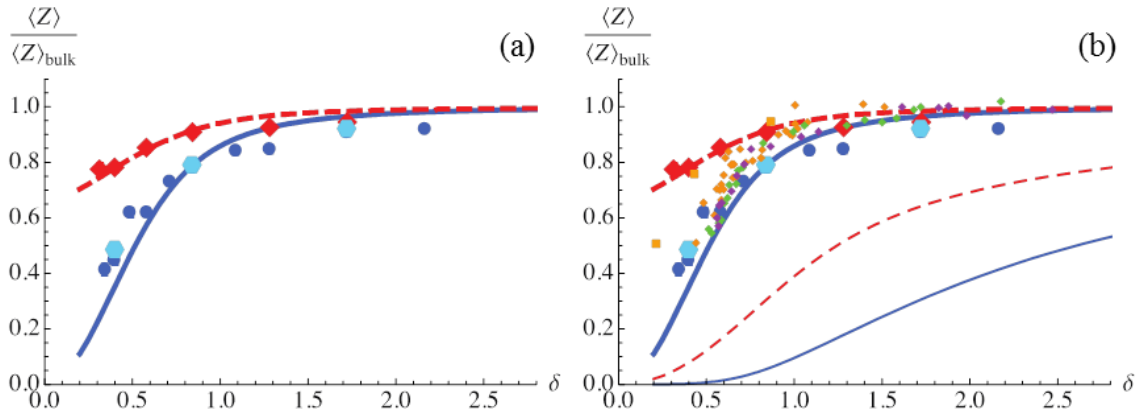

Figure 6.4. (a) Normalized number of entanglements per chain for cylindrical (thick solid line; large circles) and thin-film (thick dashed line; large diamonds) confinement. Large points are the simulation results of this work, and the thick curves are the theoretical predictions (Equation 17 in our publication).[20] Light blue hexagons are $\langle Z\rangle/\langle Z\rangle_{bulk}$ as calculated by the CReTA algorithm for a subset of the cylindrically-confined systems.[26] (b) The same plot, but with additional data from the literature. Small diamonds are experimentally estimated data for three different length polymers in thin-film confinement from Ref. [3] and small squares are thin-film simulations from Ref. [15]. The two thin lower curves show the "anisotropic packing length" argument estimate for entanglement loss in cylinders (thin solid line) and films (thin dashed line) using the theoretically predicted changes in chain end-to-end distances.

Comparing Figures 6.2 and 6.4 shows that while the confinement geometry has only a modest effect on chain conformations normal to the surface, the number of confined dimensions strongly affects PP statistics. If one assumes that even in anisotropic systems there is a simple relationship between the number of entanglements per chain and the tube diameter, $Z \sim N/N_e \sim \sigma^2/d_t^2$, then the observed reduction of Z corresponds to an increase in the tube diameter $d_t = \sigma(N_e)^{1/2}$. We find that $\delta \gtrsim 2.0$ is required for the entanglement

network to become bulk-like. This result agrees qualitatively with polymer nanocomposite experiments that find a change in the entanglement plateau modulus when the separation between nanoparticle surfaces is less than ~2.5R_{ee}.[5] Neutron scattering experiments on cylindrically confined systems reported an increase in d_t of ~15% for a system with δ ~ 0.42.[13] We typically find a larger enhancement, e.g., our model cylindrical system with δ ~ 0.49 has an effective d_t ~ 28% larger than the bulk.

Given the changes in chain dimensions, one possible phenomenological ansatz for the entanglement reduction is an anisotropic extension of packing-length arguments. The number of interpenetrating chains in the bulk scales as $R_{ee}^3/(NV_{mon}) \sim \sigma\sqrt{N}/p$, where $p = (\rho_s\sigma^2)^{-1}$ is the invariant packing length.[32-33] Packing a fixed number of chains in the pervaded volume implies $N_e \sim (p/\sigma)^2$. While it is known that the average number of chains in the pervaded volume of a given chain is not precisely constant as a function of confinement,[34] as a first order estimate one can neglect this effect and approximate $(R_xR_yR_z)/(NV_{mon}) \sim$ constant, suggesting $Z/Z_{bulk} = (R_xR_yR_z/R_{x,\,bulk}{}^3)^2 < 1$. That is, in this simple packing estimate the relative change in the pervaded volume of an oriented chain is directly mapped to the number of chains it is entangled with. Figure 6.4(b) shows that this estimation, using conformations from either the simulations or theoretical results

(Equation 1 in our publication), predicts a much stronger loss of entanglement than we observe. This overprediction is not a simple consequence of neglecting changes in local chain self-density as a function of confinement (i.e. the approximation of $(R_x R_y R_z)/(NV_{mon})$ ~ constant). Thus, a deeper understanding of entanglements is required to treat confined systems.

6.4. SUMMARY

In this chapter, we have systematically studied average measures of conformational change and entanglement density dilution in strongly confined polymer melts using both molecular-dynamics simulations and theory. Studying two distinct confinement geometries with neutral interactions with the confining walls, our simulations reveal conformational changes in response to geometric confinement. The simulations further show a systematic reduction in the entanglement density – as studied by multiple primitive-path measures – as the confinement induces progressively more orientational order in the polymer melt. To understand these results we have generalized theoretical ideas to allow first-principles, quantitative, adjustable-parameter-free predictions for the change in the end-to-end vector and average number of entanglements per chain. Very good agreement between theory and simulation is found. In addition to direct analysis of

polymer liquids, this suggests that our theoretical perspective connecting local orientational order to local entanglement density may be used to inform other more highly coarse-grained approaches, such as slip-link models of entangled polymer liquids.[35] Finally, we have established that confined polymer melts exhibit anisotropic changes in polymer conformation and topological entanglement, and our future work includes exploring how this anisotropy impacts the melt diffusion, rheology, and elastic response in these confined systems.

6.5. REFERENCES

1. Keddie, J. L.; Jones, R. A. L.; Cory, R. A., *Faraday Discuss.* 1994, *98*, 219-230.

2. Keddie, J. L.; Jones, R. A. L.; Cory, R. A., *Europhys. Lett.* 1994, *27* (1), 59-64.

3. Si, L.; Massa, M. V.; Dalnoki-Veress, K.; Brown, H. R.; Jones, R. A. L., *Phys. Rev. Lett.* 2005, *94* (12), 127801.

4. Schneider, G. J.; Nusser, K.; Willner, L.; Falus, P.; Richter, D., *Macromolecules* 2011, *44* (15), 5857-5860.

5. Anderson, B. J.; Zukoski, C. F., *Macromolecules* 2009, *42* (21), 8370-8384.

6. Mu, M. F.; Clarke, N.; Composto, R. J.; Winey, K. I., *Macromolecules* 2009, *42* (18), 7091-7097.

7. Gam, S.; Meth, J. S.; Zane, S. G.; Chi, C. Z.; Wood, B. A.; Seitz, M. E.; Winey, K. I.; Clarke, N.; Composto, R. J., *Macromolecules* 2011, *44* (9), 3494-3501.

8. Tung, W. S.; Clarke, N.; Composto, R. J.; Winey, K. I., *Macromolecules* 2013, *46* (6), 2317-2322.

9. Choi, J.; Hore, M. J. A.; Meth, J. S.; Clarke, N.; Winey, K. I.; Composto, R. J., *ACS Macro Lett.* 2013, *2* (6), 485-490.

10. Dersch, R.; Steinhart, M.; Boudriot, U.; Greiner, A.; Wendorff, J. H., *Polym. Adv. Technol.* 2005, *16* (2-3), 276-282.

11. Granick, S.; Kumar, S. K.; Amis, E. J.; Antonietti, M.; Balazs, A. C.; Chakraborty, A. K.; Grest, G. S.; Hawker, C. J.; Janmey, P.; Kramer, E. J.; Nuzzo, R.; Russell, T. P.; Safinya, C. R., *J. Polym. Sci. Pt. B-Polym. Phys.* 2003, *41* (22), 2755-2793.

12. Suh, K. Y.; Kim, Y. S.; Lee, H. H., *Adv. Mater.* 2001, *13* (18), 1386-1389.

13. Cavallo, A.; Müller, M.; Binder, K., *J. Phys. Chem. B* 2005, *109* (14), 6544-6552.

14. Cavallo, A.; Müller, M.; Wittmer, J. P.; Johner, A.; Binder, K., *J. Phys.-Condes. Matter* 2005, *17* (20), S1697-S1709.

15. Meyer, H.; Kreer, T.; Cavallo, A.; Wittmer, J. P.; Baschnagel, J., *Eur. Phys. J.-Spec. Top.* 2007, *141*, 167-172.

16. Vladkov, M.; Barrat, J. L., *Macromolecules* 2007, *40* (10), 3797-3804.

17. Martin, J.; Krutyeva, M.; Monkenbusch, M.; Arbe, A.; Allgaier, J.; Radulescu, A.; Falus, P.; Maiz, J.; Mijangos, C.; Colmenero, J.; Richter, D., *Phys. Rev. Lett.* 2010, *104* (19), 197801.

18. Desai, P. S.; Larson, R. G., *J. Rheol.* 2014, *58* (1), 255-279.

19. Baig, C.; Mavrantzas, V. G.; Kröger, M., *Macromolecules* 2010, *43* (16), 6886-6902.

20. Sussman, D. M.; Tung, W. S.; Winey, K. I.; Schweizer, K. S.; Riggleman, R. A., *Macromolecules* 2014, *47* (18), 6462-6472.

21. Kremer, K.; Grest, G. S., *J. Chem. Phys.* 1990, *92* (8), 5057-5086.

22. Plimpton, S., *J. Comput. Phys.* 1995, *117* (1), 1-19.

23. Auhl, R.; Everaers, R.; Grest, G. S.; Kremer, K.; Plimpton, S. J., *J. Chem. Phys.* 2003, *119* (24), 12718-12728.

24. Karayiannis, N. C.; Mavrantzas, V. G.; Theodorou, D. N., *Phys. Rev. Lett.* 2002, *88* (10).

25. Banaszak, B. J.; de Pablo, J. J., *J. Chem. Phys.* 2003, *119* (4), 2456-2462.

26. Tzoumanekas, C.; Theodorou, D. N., *Macromolecules* 2006, *39* (13), 4592-4604.

27. Karayiannis, N. C.; Kröger, M., *Int. J. Mol. Sci.* 2009, *10* (11), 5054-5089.

28. Hoy, R. S.; Foteinopoulou, K.; Kröger, M., *Phys. Rev. E* 2009, *80* (3), 031803.

29. Shanbhag, S.; Kröger, M., *Macromolecules* 2007, *40* (8), 2897-2903.

30. Kröger, M., *Comput. Phys. Commun.* 2005, *168* (3), 209-232.

31. Everaers, R.; Sukumaran, S. K.; Grest, G. S.; Svaneborg, C.; Sivasubramanian, A.; Kremer, K., *Science* 2004, *303* (5659), 823-826.

32. Witten, T. A.; Milner, S. T.; Wang, Z.-G., Multiphase Macromolecular Systems. Culbertson, B. M., Ed. New York, 1989.

33. Fetters, L. J.; Lohse, D. J.; Richter, D.; Witten, T. A.; Zirkel, A., *Macromolecules* 1994, *27* (17), 4639-4647.

34. Li, Y. J.; Wei, D. S.; Han, C. C.; Liao, Q., *J. Chem. Phys.* 2007, *126* (20), 204907.

35. Schieber, J. D.; Andreev, M., *Annual Review of Chemical and Biomolecular Engineering* 2014, *5*, 367-381.

Chapter 7

Local Polymer Dynamics and Diffusion in Cylindrical Nano-Confinement

The contents of this chapter have been submitted to *Macromolecules*, in a modified version.

7.1. INTRODUCTION

Polymer dynamics under different types of nano-confinement (ex: nanoparticle/polymer nanocomposites, polymer thin films, polymers confined in cylindrical nanopores, etc.) is an interesting topic and has been widely studied over the past three decades.[1] Polymer structure and dynamics are perturbed under confinement, especially when the confinement length is comparable to the size of a polymer chain (represented by the radius of gyration, R_g, or the end-to-end distance, R_{ee}). Among the various routes to impose confinement, polymers within cylindrical pores have received growing interest in the past 5 to 10 years.[2-13] For example, the structure of polymers confined in cylindrical nanopores was investigated by small-angle neutron scattering,[2, 12] and dynamics by nuclear magnetic resonance,[9-10] inelastic neutron scattering,[3-8, 11]

dielectric spectroscopy,[14-16] and calorimetry.[16-18]. Different techniques have been employed to probe polymer dynamics in various time and length scales. Because results from different experimental techniques are sometimes conflicting, a unified understanding of how cylindrical confinement affects polymer dynamics has not been achieved.

Modeling and simulations play an important role toward understanding polymer dynamics under confinement from a microscopic point of view, and provide connections between molecular mechanisms and experimentally measured observables. Changes in polymer structure and dynamics induced by nanoparticles[19-24] and thin film confinement[13, 25-29] have been studied using simulations. However, much less simulation work has been conducted on polymers under cylindrical confinement. We investigated the change in polymer structure, primitive path statistics, and polymer chain size (end-to-end distance, R_{ee}), and connected the changes in polymer structure with the reduction in the entanglement density in Chapter 6.[30] In this chapter, we will focus on the effect of cylindrical confinement on the local dynamics and polymer center-of-mass diffusion.

The reptation model has successfully described the diffusion of entangled polymers in bulk systems.[31-33] However, the limitations of the reptation model for

polymer chains under confinement have not been evaluated. From the reptation model, diffusion coefficients can be expressed as

$$D \approx \frac{R_{ee}^2}{\tau_d} \approx \frac{R_{ee}^2}{N^2}\frac{k_B T}{\xi b^2}\frac{N_e}{N} \tag{7.1}$$

where R_{ee} is the polymer end-to-end distance, τ_d is the disentanglement time, N is the number of Kuhn monomers per polymer chain, ξ is the monomer friction coefficient, b is the Kuhn length, and N_e is the number of Kuhn monomers in one entanglement strand. The term $k_B T/\xi b^2$ can also be represented as $1/\tau_0$, where τ_0 is the relaxation time of a Kuhn monomer or the shortest Rouse relaxation time. Thus, D scales with R_{ee}, τ_0, and N_e as

$$D \propto R_{ee}^2 \frac{1}{\tau_0} N_e \tag{7.2}$$

In Chapter 6, we investigated how R_{ee} and N_e are affected by cylindrical confinement.[30] Under cylindrical confinement, the polymer chain conformation is reduced in the confined direction (i.e., perpendicular to cylinder) due to the impenetrable wall, and slightly elongated by 10 to 20 % in the unconfined direction (i.e., parallel to the wall). Further, N_e increases as the diameter of the confining cylinder decreases, suggesting that strong geometric confinement can produce interchain disentanglement.

In this chapter, we first discuss the effect of confinement on the local relaxation

times using simulation and then combine this confinement effect with two other parameters, R_{ee} and N_e, to compute diffusion coefficients according to the reptation model, D_{rep}. For comparison, the polymer center of mass diffusion coefficients, D_{MSD}, are directly calculated from the MD simulations at long simulation times. Experimentally, the tracer diffusion coefficients, D_{exp}, of deuterated polystyrene (dPS) diffusing into anodized aluminum oxide nanopores pre-filled with protonated polystyrene (hPS) are measured by elastic recoil detection. These three diffusion coefficients (D_{rep}, D_{MSD}, D_{exp}) when normalized by the diffusion coefficient in the bulk exhibit faster diffusion along the cylindrical nano-confinement with increasing confinement.

7.2. MOLECULAR DYNAMICS SIMULATIONS OF CONFINED POLYMERS

Details of the generation and equilibration of our polymer systems under cylindrical confinement can be found in Chapter 6. The entangled polymer system (number of monomers, N = 350) in this chapter has a bulk root-mean-square end-to-end distance, R_{ee}, of 22.7 σ. The confining cylinders are aligned along the z axis and have diameter d, such that d/σ = 10, 14, 20, 30, and 40. In units of the polymer chain end-to-end distance, the degree of confinement δ (defined as $\delta = d_{eff}/R_{ee}$) is approximately δ = 0.40, 0.58, 0.84, 1.28 and 1.72. The way of obtaining d_{eff} can also be found in Chapter

6.

From the equilibrated configurations for each system, MD simulations were run until the diffusion regime of the mean-squared displacement (MSD) was observed. The MSD was calculated with a moving time origin to improve the statistics. The cylindrical axis of the confinement is along the *z* axis. In the rest of this chapter, anisotropy in polymer dynamics will be discussed in many cases. Displacement in the *z* direction represents the monomer movement along the cylindrical axis; whereas displacement in the *x* direction includes all the monomer movement on the *xy* plane, which is perpendicular to the cylindrical axis. In the confined systems, we break the MSD into its *x*, *y*, and *z* components to analyze the anisotropy in the mobility of the polymer segments. To investigate the dependence of local dynamics on chain length, an unentangled polymer system (N = 50, R_{ee} = 7.75σ) was also studied with δ = 1.19 to 5.00. Details for each simulation system for bulk and cylindrical confinements can be found in Chapter 6.

7.3. EXPERIMENTAL METHODS

7.3.1 Materials

Polystyrene (PS) matrix polymers were purchased from Pressure Chemical Co., Pittsburgh, USA, and infiltrated into anodized aluminum oxide (AAO) membranes by a

melt annealing method.[2, 34-35] The deuterated polystyrene (dPS) tracer polymer was purchased from Polymer Source Inc., Quebec, CA. Table 7.1 shows the molecular weight (M_w) and polydispersity (PDI) from size-exclusion chromatography for these three polystyrenes. For atactic PS, R_{ee} and R_g were calculated using a Kuhn length of 1.8nm and the molecular weight of a Kuhn monomer, 720g/mol.[36] For atactic dPS, R_{ee} was calculated by $a*(M_w/M_0)^{0.5}$, where a = 0.67nm is the statistical length for dPS and M_0 = 112g/mol.[37]

Table 7.1. Weight averaged molecular weight (M_w), PDI, end-to-end distance, and radius of gyration of the infiltrated polymers (PS) and the tracer polymer (dPS)

Polymer	M_w **(kg/mol)**	**PDI**	R_{ee} **(nm)**	R_g **(nm)**
200k PS	180.9	1.03	28.5	11.6
290k PS	249.0	1.06	33.6	13.7
400k dPS	394.8	1.02	39.8	16.2

AAO membranes were purchased from Synkera Technology Inc., CO, USA, with diameters of 18, 35, 55, and 80 nm as reported by the vender. Top view and cross-sectional views of the membranes were characterized by scanning electron microscope (SEM), and images are provided in Appendix F. These membranes yield degrees of confinement ($\delta = d/R_{ee}$) of 0.45, 0.88, 1.38, and 2 calculated based on R_{ee} for dPS (400k). Two matrix

polystyrenes were used to demonstrate that diffusion is independent of the matrix molecular weight, consistent with the reptation model.

7.3.2. Bilayer Sample Preparation

A thick polystyrene film (> 100 μm) was prepared by doctor blading, cut into the shape of the membrane, placed on top of the membrane, and pre-annealed on a hot plate at ~ 170°C to adhere the film to the membrane. The membrane with the PS film on top was then placed on a silicon wafer and annealed in a vacuum oven at 190 °C for 1 to 2 days. After annealing, polystyrene was observed to wet the interface between the membrane and silicon wafer, indicating that polystyrene infiltrated all the way through the nanopores. Residual PS on top of the membranes was scraped away using a razor blade. A thin deuterated polystyrene (dPS) film was spin coated onto a silicon wafer and its thickness (~20nm) was measured by ellipsometry. The dPS film was then floated on DI water and transferred to the PS infiltrated membrane on the same side where the thick PS film was originally attached. The bilayer samples were dried in a hood and then annealed at 160 °C in a vacuum oven with precise temperature control (within 1 °C). Two annealing times, 6 and 12 hrs, were used to obtain diffusion lengths (x) of ~ 130 nm and 180 nm,

respectively, and to demonstrate that the diffusion coefficients are independent of the annealing time. Note that these diffusion distances far exceed the R_{ee} value of 39.8 for dPS.

7.3.3. Tracer Diffusion Coefficients

Elastic recoil detection (ERD) was used to determine the tracer diffusion coefficients of 400k dPS in PS-infiltrated AAO membranes. He^{2+} ions accelerated to 3MeV, impinged on bilayer samples, and recoiled deuterium (^2D) and hydrogen (^1H) from different depths below the surface. By comparing the total counts of hydrogen from PS infiltrated membranes to a 100% hPS film, the porosities of the AAO membranes were found to range from ~ 10 to 18 v%, see Appendix G. By detecting the energies of recoiled deuterium, the depth profile of dPS in the PS-infiltrated cylindrical pores was determined. The raw data from ERD measures counts (number of deuterium) versus the energy of the deuterium and the analysis includes converting deuterium counts to dPS concentrations and converting the deuterium recoil energy to sample depth. Because the incident He^{2+} and recoiled D transverses the PS cylinders and AAO membrane, the stopping power of the matrix was calculated using the pure stopping powers of Al_2O_3 and PS weighted by

the porosity, which represents the volume fraction of the PS matrix. A detailed description of ERD and associated data reduction is given in the review paper by Composto *et al*.[38] The high stopping power of the matrix limits the probing depth to ~ 300nm. Because of the low porosity of the membranes, some dPS remains on the top of the PS-infiltrated membranes (inset of Figure 7.1), resulting in the surface peaks (solid blue lines).

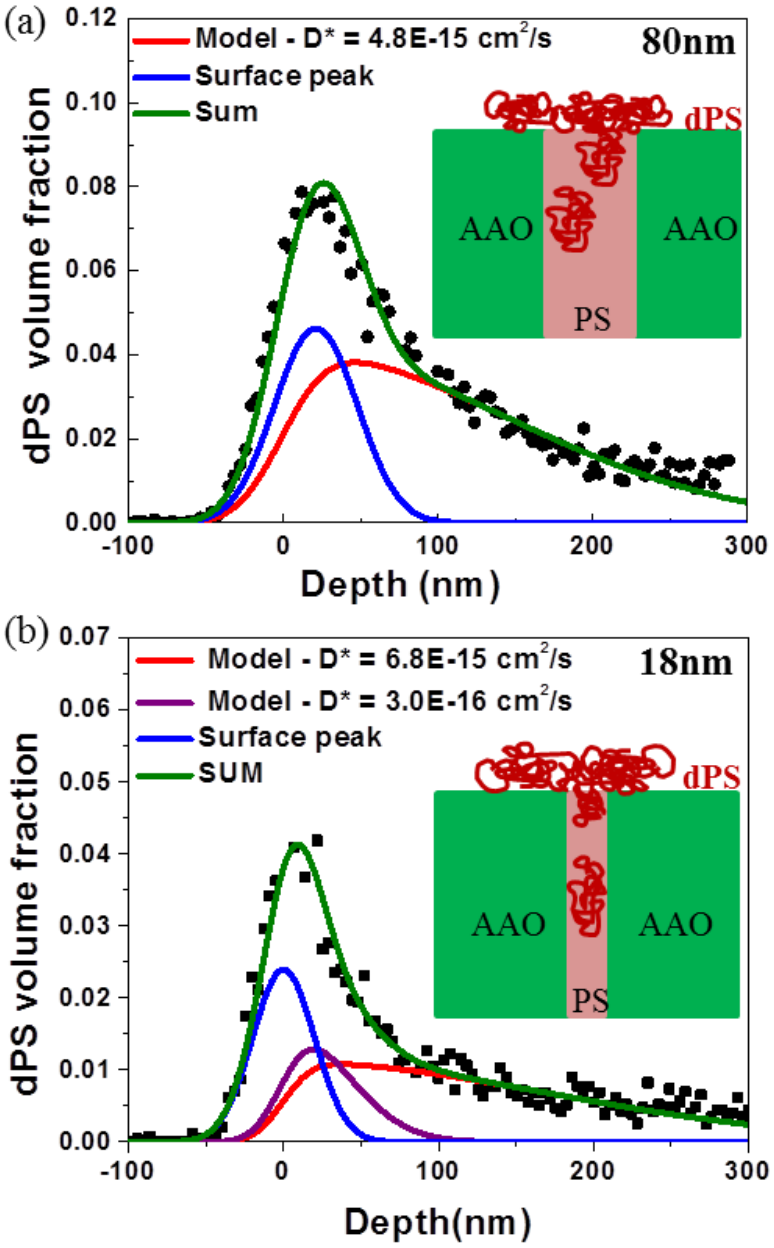

Figure 7.1. Depth profile of 400k dPS diffused into 200k PS-infiltrated AAO membranes with 80nm (a) and 18nm (b) nanopores after annealing at 160 °C for 6 h. Blue lines denote the surface peak due to the residual dPS on the membranes. The red lines correspond to the best fit of the experimental dPS volume fraction profile in the nanopores using Equation 7.3. For the narrow 18nm pores, the purple line captures the slower diffusion of dPS entering nanopores. The green lines are the summation of all curves (i.e., Equation 7.4 and residual dPS)

The depth profiles are fit by using the solution of Fick's second law convoluted with the experimental resolution (Gaussian function) to find the tracer diffusion coefficient. Fick's second law for a thin film diffusing into a semi-infinite environment (i.e., PS-infiltrated membrane), gives the concentration profile for the tracer as

$$\Phi(\mathrm{x}) = \frac{1}{2}\left[erf\left(\frac{h-x}{\sqrt{4Dt}}\right) + erf\left(\frac{h+x}{\sqrt{4Dt}}\right)\right] \quad (7.3)$$

where $\Phi(x)$ denotes the dPS volume fraction, x is depth from the sample surface, h is the original thickness of the thin dPS film (~ 20nm), t is the diffusion time, and D is the tracer diffusion coefficient of dPS. Because the parameters x, h and t are known, D is the only fitting parameter to the experimental concentration profile. The boundary condition corresponds to a finite ultra-thin tracer film diffusing into a semi-infinite media. The total amount of dPS is held fixed in the fitting, and the initial dPS in the matrix is zero at $t = 0$. A Gaussian function describes the depth resolution, ~40nm, of ERD, which was determined from the front edge of the dPS profile for an unannealed bilayer. Note that the high stopping power of the PS-infiltrated AAO matrix improves the depth resolution of ERD relative to the typical resolution of ~70nm for pure polymer matrices.[39-41] A surface peak[39] described by a step function convoluted with a Gaussian function (resolution function) is added to capture the residual dPS on top of the membranes. Figure 7.1 shows

two representative profiles corresponding to a 400k dPS tracer diffusing into a 200k PS-infiltrated AAO membranes with 80-nm and 18-nm diameter nanopores in Figures 7.1(a) and 7.1(b), respectively. For the 18-nm pores (Figure 7.1(b)), the diffusion coefficients for the tracer to enter the pore and diffuse within the pore are different. Thus, two diffusion coefficients along with a surface peak were used to fit the entire volume fraction profile. Thus, the profile for the tracer can be expressed as

$$\Phi(\mathrm{x}) = \frac{1}{2}\left[erf\left(\frac{h-x}{\sqrt{4D_f t}}\right) + erf\left(\frac{h+x}{\sqrt{4D_f t}}\right)\right] + \frac{1}{2}\left[erf\left(\frac{h-x}{\sqrt{4D_s t}}\right) + erf\left(\frac{h+x}{\sqrt{4D_s t}}\right)\right] \quad (7.4)$$

where D_f and D_s represent the diffusion coefficients corresponding to the faster diffusion within the nanopores and slower diffusion for dPS entering the nanopores, respectively. The fast diffusion coefficients will be compared to the two diffusion coefficients extracted from the MD simulations.

7.4. RESULTS AND DISCUSSIONS

7.4.1. Mean Square Displacement (MSD) vs. LJ time

The MSD along the cylinder axis (z-direction, MSD_z) as a function of LJ time for both bulk and cylindrically-confined polymers are plotted on a log-log scale in Figure 7.2(a). At very short time scales, monomer dynamics are independent of the chain

connectivity and show typical ballistic dynamics ($MSD_z(t) \sim t^2$). Beyond a characteristic time τ_0, the polymer dynamics are affected be the chain connectivity and the MSD exhibits Rouse scaling[42] with $MSD_z(t) \sim t^{1/2}$. In these two regimes, the MSD_z for the bulk and cylindrically-confined polymers are nearly indistinguishable. For these entangled polymers (N = 350), Rouse dynamics are obeyed until τ_e, namely the Rouse relaxation time for polymer chains within one entanglement strand, beyond which entanglements are expected to further decrease the scaling of $MSD_z(t)$ with t.[31-32] In this regime ($t > \tau_e$), Figure 7.2(a) shows that the dynamics of cylindrically-confined polymers become enhanced relative to the bulk polymers, suggesting that entanglements exhibit a reduced role in the mobility of the confined system. At longer time scale, center of mass diffusion for the whole polymer chain can be observed ($MSD_z(t) \sim t$) in both bulk and cylindrically-confined systems. These observations agree with what we presented in Chapter 6 demonstrating that polymer entanglement density decreases under strong cylindrical confinement.[30]

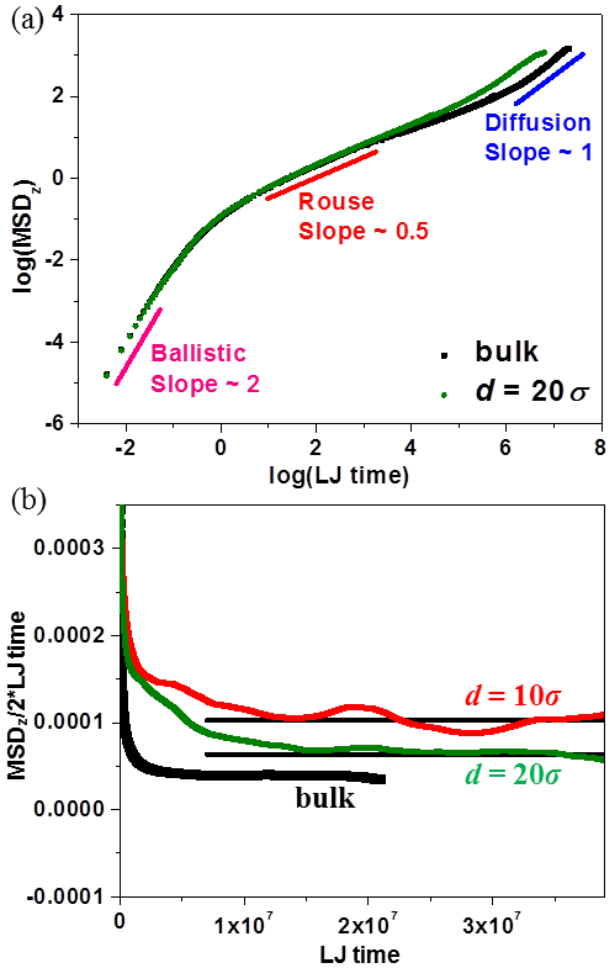

Figure 7.2. (a) Log(MSD_z) as a function of log(LJ time) obtained from MD simulations for bulk polymer and polymers under cylindrical confinement of diameter 20σ. From short time scale to long time scale, ballistic dynamics, Rouse dynamics, and the diffusive regime are observed. (b) $MSD_z/2t$ for bulk and cylindrically-confined polymers as a function of LJ time. A time-independent region is observed and diffusion coefficients are obtained from the average value across this diffusive regime.

We extract the diffusion coefficients from our $MSD_z(t)$ data by plotting $MSD_z(t)/2t$ vs. t, as shown in Figure 7.2(b). In the diffusive regime where $MSD_z(t) \sim t$,

$MSD_z(t)/2t$ becomes time-independent and the average value of this region represents the center-of-mass diffusion coefficient ($D_{MSD,z}$). Two cylinder diameters are shown in Figure 7.2(b) (10σ and 20σ) and the diffusion coefficient is larger for the smaller diameter. This finding indicates that cylindrical confinement enhances polymer mobility along the cylinder axis. These and additional values of $D_{MSD,z}$ will be discussed in more detail below.

7.4.2. Monomer Density and MSD vs. the Distance from the Confinement Wall

To further understand the effect of confinement on the local structure and dynamics of polymer chains, monomer density and MSD were calculated as a function of distance from the wall (r). Figure 7.3(a) plots the monomer density as a function of r for polymers confined inside pores with $d = 10\sigma$, 20σ, and 40σ. The monomer density fluctuates close to the wall (interfacial region), and the degree of fluctuation is independent of the diameter of the cylinder. Away from the wall, the density fluctuations attenuate and a uniform density is observed at $r > 4\sigma$. The density in the center of the cylinder depends on the degree of confinement; for smaller δ (stronger confinement), we observe a lower density in the center of the cylinder.

MSDs calculated over a short time scale in the *x*- and *z*-directions are plotted as a function of radial position *r* in Figure 7.3(b). We take as the short time scale the time for a monomer to move approximately its own size, which corresponds to $t = 4.8$; we interpret this time scale as an approximate measure of the shortest Rouse relaxation time (τ_0). As shown in Figure 7.3(b), the dynamics of monomers in the interfacial region on this time scale are suppressed, and the degree of suppression depends on δ (d/R_{ee}). Anisotropy of local dynamics is also observed, where the relaxation along the axis of the cylinder (*z*) is faster than in the confined directions (*x*). The monomer motion along the *x* direction close to the wall is directly hindered by the immobile confinement. Away from the wall, the MSD for monomers increases in both the *x*- and *z*-directions and becomes isotropic for $d = 20\sigma$ and 40σ. However, for $d = 10\sigma$, the smaller diameter prevents the dynamics from becoming completely isotropic in the center of the cylinder. By comparing the length scales associated with the density oscillations and the anisotropic short-time dynamics, we also observe that the effects of the wall on the local dynamics persist over longer length scales than the density oscillations. This is consistent with prior observations in free-standing thin films.[43]

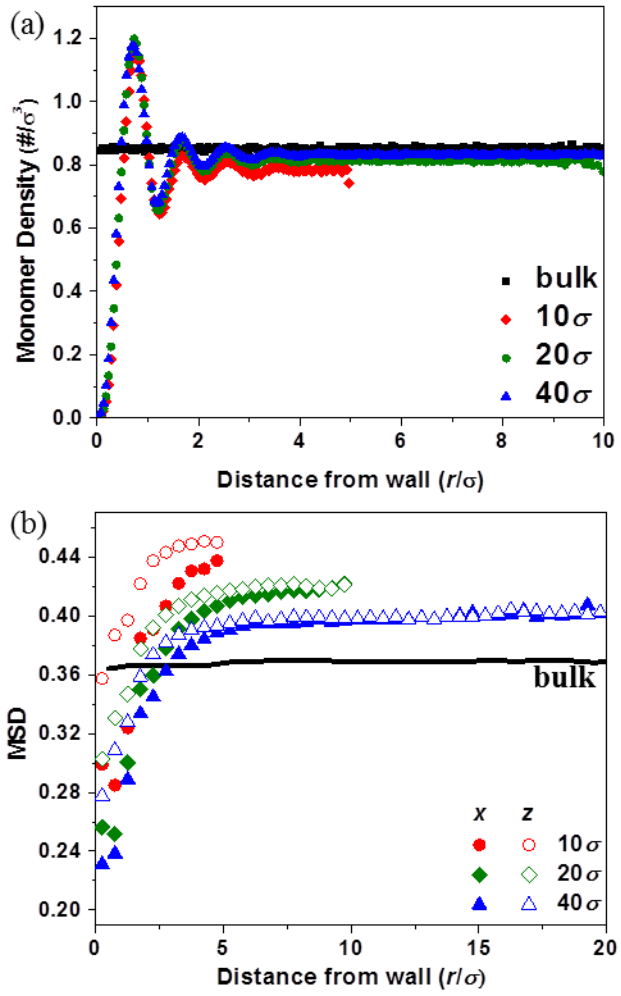

Figure 7.3. (a) Monomer density for confined polymers versus the distance from wall for d = 10σ, 20σ, and 40σ. (b) Short-time MSDs (LJ time = 4.8) along the z axis (open symbols) and the x axis (filled symbols) are plotted as a function of the distance from the wall for d = 10σ, 20σ, and 40σ. Note that the scale for the distance from wall (r/σ) is larger in part b.

Figure 7.3(b) shows that the short-time MSDs in the core region for the cylindrically-confined polymers is greater than that for bulk polymers, while the monomer density in the center of the cylinders in Figure 7.3(a) is lower. The decrease in

the density in the center is the result of fixing the *total* segment density in the cylinder. Thus, the higher than average density near the wall depletes the polymer density at center of the cylinder. To determine how this depleted density affects the short-time dynamics in the center of the cylinder, we scaled the size of the simulation box in the *z*-direction such that the equilibrium monomer density in the core region is closer to the bulk density. After adjusting the density, the MSD for cylindrically-confined polymers in the core region is comparable to the MSD for bulk polymers (Appendix H, Figure H.1), which confirms that the higher MSD in the core region in Figure 7.3(b) is induced by the lower equilibrium monomer density. Local dynamics are affected by both the direct hindrance of the confinement wall and the change of local polymer packing, such that anisotropic local dynamics are observed near the wall and faster dynamics are found in the core region. Retarded local dynamics in the interfacial region have also been observed experimentally.[4-5, 9-10] The differences of MSD in Figure 7.3(b) due to the density differences are very small compared to the range of MSD shown in Figure 7.2(a), and we do not expect these minor differences to have an appreciable effect on the calculated diffusion coefficients.

Furthermore, it is interesting to investigate if this change in local packing and

dynamics depends on the chain length. The monomer density and MSD (LJ time = 4.8) versus r/σ for N = 50 and 350 cylindrically confined to diameters of 10σ and 20σ are shown in Appendix H (Figure H.2). The monomer densities and MSDs are independent of the chain length and the widths of the interfacial regions defined by either the density fluctuations or anisotropic local dynamics are independent on the chain length.

7.4.3. Self-Intermediate Structure Factor $F_s(Q, t)$

The intermediate structure factor $F_s(Q, t)$ is the spatial Fourier transform of the self-part of the Van Hove correlation function, $G_s(\boldsymbol{r}, t)$.[3, 44] The intermediate structure factor is often used for investigating the structural relaxation of materials, which can be directly measured from neutron spin echo (NSE) experiments[4-5, 8] or obtained from the Fourier transforms of the intermediate scattering functions, $S(Q, \omega)$,[3] which are measured by quasi-elastic neutron experiments. The intermediate structure factor $F_s(Q, t)$ from simulations can be expressed as

$$F_s(Q,t) = \int G_s(\boldsymbol{r},t)e^{-\boldsymbol{Q}\cdot\boldsymbol{r}}d\boldsymbol{r} = \frac{1}{N}\sum_{1}^{N}\langle exp[-i\boldsymbol{Q}\cdot\{\boldsymbol{r}_i(t)-\boldsymbol{r}_i(0)\}]\rangle \quad (7.5)$$

where N is the total number of monomers. Three Q values, $0.1\sigma^{-1}$, $0.5\sigma^{-1}$, and $2\sigma^{-1}$, were analyzed to investigate the relaxation behavior of monomers under cylindrical confinement at three length scales ($2\pi/Q \sim 62.8\sigma$, 12.6σ, and 3.1σ). To investigate the anisotropy of the polymer relaxations, wave vectors both perpendicular (x) and parallel (z) to the cylindrical confinement were used to calculate $F_s(Q, t)$. Figure 7.4 plots intermediate structure factor as a function of $\log(t)$ along the x and z axes for three Q values. For large Q values, where small length scales are probed, the relaxation along the x axis is retarded, and this effect is more pronounced for smaller cylinders (Figure 7.4(a)). The relaxation along the z-axis is not affected or only slightly enhanced by the cylindrical confinements for large values of Q_z (Figure 7.4(d)). When Q is chosen so as to probe length scales larger than the size of the cylinder, a plateau induced by the direct confinement from the immobile wall is observed for $F_s(Q_x, t)$ (Figures 7.4(b) and 7.4(c)). In contrast, Figures 7.4(e) and 7.4(f) clearly show that relaxations along the z axis are enhanced relative to the bulk, and the difference grows appreciably as Q_z is decreased. For $Q_z = 0.1\sigma^{-1}$, the associated length scale is larger than R_{ee} for our simulated polymers, and this faster relaxation along z when cylindrically confined is consistent with the apparent faster diffusion shown above in Figure 7.2 (b).

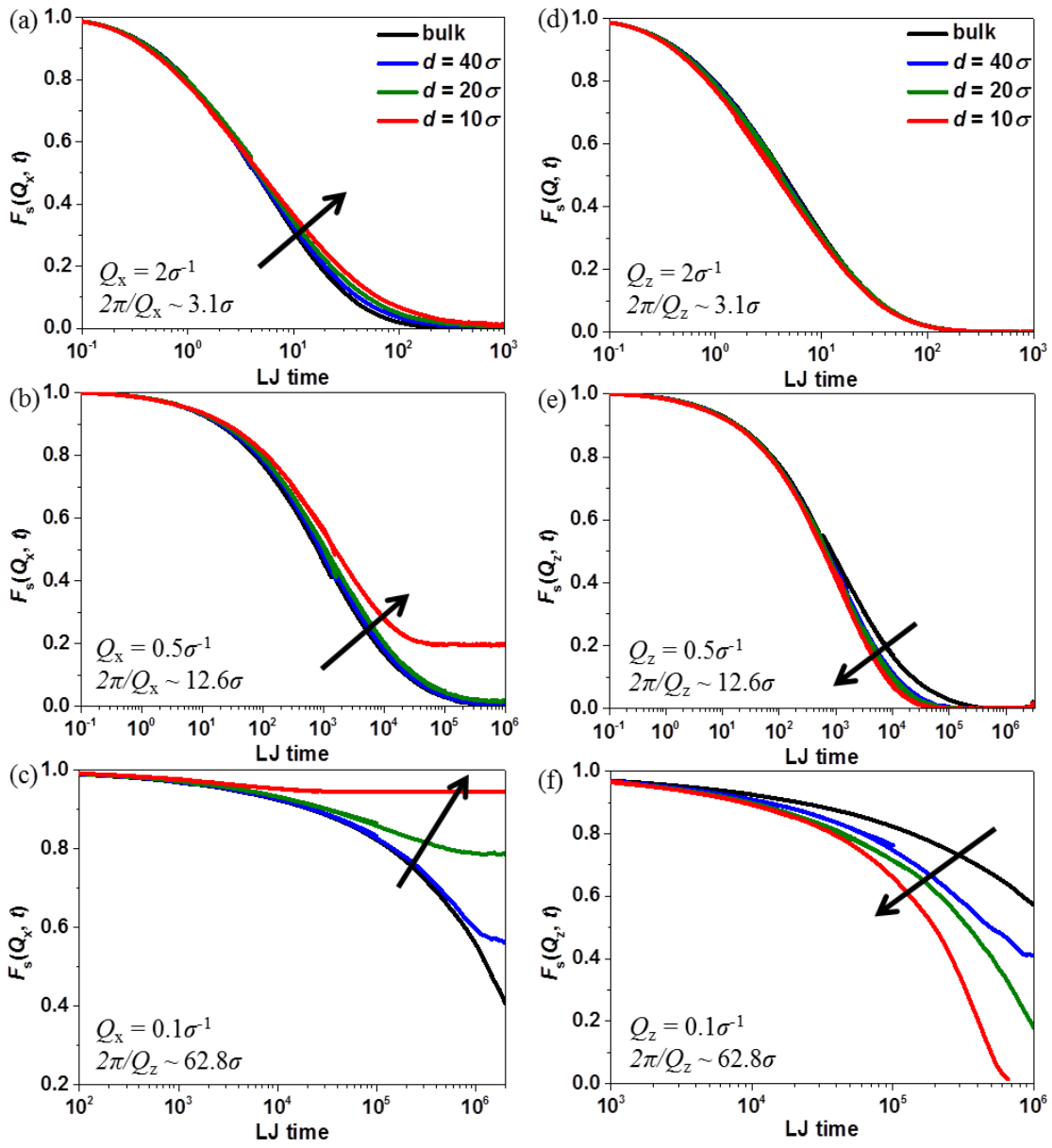

Figure 7.4. Self-intermediate structure factor $F_s(Q, t)$ for cylindrically-confined polymers ($N = 350$, $R_{ee} \sim 22.7\sigma$) along the x axis for $Q_x = 2\sigma^{-1}$ (a), $0.5\sigma^{-1}$ (b), and $0.1\sigma^{-1}$ (c) and along the z axis for $Q_z = 2\sigma^{-1}$ (d), $0.5\sigma^{-1}$ (e), and $0.1\sigma^{-1}$ (f). Arrows show the effect of increasing cylindrical confinement (smaller d) on $F_s(Q, t)$.

As noted previously, an important goal of this work is to combine the effect of confinement on chain size, local relaxation time, and entanglement density into predictions of diffusion coefficients using the reptation model. To obtain the change in local relaxation time, $F(Q = 2\sigma^{-1}, t)$ for bulk and cylindrically-confined polymers are fit to an empirical stretched exponential[45] (also called Kohlrausch-Williams-Watts, KWW, function):

$$F(Q,t) = \exp\left(-\left[\frac{t}{\tau(Q,T)}\right]^{\beta}\right) \tag{7.6}$$

where $\tau(Q, T)$ is the relaxation time and depends on Q and temperature, and β is a stretching parameter between 0 and 1. We fit $F_s(Q_z, t)$ at $Q = 2\sigma^{-1}$, which corresponds to a length scale of approximately 3 monomers where Rouse dynamics are expected to apply. We fit the portion of the relaxation function for time scales of 10 LJ time and longer, which correspond to the time scales for terminal decay of $F_s(Q_z, t)$ on this length scale. Figure 7.5(a) shows example fits to Equation 7.6 for bulk polymers and polymers confined in 10σ nanopores. Fitting results for β are 0.42 to 0.53 in the x direction and 0.51 to 0.53 in the z direction, which are close to previously reported values.[46-47] Figure 7.5(b) plots the normalized relaxation time (relaxation time for confined polymers divided by that for bulk polymers) along the x- and z-directions as a function of the

diameter of the confinement (d). The relaxation time perpendicular to the cylindrical axis (x) increases when d decreases due to the direct suppression of local dynamics from the immobile wall and the increase in local packing. Along the cylindrical axis (y), the local dynamics are slightly enhanced which is likely due to the change of the local packing as discussed in Section 7.4.2. The relaxation time along the z axis will be used in the next section for predicting diffusion coefficients using the reptation model.

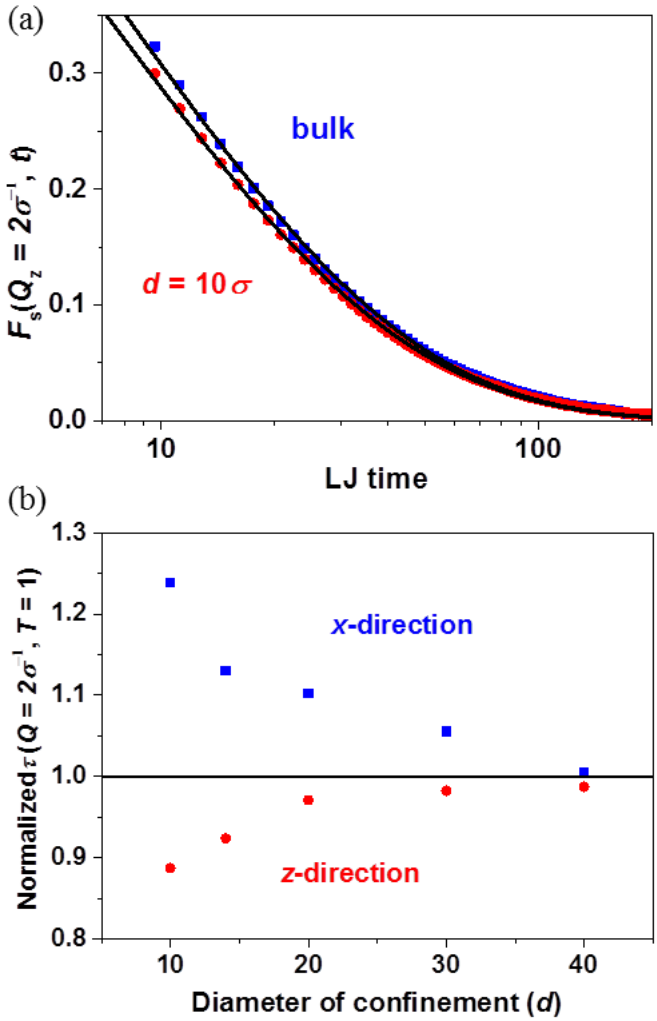

Figure 7.5. (a) Example fitting of $F_s(Q_z, t)$ for bulk polymers and cylindrically-confined polymers ($d = 10\sigma$) by Equation 7.6. (b) Normalized relaxation times from $F_s(Q, t)$ fits are plotted as a function of the diameter of confinement for monomers moving along the *x* and *z* directions.

7.4.4. Polymer Diffusion

Polymer diffusion coefficients were obtained from both simulations and experiments, and further we extract the diffusion coefficients from the simulations using

two approaches. In the first approach, we apply the reptation model to parameters extracted from the simulations and denote this diffusion coefficient as $D_{rep,z}$. Following Equation 7.2, the diffusion coefficient along the *z* direction scales linearly with the square of the chain size in the *z* direction (R_z^2) and the number of monomers in one entanglement strand (N_e) and scales inversely with the local relaxation time in the *z*-direction (τ_z). Figure 7.6 displays the normalized values for these three parameters (R_z^2, N_e, $1/\tau_z$) along with the normalized $D_{rep,z}$, where the values under confinement are normalized the bulk values. (Note that the values for R_z^2 and N_e were adopted from Chapter 6.[30]) Normalized $D_{rep,z}$ increases as the pore diameter decreases. This faster diffusion along the cylindrical pore mainly stems from a reduction in the entanglement molecular weight as the pore size decreases relative to chain size, particularly under strong confinement.

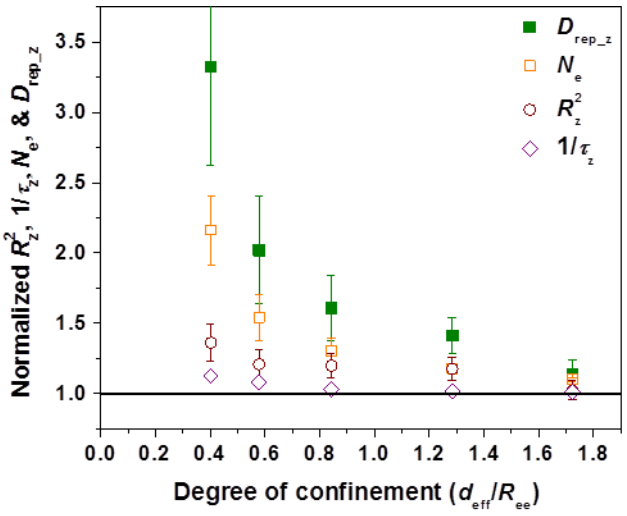

Figure 7.6. Normalized parameters R_z^2, N_e, and $1/\tau_z$ from the simulations are combined to predict the normalized $D_{rep,z}$ using the reptation model (Equation 7.2).

The second diffusion coefficient from simulations was determined by averaging the time-independent region of the $MSD_z/2t$ versus t plot shown in Figure 7.2(b) and is denoted $D_{MSD,z}$. Figure 7.7 shows $D_{MSD,z}$ normalized by $D_{MSD,z}$ from the bulk simulations as a function of degree of confinement (d_{eff}/R_{ee}). Thirdly, tracer diffusion coefficients for dPS diffusing into PS-infiltrated AAO nanopores were obtained experimentally using ERD. The tracer diffusion coefficients (D_{exp}) for 400kg/mol dPS diffusing in PS filled pores with diameters of 18, 35, 55 and 80 nm are normalized by the tracer diffusion coefficients of 400kg/mol dPS diffusing into a 200kg/mol PS matrix. Normalized D_{exp} is plotted together with the normalized $D_{rep,z}$ and normalized $D_{MSD,z}$ as a function of the

confinement parameter d_{eff}/R_{ee} for simulations and d/R_{ee} for experiments in Figure 7.7.

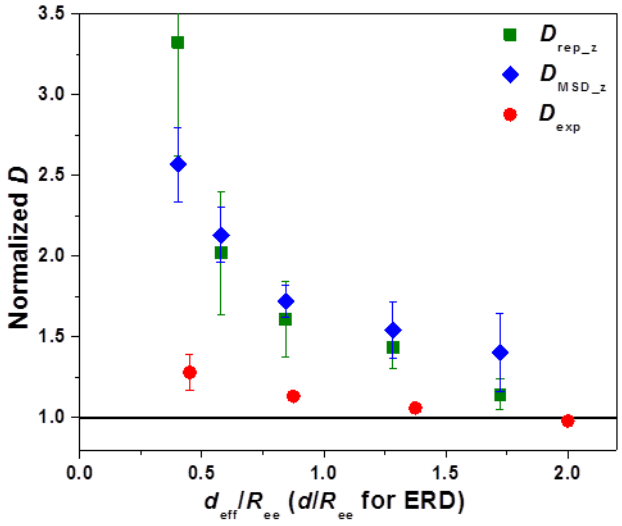

Figure 7.7. Normalized $D_{rep,z}$ from Figure 7.6(b) and $D_{MSD,z}$ obtained by averaging the long time values in Figure 7.2(b) are plotted together as a function of d_{eff}/R_{ee}. The tracer diffusion coefficients D_{exp} for 400kg/mol dPS diffusing into AAO nanopores pre-infiltrated with 200kg/mol PS with a range of pore diameters is normalized by the homopolymer diffusion and plotted as a function of d/R_{ee}.

All three normalized diffusion coefficients increase with decreasing pore size, which is increasing cylindrical confinement. When $d_{eff}/R_{ee} > 0.5$, the normalized $D_{rep,z}$ and normalized $D_{MSD,z}$ are comparable. At the highest level of confinement ($d_{eff}/R_{ee} \leq 0.5$), the normalized $D_{rep,z}$ predicted from the reptation model is ~ 40% greater than $D_{MSD,z}$. For this highly confined system with $d = 10\sigma$, the average N_e is ~ 104, obtained by $350/\langle Z \rangle$.[30] N_e ~ 104 corresponds to a tube diameter of ~12.6σ, calculated by $\sqrt{104/350} \times 22.7\sigma$

(R_{ee} for N = 350). The tube diameter in the reptation model defines the scale of the allowed transverse fluctuations of the polymer from its primitive path, and in this example the calculated tube diameter is even larger than the diameter of the confining cylinder. Clearly the reptation model should breakdown in strongly confined systems, wherein the confining walls as well as entanglements limit transverse fluctuations. The discrepancy between $D_{MSD,z}$ and $D_{rep,z}$ when $d = 10\sigma$ supports this expectation.

Figure 7.7 reports the first experimental results of polymer center of mass diffusion under cylindrical confinement. The 25% increase for $d = 10\sigma$ ($d/R_{ee} \sim 0.5$) is significant, although weaker than the simulated $D_{rep,z}$ and $D_{MSD,z}$ values. A variety of factors might contribute to the quantitative discrepancy between the normalized diffusion coefficients from experiments and simulation. The simulations use neutral, purely repulsive interactions between the polymers and the cylinder walls; although the interaction between polystyrene and aluminum oxide is expected to be weak, even a weak attraction could slow diffusion. Further, the cylindrical confinement constructed for the simulations is quite uniform in diameter, while the anodized aluminum oxide membranes contain a distribution of pore diameters and a small fraction of the pores are tapered and branched, which would also contribute to slower diffusion coefficients in the experiments.

Finally, our coarse-grained model omits the chemical structure of polymer chains, which might be important particularly under severe confinement. The relative importance of these various factors on the differences observed between D_{exp} and $D_{MSD,z}$ will be explored in future studies.

7.5. SUMMARY

We compare polymer diffusion coefficients within cylindrical nanopores from MD simulations and experiments, and the simulations also provide information about local packing and dynamics under cylindrical confinement. In the simulations, entangled polymers (N = 350) were confined in cylindrical, amorphous pores and a range of diameters (d/σ = 10 - 40) to provide degrees of confinement ($\delta = d_{eff}/R_{ee}$) from 0.40 to 1.72. The local dynamics as evaluated by self-intermediate structure factors become anisotropic under cylindrical confinement. The diffusion coefficient was determined by combining R_z^2, N_e, and $1/\tau_z$ from the simulations according to the reptation model ($D_{rep,z}$) or directly from the mean squared displacement along the cylindrical axis ($D_{MSD,z}$). Experimentally, membranes with cylindrical nanopores of various diameters were infiltrated with polystyrene and deuterated polystyrene was subsequently diffused into to these pores; different membranes were used to give degrees of confinement ($\delta = d/R_{ee}$) of

0.45 to 2. Elastic recoil detection measured the dPS concentration profile to which Fick's second law was fit to extract the tracer diffusion coefficient (D_{exp}).

Independent of the method of determining the diffusion coefficient, there is an unequivocal increase of the diffusion coefficient along the cylinder as confinement increases. From simulations, the normalized diffusion coefficients increase from about 15% to more than 200% across the range of confinement investigated. Further, $D_{MSD,z}$ and $D_{rep,z}$ are in good agreement except at the most severe confinement where the tube diameter in the reptation model becomes comparable to the diameter of the confining cylinder. The trend of faster diffusion with cylindrical confinement is weaker in the experimental results where the maximum increase is just ~25%. The lower values of normalized D_{exp} relative to normalized $D_{MSD,z}$ and normalized $D_{rep,z}$ might be attributed to a variety of factors including imperfections in the cylindrical nanopores in the AAO membranes and interactions between the AAO and the polymer.

This chapter reports that diffusion rates increase along cylindrical nanopores relative to polymer diffusion in the bulk. To generalize, diffusion increases in the direction parallel to impenetrable walls separated by lengths comparable to the size of the polymer chain, namely nanoconfinement. Faster polymer diffusion along cylindrical

confinement was found in both course-grain simulations involving idealized pores and experiments involving imperfect pores. From the simulations, we found that cylindrical nanoconfinement expands the chains conformation in the directions parallel to the confining surface while strongly compressing the chains normal to the confining surface, leading to a decrease in the extent of entanglement and slower local dynamics. According to the reptation model, these three attributes combine to increase in the diffusion coefficient, although under severe confinement where the tube diameter becomes comparable to the confining length scale an alternative method is needed to predict the diffusion coefficient. This work suggests that polymers confined to thin layers between impenetrable walls will have faster lateral diffusion relative to bulk diffusion.

7.6. REFERENCES

1. Peng, H.; Nieuwendaal, R.; Soles, C. L., Polymer Dynamics in Constrained Geometries. In *Polymer Science: A Comprehensive Reference*, Moeller, M.; Matyjaszewski, K., Eds. Elsevier B. V. : Amsterdam, 2012; Vol. 7, pp 345-376.

2. Shin, K.; Obukhov, S.; Chen, J. T.; Huh, J.; Hwang, Y.; Mok, S.; Dobriyal, P.; Thiyagarajan, P.; Russell, T. P., *Nat. Mater.* 2007, *6* (12), 961-965.

3. Krutyeva, M.; Martin, J.; Arbe, A.; Colmenero, J.; Mijangos, C.; Schneider, G. J.; Unruh, T.; Su, Y. X.; Richter, D., *J. Chem. Phys.* 2009, *131* (17).

4. Kusmin, A.; Gruener, S.; Henschel, A.; de Souza, N.; Allgaier, J.; Richter, D.; Huber, P., *Macromolecules* 2010, *43* (19), 8162-8169.

5. Kusmin, A.; Gruener, S.; Henschel, A.; Holderer, O.; Allgaier, J.; Richter, D.; Huber, P., *J. Phys. Chem. Lett.* 2010, *1* (20), 3116-3121.

6. Lagrene, K.; Zanotti, J. M.; Daoud, M.; Farago, B.; Judeinstein, P., *Eur. Phys. J.-Spec. Top.* 2010, *189* (1), 231-237.

7. Lagrene, K.; Zanotti, J. M.; Daoud, M.; Farago, B.; Judeinstein, P., *Phys. Rev. E* 2010, *81* (6).

8. Martin, J.; Krutyeva, M.; Monkenbusch, M.; Arbe, A.; Allgaier, J.; Radulescu, A.; Falus, P.; Maiz, J.; Mijangos, C.; Colmenero, J.; Richter, D., *Phys. Rev. Lett.* 2010, *104* (19).

9. Ok, S.; Steinhart, M.; Serbescu, A.; Franz, C.; Chavez, F. V.; Saalwachter, K., *Macromolecules* 2010, *43* (10), 4429-4434.

10. Hofmann, M.; Herrmann, A.; Ok, S.; Franz, C.; Kruk, D.; Saalwachter, K.; Steinhart, M.; Rossler, E. A., *Macromolecules* 2011, *44* (11), 4017-4021.

11. Krutyeva, M.; Wischnewski, A.; Monkenbusch, M.; Willner, L.; Maiz, J.; Mijangos, C.; Arbe, A.; Colmenero, J.; Radulescu, A.; Holderer, O.; Ohl, M.; Richter, D., *Phys. Rev. Lett.* 2013, *110* (10).

12. Noirez, L.; Stillings, C.; Bardeau, J. F.; Steinhart, M.; Schlitt, S.; Wendorff, J. H.; Pepy, G., *Macromolecules* 2013, *46* (12), 4932-4936.

13. Shavit, A.; Riggleman, R. A., *J. Phys. Chem. B* 2014, *118* (30), 9096-9103.

14. Schonhals, A.; Goering, H.; Schick, C., *J. Non-Cryst. Solids* 2002, *305* (1-3), 140-149.

15. Kremer, F.; Schonhals, A., *Broadband Dielectric Spectroscopy*. Springer: Berlin, Germany, 2003.

16. Schonhals, A.; Goering, H.; Schick, C.; Frick, B.; Zorn, R., *J. Non-Cryst. Solids* 2005, *351* (33-36), 2668-2677.

17. Schonhals, A.; Goering, H.; Schick, C.; Frick, B.; Mayorova, M.; Zorn, R., *Eur. Phys. J.-Spec. Top.* 2007, *141*, 255-259.

18. Schonhals, A.; Goering, H.; Schick, C.; Frick, B.; Zorn, R., *Colloid Polym. Sci.* 2004, *282* (8), 882-891.

19. Karatrantos, A.; Composto, R. J.; Winey, K. I.; Clarke, N., *Macromolecules* 2011, *44* (24), 9830-9838.

20. Karatrantos, A.; Composto, R. J.; Winey, K. I.; Kroger, M.; Clarke, N., *Macromolecules* 2012, *45* (17), 7274-7281.

21. Li, Y.; Kroger, M.; Liu, W. K., *Phys. Rev. Lett.* 2012, *109* (11).

22. Karatrantos, A.; Clarke, N.; Composto, R. J.; Winey, K. I., *Soft Matter* 2013, *9* (14), 3877-3884.

23. Brown, D.; Mele, P.; Marceau, S.; Alberola, N. D., *Macromolecules* 2003, *36* (4), 1395-1406.

24. Desai, T.; Keblinski, P.; Kumar, S. K., *J. Chem. Phys.* 2005, *122* (13).

25. Cavallo, A.; Müller, M.; Binder, K., *J. Phys. Chem. B* 2005, *109* (14), 6544-6552.

26. Cavallo, A.; Müller, M.; Wittmer, J. P.; Johner, A.; Binder, K., *J. Phys.-Condes. Matter* 2005, *17* (20), S1697-S1709.

27. Meyer, H.; Kreer, T.; Cavallo, A.; Wittmer, J. P.; Baschnagel, J., *Eur. Phys. J.-Spec. Top.* 2007, *141*, 167-172.

28. Vladkov, M.; Barrat, J. L., *Macromolecules* 2007, *40* (10), 3797-3804.

29. Li, Y. J.; Wei, D. S.; Han, C. C.; Liao, Q., *J. Chem. Phys.* 2007, *126* (20).

30. Sussman, D. M.; Tung, W. S.; Winey, K. I.; Schweizer, K. S.; Riggleman, R. A., *Macromolecules* 2014, *47* (18), 6462-6472.

31. Degennes, P. G., *J. Chem. Phys.* 1971, *55* (2), 572-&.

32. Doi, M.; Edwards, S. F., *Journal of the Chemical Society-Faraday Transactions Ii* 1978, *74*, 1789-1801.

33. Green, P. F.; Mills, P. J.; Kramer, E. J., *Polymer* 1986, *27* (7), 1063-1066.

34. Zhang, M. F.; Dobriyal, P.; Chen, J. T.; Russell, T. P.; Olmo, J.; Merry, A., *Nano Lett.* 2006, *6* (5), 1075-1079.

35. Kim, E.; Xia, Y. N.; Whitesides, G. M., *Nature* 1995, *376* (6541), 581-584.

36. Rubinstein, M.; Colby, R. H., *Polymer Physics*. Oxford University Press: New York, 2003.

37. Bates, F. S.; Wignall, G. D., *Phys. Rev. Lett.* 1986, *57* (12), 1429-1432.

38. Composto, R. J.; Walters, R. M.; Genzer, J., *Mater. Sci. Eng. R-Rep.* 2002, *38* (3-4), 107-180.

39. Gam, S.; Meth, J. S.; Zane, S. G.; Chi, C. Z.; Wood, B. A.; Seitz, M. E.; Winey, K. I.; Clarke, N.; Composto, R. J., *Macromolecules* 2011, *44* (9), 3494-3501.

40. Mu, M. F.; Clarke, N.; Composto, R. J.; Winey, K. I., *Macromolecules* 2009, *42* (18), 7091-7097.

41. Mu, M. F.; Composto, R. J.; Clarke, N.; Winey, K. I., *Macromolecules* 2009, *42* (21), 8365-8369.

42. Rouse, P. E., *J. Chem. Phys.* 1953, *21* (7), 1272-1280.

43. Shavit, A.; Riggleman, R. A., *Macromolecules* 2013, *46* (12), 5044-5052.

44. Ryong-Joon, R., *Methods of X-ray and Neutron Scattering in Polymer Science*. Oxford University Press: New York, 2000.

45. Williams, G.; Watts, D. C., *Transactions of the Faraday Society* 1970, *66* (565P), 80-&.

46. Colmenero, J.; Alegria, A.; Arbe, A.; Frick, B., *Phys. Rev. Lett.* 1992, *69* (3), 478-481.

47. Richter, D.; Monkenbusch, M.; Arbe, A.; Colmenero, J., Neutron Spin Echo in Polymer Systems. In *Neutron Spin Echo in Polymer Systems*, Springer-Verlag Berlin: Berlin, 2005; Vol. 174, pp 1-221.

Chapter 8

Local Dynamics of Polystyrene Confined in AAO Nanopores Probed by Quasi-Elastic Neutron Scattering

This work was accomplished in collaboration with Dr. Madhusudan Tyagi at National institute of Standards and Technology, Center for Neutron Research, Gaithersburg. The contents of this chapter have been in preparation for submitting to *Macromolecules*, in a modified version.

8.1. INTRODUCTION

In this chapter, we focus on the local dynamics of PS confined in Anodized aluminum oxide (AAO) membranes with the degree of confinement, defined as nanopore diameter (d)/polymer end-to-end distance (R_{ee}), ranging from 0.6 to 2.6. Anodized aluminum oxide membranes have been widely used to study polymer structure and dynamics under cylindrical nano-confinedments because they provide well defined cylindrical nanopores with consistent pore diameters across the whole membrane. Small angle neutron scattering (SANS) has been used to study the structure and found no significant change for polymer chain conformation when d/R_{ee} as small as 0.25.[1-2]

Polymer dynamics are often probed by nuclear magnetic resonance (NMR) and quasi-elastic neutron scattering (QENS). Using field cycling (FC) NMR (time scale ~ 1ns to 100μs), Kimmich, Fatkulline, and co-workers reported confinement effects for confinement sizes range from 5 to 1000nm which is much larger than the radius of gyration (R_g) of a single polymer chain, and it was called "corset effect".[3-5] Ok *et al*. applied double-quantum (DQ) NMR to investigate highly entangled polybutadiene (PB) confined in AAO membranes with the degree of confinement (d/R_{ee}) ~ 0.74 and 2.2. They reported a ~ 3nm surface layer around the neutral confinement wall, where anisotropic chain motions at time scale beyond entanglement time were identified.[6] A following study of PB confined in AAO using FCNMR was performed by Hofmann *et al*., and they found a slowdown of the collective polymer dynamics (Rouse regime) under confinement.[7] However, the corset effect was not identified.

Quasi-elastic neutron scattering which covers ~ 10fs to 100ns time scale and ~ 1Å to 700Å length scale is another common technique for studying polymer dynamics. In these time scale and length scale, polymers can show a range of different kinds of motions. At very short time scale (~ 10fs to 10ps), polymer can exhibit motions like vibrations, side group rotations, and some local conformational transition. At longer time

scale (~10ps to 1ns), segmental motions which is also assigned (α-relaxation) can be observed. For time scale ~ 1ns to 100ns, Rouse dynamics starts to show up and for entangled systems, reptation motion may be observed. Chissopoulou *et al*. used high-resolution neutron backscattering (time scale ~ 10ps to 1ns) to study the rotation motion and segmental motion of Poly(methyl phenyl siloxane) confined in ~1-2nm layered organosilicate.[8] They found that the rotation motion is not affected by the confinement, but the segmental motion in confinement is faster than that in bulk. Krutyeva *et al*. combined time of flight spectrometer (time scale ~ 100fs to 10ps) and backscattering spectrometer (time scale ~ 10ps to 1ns) to study Poly(ethylene oxide confined in an anodic aluminum oxide membranes (d/R_{ee} ~2).[9] They claimed no confinement effect was observed for Rouse dynamics, but the effect was observed in shorter length scale where polymer exhibits segmental relaxations. In the paper, the author also questioned the corset effect reported by Kimmich *et al.*[3-5] Kusmin *et al.* used Neutron Spin Echo (NSE) to study unentangled and weakly entangled PEO confined in porous silicon ($d/R_{ee} >> 1$).[10] They found an evidence of a region with reduced dynamics close to the pore wall (bound layer size ~ Flory radius of polymer chains) and a region with bulk-like dynamics in the pore center. These bound layers were also reported in the

author's following work which investigates n-hexatriacontane confined in similar pores.[11] Evidences of confinement effects on the reptation mechanism were firstly reported by Martin *et al*. using NSE to investigate PEO severely confined in AAO membranes (d/R_{ee} ~ 0.43 and 2.6).[12] The author observed a clear slowing down for rouse dynamics for confined polymers comparing to the bulk polymers. An expanded entanglement network (increased tube diameter for reptation model) was also reported which shows that confinement effect can affect the topological structure of polymer chains. Chapter 6 and 7 combining simulation and theory investigated the structure and dynamics of polymers under cylindrical confinement and reported a diluted entanglement network due to this direct geometric effect.[13] Lagrene *et al*. applied NSE on weakly confined PEO in AAOs (d/R_{ee} > 1), and did not find any change in the entanglement networks.[14-15] Recently, Krutyeva *et al*. investigated unentangled polydimethylsiloxane (PDMS) confined in AAO nanopores (d/R_{ee} ~ 3) and proved again the idea of two-phase model. PDMS in the boundary region is anchored at several points to the confinement wall, and PDMS in the center of cylindrical confinement exhibits bulk-like dynamics. An interphase region where anchored PDMS interact with freely moved PDMS through interpenetrating the loop between two anchor points.[16]

So far, most of the polymers confined in cylindrical confinements studied by QENS are PEO and PDMS. Here, we investigate polystyrene (PS) confined in AAO nanopores with a systematic change of the degree of confinement from d/R_{ee} ~ 2.6 to 0.6. High flux back scattering with the time scale ~ 10ps to 1ns and the length scale ~3Å to 30 Å were applied to study the confinement effect on the local dynamics of PS. In this time scale, polymer dynamics was separated into two regimes. In shorter time scale, fast motions like vibrations and side group rotations were probed. In longer time scale, slow motions like segmental motions (α-relaxation) can be observed. To separate these two dynamics, QENS data were fit by a model composed of two Lorentzian functions represents fast and slow motions, respectively. Fitting QENS data based on Lorentzian functions have been shown to provide qualitative interpretations for polymer dynamics.[17-22] We found that the full width half maximum (FWHM) for the Lorentzian function represents the fast motions is not affected by the confinement or it is too fast so that the change is outside of the energy window of HFBS. A non-asymptotic decrease for FWHM of the Lorentzian function represents the slow motions was observed. Elastic incoherent scattering factor (EISF) for PS confined in AAO nanopores is higher than that for bulk, and PS in 80nm nanopores has the highest portion of not moving hydrogen.

Combining the confinement effect on the slow relaxation mode and EISF, the change of mean square displacement (MSD) for confined PS will be discussed.

8.2. EXPERIMENTAL METHODS

8.2.1. Sample Preparation

200kg/mol polystyrene (PS) purchased from Pressure Chemical Co., Pittsburgh, USA, were infiltrated into anodized aluminum oxide (AAO) membranes by a melt annealing method.[1, 23-24] Molecular weight of 180.9 kg/mol and polydispersity of 1.03 for the 200kg/mol PS were measured by size-exclusion chromatography. R_{ee} ~ 28.5nm for 200k PS were calculated based on the Kuhn length of 1.8nm and the molecular weight of Kuhn monomer, 720g/mol.[25] AAO membranes with four different diameters (18nm, 35nm, 55nm, and 80nm are provided by the vender) were purchased from Synkera Technology Inc., CO, USA. The top view and the cross section view of the membranes were characterized by scanning electron microscope, and associated images can be referred to Appendix F. These membranes give us degrees of confinement (d/R_{ee}) ~ 0.6, 1.2, 1.9, and 2.8. A thick polystyrene film (> 100 μm), cut into the shape of the membrane, was put on top of the membrane and pre-anneal on a hot plate so that the thick polystyrene film was attached to the membrane. The bilayer sample was then put on a silicon wafer and annealed

in a vacuum oven at 195°C. Notice that the polymer film is on top of the membrane, instead of at the interface between the membrane and the silicon wafer. After annealing for certain amount of time, the bilayer sample was taken out and the residue polymers on the top surface were removed by a sharp blade. The mass of the membrane was then measured to compare with the mass of the same membrane when it was empty. The success of infiltration can be proved by the mass increasing of the membrane. Moreover, after annealing for long enough time, polystyrene will wet the interface between the membrane and the silicon wafer, then we are sure that polystyrene infiltrated all the way through the nanopores. However, 100% of infiltration of all nanopores is uncertain. Figure 8.1 shows the mass increase of membranes normalized by the porosity of the membranes versus annealing time for membranes with different diameters. Here, the normalized mass increase can also be understood as the infiltration rate. 35nm samples have the highest infiltration rate, and as pore diameter increases (55nm and 80nm samples), the infiltration rate decreases. This phenomenon may be related to the viscosity decrease for polymers under confinement,[1] or it can simply due to higher fraction of dead-end nanopores for larger diameter membranes. 18nm sample does not have even higher infiltration rate than 35nm samples, which may due to an extra enthalpy penalty for polymer chains to get into

the pores because ($d/R_{ee} < 1$).

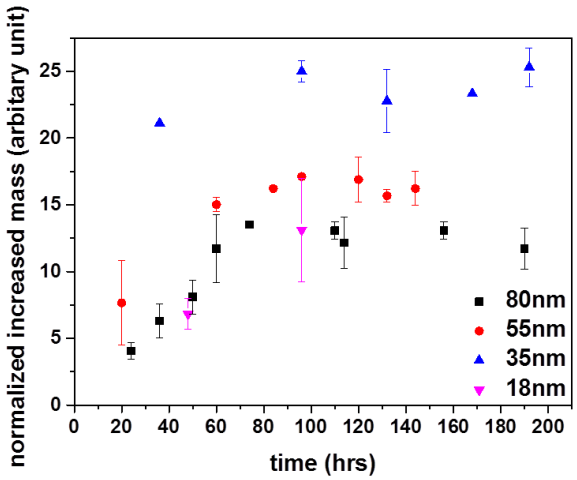

Figure 8.1. Normalized mass of PS infiltrated into AAO membranes as a function of annealing time for different diameter nanopores. Mass is normalized by the porosity of the membranes, obtained from the elastic recoil detection experiments (Appendix G), so that y axis can also be viewed as the infiltration rate.

Percentage of filling can be estimated by dividing the final increased mass of PS by the calculated maximum mass which is possible to be infiltrated into membranes. The maximum mass is simply the shell volume of the membrane times the associated porosity and times the density of polystyrene. Assuming the density of PS is not changed under confinement, the calculated maximum mass and the final increases mass, and the percentage of filling for different pore diameters are shown in Table 8.1. The lower percentage of infiltration may also imply higher fraction of dead-end nanopores.

Table 8.1. Calculated maximum mass of infiltration and the final increases mass for PS, and the percentage of filling for different pore diameter samples

	80nm	55nm	35nm	18nm
Maximum mass of infiltration (mg)	5.44	5.44	4.41	8.97
Final increased mass of PS (mg)	1.3	1.74	2.28	2.4
Percentage of infiltration (%)	24	33	52	27

8.2.2 Quasi-Elastic Neutron Scattering

Bulk PS and AAO membranes infiltrated with PS were measured by the High-Flux Backscattering (HFBS, NG2) at NIST center of neutron research, Gaithersburg, MD, USA.[26] The measurable energy change of neutrons ranges from about -17μeV to +17μeV, with a resolution ~ 0.8μeV, defined by the full-width at half maximum of the peak for elastic scattering. This energy range can be converted to a probing time scale ranges from ~ 40ps to 2ns. QENS data for a vanadium sample measured at 50K is used as a resolution function when analyzing the QENS data for the bulk PS sample. QENS data for 35nm membranes infiltrated with PS measured at 50K is used as a resolution function for analyzing the QENS data for membranes infiltrated with PS. There are sixteen detectors at different angles which gives a range of Q from $0.31 Å^{-1}$ ~ $1.71 Å^{-1}$. Fixed window scans were conducted from 50K to 453K for every sample, and then QENS data were collected at

440K and 455K for 14 hours and 18 hours, respectively.

8.3. THEORETICAL BACKGROUND

Inelastic neutron scattering is measuring the double differential scattering cross section ($d^2\sigma/d\Omega d\omega$), which is describing the probability of scattering of neutrons by materials per unit solid angle per unit energy transfer. The double differential scattering cross section can be further separated into incoherent and coherent scattering shown below

$$\frac{d^2\sigma}{d\Omega \mathrm{d}\omega} = \left(\frac{d^2\sigma}{d\Omega \mathrm{d}\omega}\right)_{inc} + \left(\frac{d^2\sigma}{d\Omega \mathrm{d}\omega}\right)_{coh} \tag{8.1}$$

High flux back scattering is mainly measuring the incoherent inelastic neutron scattering from hydrogens, so the rest of the discussion will focus on $(d^2\sigma/d\Omega d\omega)_{\mathrm{inc}}$. The incoherent scattering cross section can be expressed as

$$\left(\frac{d^2\sigma}{d\Omega \mathrm{d}\omega}\right)_{inc} = \frac{k_1}{k_0}\frac{N b_{inc}^2}{2\pi}\int_{-\infty}^{\infty}\int G_s(\boldsymbol{r}, t) e^{-(\boldsymbol{q}\boldsymbol{r}-\omega t)} d\boldsymbol{r} dt \tag{8.2}$$

where k_0 and k_1 are absolute value of wave vectors for incident and scattered neutrons, respectively. N is the total number of nuclei, b_{inc} is the incoherent scattering lengths of the nuclei, and $\boldsymbol{q}$ is the scattering vector ($\boldsymbol{q} = \boldsymbol{k_1} - \boldsymbol{k_0}$). $G_s(\boldsymbol{r}, t)$ is the self-part of *van Hove correlation function*,[27-28] which describe the probability of the particle, originally was at position 0 at time = 0, will be at position $\boldsymbol{r}$ at time = t. The incoherent scattering cross

section can also be expressed as

$$\left(\frac{d^2\sigma}{d\Omega \mathrm{d}\omega}\right)_{inc} = \frac{k_1}{k_0} N b_{inc}^2 S_s(\boldsymbol{q}, \omega) \tag{8.3}$$

where $S_s(\boldsymbol{q}, \omega)$ is called the self-part of the dynamic structure factor. By comparing Equation 8.2 and Equation 8.3, we can see that $S_s(\boldsymbol{q}, \omega)$ is the Fourier transform of $G_s(\boldsymbol{r}, t)$ with respect to space (***r***) and time (t).

In HFBS experiments, the neutron intensity after correction gives $S_s(\boldsymbol{q}, \omega)$, which is also called the experimental scattering function. The scattering function can be expressed as

$$\begin{aligned} \mathrm{S}(Q, \omega) = \mathrm{DWF}(Q)\big[&\mathrm{EISF}(Q)\delta(\omega) \\ &+ \big(1 - \mathrm{EISF}(Q)\big) S_{quasi}(Q, \omega)\big] \otimes R(\omega) \end{aligned} \tag{8.4}$$

where $\otimes$ represents convolution, DWF(ω) is the Debye-Waller factor, and $R(\omega)$ is a resolution function. This equation basically shows that the self-dynamic structure factor can be separated into two parts. One part of the nuclei (represented by a delta function) is not moving during the time window (energy range of HFBS) and within the probe length scale (corresponding Q) of the measurement, and EISF(Q) represents the elastic incoherent scattering factor, which account for the fraction of these non-moving nuclei. $S_{quasi}(Q, \omega)$ is the associated dynamic structure factor for moving nuclei. For polymer

systems, Lorentzian function that represents a single relaxation mode is one of the simplest functional forms for describing $S_{quasi}(Q, \omega)$. Notice that the Fourier transform of a Lorentzian function in energy space is an exponential decay function in time space. Therefore, the characteristic relaxation time (t_0) for the exponential decay function can be easily calculated from FWHM of the Lorentzian function through $t_0 = (FWHM/2)^{-1}$. Many previous studies used Fourier transform of a stretched exponential function to represent $S_{quasi}(Q, \omega)$ when dealing with polymer systems.[9, 29] In energy space, it is equivalent to fit the quasi-elastic scattering intensity with a summation of multiple Lorentzian functions (multiple relaxation modes).

To simplify the fitting process and to make the discussion of results easier, we decided to fit the data with two Lorentzian functions to extract two relaxation times.[17-18, 20-22, 28, 30] One Lorentzian function represents a slow relaxation mode, and the other captures a fast relaxation mode. In our case, the slow relaxation mode refers to the segmental motions of PS, and the fast relaxation corresponds to the local conformation relaxation and phenyl ring rotation. A Lorentzian function can be expressed as

$$\text{Lorentzian}(\text{FWHM}(Q), \omega) = \frac{1}{\pi} \frac{(FWHM/2)}{(\hbar\omega)^2 + (FWHM/2)^2} \tag{8.5}$$

where FWHM represents full-width at half maximum of a Lorentzian peak. Higher

FWHM means smaller relaxation time, which means faster relaxation dynamics. In this chapter, the total spectrum of incoherent scattering is fit by convolution of a resolution function and the summation of a delta function (elastic scattering) and two Lorentzian functions (slow and fast relaxation modes). All data were reduced and fit using the DAVE software package.[31] We noticed that the FWHM for the fast relaxation mode has a value between 25 μeV~ 35 μeV for 455K data and 15 μeV~ 25 μeV for 440K and is independent of *Q* and the degree of confinement. To decrease the freedom of data fitting, FWHM of the fast mode was fixed at a value ~ 30 μeV for 455K and ~ 20 μeV for 440K obtained from averaging all the fitting results of $FWHM_{fast}$ for all samples at every different *Q* values at the same temperature. This is assuming that the fast relaxation mode is not affected by the nanopore confinement and the probing length scale. Therefore, here, the discussion will focus on the change of the slow relaxation mode due to the different degrees of confinement.

8.4. RESULTS AND DISCUSSION

8.4.1. FWHM for the Slow Relaxation Mode

Quasi-elastic neutron scattering of bulk polystyrene and polystyrene confined in AAO nanopores with four different diameters (18nm, 35nm, 55nm, and 80nm) are

measured at 440K and 455K. The associated scattering intensities are fit by a delta function and two Lowrentzian functions (represents slow and fast relaxation modes) as described in the last section. $FWHM_{fast}$ were fixed at ~ 30 μeV and ~ 20 μeV across all samples at 455K and at 440K, respectively. Figure 8.2(a) shows the fitting results of $FWHM_{slow}$ (segmental motions) as a function of Q^2 for bulk PS and PS confined in 18nm and 55nm nanopores. The time scale and length scale probing here are ~ 100 ps to 1 ns and ~ 4 Å ~ 30 Å, respectively. It is clearly shown that the dynamics are slowing down due the confinement. However, the dynamics for PS confined in 35nm, 55nm, and 80nm nanopores are almost the same (Figure 8.2(b)).

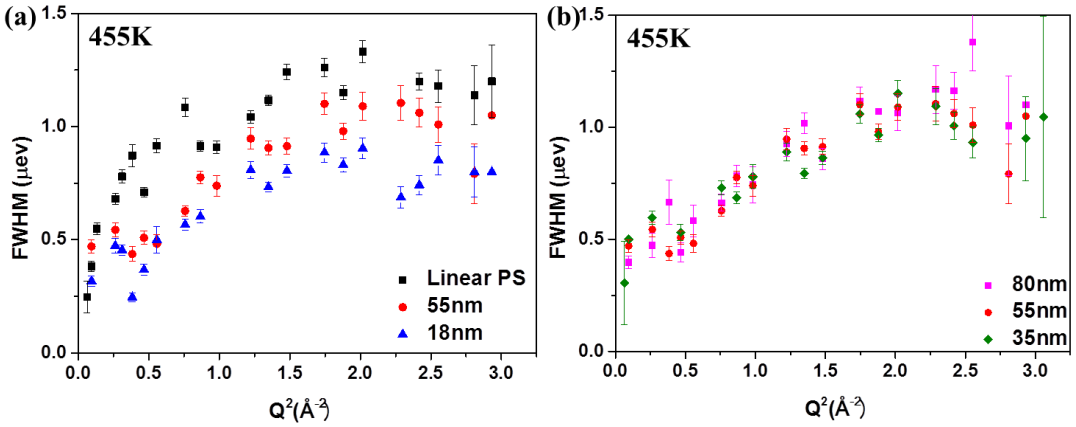

Figure 8.2. (a) fitting results of FWHM for the slow relaxation mode as a function of Q^2 for linear PS and PS confined in 55nm and 18nm nanopores. (b) Fitting results of FWHM for the slow relaxation mode as a function of Q^2 for PS confined in 35nm, 55nm, and 80nm nanopores.

Notice that for 35nm, 55nm, and 80nm nanopores, the degree of confinement (d/R_{ee}) is > 1. This non asymptotic slowing down implies that when polymers are firstly confined into a cylindrical confinement, the dynamics slows down, but the level of slowing down does not depends on the diameter when the diameter is still greater than the size of polymer chains at its equilibrium states. Only when the diameter is smaller than the equilibrate chain size, the dynamics is further retarded.

The shape of the FWHM vs Q^2 curve shows a typical jump diffusion behavior.[22, 28, 32] At low Q region (probing at large length scale), hydrogens are moving like continuous translational diffusion (Fick's Law) where FWHM ~ DQ^2. D represents the diffusion coefficients of the translational diffusion. At high Q region (probing at small length scale), detailed mechanisms of diffusion is revealed, where the continuous diffusion is composed of infinitely small and elementary jumps. FWHM starts deviating from the DQ^2 dependence. Jump diffusion can be understood as a hydrogen vibrating at its original position for certain time (waiting time τ) and jump to the next position in a negligible jump time.[28] Detailed derivation will not be discussed here. Singwei and Sjölander showed that for jump diffusion[33]

$$FWHM(Q)/2 = \frac{DQ^2}{1 + DQ\tau} \tag{8.6}$$

which will retrieve the DQ^2 dependence at small Q limit. We used Equation 8.6 to fit the FWHM vs Q^2 data for linear PS which shows a typical jump diffusion behavior (Figure 8.3(a)). Diffusion coefficients of ~ 2.5nm^2/ns for segmental motions and ~ 1.46 ns waiting time for bulk PS can be extracted from the fitting.

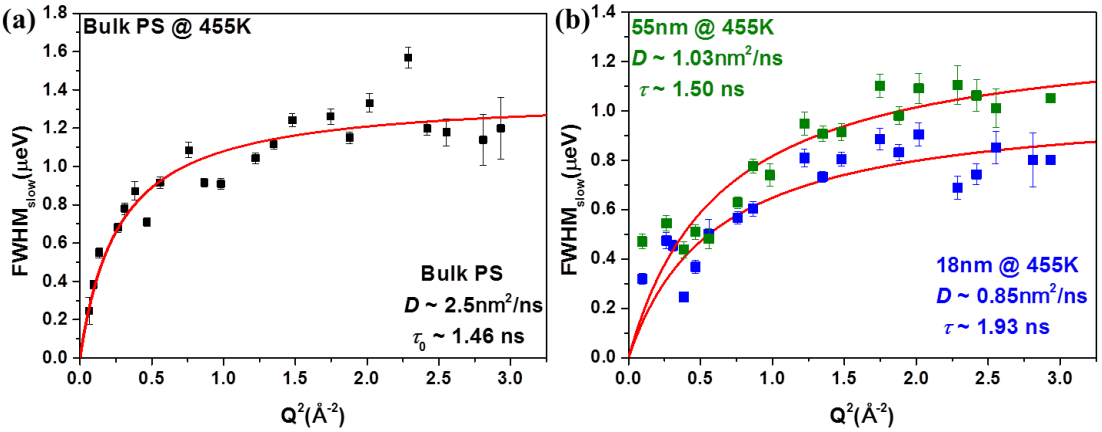

Figure 8.3. (a) $FWHM_{slow}$ vs Q^2 for bulk PS at 455K and associated fitting to Equation 8.6 (b) $FWHM_{slow}$ vs Q^2 for PS confined in 55nm and 18nm diameter nanopores at 455K. Data at $Q^2 > 0.5$Å^{-2} are fit to Equation 8.6 to obtain an estimated waiting time τ_0.

However, for confined polymers, the Q dependence of FWHM (Figure 8.3(b)) at low Q region ($Q^2 < 0.5$ Å^{-2}) does not show the typical continuous diffusion behavior. Instead, it plateaus at a constant value, which can be explained as a continuous diffusion

within a bounded media.[28] Diffusion of hydrogens is confined in an area so that when probing at larger length scale (smaller *Q*), diffusion of longer distance (longer relaxation time) does not appear. Instead, only diffusion within the boundary is revealed, which has about the same relaxation time ($FWHM_{slow}$). Due to the fact that $FWHM_{slow}$ at low *Q* region is very close to the instrument resolution limit, we do not tend to further discuss this behavior. In the medium Q range ($0.5\ Å^{-2} < Q^2 < 1.25\ Å^{-2}$), a DQ^2 dependence is clearly seen, which means at this length scale, hydrogen behaves more like continuous diffusion. At high Q range ($1.25\ Å^{-2} < Q^2$), the jump diffusion behavior is revealed again. $FWHM_{slow}$ above $0.5\ Å^{-2}$ were fit to Equation 8.6 to obtain *D* and τ for confined PS, shown in Figure 8.3(b). results for fitting parameters *D* and τ are listed in Table 8.2 and associated fitting for other samples at 455K and all samples at 440K are shown in Figure 8.4.

Table 8.2. Associated fitting results for D and τ for bulk PS and confined PS at 440K and 455K

	D @ 440K (nm^2/ns)	τ @ 440K ns	D @ 455K (nm^2/ns)	τ @ 455K ns
Bulk PS	1.76 ± 0.33	1.78 ± 0.09	2.49 ± 0.39	1.46 ± 0.06
80nm	0.65 ± 0.12	1.78 ± 0.18	1.11 ± 0.18	1.47 ± 0.11
55nm	0.68 ± 0.13	1.86 ± 0.17	1.03 ± 0.18	1.50 ± 0.12
35nm	0.62 ± 0.11	1.88 ± 0.17	1.02 ± 0.19	1.56 ± 0.11
18nm	0.44 ± 0.10	2.33 ± 0.28	0.85 ± 0.16	1.93 ± 0.15

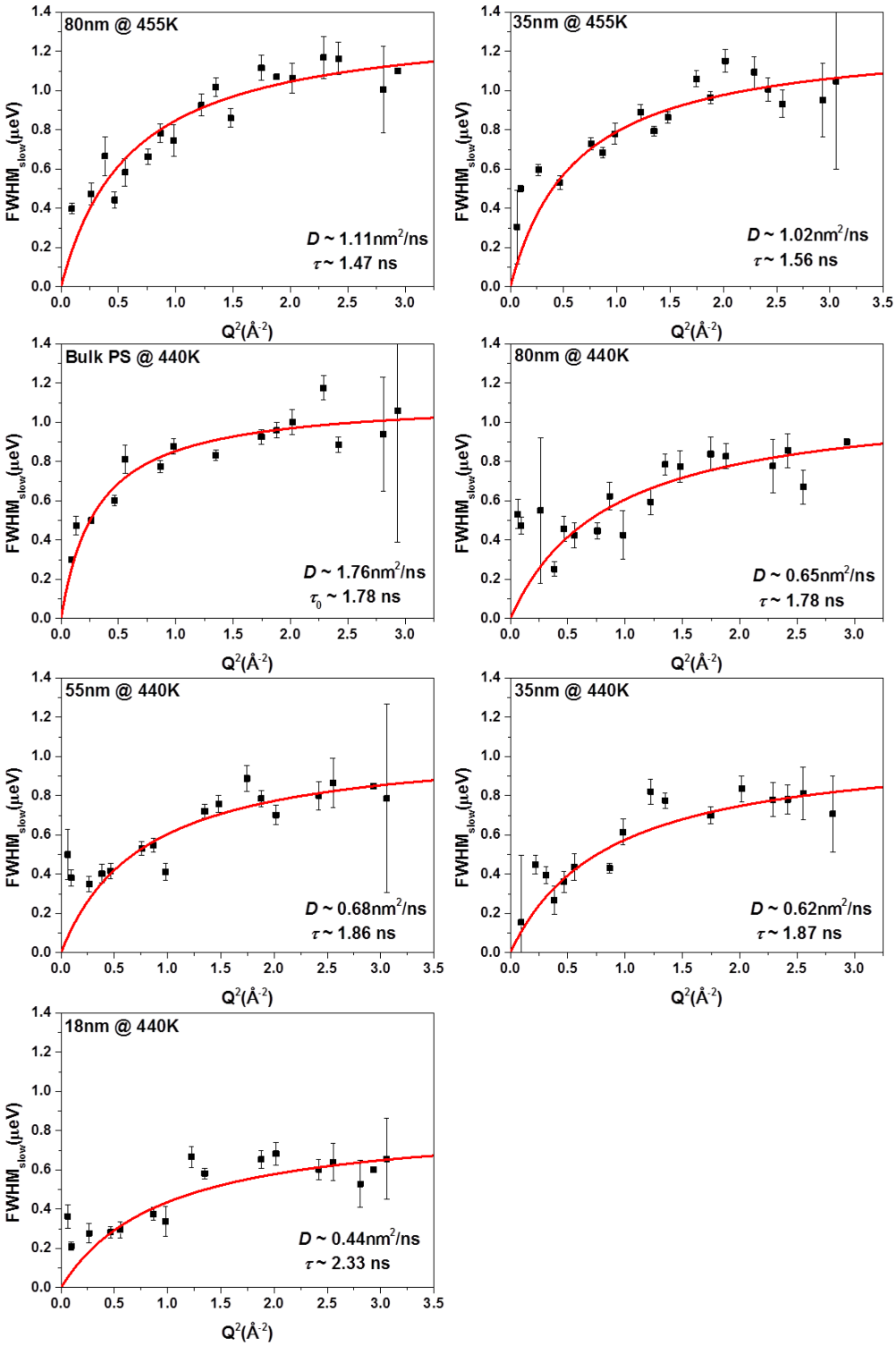

Figure 8.4. FWHMslow vs Q^2 for PS confined in 55nm and 80nm nanopores at 455K and all samples at 440K and associated fitting to Equation 8.6.

Normalized D (D for confined PS/ D for bulk PS, D_0) and normalized τ (τ for confined PS/τ for bulk PS, τ_0) as a function of nanopore diameter are plotted in Figure 8.5. It can be seen Figure 8.5(a) that the rigid cylindrical confinement strongly suppress the diffusion coefficients of the segmental motion. D slowly decreases when $d/R_{ee} > 1$, and shows a more pronounced drop when $d/R_{ee} < 1$. Moreover, confinement effect on D is more pronounced at lower temperature. Similarly, waiting time slightly increases when $d/R_{ee} > 1$, and has a larger increment when $d/R_{ee} < 1$. The confinement effect on the waiting time is almost the same for the two temperatures.

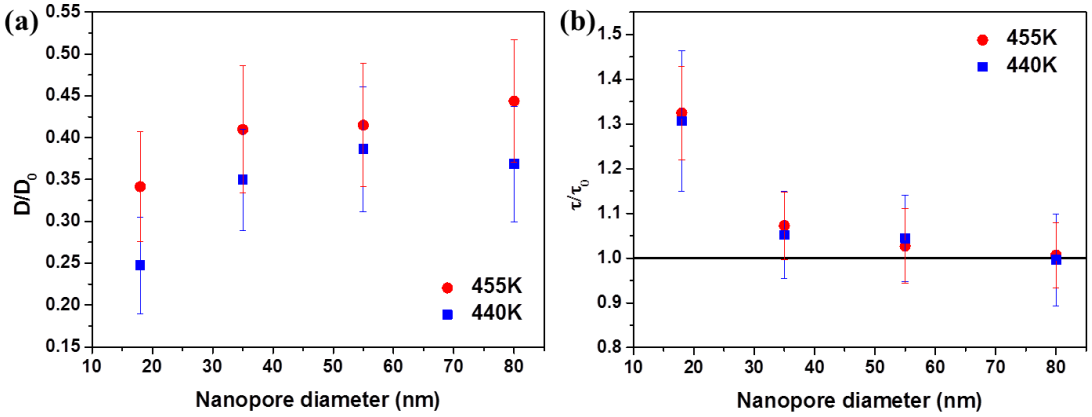

Figure 8.5. (a) Normalized D and (b) Normalized τ as a function of nanopore diameter

8.4.2. Elastic Incoherent Scattering Factor (EISF)

EISF is the ratio of the pure elastic scattering peak to the total scattering, represents

the portion of hydrogens which are not moving or move too slow to be detected by neutrons contribute to the elastic scattering peak. Figure 8.6(a) shows the EISF as a function of *Q* for bulk PS and PS confined in 55 nm and 18 nm nanopores. It can be clearly seen that EISF is only slightly higher when confined in rigid nanopores, which means more hydrogens are freeze. However, Figure 8.6(b) shows that PS confined in 80nm nanopores plateaus at even higher EISF than bulk PS and PS confined in 18nm nanopores at high *Q* regime. This implies that PS confined in 80nm nanopores has the highest fraction of freeze hydrogens among all samples.

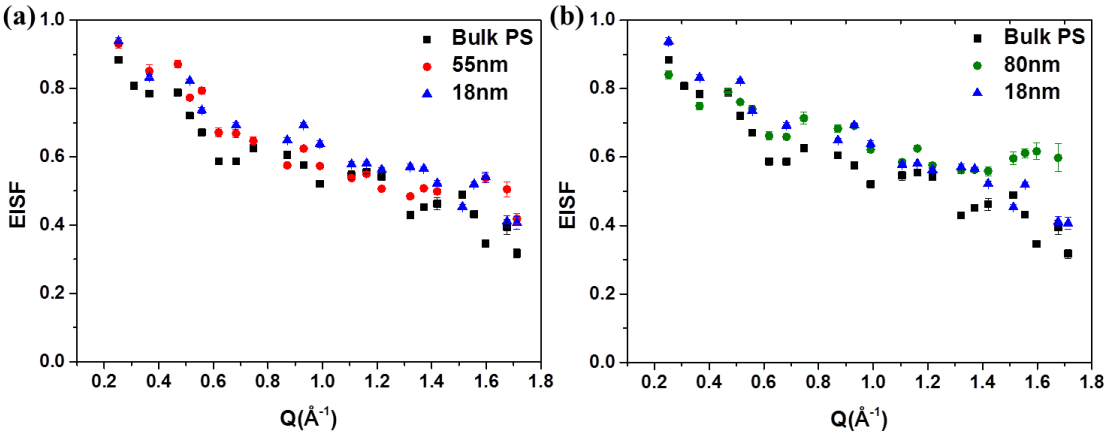

Figure 8.6. (a) EISF for bulk PS and PS confined in 55nm and 18nm nanopores (b) EISF for bulk PS and PS confined in 80nm and 18nm nanopores

The change of EISF is quite subtle among different samples. As mentioned when

discussing the QENS data, hydrogens for confined PS may diffuse within boundaries. The easiest model to test is diffusion in a spherical boundary. EISF for hydrogen diffuse in a spherical boundary can be fit to[34]

$$\mathrm{EISF(Q)} = \phi + (1-\phi)\left(\frac{3j_1(QR)}{QR}\right)^2 \tag{8.7}$$

where ϕ represents the fraction of hydrogens that are not moving within the probing time scale of the measurement and j_1(QR) is the first order Bessel function, expressed as

$$j_1(QR) = \frac{\sin(QR)}{(QR)^2} - \frac{\cos(QR)}{(QR)} \tag{8.8}$$

where R is the radius of the spherical boundary. EISF results for all samples at two temperatures at 455K and 440K are fit to Equation 8.7, as shown in Figure 8.7. Fitting results for parameters R and ϕ are shown in Table 8.3.

Table 8.3. Results for R and ϕ obtained by fitting EISF vs. Q data to Equation 8.7

	R @ 440K (nm)	ϕ @ 440K (v%)	R @ 455K (nm)	ϕ @ 455K (v%)
Bulk PS	1.17 ± 0.06	1.78 ± 0.09	1.21 ± 0.05	45.0 ± 1.41
80nm	1.05 ± 0.1	72.7 ± 1.32	1.13 ± 0.06	59.5 ± 1.06
55nm	1.12 ± 0.07	66.4 ± 1.14	1.03 ± 0.06	51.4 ± 1.59
35nm	1.18 ± 0.09	69.4 ± 1.13	1.05 ± 0.05	52.3 ± 1.09
18nm	1.19 ± 0.07	70.9 ± 0.83	0.98 ± 0.06	54.0 ± 1.41

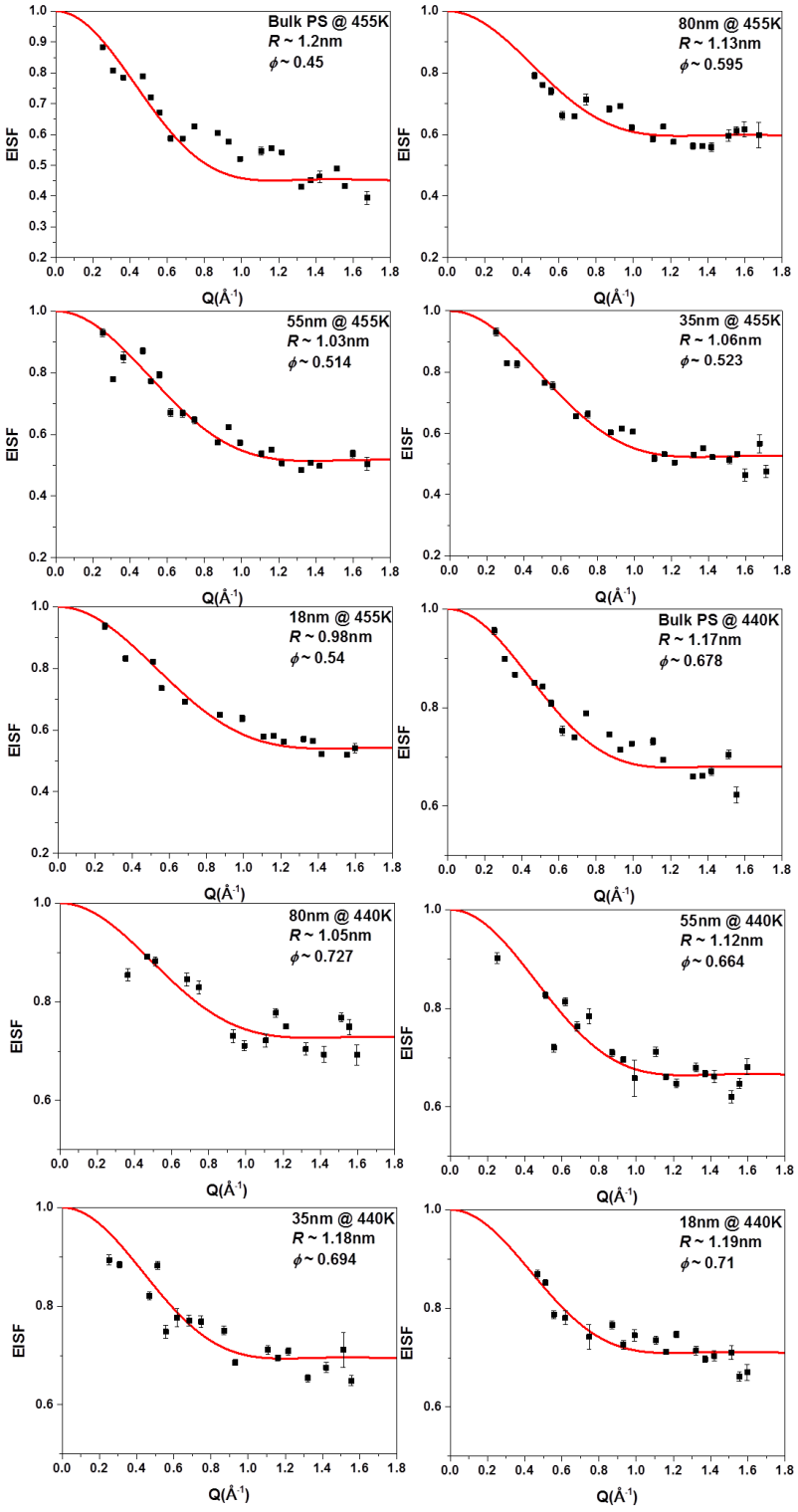

Figure 8.7. EISF as a function of *Q* for all samples and the associated fitting to Equation 8.7.

It can be seen from the fitting that EISF plateaus at the value of ϕ at high Q regime, and the slope of the drop at low Q regime depends on R. Figure 8.8 shows the normalized R and ϕ as a function of the nanopores diameters. Figure 8.8(a) shows a minimum for ϕ which implies a non-asymptotic change for the fraction of freeze hydrogens when the degree of confinement decreases. There are more freeze hydrogens at lower temperature. In Figure 8.8(b), we can see that the size of the boundary is not affected by the confinement at 440K. It is slowly decreasing when nanopores diameter decreases at 455K, but the change is subtle. Notice that the fitting parameter R strongly depends on the slope of the drop at low Q regime. Since the data at low Q usually have lower signal-to-noise ratio, the fitting results of R have large error bars, as shown in Table 8.3.

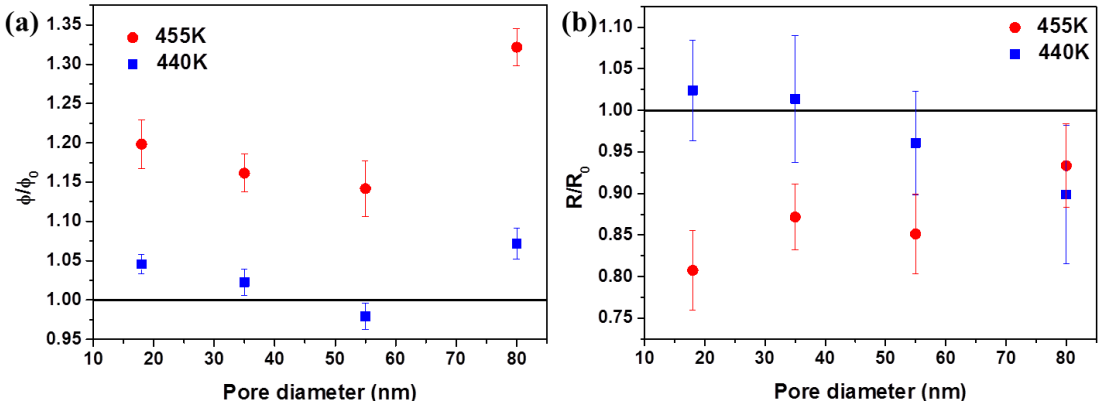

Figure 8.8. (a)Normailized ϕ and (b) normalized R as a function of the pore diameter.

8.4.3. Mean Square Displacement vs. Temperature

In HFBS experiments, fixed window scan was also conducted and mean square displacement was obtained as a function of temperature according to

$$\mathrm{MSD(T)} = -3Q^{-2} ln[I_{el}(Q,T)/I_{el}(Q,50K)] \quad (8.9)$$

where I_{el} is the elastic neutron scattering intensity. In our case, all MSDs are normalized to 50K, which means MSD at 50K for every sample is 0. Figure 8.9 plots -3ln[I_{el}(*Q, T*)/ I_{el}(*Q, 50K*)] versus Q^2 for all samples at 6 temperatures. At low *Q*, -3ln[I_{el}(*Q, T*)/ I_{el}(*Q, 50K*)] shows a linear dependent on Q^2, where we did a linear fitting to extract MSD(T). At higher Q^2, -3ln[I_{el}(*Q, T*)/ I_{el}(*Q, 50K*)] starts to deviate from the linear dependence.

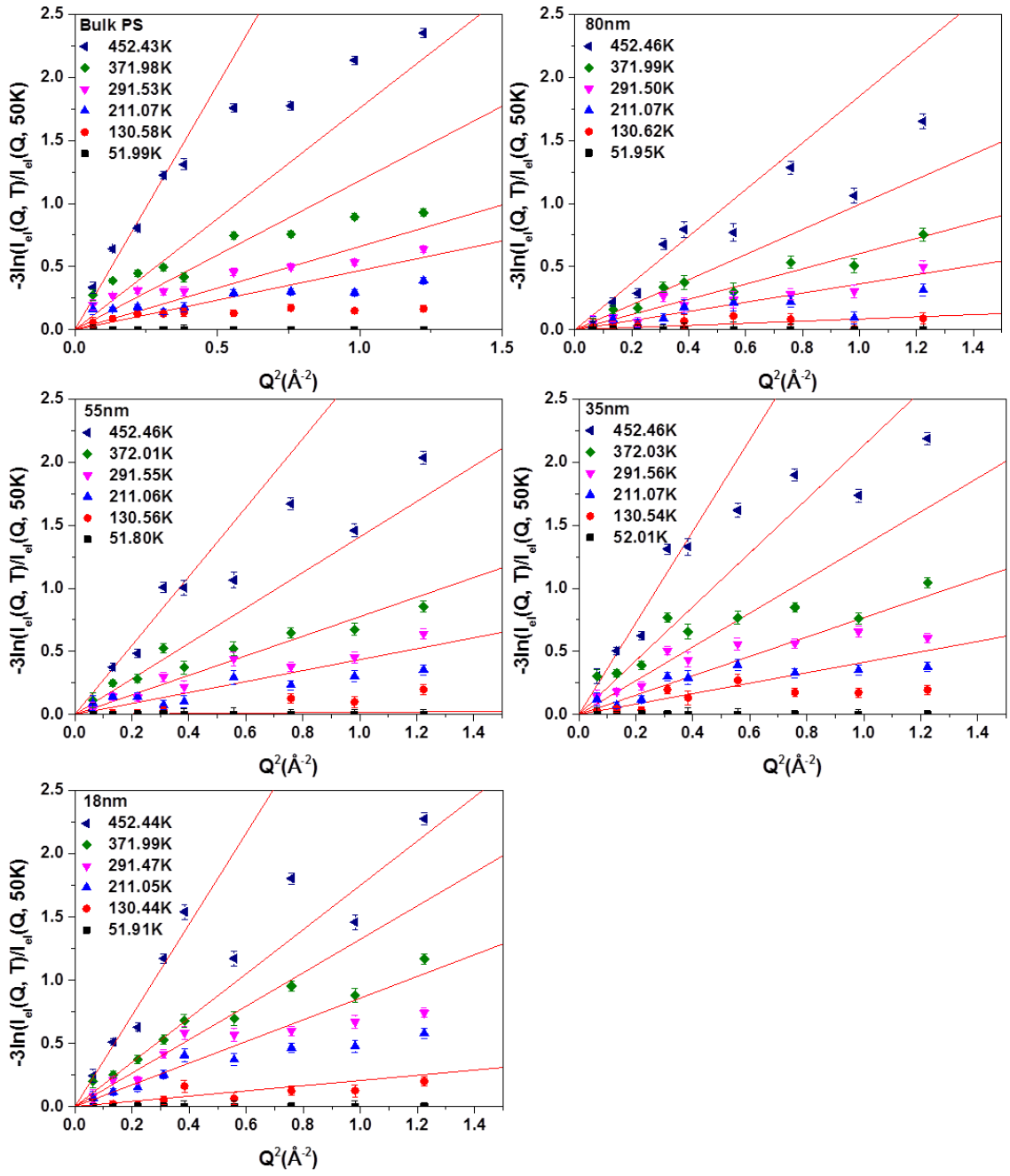

Figure 8.9. -3ln[$I_{el}(Q, T)/ I_{el}(Q, 50K)$] versus Q^2 for bulk PS and PS confined in nanopores and associated linear fitting for the lowest five Q values.

MSD as a function of temperature for bulk PS and PS confined in different diameter nanopores is shown in Figure 8.10(a). It can be clearly seen confined PS shows lower MSD comparing to the bulk PS at temperature above T_g. Below T_g, PS confined in 18nm and 35nm nanopores shows higher MSD, especially above the onset temperature of some fast motions at around 200K.[35] Here, we do not plan to further discuss the confinement effect on these fast motions. To focus on the confinement effect for MSD above T_g, data between 250K to 350K are fit linearly, and this straight line are extrapolated to ~460K. All the MSD data beyond 250K are subtracted to this line and plotted in Figure 8.10(b) as ΔMSD vs. temperature.

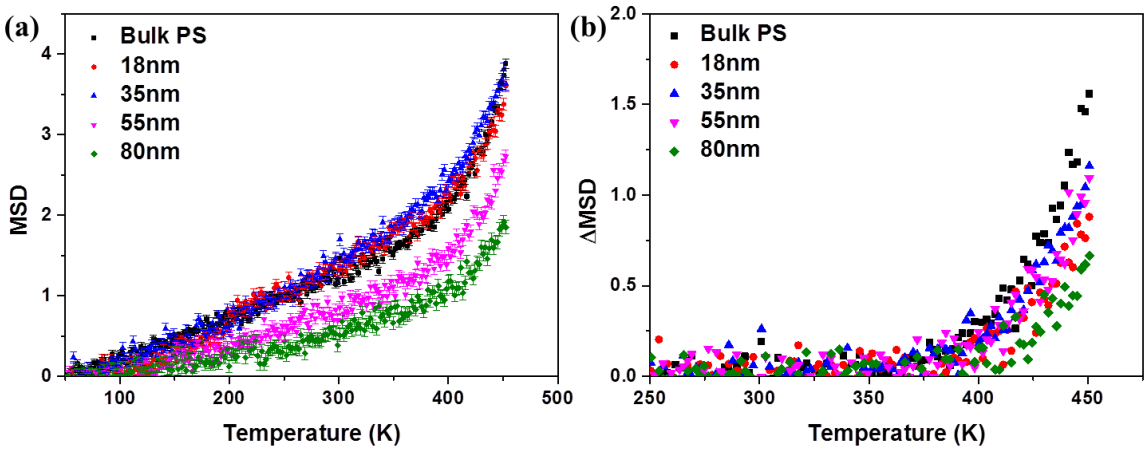

Figure 8.10. (a) Mean square displacement as a function of temperature for bulk PS and confined PS. (b) The increase of mean square displacement above T_g for bulk PS and confined PS.

It can be seen that beyond T_g, bulk PS has the highest ΔMSD, 35nm and 55nm samples have about the same MSD, which is lower than that for bulk PS. 18nm has even lower MSD. However, 80nm sample shows the lowest ΔMSD. This ΔMSD is corresponding to the segmental motion of polymer chains, which related to the slow relaxation mode probed in QENS experiments. From our QENS results, we noticed that 80nm sample has higher portion of freezing hydrogen (higher EISF) as shown in Figure 8.8(a) and retarded slow relaxation mode. That may be the reason why 80nm sample has the lowest ΔMSD at high temperature. For 35nm and 55nm samples, they have about the same amount of freezing hydrogen and about the same diffusion coefficients and waiting time (Figure 8.5), and they show about the same ΔMSD. For 18nm, although the amount of freezing hydrogen is higher than that for 35nm and 55nm samples, the slow relaxation mode is further retarded so that 18nm has lower ΔMSD.

For a rigid cylindrical nano-confinement system, interface effect and confinement effect are introduced to explain how the polymer dynamics is affected by this nano-confinement.[36] Interface (adsorption) effect focus on the polymers close to the interface between polymers and the rigid wall. The change of dynamics depends on the interaction between polymers and the wall, and it has been shown in the literature that an

interfacial regime exists and polymers in this regime shows different dynamics.[7, 10-11] Priestley *et al*. shows that interfacial area for supported thin film system reduced the structure relaxation rates. The perturbation range can be up to ~100 nm for the substrate interface regime, and ~25 nm for the free surface regime.[37] In our case, we do not expect to have a strongly bounded PS layer due to the non-favorable interaction between PS and aluminum oxide. However, PS close to the rigid wall may still be affected and shows different dynamics,[38] for example: direct hinder of dynamics from the rigid confinement as shown in Chapter 7. So far, most of the neutron scattering study focus on PEO and PDMS, which may have favorable interaction with AAO surfaces. For confinement effect, polymer chain packing is affected by this rigid confinement,[13] which may also induce a change in polymer dynamics. It has been shown that the confinement effect in the core regime can facilitate the polymer dynamics.[36, 38-43] The non -asymptotic change we observe here for PS confined in AAO nanopores may due to the counterbalance between these two effects. When d/R_{ee} is > 2 (80nm sample), the interface effect dominates the change in polymer dynamics. Some hydrogens are freeze and segmental motion is retarded at the interface area. Away from the interface, PS may still act like in a bulk system. Notice that the infiltration percentage is quite low for 80nm samples. Since d/R_{ee} is > 2, it is also possible

that PS only forms a interfacial layer,[23] instead of completely fill the nanopores. In this case the interfacial region will account more for the change in dynamics. When $2 > d/R_{ee} > 1$, confinement effect starts to affect the polymer chain packing in the core regime. Assuming the thickness and the degree of retardation of the interfacial region stays the same, when pore diameter decreases, the interfacial region accounts for higher *v*% of all confined PS. However, PS dynamics facilitate at the core region, and the average dynamics is determined by the counterbalance between these two regions. Therefore, for 35nm and 55nm, we do not observe a pronounced change for the slow relaxation mode. Another evidence of the confinement effect is that some original freeze hydrogens now start moving (can be in the interface region or in the core region). We can only account for the average fraction of freeze hydrogens and average relaxation time for the slow relaxation mode. It is difficult to determine how these two factors change respectively in the interface region and in the core region. When we further confined polymers to $1 > d/R_{ee}$, It is possible that the interfacial region now accounts for all confined PS so that the counterbalance effect is lost. Therefore, further retardation of the slow relaxation mode is observed. Combining the change on the slow relaxation mode and EISF can help us understand the non-asymptotic change for ΔMSD. However, it is difficult to compare 18nm samples and 80nm samples,

since one has slower dynamics and the other one has more freeze hydrogens.

8.5. SUMMARY

In this chapter, we studied the local dynamics of polystyrene confined in AAO nanopores with different diameters, and compare to that for bulk polystyrene. We focus our discussion on the segmental motion of PS, which is represented by the slow relaxation mode in the fitting process. Changes in both the slow relaxation mode (segmental motion) and the fraction of hydrogen which is not diffusing within the experimental time window (~ 10ps to 1ns) were observed. The slow relaxation mode is retarded when confined in nanopores, but the degree of retardation is about the same or only slightly decreases when d/R_{ee} >1. Only when 1 > d/R_{ee}, the slow relaxation mode is further retarded. For EISF, a non- asymptotic change was also observed. 80nm samples has higher fraction of immobile hydrogen. When the pore diameter decreases, EISF decreases to the value close to that for bulk PS. EISF for confined PS shows the behavior of diffusion in a spherical boundary, where the size of the boundary is slightly decreasing when the pore diameter decreases. At the end, we also discuss the MSD for bulk and confined PS, and we focus on the MSD above T_g (ΔMSD). It is clearly shown that PS under confinement has lower ΔMSD. Among all confined samples, 80nm sample has the lowest ΔMSD due to both the retardation of the

slow dynamic motion, and the increase of the portion of non-moving hydrogens. 35nm and 55nm sample have about the same ΔMSD, which is higher than 80nm sample, because they have lower fraction of non-moving hydrogens. 18nm sample has lower MSD due to the further retardation of the slow relaxation mode. However, the comparison between 18nm and 80nm is difficult, because one has slower dynamics, and the other has higher fraction of immobile hydrogen. These behaviors may due to the counterbalance between the interface (adsorption) effect and confinement effects. To further understand this non asymptotic change in polymer dynamics induced by cylindrical nano-confinement, an atomistic simulation for polymers under nano-confinement may be helpful. It can be a hybrid of interfacial effect and effect on polymer chain packing. However, it is difficult to conclude the change is mainly in the interface region, the core region or both, due to the fact that we are measuring the average behavior of all hydrogens.

8.6. REFERENCES

1. Shin, K.; Obukhov, S.; Chen, J. T.; Huh, J.; Hwang, Y.; Mok, S.; Dobriyal, P.; Thiyagarajan, P.; Russell, T. P., *Nat. Mater.* **2007,** *6* (12), 961-965.

2. Noirez, L.; Stillings, C.; Bardeau, J. F.; Steinhart, M.; Schlitt, S.; Wendorff, J. H.; Pepy, G., *Macromolecules* **2013,** *46* (12), 4932-4936.

3. Kausik, R.; Mattea, C.; Fatkullin, N.; Kimmich, R., *J. Chem. Phys.* **2006,** *124* (11).

4. Mattea, C.; Fatkullin, N.; Fischer, E.; Beginn, U.; Anoardo, E.; Kroutieva, M.; Kimmich, R., *Appl. Magn. Reson.* **2004,** *27* (3-4), 371-381.

5. Fatkullin, N.; Kimmich, R.; Fischer, E.; Mattea, C.; Beginn, U.; Kroutieva, M., *New J. Phys.* **2004,** *6*.

6. Ok, S.; Steinhart, M.; Serbescu, A.; Franz, C.; Chavez, F. V.; Saalwachter, K., *Macromolecules* **2010,** *43* (10), 4429-4434.

7. Hofmann, M.; Herrmann, A.; Ok, S.; Franz, C.; Kruk, D.; Saalwachter, K.; Steinhart, M.; Rossler, E. A., *Macromolecules* **2011,** *44* (11), 4017-4021.

8. Chrissopoulou, K.; Anastasiadis, S. H.; Giannelis, E. P.; Frick, B., *J. Chem. Phys.* **2007,** *127* (14).

9. Krutyeva, M.; Martin, J.; Arbe, A.; Colmenero, J.; Mijangos, C.; Schneider, G. J.; Unruh, T.; Su, Y. X.; Richter, D., *J. Chem. Phys.* **2009,** *131* (17).

10. Kusmin, A.; Gruener, S.; Henschel, A.; de Souza, N.; Allgaier, J.; Richter, D.; Huber, P., *Macromolecules* **2010,** *43* (19), 8162-8169.

11. Kusmin, A.; Gruener, S.; Henschel, A.; Holderer, O.; Allgaier, J.; Richter, D.; Huber, P., *J. Phys. Chem. Lett.* **2010,** *1* (20), 3116-3121.

12. Martin, J.; Krutyeva, M.; Monkenbusch, M.; Arbe, A.; Allgaier, J.; Radulescu, A.; Falus, P.; Maiz, J.; Mijangos, C.; Colmenero, J.; Richter, D., *Phys. Rev. Lett.* **2010,** *104* (19).

13. Sussman, D. M.; Tung, W. S.; Winey, K. I.; Schweizer, K. S.; Riggleman, R. A., *Macromolecules* **2014,** *47* (18), 6462-6472.

14. Lagrene, K.; Zanotti, J. M.; Daoud, M.; Farago, B.; Judeinstein, P., *Phys. Rev. E* **2010,** *81* (6).

15. Lagrene, K.; Zanotti, J. M.; Daoud, M.; Farago, B.; Judeinstein, P., *Eur. Phys. J.-Spec. Top.* **2010,** *189* (1), 231-237.

16. Krutyeva, M.; Wischnewski, A.; Monkenbusch, M.; Willner, L.; Maiz, J.; Mijangos, C.; Arbe, A.; Colmenero, J.; Radulescu, A.; Holderer, O.; Ohl, M.; Richter, D., *Phys. Rev. Lett.* **2013,** *110* (10).

17. Hong, P. D.; Chuang, W. T.; Yeh, W. J.; Lin, T. L., *Polymer* **2002,** *43* (25), 6879-6886.

18. Paradossi, G.; Cavalieri, F.; Chiessi, E.; Telling, M. T. F., *J. Phys. Chem. B* **2003,** *107* (33), 8363-8371.

19. Arbe, A.; Colmenero, J., *Phys. Rev. E* **2009,** *80* (4).

20. Roh, J. H.; Tyagi, M.; Briber, R. M.; Woodson, S. A.; Sokolov, A. P., *J. Am. Chem.*

Soc. **2011,** *133* (41), 16406-16409.

21. Kofu, M.; Someya, T.; Tatsumi, S.; Ueno, K.; Ueki, T.; Watanabe, M.; Matsunaga, T.; Shibayama, M.; Sakai, V. G.; Tyagi, M.; Yamamuro, O., *Soft Matter* **2012,** *8* (30), 7888-7897.

22. Roh, J. H.; Tyagi, M.; Hogan, T. E.; Roland, C. M., *J. Chem. Phys.* **2013,** *139* (13).

23. Zhang, M. F.; Dobriyal, P.; Chen, J. T.; Russell, T. P.; Olmo, J.; Merry, A., *Nano Lett.* **2006,** *6* (5), 1075-1079.

24. Kim, E.; Xia, Y. N.; Whitesides, G. M., *Nature* **1995,** *376* (6541), 581-584.

25. Rubinstein, M.; Colby, R. H., *Polymer Physics*. Oxford University Press: New York, 2003.

26. Meyer, A.; Dimeo, R. M.; Gehring, P. M.; Neumann, D. A., *Rev. Sci. Instrum.* **2003,** *74* (5), 2759-2777.

27. Ryong-Joon, R., *Methods of X-ray and Neutron Scattering in Polymer Science*. Oxford University Press: New York, 2000.

28. Marc, B., *Quasielastic neutron scattering: Principles and Applications in Solid State Chemistry, Biology and Materials Science*. CRC Press: Adam Hilger, Bristol and Philadelphia, 1988.

29. Williams, G.; Watts, D. C., *Transactions of the Faraday Society* **1970,** *66* (565P), 80-&.

30. Lyonnard, S.; Berrod, Q.; Bruning, B. A.; Gebel, G.; Guillermo, A.; Ftouni, H.; Ollivier, J.; Frick, B., *Eur. Phys. J.-Spec. Top.* **2010,** *189* (1), 205-216.

31. Azuah, R. T.; Kneller, L. R.; Qiu, Y. M.; Tregenna-Piggott, P. L. W.; Brown, C. M.; Copley, J. R. D.; Dimeo, R. M., *J. Res. Natl. Inst. Stand. Technol.* **2009,** *114* (6), 341-358.

32. Bertrand, C. E.; Chiang, W. S.; Tyagi, M.; Chen, S. H., *J. Chem. Phys.* **2013,** *139* (1).

33. Singwi, K. S.; Sjolander, A., *Physical Review* **1960,** *120* (4), 1093-1102.

34. Volino, F.; Dianoux, A. J., *Mol. Phys.* **1980,** *41* (2), 271-279.

35. Inoue, R.; Kanaya, T.; Nishida, K.; Tsukushi, I.; Telling, M. T. F.; Gabrys, B. J.; Tyagi, M.; Soles, C.; Wu, W. I., *Phys. Rev. E* **2009,** *80* (3).

36. Peng, H.; Nieuwendaal, R.; Soles, C. L., Polymer Dynamics in Constrained Geometries. In *Polymer Science: A Comprehensive Reference*, Moeller, M.; Matyjaszewski, K., Eds. Elsevier B. V. : Amsterdam, 2012; Vol. 7, pp 345-376.

37. Priestley, R. D.; Ellison, C. J.; Broadbelt, L. J.; Torkelson, J. M., *Science* **2005,** *309* (5733), 456-459.

38. Park, J. Y.; McKenna, G. B., *Phys. Rev. B* **2000,** *61* (10), 6667-6676.

39. Schonhals, A.; Goering, H.; Schick, C.; Frick, B.; Mayorova, M.; Zorn, R., *Eur. Phys. J.-Spec. Top.* **2007,** *141*, 255-259.

40. Schonhals, A.; Goering, H.; Schick, C.; Frick, B.; Zorn, R., *J. Non-Cryst. Solids* **2005,** *351* (33-36), 2668-2677.

41. Schonhals, A.; Goering, H.; Schick, C.; Frick, B.; Zorn, R., *Colloid Polym. Sci.* **2004,** *282* (8), 882-891.

42. Schonhals, A.; Goering, H.; Schick, C.; Frick, B.; Zorn, R., *Eur. Phys. J. E* **2003,** *12* (1), 173-178.

43. Schonhals, A.; Goering, H.; Schick, C., *J. Non-Cryst. Solids* **2002,** *305* (1-3), 140-149.

Chapter 9

Summary and Future Work

In this thesis, we studied polymer structure and dynamics for polymer nanocomposites and polymers in cylindrical nanoconfinement. Specifically, we studied polymer chain conformations in CNT/PS system, temperature dependence of polymer diffusion in MWCNT/PS and silica NP/PS nanocomposites, as well as polymer structure (R_{ee} and N_e), local dynamics, and center-of-mass diffusion in cylindrical nanoconfinement. The first section of this thesis focuses on the confinement in polymer nanocomposites. We investigate the effect of carbon nanotubes (CNTs) on polymer structure using SANS and the temperature dependence of polymer diffusion in MWCNT/PS and silica NP/PS nanocomposites using ERD. The second part of this thesis systematically investigates polymer structure (R_{ee} and N_e), local dynamics, and center-of-mass diffusion in cylindrical confinement using computer simulations and experiments.

9.1 CONCLUSION

Chapter 2 and 3 are the first experimental works investigating the effect of

cylindrical nanofillers (CNT) on polymer (polystyrene) chain conformation using SANS. We observed a chain expansion (~ 30% for 10 wt% SWCNT loading) when the ratio between the radius of CNTs (r) and the size of polymer chains (R_g) is smaller than 1 (~ 0.4 for single-wall CNT). On the other hand, when r/R_g is ~ 1 (~ 0.9 for multi-wall CNT), chain size stays the same or slightly decreases. By investigating chain conformation in aligned SWCNT/dPS + hPS nanocomposites, we further confirmed that the expansion of polymer chains is perpendicular to the direction of SWCNTs. In addition to the size ratio between polystyrene and CNT, the mechanisms of the expansion are also related to the mesh sizes of CNT networks. In an isotropic dispersion of SWCNTs, when chain size is larger than the mesh size, polymer chains circumvent SWCNTs and expand uninhibited from confined in meshes. However, for MWCNTs at the same wt%, the number density of MWCNT is much lower resulting in a larger mesh size distribution allowing the polymer chains to retain the bulk chain conformation.

When SWCNTs are aligned by fiber spinning, anisotropic rod networks were induced, which results in smaller mesh size distributions perpendicular to the alignment direction and larger mesh size distributions parallel to the alignment direction. Polymer chains experience smaller mesh sizes perpendicular to the alignment direction and adopt an

expanded chain conformation to circumvent the SWCNTs. Simultaneously, polymer chains experience larger mesh sizes parallel to the alignment direction and adopt less expanded chain conformations to produce anisotropic polymer conformations with $R_g^{per} > R_g^{par}$. Moreover, when r/R_g is large (~1 or >1), circumventing CNTs may causes higher entropic penalty, which may also prohibit chain expansion in MWCNT/dPS + hPS nanocomposites. Through these studies, we understand the effect of cylindrical shape nanofillers on polymer chain conformation and the mechanism of polymer chain expansion around cylindrical nanofillers. However, these results cannot directly explain the diffusion minimum previously observed in the CNT/PS systems. Further study on how CNT affect local relaxation and N_e may be required to explain the diffusion minimum.

To further understand polymer diffusion in CNT/PS nanocomposites. The temperature dependence of polymer tracer diffusion is investigated in Chapter 4, and the diffusion minimum is observed in 7 temperatures from 152°C to 214°C. The diffusion minimum is shallower at higher temperatures which suggests that the mechanisms causing the tracer diffusion to slow down at low MWCNT loading (<2wt%) is less pronounced at higher temperatures. The WLF equation successfully describes the

temperature dependence of tracer diffusion coefficients at fix MWCNT concentration. This implies that in MWCNT/PS nanocomposites, local friction coefficients are still associated with the fractional free volume in the polymer matrix. It is found that the minimum in the thermal expansion coefficient of free volume (α_f) happens at 2wt%, at which the diffusion minimum is observed.

In contrast to the CNT nanocomposites, polymer diffusion in silica/PS nanocomposites shows a monotonic decrease when silica concentration increases. The temperature dependence of the tracer diffusion in silica/PS is also investigated in Chapter 5. The monotonic decrease is more pronounced at higher temperatures, which suggests that the mechanism causing the diffusion to slow down is more pronounced. Temperature dependence of the tracer diffusion coefficients at fixed silica concentration can be fit to the WLF equation, and a slightly decreasing α_f as a function of silica concentration is observed. However, an increase of α_f is observed for α_f obtained from the time-temperature superposition of rheology data at different temperatures. Through the temperature dependence study, we found that polymer diffusion is affected in different ways when adding different types of nanofillers, and the mechanisms of the slowing down of polymer diffusion can be more or less pronounced at higher temperatures.

Moreover, for polymer nanocomposites, rheological tests and tracer diffusion experiments measure dynamical relaxation from different components of the composites, so different trends of α_f as a function of silica concentration may be observed. It will be interesting to study the temperature dependence of polymer chain size (R_g), local relaxation time, and N_e in polymer nanocomposites. Knowing how nanofillers affected these parameters and their associated temperature dependences can help us further understand the change in diffusion coefficient and the temperature dependence of it.

In the second section of this thesis, we studied the effect of cylindrical confinement using simulations and experiments. We systematically studied the applicability of the reptation model in cylindrical confinement using computer simulations. In Chapter 6, we use molecular dynamics (MD) simulation to investigate equilibrium chain conformation in cylindrical nanoconfinement with an amorphous confining wall. We found that polymer chain size was reduced in the confined direction due to the direct compression from the impenetrable wall while slightly elongated along the cylindrical axis (~20% at d_{eff}/R_{ee} ~ 0.4) due to the excluded volume effect. Additionally, N_e increases when the diameter of cylinder decreases. A theory was developed by our collaborator, Dr. Daniel Sussman, to investigate the effect of

nanoconfinement on the topological properties of polymer chains. The theory assumed that the preferential orientation of the end-to-end vector induced by the confinement can be transferred to the preferential orientation of primitive path steps (PPS). With the distribution of the preferential orientation of PPS, we successfully predicted the increase of N_e for polymer chains in cylindrical and thin film confinements. This is the first simulation work to study polymer structure in cylindrical confinement and development of a theory to correlate the change of R_{ee} with the change of N_e.

Based on this knowledge of how polymer structure changes under cylindrical confinement, we investigated the effect of cylindrical confinement on polymer local dynamics and center-of-mass diffusion using MD simulations and experiments in Chapter 7. From simulations we found that local dynamics and local chain packing are both affected by the cylindrical confinement and are correlated to one another. The average relaxation time decreases along the cylindrical axis and increases perpendicular to the cylindrical axis. Combining the change in local relaxation time along the cylindrical axis with the change in R_{ee} and N_e found in Chapter 6, we were able to predict the center-of-mass diffusion coefficients (D_{rep}) of polymer chain along the cylindrical axis through the reptation model. We found that polymer diffusion coefficient (D_{rep}) increases

when cylindrical diameter decreases, and the increases of D_{rep} is mainly due to the increase in N_e. On the other hand, polymer diffusion coefficients can be directly calculated from the log(MSD_z) versus log(LJ time) plot in the diffusion regime (D_{MSD}). D_{rep} agrees with D_{MSD} well at $d_{eff}/R_{ee} > 0.5$, but a discrepancy was observed when $d_{eff}/R_{ee} < 0.5$. This may suggest the failure of the bulk reptation model for polymers at extreme confining states.

Polymer center-of-mass diffusion was also measured experimentally. Diffusion coefficients obtained experimentally (D_{exp}) were compared to D_{rep} and D_{MSD}. We found that D_{exp} also increases when the diameter of the cylindrical confinement decreases. However, the extent of increase is much lower than that for D_{rep} and D_{MSD}. This may be due to the fact that in simulations we did not consider the interaction between polymers and confinement wall, the detail chemical structure of polymers, and the topological properties of the confinement nanopores.

Furthermore, we studied the local dynamics of polystyrene confined in AAO nanopores with different diameters using quasi-elastic neutron scattering (QENS) in Chapter 8. The length scale and time scale studied are smaller and faster than that for our simulations, and therefore, direct comparison is not achievable. Changes in both the slow

relaxation mode (segmental motion) for PS and EISF, the fraction of non-diffusive hydrogen within the experimental time window (~ 10ps to 1ns), were observed. Non-asymptotic changes were observed in segmental motion, EISF, and ΔMSD (extent of MSD increase above T_g), and these non-asymptotic changes may due to the counterbalance between interfacial adsorption effects and confinement effects. This heterogeneity for polymer local dynamics is similar to what we observed in computer simulations, where we observed a retarded local relaxation close to the confinement wall and an accelerated relaxation in the central region of the confinement. However, our simulation does not consider the detailed chemical structure of polymers. To further understand this non-asymptotic change in polymer segmental motion, EISF, and ΔMSD induced by cylindrical nano-confinement, an atomistic simulation for polymers in cylindrical nano-confinement where interfacial and confinement effects can be separated would be essential.

Our interesting findings have improved the understanding of polymer physics under these two types of confinements. Through our work on polymer structure in CNT/PS nanocomposites, we understand how cylindrical nanofillers affect polymer chain conformation. The mechanisms of chain expansion found here can also be applied to

other cylindrical nanofillers/polymer systems, like nanowires or nanorods. Our work on the temperature dependence of polymer diffusion in CNT/PS and silica/PS nanocomposites may help us find better materials processing temperatures when manufacturing products with these nanocomposites. Finally, our finding in polymer structure and dynamics in cylindrical nanocomposites helps us understand and predict the behaviors of polymers under severe confinement, which may be essential when utilizing polymer in extremely confined circumstances. I hope that these findings can inspire future work to further broaden our knowledge for confined polymer systems, and help society to make better designs and manufacturing methods of various products made of polymer nanocomposites or confined polymers.

9.2 FUTURE DIRECTIONS

9.2.1. Chain Conformation in MWCNT/PS Nanocomposites with $r/R_g < 1$

In the future, it would be interesting to investigate chain conformation in MWCNT/PS nanocomposites using higher molecular weight PS so that $r/R_g < 1$. It can also be tested to see if chain expansion can be observed when the size of PS is larger than the mesh sizes of MWCNT rod networks. It will also be interesting to further elucidate the size ratio (r/R_g) at which polymer chain expansion is observed. For example, the size

of fillers can be controlled to below and above the tube diameter of entangle polymer matrices. With nanorods, which have much narrower size distribution, we can control the size ratio (r/R_g) more precisely.

9.2.2 Chain Conformation in Nanorod/Polymer Nanocomposites with Favorable Interaction

It will be worth investigating a system which has strong favorable interactions between anisotropic fillers and polymer matrices, and see if chain expansion along the direction of the nanofillers is observed. The effect of the interaction between polymers and nanofillers can be combined with the size effect observed in this thesis to further understand polymer chain conformation next to cylindrical nanofillers.

9.2.3. Polymer Structure and Dynamics in Cylindrical Nanoconfinement with Attractive Interaction

Since the computer simulations in this thesis do not consider the interaction between confinement wall and polymers, it will be interesting to investigate how does favorable interaction affects polymer structure and dynamics in cylindrical confinement.

Testing different combinations of cylindrical confinement wall chemistries and polymers to experimentally study the effect of interaction between confinement wall and polymers or the properties of polymers (e.g. bond stiffness) would be valuable understand these systems. To further support our simulation results, it is worth probing polymer chain conformation in nanopores using experiments. Appendix I provides preliminary results on polymer chain conformations in AAO nanopores probing by SANS.

9.2.4. Computer Simulations of CNT/Polymer Nanocomposites

Since polymer diffusion and polymer structure in CNT/PS nanocomposites have been studied in the literature and in this thesis. To use the reptation model to understand the diffusion minimum, it will be very helpful to use computer simulation to systematically investigate how polymer structure and dynamics are affected by cylindrical fillers. Particularly, if we can investigate nanocomposites with high nanofillers loadings, it can also help us understand how polymer structure changes when the mesh size is smaller than the chain size, which was investigated experimentally in Chapter 2 and 3. We can also look at local relaxation time and N_e for polymer chains in the nanocomposites. Combing the findings of polymer structure, local relaxation time, and N_e,

we can predict the change in polymer diffusion, similar to what we did in Chapter 7.

9.2.5. Theoretical Calculation or Computer Simulation for Polymers next to Flat or Curved Surfaces

To understand polymer chain conformations next to flat or curved surfaces assuming no preferential interaction between polymers and surfaces, it is important to investigate the entropy loss for polymer chains when they are very close to a surface. This can also help us understand at which size ratio between spherical nanoparticle and polymer chain will chain expansion be observed. Moreover, we can also studied the entropy loss for polymer chains confined in a bottleneck-like structure so that we can further understand the entropic barrier assumption for polymer diffusion in silica/PS nanocomposites reported in Chapter 5.

Appendix A

Carbon Nanotube Purification and CNT/PS Nanocomposites Fabrication

This appendix includes all the materials needed for carbon nanotube purification and CNT/PS nanocomposites fabrication and the associated standard operating procedures for these two materials preparation processes. The document was originally made by Kristin Metkus in Fall, 2009, and was updated by Dr. Mishelle Seitz and Vikki Bird in Summer, 2010.

Note: Almost everything can be completed in the fume hood and should be completed in the fume hood, whenever possible. Read all relevant MSDS sheets (Dimethyl formamid/ Hydrochloric acid/ Carbon nanotubes)

A.1. MATERIALS

- Carbon nanotubes (CNTs): purchased raw (unpurified) HiPco-single walled tubes from Unidym
- Hydrochloric acid (Acros Chemicals- HCl, for analysis, ca. 37% solution in water): ~125mL per ~1 g of CNTs

- Dimethyl formamide (Acros Chemicals- DMF, pure, for HPLC): ~1 L
- Polystyrene (PS)
- Millipore water: unlimited (obtained from Composto lab, pay attention to numerical read out should be ~18, if it drops, wait before filling more water)
- pH indicator strips: >20
- Filter paper: Whatman, 542, 125mm diameter, cat # 1542125 (for coagulation filtration of DMF)
- Glass beakers: depending on composite volume between 250mL, 600 mL, and 1L
- Glass pipettes: many
- Glass containers with lids (either 125 mL, 250 mL, or 500 mL)
- 20 mL glass scintillation vials (for weighing PS stock solution or CNT/DMF solutions before transfer to larger jar)
- Magnetic stirrers and stirring plates
- Porous, glass ceramic filter (Buchner funnel: Pyrex 36060, ASTM 4-5.5 F, 250 ml) for filtration of acid/CNTs
- Coors normal filter + filter paper for coagulated CNT/PS (much easier to get off filter paper than off glass ceramic filter, less chance of breaking filter)

- Erlenmeyer flask with vacuum hose (Kimax Kimble Filter Flask, 500mL, No. 27060) also handy to use a 1000mL for CNT washing and larger volume coagulation steps
- Need rubber gasket that fits between filter and flask to allow a vacuum to be pulled
- Plastic wash bottle filled with water is useful for washing down filter sides/beaker to ensure all composite is transferred to filter paper
- Parafilm – to secure lids during sonication in case jar is accidentally dropped into sonicator bath
- Ring stand/clamps – to hold jars in sonicator: you can fit 4-5 125 mL jars in sonicator at once, also to secure filtration set up
- Gloves resistant to DMF – should be either natural rubber or neoprene. Nitrile gloves are not resistant to DMF!
- Spatula – needs to be acid resistant if coming into contact with acid washed tubes before filtrate is washed to a neutral pH – HCl reacts strongly with most metals!
- Disposable Al weighing dishes, Al foil
- Platinum TGA pans – to check CNT purity (Al pans only can be used to 600C, and you need to run to 800C). Winey group has a set as does Andrew McGehee
- Sonicator (Fischer Scientific FS60H, 6 qt, 100W/ 42 kHz output)

Note about waste: For the entire fabrication process, it is necessary to have 2 different liquid waste containers: one for HCl/ H_2O waste from the purifying process and one for DMF/ H_2O waste from the coagulation. It is also necessary to be able to safely dispose of glass and other materials (paper towels, etc.) that contain CNT suspensions. Make sure waste is dry before removing from hood (Do not let DMF evaporating in the lab)

A.2. CNT PURIFICATION[1]

1. Determine the amount of carbon nanotubes (CNTs) needed and double this number. The purification process will decrease the actual CNT quantity by a significant amount (~ ½)

Reasons: As made HiPco tubes have approximately 33 *wt*% Fe, and after purification it is ~5 *wt*%, so even if you recover all your material off filters/jars/etc, you will lose approximately 1/3 of the mass. You also need some material to check via TGA, some will be lost during determination of stock solution concentration, some used to make samples to determine bundle diameter/length. Be generous in the amount of CNTs purified.

Ex: 1*g* of 1*wt*% CNT/PS composite requires 0.01*g* of CNTs; for all 10*wt*%'s (0.1, 0.3, 0.5, 0.7, 1, 2, 4, 6, 8, 10*wt*%), you will need 0.326*g* CNTs if you are making approximately 1 *g* of each concentration, so purify 1*g* CNT to make sure you have enough after the filtration

process.

Note: Even if only one wt% composite is to be made, the master CNT / DMF solution that results can sit in the fume hood indefinitely and be used at a later time. So, purify more CNTs than you need so that you do not have to go through the purification process again when you want to make more composites.

Note: Unidym only ships tubes damp (in water/ethanol mixture), to determine actual amount of nanotube material, weight some damp, allow them to dry (in glove box) then reweigh. Alternatively you can run TGA on damp material to estimate solids content. After sample is opened, some drying would be expected, so best to double check this.

****For each new batch of CNTs, purify a small test batch, ~100 mg to check procedure before purifying larger batch, also run TGA on as received material****

2. Place CNTs in glass dish. Cover with aluminum foil. Place in furnace at 250°C for 24 hours in air, to allow for oxidation to occur.

a. Kristin/Minfang (MF) used box furnaces in the basement, Michelle/Vikki used vacuum oven in lab closest to the window and used heated in stagnant air (dial setting 17 = ~250°C, make sure to let oven heat up before putting in CNTs). Basement furnace is recommended.

b. Reference[1] calls for heating at 200 °C for 24hrs, however we used 250°C. A small test batch run at 200 °C had ~8.6 wt% Fe remaining while one run at 250°C had 5.3 wt% Fe.

3. Remove CNTs from the oven and allow them to cool to room temperature.

****From this point on, you never want to let the CNTs get dry, filter to a sludgy state but do not dry them out – they can irreversibly aggregate if dry****

4. Heat sonicator water to ~80 °C (boiling water on hot plate then filling sonicator is the fastest way to do this, otherwise sonicator will heat slowly over time as it is run). Place CNTs into a glass jar. For every 1*g* of CNTs, add 125mL of concentrated (~37%) HCl acid to CNTs in glass container. Select a larger jar so that there is sufficient head room for evolved gases as you do not want an exploding hot acid jar in the sonicator. Close lid loosely. As soon as acid added it should turn yellow and evolve gas.

5. Sonicate HCl / CNT mixture in heated water (80°C) for ~30min. The solution will be very dark yellowish and difficult to see through.

6. Mixture will then be filtered. Set up Erlenmeyer flask vacuum attachment piece in fume hood (Figure A.1). Be sure to clamp this entire system securely so that it has no chance on falling. Larger flask is recommended so that you can filter the acid and rinse with DI water a few times before having to empty the flask and continue rinsing.

Figure A.1. If using a ceramic porous filter (right, above) no filter paper is needed. If using a normal filter with holes (left, above), choose filter paper that will not dissolve in strong acid. Attach vacuum hose to system. Make sure vacuum is working. Glass ceramic filter is strongly recommended.

7. Pour sonicated HCl / CNT mixture into filter set-up. Turn on vacuum, filtrate the HCl until CNTs look sludgy and most HCl is visibly removed. Filtrated HCl will be light yellowish. Dispose of HCl solution in appropriate waste container.

8. Leave CNT mat on filter and continue rinsing with DI water. As flask gets full, carefully move filter with CNTs to beaker, empty, replace and continue washing. Continue until the filtrate pH matches that of the original DI water.

a. Transfer material to a jar, fill with some DI water (approx 125ml/1 g CNT materials started with), sonicate for 30 minutes, filter through glass ceramic filter again
b. Remove a small amount of purified materials to run TGA on to confirm final residual Fe (put this in a glass of a Al dish and allow to dry before running TGA
c. Transfer material (still slightly damp) to a new jar, add DMF (approximate 125ml/1 g CNT) and sonicate for 20 minutes, filter this solution and rinse with DMF (to remove any residual water)
d. Transfer DMF washed filtrate to new jar, add DMF (again approx 125 ml/ 1 g CNT), sonicate for 24 hours (water not heated to begin but over course of a day will heat up to ~ 40-50°C), need to top up water level occasionally to ensure jar is always in contact with bath

e. After a day of sonication the solution should look uniformly black and almost 'fluffy' indicating better dispersion

A.3. DETERMINING THE WT% OF CNT IN CNT SUSPENSION:

Note: At this point, the CNT/DMF *solution can sit safely in the fume hood (covered with a lid and parafilm) indefinitely. When it is to be used at a later date, simply begin the instructions from step 12.*

10. Sonicate the CNT/DMF mixture in glass container with lid at *room temperature* for about 30min. (if it has been sitting around since 24 hours, sonication can help CNTs to re-disperse)

11. To determine if the CNTs are suspended, use spatula to scoop out a bit of the solution. If the solution has no visible agglomerates and is optically opaque, the CNTs are dispersed well.

12. Determine the concentration of CNTs in DMF in the stock solution.

******This concentration determination is critical and must be done carefully******

You are measuring very small masses (~0.1 mg) very close to the noise of the scale, so you must take care to ensure an accurate measurement. I recommend you triple weigh the dish when empty, when filled with solution, and when dried out to minimize errors. Also

measure at least three dishes (the larger Al dishes = better accuracy). There is a trade off in CNT concentration – the higher the concentration in DMF the better the accuracy of this method; however the poorer the dispersion is expected to be.

13. Measure weight of empty Al dish. Add some CNT stock solution to dish (transfer via glass pipet), measure weight of filled dish (I recommend covering dish with petri dish while transferring it to balance to minimize amount of DMF evaporation outside of the hood), place filled dish on hot plate (in hood) and let DMF evaporate (this takes a few minutes), you want to make sure it well dried before weighing dish again. Don't set the hotplate too high – you do not want to rolling boil causing CNTs to leave the dish. From mass of stock solution and residual mass when dried you can work out mg CNT/ mg stock solution.

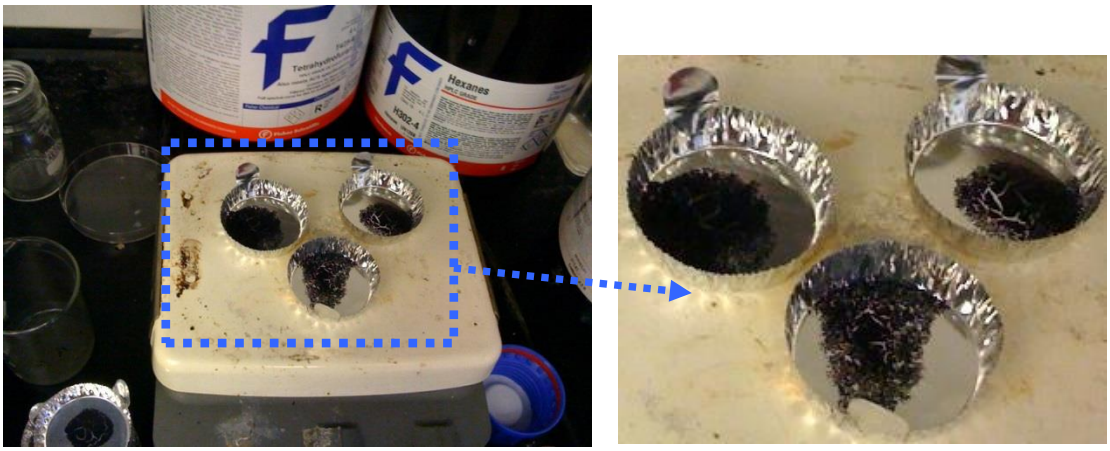

Figure A.2. Dried CNTs in Al dishes.

Table A.1. The above table shows an example of calculations done for 3 samples of a CNT/DMF solution. By averaging the mg CNT / mL DMF column, 1.859 mg CNT per mL DMF can be obtained.

	Before bake			**After bake**			
	dish (g)	**dish+DMF/ CNT (g)**	**DMF/CNT (g)**	**dish+CNT (g)**	**CNT (g)**	**DMF (g)**	**CNT (mg) / DMF (mL)**
Sample 1	1.2584	2.2022	0.9438	1.2602	0.0018	0.9420	2.02418
Sample 2	1.2595	2.1476	0.8881	1.2607	0.0012	0.8869	1.43329
Sample 3	1.1032	2.0044	0.9012	1.1050	0.0018	0.8994	2.12006

A.4. PREPARING CNT/PS NANOCOMPOSITES BY THE COAGULATION METHOD[2]

Note: at this point you may need to make a larger spreadsheet to calculate the amount of stock solution/ DMF needed for dilution/ amount of PS solution/ etc needed for each of your composites.

14. For coagulation you want to work at 0.25 mg CNT/ 1 ml DMF. This means you will have to transfer a known amount of the stock solution then add DMF to dilute it to below this level. Keep in mind the 125 ml and larger jars are too heavy for the lab balance. Our method was weigh a 20 ml vial, fill it with the approximate amount of stock solution required, weigh the filled vial (hence getting a mass of stock solution and thus the mass of

CNT). We then transferred this solution via pipet to a larger jar, then used DMF to rinse the 20 mL vial and the pipet (to ensure all the CNTs were transferred), then topped up the jar with the rest of the DMF required to reach an approximate concentration of 0.25 mg CNT/ ml DMF.

15. To avoid any settling/aggregation you want to transfer the stock solution very close to the time that you determined its concentration. If you are making a set of composites with a range of compositions, it is recommended that you transfer all the stock solution needed for all of them all together. If you let the stock solution sit around for a while, you must recalculate the concentration (also keep in mind that the length of the CNT bundles can change with sonication time so you want to strive to have a uniform sonication history for all you samples, or at the very least re-determine the bundle size if the sonication history has varied).

16. Once the appropriate amount of CNT stock solution has been diluted, it needs to be sonicated for 24 hrs. At the end of 24hrs the appropriate amount of a PS stock solution will be transferred to it and then immediately coagulated to minimize any aggregation.

Note: If making a range of composites, we recommend staggering the start of sonication by at least 30 minutes between samples as this will ensure enough time to coagulate and filter

a composite before you need to remove the next sample from the sonicator. If they all start at the same time you will either have varied sonication histories or will have to let solutions sit different amounts of time before coagulating – neither of which is ideal.

17. Prepare a polystyrene/DMF solution (depending on MW 5-10 wt% PS in DMF should work fine). Let this solution stir at least over night to ensure the polymer is well dissolved.

18. Again to determine the amount of PS transferred, we weighed 20 ml vials, filled with solution, weighted again. After the CNT/DMF solution had been sonicated for 24 hours, it was removed from the sonicator, the weighed PS solution as transferred quickly via pipet (the pipet was rinsed with a small amount of DMF to minimize any PS remaining on it). The sample was then swirled for a count of 30, and then sonicated for a count of 30 seconds. Next it was rapidly pipette into an excess of DI water (need at least a 5:1 DI water: DMF volume). After transferring the PS solution, the vial was closed and then reweighed to account for many materials that stuck to the sides and was not transferred.

Note: The polymer solution is coagulated using shear forces of water in the beaker, using the fact that water and DMF are miscible and polymer/CNT are hydrophobic.

19. The water was placed in a beaker with a large stir bar on a hot plate and stirred vigorously while the DMF/PS/CNT mixture was pipetted. As soon as the DMF hits the water it should look grey/black and become opaque. Depending on the volume of DMF the transfer should take 1-2 minutes. Previous students (Fangmin Du) have used a blender instead of a beaker/stir bar for the coagulation.

20. After all the sample has been transferred to the water, the resulting suspension is filtered through filter paper on a regular filter. For low CNT concentrations this goes fairly rapidly and the residue looks light grey. For higher CNT concentrations this can take ~20-30 minutes and the residue will look muddy/sludgy and will be darker. Take care that the filter paper is well seated before filtering (wet with DI water and pull vacuum to seat, if the filtrate is not clear then some is going under the filter paper and it needs to be re-filtered to collect the composite). Put filtrate into DMF/Water waste container. If any gets under the filter, you can re-filter the filtrate to recover it.

21. The residue can be rinsed with DI water or methanol before being scrapped from the filter (easiest to do this if it is still slightly damp and muddy, but you don't want it to be too sludgy or soupy). Transfer to an aluminum dish and cover with Al foil with small perforations to let dry in the hood for at least a day.

Note (Kristin): If the composite you coagulated is above 6wt%, then you must take the coagulated mixture of water / DMF / CNT (with higher wt %, i.e. above 6wt%, you will notice the coagulated solution will be dark, instead of having solid pellets precipitate like that of low CNT wt%) and run it in the centrifuge. Take centrifuge plastic vessels (50mL each) and run centrifuge at 5000rcf for 10 minutes. This will allow for the very fine composites to agglomerates, making filtering easier.

Figure A.3. Resulting composites may look different depending on the wt% of CNTs. After filtering, wet composite are scraped off from the filter (Left). After drying, all composites should look uniform and black (middle). After pressing they should look black and shiny (right).

22. Place in vacuum oven (using liquid nitrogen cooled solvent trap) for 24 hours at T = 125°C (this is to achieve a temperature of~ 25°C above the T_g of the PS; if a different polymer is used, this oven temperature may need adjusted.) When done, empty solvent trap

into DMF waste container. Depending on how wet the samples were when they go into the oven, you need to take care that the solvent trap does not clog. If it does the pressure in the oven wills start to rise. To fix this, close all the valves to the oven (to minimize any escape of DMF vapors into the lab), turn off vacuum, remove solvent trap, warm it up, empty and dry it, replace, pull vacuum again and open oven valve. A methanol rinse of the material may help with this as it will evaporate more quickly than water/DMF at room temperature.

23. Pressing: composites can be pressed between stainless steel plates. Al is not recommended as mold material can composite can deform mold making it hard to remove samples, brass or stainless steel work well. Press at 150°C and between 1-2 tone of pressure.

A.5. DETERMINING RESIDUAL FE CONTENT

Run TGA in ***platinum*** pans. Heat to 800°C at 5°C /min with air flow at 100 mL/min. If sample hasn't been thoroughly dried you may want to hold at ~120°C or 160°C for 30 minutes to allow residual water or DMF to come off. Take dry weight at 200C and residual weight at 800°C. Assume that all residue mass is Fe_2O_3 (this could in theory be checked via powder X-ray diffraction on the residual – the residual will be bright red). To calculate residual Fe

$$\frac{m_{800}}{m_{200}}\left(\frac{2m_{Fe}}{2m_{Fe}+3m_{O}}\right)=\frac{m_{800}}{m_{200}}\left(\frac{2*55.85}{2*55.98+3*16}\right)=0.7\frac{m}{m} \quad \text{(A.1)}$$

For purified tubes TGA should be smooth decrease starting around ~400°C. For as received material you may see an increase in mass and spike in heat flow due to formation of lots of Fe_2O_3. Also the onset of mass loss may happen earlier, be finished at a lower temperature.

A.6. DETERMINING THE CNT BUNDLE SIZE[3, 4]

Set aside some of the diluted CNT/DMF stock solution just as if you were making another composite (you don't need very much 10 ml is fine). Sonicate the same as you did for the composites. In order to prevent aggregation of the CNTs during solvent evaporate, it is preferred to use an APTES coated Silicon wafer (for an explanation of preparation of this wafer see Stijn Brand's master's thesis or ask the Composto group as they do this regularly). Dip the treated wafer into the the CNT/DMF solution briefly (~1s) then immediately rinse with methanol and blow dry with either compressed nitrogen or Argonne. It is recommended to prepare several samples to ensure some will be suitable for bundle size determination. Store sample covered to prevent contamination and image using an AFM in tapping mode. You are looking for dispersed bundles. Diameters are

determined from line scans across the height images while lengths were easier to measure using the amplitude or phase images in photoshop. Ideally the AFM sample should be prepared at the same time as the coagulated composites and should have the same history/concentration as the composites. The only difference is that no polymer solution will be added.

Note: If you just allow DMF to evaporate slowly you just end up with large mats of CNTs and it is not possible to determine L/D. Rinsing with methanol also helps remove CNTs that are not firmly affixed to the substrate improving the sample. Minfang says that it may be possible to get a good sample on an untreated wafer if you blow dry immediately with nitrogen, but I found that not to be successful.

A.7. REFERENCES

1. Zhou, W.; Ooi, Y. H.; Russo, R.; Papanek, P.; Luzzi, D. E.; Fischer, J. E.; Bronikowski, M. J.; Willis, P. A.; Smalley, R. E., *Chem. Phys. Lett.* **2001,** *350* (1-2), 6-14.

2. Du, F. M.; Fischer, J. E.; Winey, K. I., *J. Polym. Sci. Pt. B-Polym. Phys.* **2003,** *41* (24), 3333-3338.

3. Bryning, M. B.; Islam, M. F.; Kikkawa, J. M.; Yodh, A. G., *Adv. Mater.* **2005,** *17* (9), 1186-1191.

4. Stijn Brand's Master Thesis, 2004, "The effect of purification, sonication and nitric acid reflux on the length and diameter distributions of single walled carbon nanotubes: An atomic force microscopy study".

Appendix B

I-V Measurements on CNT/PS Nanocomposites

I-V measurements were conducted on our CNT/PS nanocomposites to confirm the rod network formation. All *I-V* curves for nanocomposites were measured and fit using the fluctuation-assisted tunneling model to get the high field conductance (G_h). Then G_h was converted to conductivity according to the sample geometry. The conductivities for all our nanocomposites are shown in Figure B.1. Note that the jump in conductivity happens at lower CNT concentration for SWCNT/dPS+hPS nanocomposites, which means the critical concentration ϕ_c is lower. This is expected since SWCNTs have higher number densities and aspect ratios. After percolation, MWCNT/dPS+hPS nanocomposites have much higher conductivities than SWCNT/dPS+hPS nanocomposites; this is because MWCNTs are better conductors.

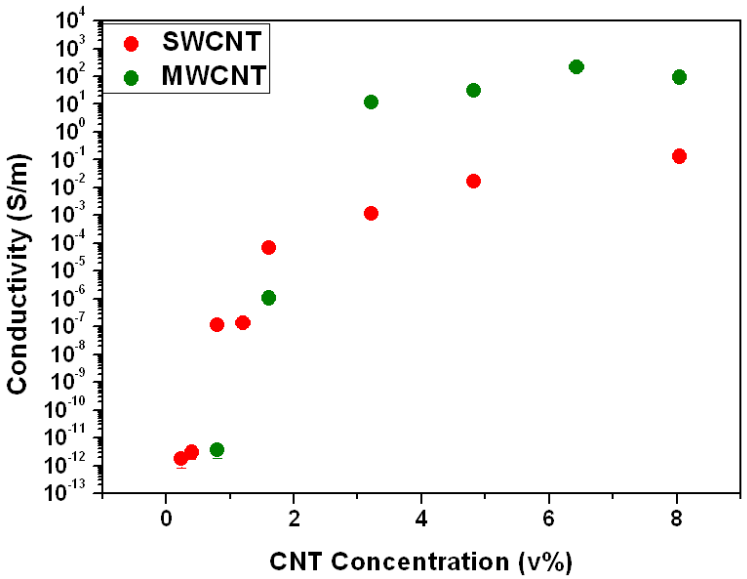

Figure B.1. Conductivity for SWCNT/dPS+hPS and MWCNT/dPS+hPS nanocomposites as a function of CNT loading.

The critical concentration for electrical percolation can be obtained by fitting the conductivity data to the equation

$$\sigma = C\left(\frac{\phi - \phi_c}{\phi_c}\right)^{\alpha} \tag{B1}$$

where σ is the conductivity, ϕ represents the CNT volume fraction, ϕ_c is the critical volume fraction, and C and α are fitting parameters. Notice that this equation only applies when the concentration is above the percolation concentration. Figure B.2 shows the fitting results and the critical concentrations for the SWCNT and MWCNT nanocomposites are 0.47v% and 1.45v%, respectively. This agrees with our fitting results for parameter *B*,

where we found SWCNT composites have much higher values of *B* than MWCNT composites, and B starts to increases at lower concentration for SWCNT composites. In a conclusion, electrical measurement on CNT/dPS+hPS nanocomposites confirms the rod network formation in our composites.

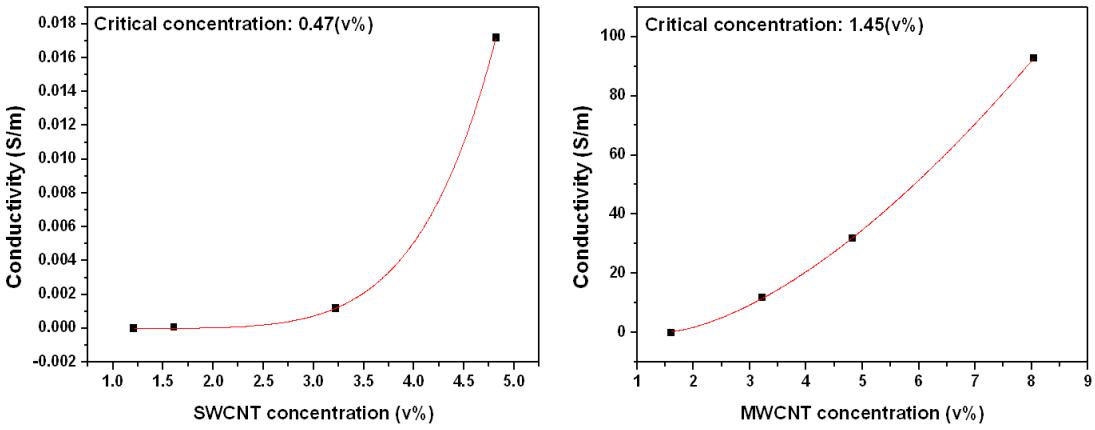

Figure B.2. Fitting the conductivity of SWCNT/dPS+hPS and MWCNT/dPS+hPS nanocomposites as a function of the CNT concentration with Equation S1 The percolation concentration is higher for SWCNTs (0.47v%) than MWCNTs (1.45v%).

Appendix C

Standard Operating Procedure for SpinLine

Instrument: SpinLine (DACA Instruments)

Location: LRSM 220B

Edition 1: Minfang Mu (Jan. 30, 2006)

Edition 2: Wei-Shao Tung (Dec. 11, 2014)

Required Personal Safety Equipment:

Safety goggles & heat resistant gloves

C.1. OVERVIEW OF PROCEDURE

The SpinLine is an instrument designed to extrude small quantities of polymer or composite fibers in a precise and controlled way. This procedure describes the operating steps and the safety limits for the instrument.

C.2. DETAILED PROCEDURE

1. Power on the Winder by pressing the button on the right side at the back of the Winder. Press the traverse ON-OFF switch (green button on the extruder) if you

want to control the traverse speed. The width of the movement of the traverse guide can be controlled by adjusting the two knobs in front of the traverse guide.

2. Set up the barrel: Put in the interior part of the barrel (sample chamber). Pick the desire spinneret (with 0.5mm, 1.0mm, or 1.5mm) and mount it on the bottom of interior part. Assemble the outer part of the barrel (heating element), and load your material (see operation manual on page 20 for more details).
3. Power on the Piston Extruder by pressing the ON button located on the right side at the backside of Piston Extruder.
4. Set the temperature of the barrel through turning on the orange HEATER button and adjusting the "▲" and "▼" button. The temperature cannot be higher than **360^{o}C**.
5. Heat up your sample to the desired temperature and let it sit for 20 to 30 minutes to make you sure your sample is at its melt state.
6. The movement of the piston and winder is controlled by the controller. When you turn on the instrument, the controller will show some options. You can choose "continue" or "quit". If you choose continue, the following options are available:

a. EXTRUDER ONLY: Operate only the Piston Extruder. The winder should be turned off.

b. WINDER ONLY: Operate on the winder. The Piston Extruder will not operate.

c. EXTRUDER WINDER: Operate the Piston Extruder and the Winder and be useful for quick spinning of the fiber.

7. Set the hardware limit: Choose HW LIMIT and the piston will find its starting position.
8. Set the spool diameter 75 and press enter.
9. Set the desired winder initial speed and the adjustment increment (Notice: the best winder rate depends on your materials and your desired fiber diameter).
10. Choose the barrel to tell the program which of the three cylinders is attached to the Piston Extruder.
11. Set the piston to ST. POS. (starting position and the tip of the piston should be 3-5 cm into the barrel).
12. Set the piston initial speed (1mm/min) and adjustment increment (1-2 mm/min).

13. Now, the main menu is displayed. Each option controls different parts of the SpinLine. Start or stop spinning by pressing the Start/Stop button. Control the winder or extruder by pressing INC or DEC button. During the experiment, if the load is above **4585N**, the entire system will shut down.
14. Initially if the piston moves too slowly, it will take a long time to reach the samples and to start the extrusion, so use the piston speed as 3-4 mm/min. Once it touches the samples (as your samples start to be extruded out from the spinneret hole or an increase in the load), reduce the piston speed to 1-2 mm/min or as desired for the experiment.
15. When the extruded rods come out, pull it with tweezers and attach it with the winder using a scotch tape. Initially, the winder speed should be very slow which helps to attach fiber to it. Then increase the winding speed by pressing the INC button under WINDER.
16. The experiment can be ended by pressing QUIT button or when the materials in the extruder in run out. Press QUIT and F6-DONE button to end the experiment.

17. After you finish your experiment, you should dissemble the barrel when it is still **hot** (Notice: make sure you wear gloves). Clean the hardware after it is cooled down.

C.3. ISSUES TO CONSIDER

Establish best practices to ensure the highest quality fibers. Provide cautions and guidelines to protect the instrument from unintentional damage. Make sure your sample as void free, because too much bid voids may cause the fiber to break during the process. You can use hot press to press out the voids in your material, or you can anneal your material inside the extruder by applying some pressure at high temperature. After dissemble the barrel, make sure you put a warning sign to let other people know it is hot.

C.4. STANDARD OPERATING CONDITIONS FOR DIFFERENT MATERIALS

Polymethyl-methacrylate (100kDa) & PMMA/SWNT (2 wt%) composite:
Temperature: 200 $^{\circ}$C
Spinneret speed: 1mm/min
Spinneret diameter: 0.5mm
Winder speed: 1-21 m/min
Polyethylene & PE/SWNT (20 wt%) composite:
Temperature: 150 - 160 $^{\circ}$C
Spinneret speed: 1mm/min
Spinneret diameter: 0.5mm
Winder speed: high to 50 m/min for PE; high to 5m/min for composite

Appendix D

Fitting Uncertainty for ERD data

Figure D.1 shows the uncertainty of fitting in general when we fit an example depth profile obtained from ERD to convolution of Fick's second law and a Gaussian function.

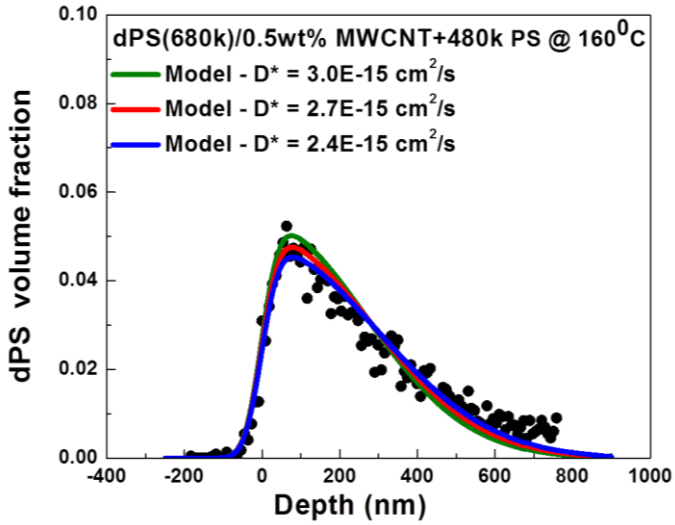

Figure D.1. The depth profile of 680k dPS partially diffused into 0.5wt% MWCNT/PS nanocomposites after annealing at 160 °C for 40 hours. Lines correspond to the convolution of a Gaussian function and Equation 4.3, where h = 18 nm and three different diffusion coefficients as given in the figure. This figure illustrates the uncertainty in fitting the diffusion coefficients using the depth profile with the convolution of Fick's second low and a Gaussian function. The uncertainty is about 10 %. The diffusion coefficient we obtained from the fitting is 2.7E-15 cm^2/s, and ± 10 % of that diffusion coefficient still provide relatively good fits.

Appendix E

Standard Operating Procedure for Rheometrics RSA-II Rheometer

Location: Room 220B

Edition 1: Nancy Zhou and Mingang Mu (Feb. 2, 2006)

Edition 2: Wei-Shao Tung (Dec. 10, 2014)

Required Personal Safety Equipment:

Safety goggles & heat resistant gloves

E.1. OVERVIEW OF PROCEDURE:

The RSA-II rheometer is a dynamic mechanical analyzer dedicated to characterizing rheological properties of solid materials, which can be of film, fiber, or block form. Tensile properties measured by the RSA-II rheometer include storage modulus, loss modulus, complex modulus, phase angle shift, tan(delta), complex viscosity, and relaxation modulus.

E.2. DETAILED PROCEDURE:

1. Drain the water in the air separator filter (next to the hot press instrument) and make sure the compressed air is dry
2. Turn on the compressed air valve located on the wall (behind the hot press instrument). Turn counterclockwise for about 45°
3. Check the pressure on the two pressure gauges located on the backside of the rheometer. The left gauge should read ~ 50 psi if using air to heat up samples and ~ 40 psi if using nitrogen to heat up samples. The right gauge should read 40-42 psi. It is important to make sure that the air pressure is correct.

Do not turn the instrument on until you have done step 1 to step 3

4. If you want to test your samples under air atmosphere then jump to step 5 and then step 7. If you want to test samples under inert atmosphere or at temperature lower than room temperature then connect the liquid nitrogen tank to the LN_2 controller (Notice: connect to the liquid port not the gas port). Turn the valve on the liquid nitrogen tank on.
5. Power on the instrument by:
    a. Press the ON button located on the control computer

b. Turn on the switch (red) located on the right side of the environmental control panel

c. Press the ON button on the system control panel

6. Switch the "LN_2/GAS" button to LN_2 by pressing on it (Notice: the bulb is broken so that entire button will not be lit). Make sure the oven air pressure is at 40-42 psi. If not, tune it with the regulator.

7. Let the instrument warm up for about 30 minutes before turning on the motor for sample testing. If using LN_2, also make sure the "LN_2 Ready" button light up before testing, it usually takes about 15 ~ 20 minutes. Notice that it is normal at this point for the Xducer bearing overload light to be lit.

8. After about 30mins, press the Motor ON/OFF button located on the test station. The motor is on if the light on the button is lit. This energizes the motor (bottom) and the transducer (top). At this moment, both bearing overload lights should not be on.

9. Start the TA Orchestrator software and wait until the software shows "online". You can also manually set it to online by going into the Utilities menu.

10. Go to the Utilities menu and choose “Calibrate Instrument” and press “XducerCal”. Mount the hook and press “Zero”, and then a window will jump out to ask you hang on the weight. Hang on the 500g weight and see if the value is close to 500g. If the value is very close to 500, like 500 ± 0.01, then press “Accept”. If not, press “Force Cal”, and input 500 then press “Calibrate now”.
11. Turn off the motor and install the fixtures, which depend on the type of mechanical test you want to conduct. Refer to the Rheomotrics Manual for more information on each fixture, its testing limits, and sample requirements.
12. Go to the Utilities menu and choose “Set Auto Tension Limits”. Set the value according to your sample geometry. The following values are used in general, but they may vary for your particular test, so find the most ideal value for your test.
    a. Fiber/Film Fixture: 4mm Tension 1mm Compression
    b. Shear Sandwitch: 0.5mm Compression 4.5mm Tension

    Select the appropriate combination and press OK.
13. Go back to the Utilities menu again and select “Tool Calibration”. Only the fixtures should be mounted (no samples). Press OK then the upper tool will move

to six different positions in a increment of 0.5mm and determine the tool calibration necessary and return back to its home position.

14. Double check that the tool calibration has been accurately performed by pressing the meter 10X button located on the top of the system control box. The force meter should be reading 0%. If not, adjust the adjacent zero knob until the reading is 0%.
15. Load your sample in the fixtures and tighten the screws (Notice: do not tighten is too much, or the Xducer bearing overload light will be lit). Close the oven door and the left gauge should read 40-42 psi while the right gauge still reads 40 psi.
16. Click on the Green Start in the upper left corner in the TA Orchestrator program. Name your file, add notes to the file, change sample geometry which should be consistent with your fixture, and edit test.
17. For shear sandwich test, heat up your sample above its glass transition temperature and let it sit for ~ 15 minutes, and then open the oven door to further tighten the screws (Notice: make sure that you wear the heat resistant gloves).
18. When your tests are finished and you are ready to shut down the instrument, first turn off the motor. If LN_2 is used, close the valve on the LN_2 tank.

19. Dissemble your fixtures. Be careful to not apply too much pressure to the motor and transducer when taking off the fixtures.
20. Turn off the system control panel and the side switch
21. Turn the control computer off
22. Close the compressed air valve

E.3. ISSUES:

It is important to make sure that the air fed into the rheometer is dry and at an accurate pressure. Check the pressure gauges regularly to make sure that there is no an inconsistency in the compressed air line. If there is an over bearing on the transducer, this instrument will shut the motor off automatically and end the test. This sometimes happens when LN_2 runs out in the middle of the test. Do not let the temperature drop below your sample T_g to remove your sample. Remove your sample when it is still in its melt form or otherwise it will be very hard to dissemble your samples from the fixtures, and you may apply too much force on the transducer and ruin it.

Appendix F

SEM Images of Anodized Aluminum Oxide Membranes

This appendix provides the SEM images of the top view and the cross section view of the AAO membranes used in Chapter 7 and Chapter 8.

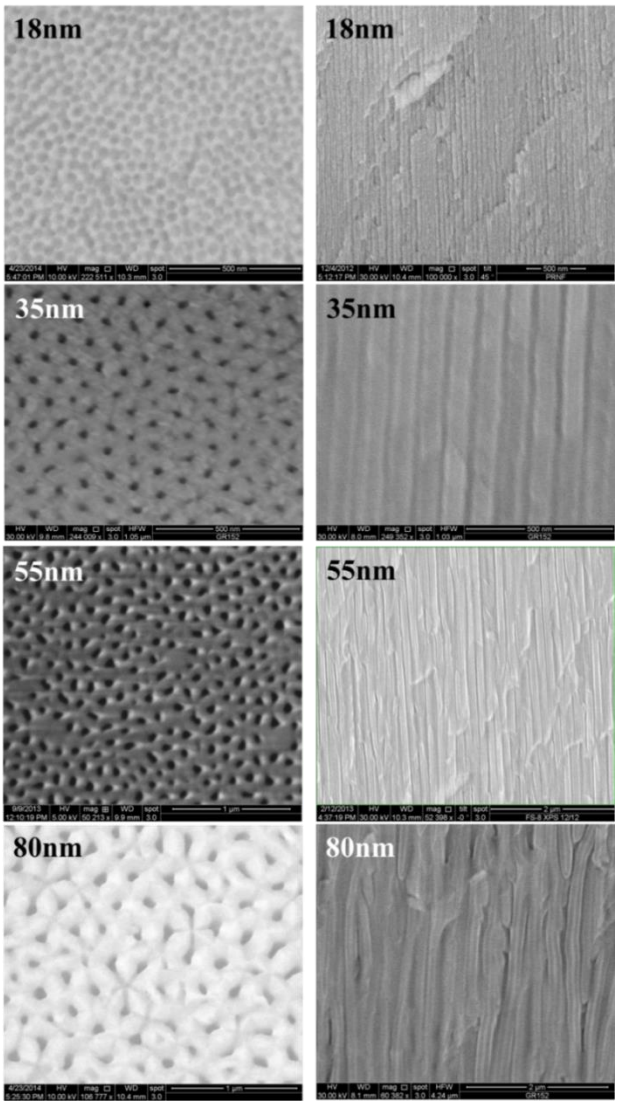

Appendix G

Porosity of AAO membranes by ERD

This appendix shows obtaining the porosity of AAO membranes by ERD measurements, which are associated supplemental information for Section 7.3.3. The ERD measurement on AAO membranes is on the side where a thick PS film is placed during the infiltration process. Figure G.1 compares the signal of hydrogen from a thick PS film (> 10μm) to that from a PS infiltrated AAO membrane with 55nm pore diameter. Counts on the y axis are proportional to the volume fraction of hydrogen in the samples. By dividing the counts from the PS-infiltrated AAO membranes in the flat region of the ERD spectra to the thick 100% PS, we estimate the volume fraction of hydrogen in our membranes, which represents the porosity of the membranes.

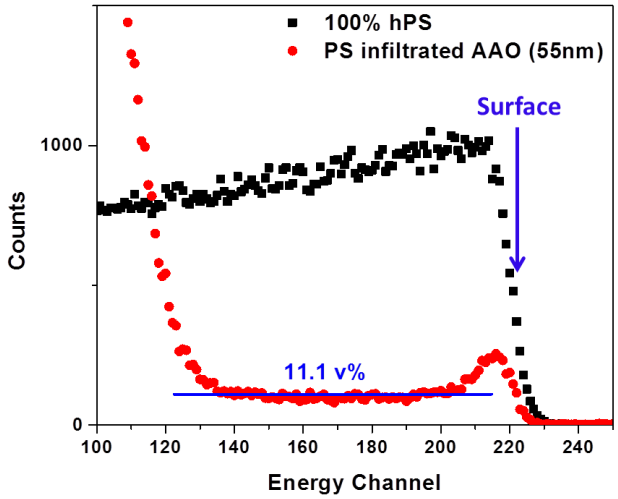

Figure G.1. Counts of hydrogens measured from ERD for a 100% thick PS film and for a PS infiltrated AAO membranes with 55nm pore diameter.

Appendix H

Effect of Monomer Density and Chain Length on Polymer Local Dynamics

This appendix shows how monomer density and local dynamics are affected by scaling of the simulation box, and the comparison of local dynamics between N = 50 and N = 350. These are associated supplemental information for Section 7.4.2. Figure H.1 (a) shows the monomer density as a function of the distance from wall before and after the scaling of the simulation box in the z direction. Associated MSD (T = 1, LJ time = 4.8) versus r along the z and the x axis before and after scaling is shown in Figure H.1. (b).

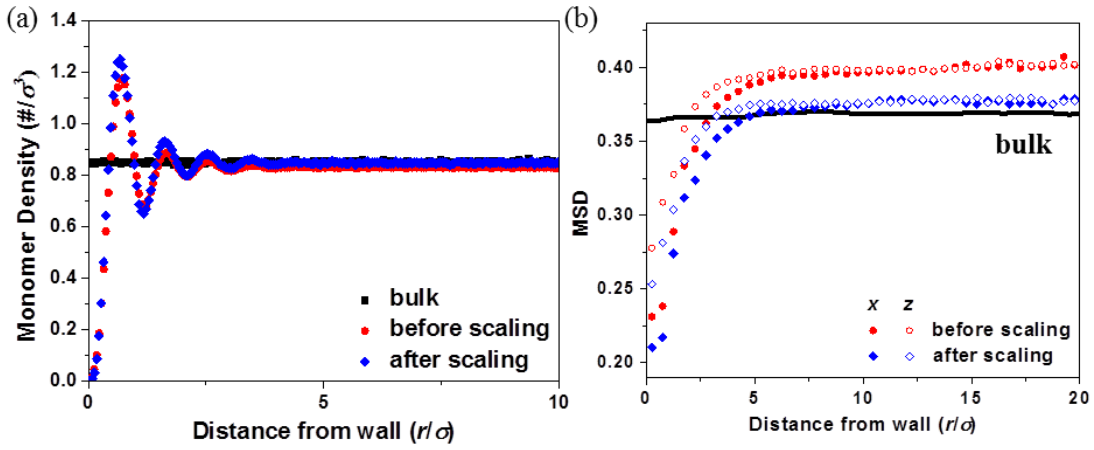

Figure H.1. (a) Monomer density as a function of the distance from wall for d = 40 σ before and after scaling the simulation box. (b) MSD (T = 1, LJ time = 4.8) versus r along the z axis (empty symbol) and the x axis (filled symbol) for d = 40 σ before and after the scaling.

Figure H.2 shows the monomer density and MSD (LJ time = 4.8) versus r for N = 50 and 350 confined to both 10σ and 20σ cylindrical confinements. It can be seen that the fluctuation of the monomer density and the equilibrated density do not depend on the chain length. Although the local MSD for N = 50 polymers is slightly higher than the N = 350 polymers, which may due to the 7-fold increase in chain ends for N = 50 polymers, it is ignorable.

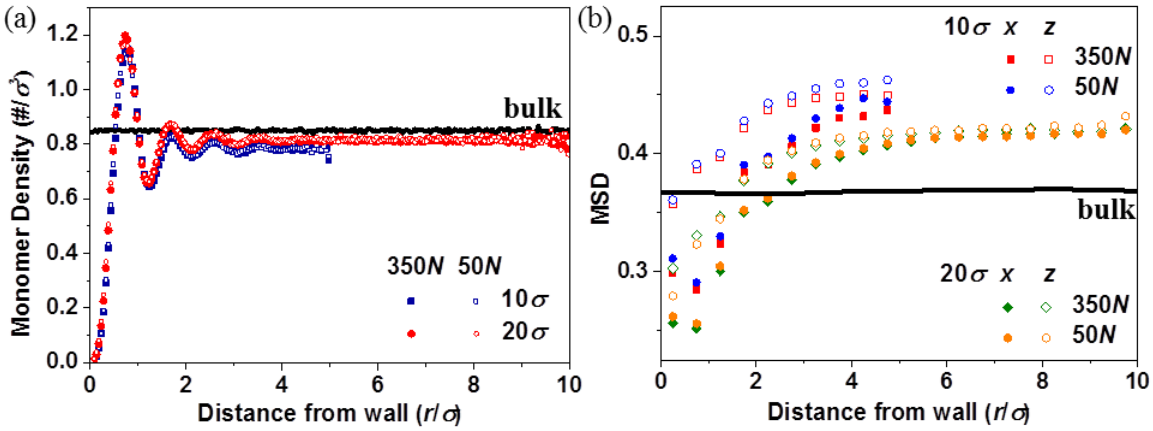

Figure H.2. (a) Monomer density versus r for 50N and 350N polymers confined in 10σ and 20σ cylindrical confinements. (b) MSD (T = 1, LJ time = 4.8) versus r along the z axis (empty symbol) and the x axis (filled symbol) for N = 50 and 350 polymers confined in 10σ and 20σ cylindrical confinements.

Appendix I

Polymer Chain Conformation for Polystyrene Confined in AAO Nanopores Using SANS

Overview

This appendix describes the preliminary results for probing the polymer chain conformation of polystyrene confined in AAO nanopores using small angle neutron scattering (SANS).

I.1. SAMPLE PREPARATION AND CHARACTERIZATION

AAO membranes were purchased from Synkera Technology Inc., CO, USA, with nanopore diameters (d) ranging from 18nm to 150nm as reported by the vendor. Protonated-polystyrene (M_w = 395 kg/mol, PDI = 1.05) and deuterated-polystyrene (M_w ~ 394.08kg/mol, PDI = 1.02) were purchased from Polymer Source Inc., Quebec, CA. Because the incoherent scattering length of hydrogen is very high, only the scattering from dPS was analyzed to obtain the chain size. The bulk end-to-end distance, R_{ee}, of dPS is around 39.8nm, and gives a range of d/R_{ee} ~ 0.46 to 3.83. Polystyrene was infiltrated into membranes with a melt annealing method. Details of the method can be found in

Chapter 7.

Samples were characterized by small-angle neutron scattering (SANS) on NG3 and NG7 instruments at the NIST Center for Neutron Research in Gaithersburg, MD, USA. For NG3, three sample-detector distances, L = 1.3 and 4m with λ = 6 Å and L = 13m with λ = 8.4 Å, provided a q-range of 0.001$Å^{-1}$ to 0.4 $Å^{-1}$. For NG7, three sample-detector distances, L = 1, 4, and 13.5m with λ = 6 Å, provided a q-range of 0.001$Å^{-1}$ to 0.5 $Å^{-1}$. A detailed description of the calibration method and data reduction process can be found in Chapter 2.

To find the contrast matching condition of the membranes, mixtures of dPS and hPS with dPS/hPS volume ratio = 0/100, 20/80, 40/60, 60/40, 80/20, and 100/0 were prepared and infiltrated into the membranes. Results of contrast matching experiments will be discussed later.

I.2. STRUCTURE OF EMPTY MEMBRANES

To probe the structure of polymer chains in AAO nanopores, it is important to first understand the structure of the nanopores. The incident neutron beam direction was parallel to the cylindrical axis of nanopores as shown in Figure I.1 (a), and associated neutron scattering intensities for empty membranes with different diameters are presented

in Figure I.1 (b). For each diameter, two membranes were measured to ensure that the structural variation among different membranes was negligible.

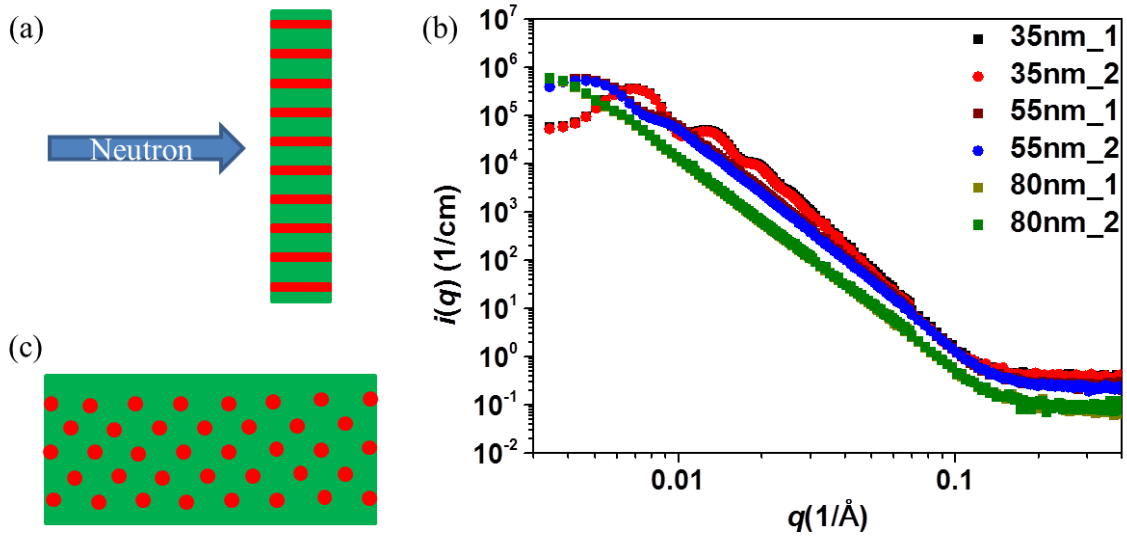

Figure I.1. (a) Schematic of incident neutron beam and AAO membranes. Beam direction is parallel to the cylindrical axis of nanopores. (b) Neutron scattering intensities for empty membranes with 35nm, 55nm, and 80nm diameter nanopores. For each diameter, two individual membranes were measured. (c) Schematic of the top view of the membranes, showing hexagonal packing of nanopores as seen along the beam direction.

As can be seen in Figure I.1 (b), scattering intensities for membranes with the same diameter are perfectly overlapped, which indicates that the structure of nanopores is identical. Moreover, we can clearly see structural peaks, which come from the hexagonal packing of parallel nanopores (Figure I.1 (c)). The first structural peak comes from the

closest neighbor nanopores and higher-order peaks correspond to contributions from the next nearest neighbors (second-order peak corresponds to second nearest neighbors, etc.).[1] The primary peak moves to smaller q for larger pore diameter because the distance between nanopores increases.

I.3. SCATTERING OF FILLED MEMBRANES

We first tested how different degrees of infiltration affect the total scattering intensity. We controlled the degree of infiltration by using different annealing times during melt annealing infiltration. Figure I.2 shows the scattering intensity of an empty 35nm membrane and two 35nm membranes with different degrees of infiltration for dPS. Samples are measured in air, so the scattering strength of nanopores is coming from the scattering length density difference ($\Delta\rho$) between aluminum oxide and air. The scattering length density of aluminum oxide (ρ_{AAO}) is ~ 4.6×10^{10} cm^{-2} assuming a mass density of ~ $3.2 g/cm^3$.[1] When dPS ($\rho_{dPS} = 6.47 \times 10^{10}$ cm^{-2}) is infiltrated into the membrane (red data), the scattering length density difference decreases so that the overall scattering intensity is lower as shown in Figure J.2. Higher degree of infiltration (blue data) shows even lower intensity because more AAO – air interfaces are substituted by AAO – dPS interfaces.

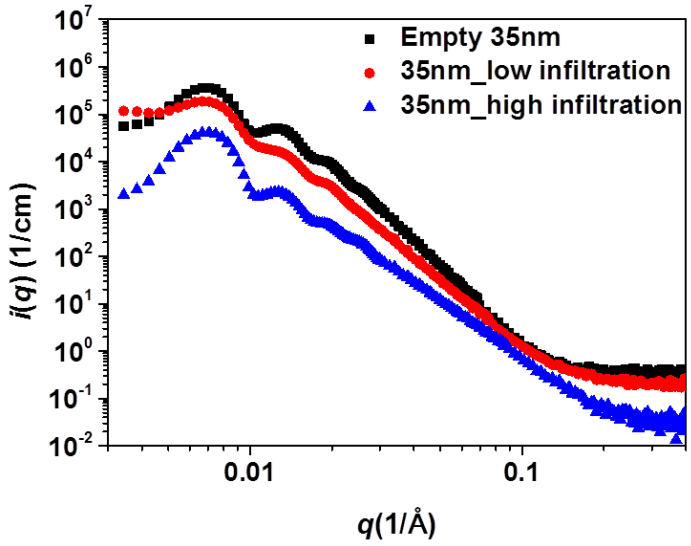

Figure I.2. Neutron scattering intensity for an empty 35nm membrane and two membranes with two degrees of infiltration of 400k dPS.

The main purpose of this work is to study the chain conformation of polystyrene confined in AAO nanopores. However, the scattering from the membrane itself is very strong. To decrease the scattering intensity from the membrane, we tried to contrast match the scattering length density of aluminum oxide. As mentioned in Section I.1, mixtures of dPS and hPS with 6 dPS/hPS volume ratios were infiltrated into membranes with 35 nm nanopores. Associated neutron scattering intensities are shown in Figure I.3 (a). The scattering curves for membranes infiltrated with different volume ratios of dPS/hPS have almost the same shape, but different intensities. Intensity at q = 0.00707 $Å^{-1}$, the position of the first structural peak for 35nm membranes, is plotted as a function

of dPS volume fraction in Figure I.3 (b), and the data can be fit to the equation

$$i\left(q = 0.00707\text{Å}^{-1}\right) = const. + [x\rho_{dPS} + (1-x)\rho_{hPS} - \rho_{AAO}]^2 \qquad \text{(I.1)}$$

where x is the volume fraction of dPS. The details of the derivation of Equation I.1 can be found in Chapter 2. Ideally, when $x\rho_{\text{dPS}}$ + (1-x) ρ_{hPS} is equal to ρ_{AAO}, the scattering intensity contribution from the AAO membrane will be the lowest as shown in Figure I.3 (b). From the fitting, the contrast matching condition can be determined as x ~ 0.72. ρ_{AAO} can also be calculated using ρ_{dPS} = 6.47 × 10^{10} cm^{-2}, ρ_{hPS} = 1.42 × 10^{10} cm^{-2}, and the contrast matching condition of x ~ 0.72, which gives ρ_{AAO} ~ 5 × 10^{10} cm^{-2}, which is close to the literature value of 4.6 × 10^{10} cm^{-2}.

For polymer chain scattering, we expected to see a shoulder at q ~ 0.01 Å^{-1}, similar to what we observed in Chapter 2. At higher q region, a q^{-2} dependence of total intensity should be observed. However, the scattering from the membranes was still very strong and dominated the total scattering intensity even at the contrast matching point, which prohibited further analysis of polymer chain scattering.

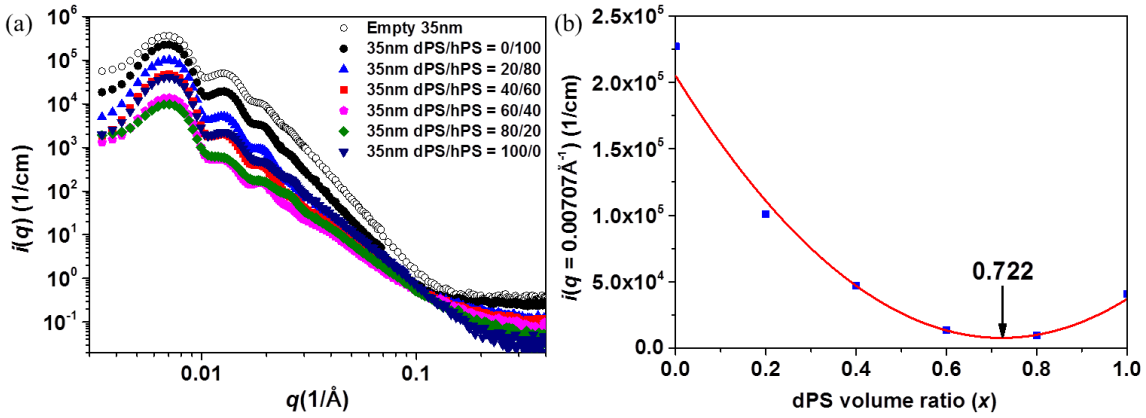

Figure I.3. (a) Scattering intensities of an empty 35nm membrane and filled membranes with different dPS/hPS volume ratios. (b) Intensity (q = 0.00707 Å $^{-1}$) as a function of dPS volume fraction and associated fitting to Equation I.1.

There are two main difficulties of contrast matching for AAO membranes. First of all, the porosity of membranes is only about 10 ~ 15v%. Using a small amount of polymer to contrast match the scattering from membranes is difficult. Moreover, 100% infiltration is very hard to achieve, which means there are always some fragments of empty nanopores contributing to the total scattering intensity. The other reason is that the scattering length density of the membrane itself may not be uniform. Scattering length density is proportional to the mass density of aluminum oxide, which may not be uniform across the whole membrane. This also brings more difficulties to the contrast matching experiments.

I.4. SUMMARY

In this appendix, preliminary results were discussed for probing chain conformations of polystyrene confined in AAO nanopores using SANS. Structural peaks were observed in the scattering from empty membranes, which come from the hexagonal packing of nanopores. From contrast matching experiments, we found the contrast matching condition for the dPS volume fraction $x \sim 0.72$. However, perfect contrast matching is very hard to achieve due to the difficulty of obtaining 100% infiltration and non-uniform scattering length density of aluminum oxide. In the future, a better contrast matching method needs to be designed (e.g., immerse the filled membrane in contrast-matched solvent) or a different measurement geometry should be used (e.g., oblique neutron incidence).[2]

I.5. REFERENCES

1. Marchal, D.; Deme, B., *J. Appl. Crystallogr.* **2003,** *36,* 713-717.

2. Shin, K.; Obukhov, S.; Chen, J. T.; Huh, J.; Hwang, Y.; Mok, S.; Dobriyal, P.; Thiyagarajan, P.; Russell, T. P., *Nat. Mater.* **2007,** *6* (12), 961-965.